DISSERTATION

SYSTEM ENGINEERING APPROACH TO MITIGATE EFFECTS OF ATMOSPHERIC TURBULENCE FOR TERRESTRIAL HORIZONTAL PATH IMAGING SENSORS

Submitted By

John M. Hall

Department of Systems Engineering

In partial fulfillment of the requirements

For the Degree of Doctor of Philosophy

Colorado State University

Fort Collins, Colorado

Spring 2026

Doctoral Committee:

Advisor: Steven Simske

Diego Krapf
Greg Marzolf
Jeremy Daily

ABSTRACT

SYSTEM ENGINEERING APPROACH TO MITIGATE EFFECTS OF ATMOSPHERIC TURBULENCE FOR TERRESTRIAL HORIZONTAL PATH IMAGING SENSORS

This dissertation shall demonstrate how the system engineering process enables development of a novel and feasible approach toward mitigating in real time the image degrading effects of optical turbulence in a horizontal atmospheric path when viewed using an electro-optical imaging system. This work concentrates on the early phases of the system engineering process. The critical output products are a detailed system concept model, a draft specification, and an associated feasibility analysis which verifies the approach is both physically possible and economically achievable. A new optical ray-trace analytical method is disclosed which enables both the development and validation of the system concept. Feasibility analyses show that the technology required is within reach of the current state-of-the-art, and also reveal the risks and technology gaps which may yet need to be resolved in future work.

Keywords: *atmospheric turbulence, aberration theory, system engineering, Capella, system-based modeling, optical system design and modeling, opto- mechanical design, radiometry, photo-detector, Johnson Criteria, video processing, displays, human visual system*.

TABLE OF CONTENTS

Chapter 1 - Introduction

Strong turbulence within the Earth's atmosphere creates optical aberrations which degrade the image quality of electro-optical imaging sensor systems [1]. The effects are particularly pronounced when the viewer's line of sight is a long horizontal path through the thickest part of the Earth's atmosphere near sea-level. Turbulence effects come from random processes within the structure of the atmosphere, and thus optical correction of turbulence aberrations in real time is a significant challenge. The purpose of this work is to apply the System Engineering method to capture the critical functional requirements and then begin the development of a new system architecture which is optimized for the task. The engineering effort requires expertise in multiple technical disciplines including radiometry, thermodynamics, atmospheric behavior, optical design, opto-mechanical design, photo-detector operation, microprocessors, and image processing algorithms. The discipline of Systems Engineering provides a framework of general processes by which the technical expertise can be brought together and then optimize a system design to provide the best performance within various constraints. The scope of this work focuses primarily upon the initial phases of the system engineering development process, which includes concept development and feasibility analysis. The remainder of this introductory section will better explain what is meant by an "imaging sensor", the general nature of atmospheric turbulence, the system engineering process, and the product development life-cycle rating scale known as the Technology Readiness Level (TRL).

1.1 Long Range & Real Time Imaging Sensors.

A long range imaging sensor in this context is an apparatus which receives electromagnetic radiation from a distant target and then projects a magnified image of that target which is viewed by an observer. Referring to Figure 1-1 below, the angular subtense of the target is assigned the variable θ, the apparent angular size of the projected image of the target is θ', and the system magnification (M) is given by M = θ' ÷ θ in units of radians or degrees as desired. The atmospheric turbulence phenomena occurs between the object and the entrance aperture of the imaging sensor. For long range viewing, it shall be assumed that the object distance, measured in perhaps units of kilometers, is significantly longer as compared to the dimensions of the sensor itself, which may be measured in units of millimeters or centimeters.

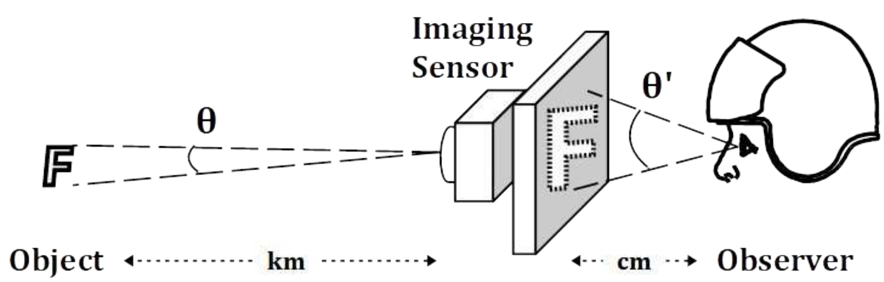

Figure 1-1: Long Range Imaging Sensor Illustration

There are many possible configurations for a long-range, real-time imaging sensor. The all-optical, "Galilean Telescope", which is comprised of a positive powered front objective lens followed by an air gap concluding with a negatively powered eyepiece lens [2], is an example of an early type of optical imaging sensor operating at the speed of light. In modern times, the use of electronic detector arrays and phosphor-screen displays interposed between the objective lens and eyepiece lens have enabled many new features unavailable to all-optical solutions, but in all cases the magnification (M) remains a fundamental parameter. The advance of electro-optical sensor technology brings many new functional aspects into consideration. For the purpose of this document, *real time imaging* is defined as the condition when the time period in which all process events involved in creating and displaying the sensor output image on a continuous basis occurs within 33⅓ msec of the events occurring in the real world scenery being viewed. The value of the actual delay between motion in the real scene versus motion shown in the imaging sensor's output display is called the *lag time*. For an all-optical sensor, the lag time is simply a function of the speed of light ($c = 3 \times 10^8$ m/sec) over the range to the target, which is negligible in most terrestrial horizontal path cases. However, when an astronomer views celestial objects beyond the solar system, the lag time can be measured in years! In an electro-optical sensor, typically there will be some form of electronic clock which sets a time period between new "frames" of data which contain refreshed imagery from the real world scene. The frame concept dates back hundreds of years when it was discovered that a sequence of still images, or frames, could be set into motion to simulate motion of "living creatures" [3]. If the motion is faster than the integration time of the eye, the human observer will perceive the sequence of still images as if it were continuous motion. The frame terminology was later adopted in the motion picture industry [4] wherein the image frames were captured on photographic plastic films, mounted to a rotating reel, and projected onto a theater screen. The integration time of the eye varies with parameters such as ambient light level. Motion picture theaters darken the room lighting to increase the eye integration time, and in those cases a 24 Hz frame rate, or about a 42 msec time period between each new frame, is usually acceptable to most people. Below this minimum rate, the human will perceive a strobe effect or "flicker" which can be quite taxing on the nervous system and will cause fatigue and headache [5]. The Electronic Industry Association (EIA) analog RS170 broadcast television standards increased the frame rate to 30 Hz, or a 33⅓ msec time period which better enables viewing in average room lighting [6][7], and therefore this has been adopted as the critical threshold rationale for a "real time" imaging sensor.

1.2 Turbulence Impacts.

Atmospheric turbulence phenomena results from slight changes in the index of refraction of the air. It can sometimes be seen with the unaided human eye, especially over large areas of paved asphalt surfaces during hot summer days. Turbulence has also been noted by historical figures such as Isaac Newton , who is credited with noting that the atmosphere may have an optical effect during astronomical observations [8]. Sensors designed for long range applications are more sensitive to turbulence effects which can be quite severe, resulting in a significant reduction in the ability of the sensor to resolve a given target at a specific long range [9][10]. Turbulence mitigation for electro-optic sensors working along the horizontal path through the atmosphere has been an ongoing problem for decades [11], and to this day remains a major challenge especially when high image quality is required in "real time". Attempts to mitigate the turbulence effects have been investigated for decades, but with limited success. The application of skyward-looking astronomical "adaptive optics" techniques has thus far not proven successful for terrestrial path applications, and likely never will, as discussed in detail by Gronau [12]. When series of consecutive images are collected over time, a technique often referred to as "Lucky Patch" imaging [13] has proven some success, but this approach cannot provide "real time" operation because of its inherent temporal nature. Perhaps the most successful commercial implementation of lucky patch techniques to date is the "TMSR" algorithm discussed by Droege [14], which is dependent on multiple frames separated by a time greater than a single frame rate. While the TMSR system does provide frame updates in real time, the current output frame is dependent upon the prior output frames and hence the lag exceeds the requirement for real time. The current approaches and their limitations will be investigated in greater detail in later sections of this document; the primary purpose within this introductory section is to provide evidence that there is no existing solution for the real-time turbulence correction problem, and therefore there is a valid need to engage the system engineering development process.

1.3 System Engineering Process.

The discipline of system engineering has evolved over time, just as machines and devices themselves have become more complicated and involve greater numbers scientific disciplines and areas of expertise. The definition of a system does not have universal consensus. One definition proposed by Kossiakoff [15] is as follows: "*a set of interrelated components working together toward some common objective*." Kossiakoff goes on the explain that *complexity* and *diverse interaction* among the system components are also necessary factors. For example, simple machines such as a wheeled cart, or even a more complex bicycle, would perhaps not normally be considered systems, whereas a modern automobile with integrated mechanical, electrical, and software functions would likely be regarded as a complex system. Also within the same context is the assumption that the system is *human-made*, and thus naturally occurring phenomena such as weather patterns or living cell structures, while complex, are excluded from most definitions. Therefore, the following is proposed as a working definition of a "system" in this context: *An engineered system is a complex set of interactive components assembled and working together toward one or more common functions*.

There are a variety of system process and life cycle descriptions available in the literature. Figure 1-2 below shows major phases of the system life cycle as derived from the INCOSE Handbook for Systems Engineering [16]. The figure illustrates that while there is an overall progression forward through time, the engineering process frequently encounters iterative loops which reach back to previous activities in order to make improvements and upgrades.

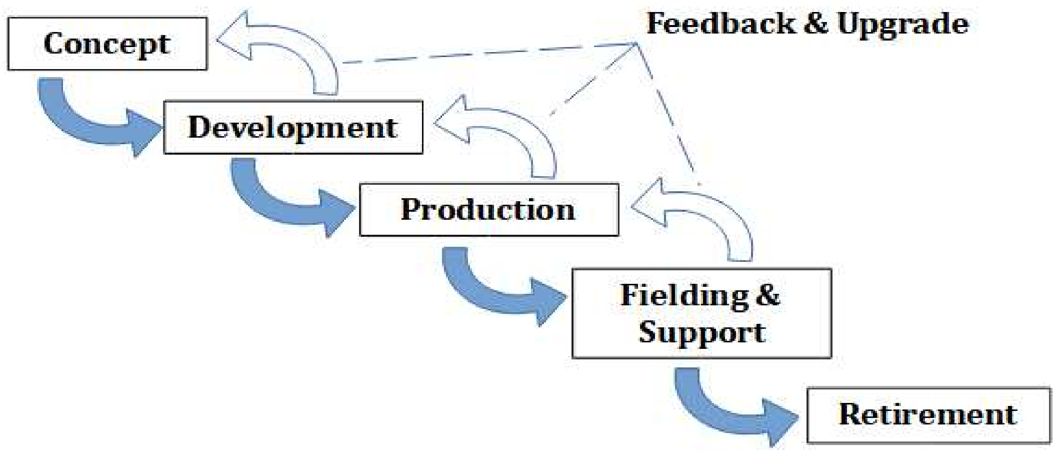

Figure 1-2: General System Engineering Life-cycle Process

The system engineering life-cycle process during each stage involves a repetitive process of defining requirements and functions, creating physical designs, and then validating that the design is correct. In many situations, changing a parameter in one area of a system will impact several other areas, and so constant looping and iteration is expected during the engineering process. The bulk of this dissertation hereafter concentrates on the first areas of the engineering process which involve concept building and then initial stages of engineering development. The effort thus heavily involves activities such as gathering requirements, analyzing approaches toward a solution, performance modeling of one or more possible solutions, and then outputting a feasible concept as defined by supporting analyses and a system-level development specification.

1.4 Technology Readiness Level (TRL).

The United States Department of Defense (DoD), recently designated in late 2025 as the Department of War, has assigned a technology maturity rating scale for its development activities which is quite complementary with the generalized system engineering process summarized in the previous section. The Technology Readiness Level (TRL) scale ranges from 1 - 9, with each level meeting a set of criteria or milestone events during the life of the system project. Figure 1-3 below is derived from DoD 5000.2-R [17] and is commonly referenced in many DoD publications.

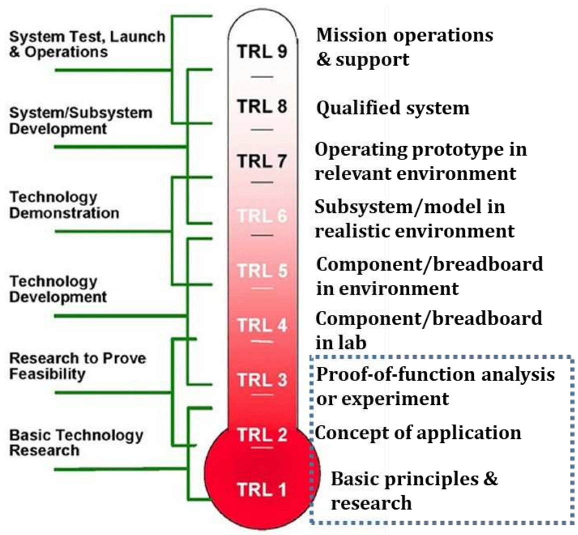

Figure 1-3: Technology Readiness Level for Product Lifecycle Per DoD 5000.2-R

The adjectival descriptions of the lowest and highest TRL ratings are straightforward to comprehend, but the descriptions of the mid-level scale positions 4, 5, & 6 can sometimes be confusing. Therefore, a set of examples is provided in the next following Figure 1-4 which are specific to an electro-optical imaging sensor designed to mitigate the effects of optical turbulence. TRL-1 begins with an accumulation of publications, university research, and lessons learned with past sensor systems when they have encountered atmospheric turbulence. From the body of knowledge, an operational concept of application of new technology or approach to solve the real-time turbulence image degradation problem is conceptualized for TRL-2. The next stage TRL-3 involves determining via math models, analysis, experiment, or computer simulation that the technical approach might meet the system needs. At this stage, an examination of critical sub-systems, components, and technology gap areas may also be included. In effect, TRL-3 is comparable to the completion of the Concept Development phase of the system engineering process. By TRL-4, the most critical components and subsystems are constructed and operated in a "breadboard" laboratory setting. This is representative of the early tasks in the Engineering Development phase where hardware and software tasks are accomplished. The next TRL-5 involves a revision of the critical functional apparatus such that it can be placed in a relevant environment to demonstrate effectiveness. This stage often involves interfacing with other systems such as test platforms. And in the case of an imaging sensor, it also involves looking at real targets through real atmospheres. A successful TRL-6 event is where the system scope is expanded to address new requirements for interoperability, command & control, data management, and other external requirements. For military platforms, addressing issues such as electromagnetic interference (EMI) or aircraft flight-worthiness are potential examples of TRL-6 activities. TRL-7 is the realization of a fully integrated system which is ready for operational testing by people who would be the actual users of a fielded system. This is a critical stage where all the performance aspects of the system are reviewed and validated by the customer. A decision to move into production is usually made upon completion of TRL-7. If the production decision is authorized, then TRL-8 is the achievement of a production-qualified system and begins the Post Development engineering phase. This involves creating the manufacturing work plans and quality test procedures such that multiple systems are all fabricated according to controlled processes. Typically a Low Rate Initial Production (LRIP) activity is done wherein a small but statistically significant quantity of units are built according to the manufacturing plans, and then quality testing rigorously checks each performance parameter to make sure every production unit is compliant. And finally, the TRL-9 designation is achieved when the system has been in production for some time, and the full lifecycle including eventual end-of-life disposition has been exercised.

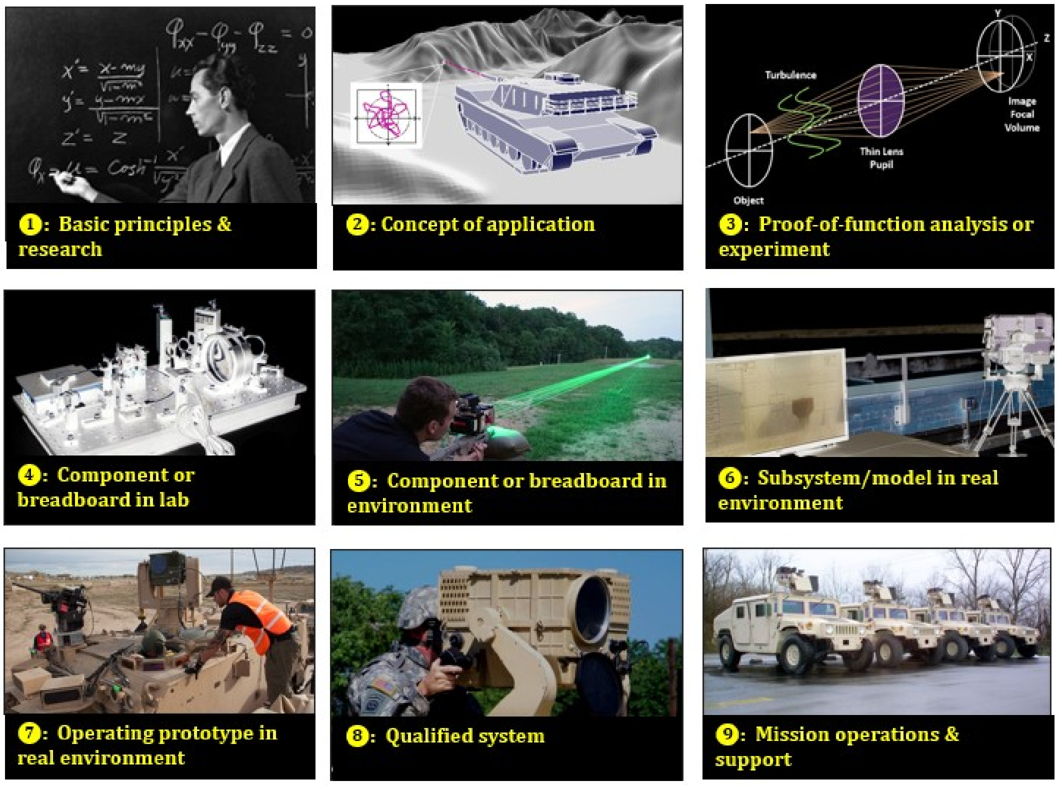

Figure 1-4: Graphical Illustrations of the TRL Categories

The TRL path is a helpful means to assess the maturity level of the system development. Perhaps even more importantly, it also provides the road-map of the major milestone events required to progress through the system development cycle. However, the engineering effort to achieve these TRL milestones may not be so linear. Successes and failures at various validation milestone events may result in looping back to earlier engineering phases to re-optimize or correct the system design.

Chapter 2 - Customer Objectives & Concept of Operation

One of the first major steps in the Concept Development phase of the system engineering process is to elicit the primary customer's desired performance objectives, as well as those of any other stakeholders or external restraints. Performance objectives may need to be extracted from entities who may not have expertise in defining formal system requirements, and so a process of *elicitation* is employed to ensure that the customer's desires are fully understood and properly documented [18]. Elicitation might involve customer interviews, surveys, analysis of similar systems, reviews of government standards, and so on. An effective technique which can be very useful during the elicitation process is to develop a Use Case study which will be discussed in the following section. It may also be mentioned now that in later stages of the system engineering the process, the Use Case can be helpful for planning an *operational test*, wherein the system is tested to see if it meets mission needs in the field.

2.1 Use Case.

A Use Case analysis is a way to document the expected uses, operations, and interactions with the system. It is essentially a story narrative describing how the system will likely be used. In this way, personnel with little experience in documenting formal requirements can more easily uncover requirements that might otherwise be missed. The Use Case is typically comprised of a general context statement, a Main Scenario which outlines the intended normal use of the system, an Alternative Scenario which describes operation of the system which is perhaps not normally expected, and finally an Exception Scenario which describes system operation during some form of adverse condition or failure. Authors have suggested there are up to eleven general rules for scenario documentation [18], of which the key aspect is to be as direct as possible using present tense, named actors, and simple subject-verb sentence structures. The narrative should facilitate an accurate imagination of using the system. A relevant Use Case related to imaging through atmospheric turbulence is presented as follows:

Context: Ms. Claire Voyance is a border patrol agent. She is responsible for night-time video surveillance of a region of land extending to about 2.5 km beyond the borderline which she patrols using a truck loaded with video equipment. Most of the landscape is harsh desert territory. Atmospheric turbulence is blurring the imagery of the sensors currently in use, and thus the false alarm rate is excessively high. This problem needs to be addressed by a new electro-optical sensor system.

Main Scenario: Claire begins the night shift at dusk. Claire enters the hangar and loads and straps down the video equipment into the back of her truck. The equipment includes a portable tripod with integral pan & tilt mechanisms, a gas-powered electrical generator, and various electro-optical sensors. All equipment is stowed inside transport cases. Claire then drives out along the border line route to one of many lookout positions. The lookout posts are pre-selected to maximize the viewing coverage. Claire arrives at the desired post and unloads the equipment from the back of the truck. Claire unpacks the tripod, sets up the generator, and affixes the video sensor to the tripod. Claire attaches cables as appropriate. Claire powers up the sensors and begins a series of panning sweeps to see what is happening within the search sector. Claire views the video imagery directly on the integral sensor screen monitor. The system automatically adjusts the image to mitigate the effects of atmospheric turbulence. If an unauthorized vehicle or suspicious activity is identified, Claire reports via radio back to headquarters of a potential breach or intrusion. When the surveillance period ends, Claire re-packs the equipment and loads it back into the truck. During an eight hour work shift, Claire may move to one or possibly two other locations and repeat the same procedures. Claire returns to the hangar at the end of the shift. Claire unloads the equipment from the truck and stores it within the proper warehouse shelves.

Alternative Scenario #1: Instead of mounting the sensor to a portable tripod, Claire mounts the sensor to a fixture which is integral to the truck. The sensor may be locked in the straight-ahead position or perhaps aimed to one side. This is analogous to the "dash cam" systems used by other law enforcement agencies. Claire drives the truck at low speeds, typically 15-20 mph, and views the imagery on a separate remote dashboard monitor.

Alternative Scenario #2: Instead of a power generator, Claire powers the system via a battery pack.

Exception Scenario: A system fault indicator lights up during system boot. Claire reads the fault warning on the system display. Claire re-packs the truck and drives back to the hangar. Claire fills out a discrepant material form describing the problem. Claire checks in the discrepant material and checks out a replacement unit. Claire re-packs the truck and drives out to complete the next shift.

2.2 Statements of Objectives.

After reviewing the Use Case and receiving agreement from the customer, a set of objectives can be documented. The customer requires an ability to identify a specific target object at a range distance at which there is a good chance that atmospheric turbulence effects can have a significant adverse impact on performance. Other performance factors such as "real time" imaging are also critically important. And finally, a few objectives regarding the physical aspects of the system are provided to help bound the classic features of size, weight, and power. The following seven performance objectives serve to capture the customer's objective needs:

OBJ.1 Shall be an electro-optical video imaging sensor for use with human observer.

OBJ.2 Ability to identify a commercial truck target at a range of at least 2.5 kilometers.

OBJ.3 Passive operation (i.e., no light sources) both night and day.

OBJ.4 No noticeable time lag between real scene and the sensor's output image.

OBJ.5 Range capability is required during atmospheric turbulence conditions year-round.

OBJ.6 One-person lift onto a tripod and operable atop a pan/tilt mechanism.

OBJ.7 Power provided will be 24V DC supplied power, maximum current draw 60 amps.

2.3 Initial System Definition.

The combination of the Use Case descriptions and the customer objectives allows the system engineer to begin visualizing the system. An excellent graphical tool to capture this visualization is the Integrated Definition Zero (IDEF0) chart format [15], which can start at the top system level and then be repeated for each sub-system and component as the design evolves [19]. The IDEF0 sketches the system concept using four basic external considerations or interfaces as follows: inputs, controls, mechanisms, and outputs, along with a description of the system's own internal functions. This can be depicted graphically to facilitate the visualization as per the following example in Figure 2-1:

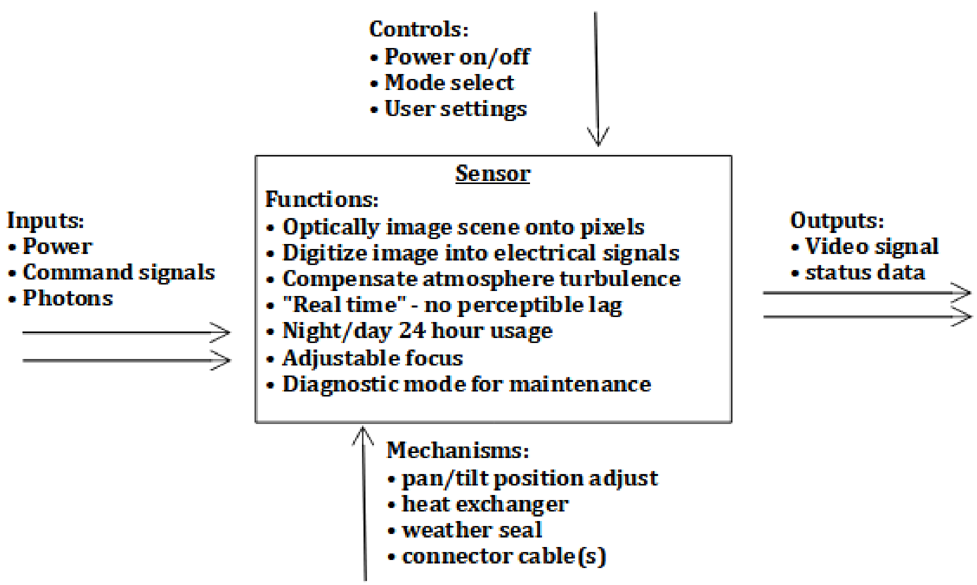

Figure 2-1: IDEF0 Functional Model for a Sensor System

2.4 System Technical Challenge Identification.

Now that a general understanding of the system objectives has been formed, it is also important to identify critical technical challenges which must be satisfied if the engineering process is to proceed. At a high level, the following questions outline some of the most important challenges at this early process stage:

- Does a mathematical model exist which can be used to estimate the sensor performance, both with and without turbulence effects, for targets at various ranges?
- Is there a physics model which fully characterizes the optical behavior of a compensation method when imaging through atmospheric turbulence?
- What are the limitations of the current art, and why has no solution yet been manufactured?
- What other external or unstated factors are going to impose requirements and limitations upon the feasibility of a system approach?

Each of these questions will be addressed in subsequent sections of this dissertation. In some cases such as sensor modeling in general, the engineering theory is well developed and simply needs to be organized in a manner conducive to the specific engineering tasks at hand. In other cases such as for the optical turbulence physics model, a new technique is needed and thus will be developed and validated. The questions of prior art limitations and unstated requirements will be addressed throughout the dissertation, and will culminate in the end within the deliverable performance specification output.

2.5 System Modeling Software Tool.

There are a variety of system modeling software packages available, both commercial and open source. Many of them are based on the standard system modeling language (SysML), which in turn is an enabling technology for more advanced model-based system engineering (MBSE) tools. These software tools provide convenient means of capturing inputs, defining relationships between various system elements, and creating graphical representations of various system aspects. The Capella software package (http://mbse.capella.org) is based on the Architecture Analysis & Design Integrated Approach (ARCADIA) [20] which shall be used herein. It is open source, freely available to students and professionals. One of the first activities suggested by Capella is to define the "class" of system to be developed. In a sense this is a "pre-engineering" step which provides context for the fundamental technology to be used by the system. Section 1.1 already discussed the general nature of an imaging sensor, and within that boundary are a variety of typical classes which comprise the family of available options. Figure 2-2 below breaks down four common sensor classes of imaging sensors based upon distinct fundamental principles of visible light, infrared light, radar, and acoustic sensing. Recalling the customer requirements for target identification during night or day, the infrared light class of sensor system is chosen. Several options can be ruled out at the onset of the project. Visible light is insufficient during night conditions unless there is an external light source. Radar is effective night and day, but the centimeter-scale wavelength has limited resolution for the customer's target. Acoustic sensors require that the target be emitting sound waves of greater magnitude than the surrounding environment, which is not an operational stipulation provided in the customer objectives. The results of this class selection exercise lead to the selection of an infrared light sensor system.

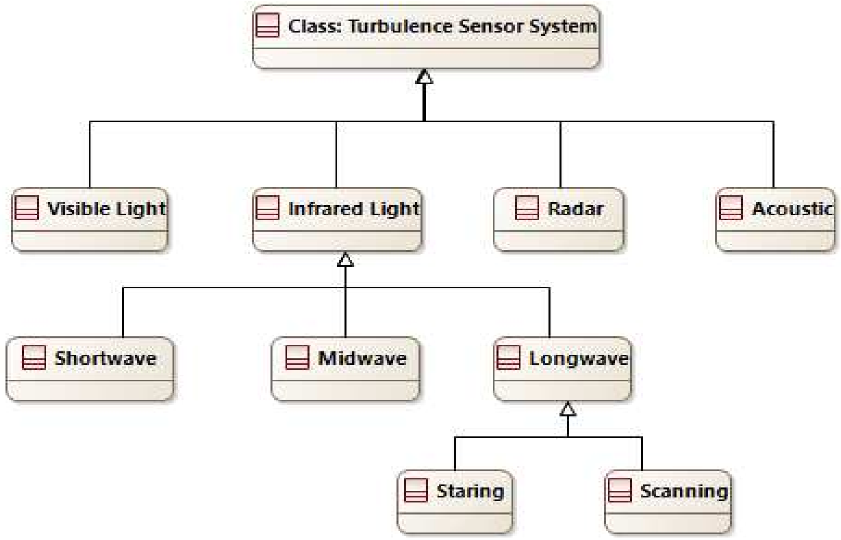

Figure 2-2: Sensor Class Diagram

The Capella diagram in Figure 2-2 then provides further breakdown of the infrared light type of sensor, with sub-categories based upon the shortwave, mid-wave, and long-wave spectral pass bands in the earth's atmosphere. The merits of these will be discussed fully in later sections, with long-wave infrared being the most desired sub-class. And then finally, within the sub-class there exists another distinction between scanning and staring systems, which has to do with whether the detector device itself is a single element, a row of elements, or or a two-dimensional array of pixels. The details of the sub-class architectures will also be discussed in later sections.

The customer use-case scenarios can also be captured within Capella, and a variety of useful analysis and graphic representations can be made. The first of these is a basic operational capabilities diagram as shown in Figure 2-3 below. The diagram includes the critical actors, such as the human operator Claire Voyance, as well as non-human entities such as the atmosphere, target, and background. Each actor conducts an operation such as emitting and turbulating photons, receiving photons, and identifying the target.

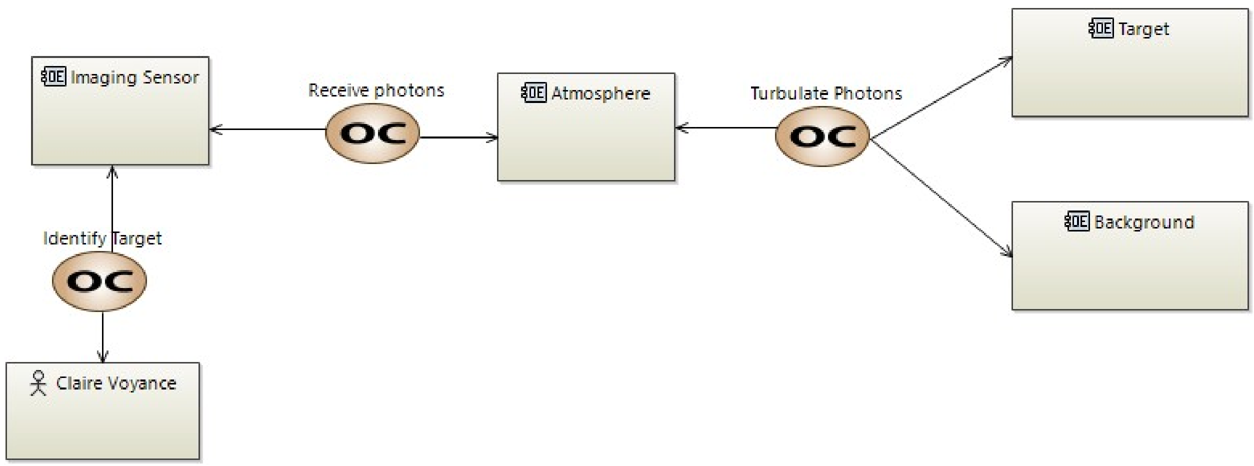

Figure 2-3: Initial Operational Capabilities Diagram

The core operational capabilities can then be broken down into core functions, and mapped into a time sequence as shown next in Figure 2-4 below. The Capella graphics generator assigns each actor a "swim lane" containing the critical functions arranged in temporal sequence. Functions such as "Photon path alteration", "Phase and Intensity Compensation", and "Compose Video Frame" are now added to the model.

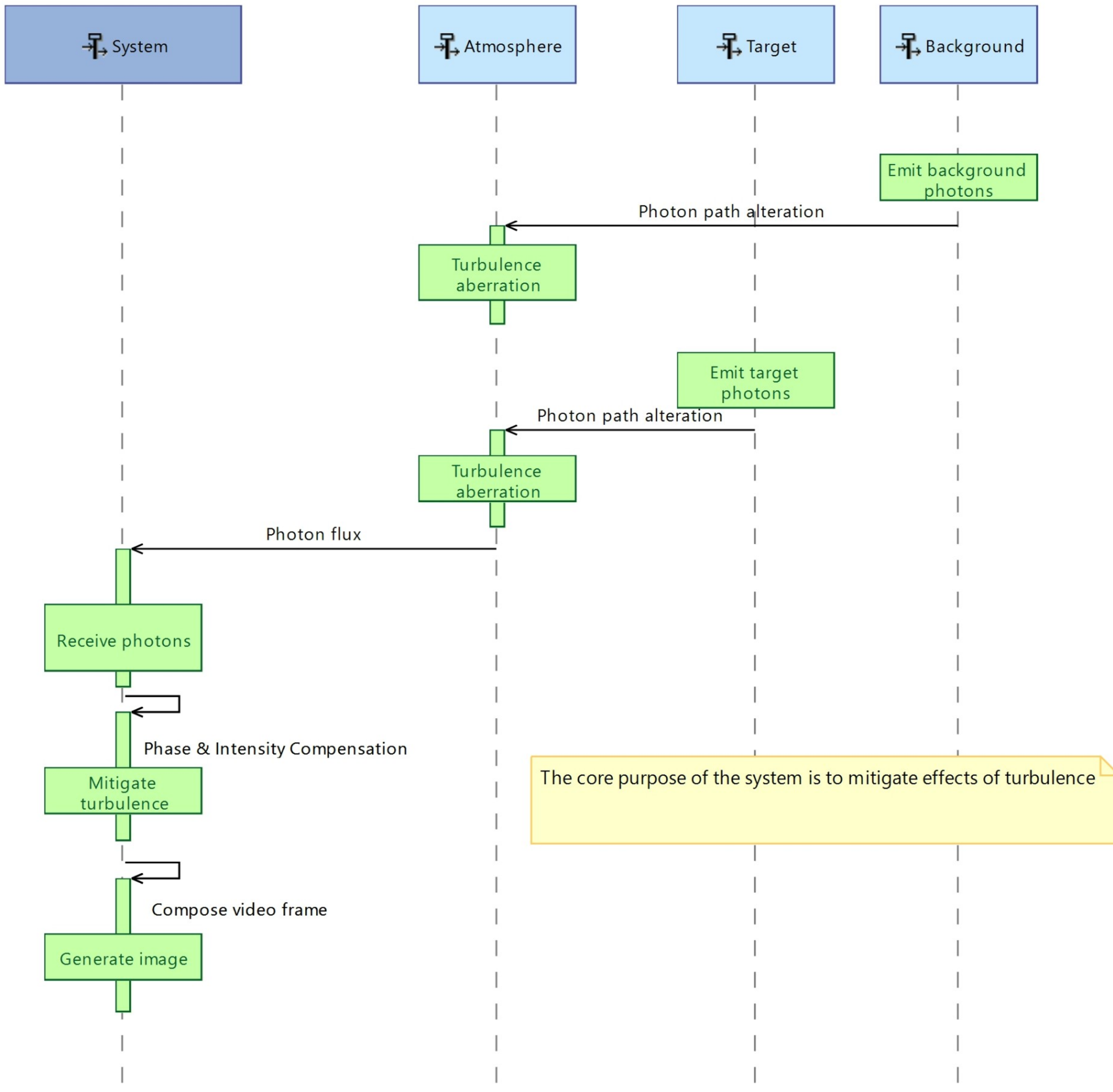

Figure 2-4: Core Function Sequence

Similar functional decomposition can be executed for all aspects of the system, and a final system architecture diagram is shown in Figure 2-5 below. The Capella-generated system architecture diagram captures the essence of the IDEF0 diagram shown previously, and adds more details of the functional exchanges and interfaces between actors and system elements. It is particularly useful for itemizing the human (i.e., Claire Voyance) exchanges and functions as described in the use cases, to include not only the sensor functions, but also the activities of obtaining, mounting, and returning the system to its storage location.

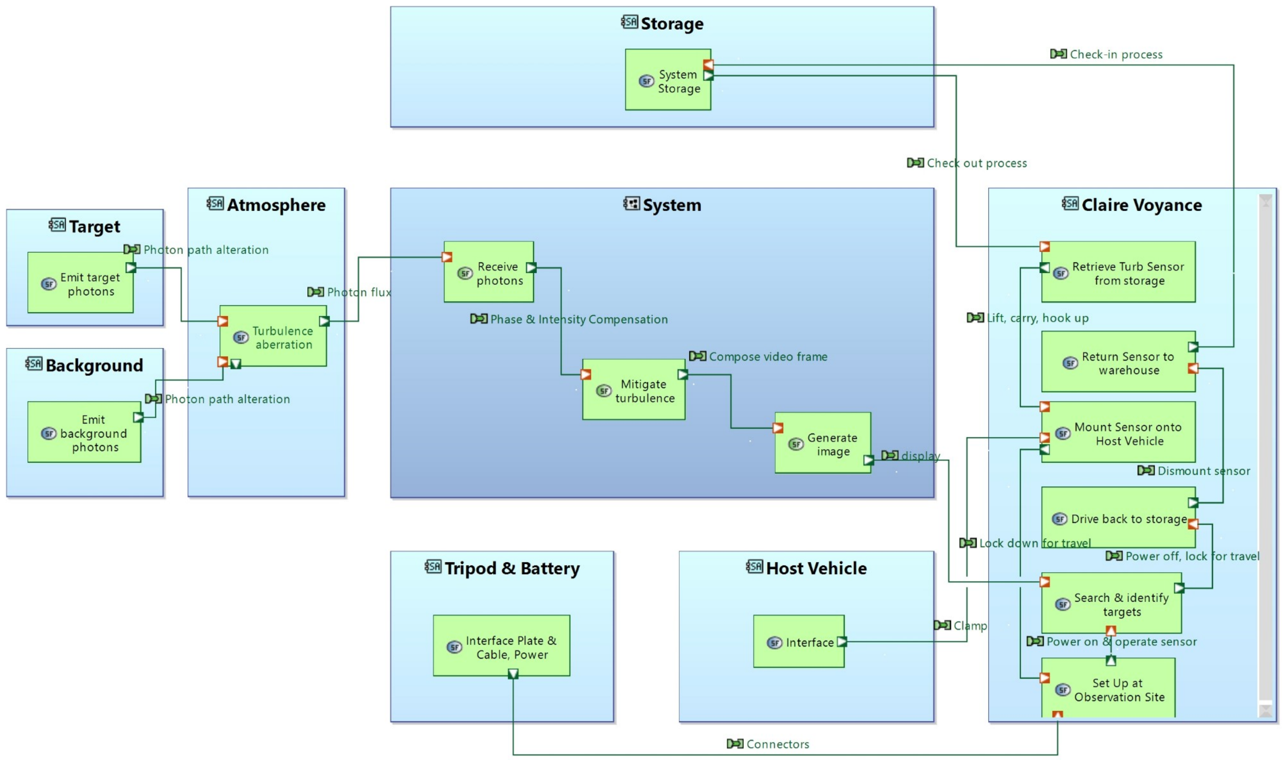

Figure 2-6: System Architecture Diagram

With the overall system architecture now defined, the next step is to develop a mathematical model which calculates sensor performance from a set of critical input parameters. The next section will explain these steps in detail.

Chapter 3 - Sensor Performance Model

The approach often used in developing a mathematical model for imaging sensor performance is based upon establishing the "building blocks" which are common to most sensor systems. The system block diagram may thus include the target, atmosphere, illumination, optics, detector, image processor, output display, and finally the human operator. From a mathematical point of view, each of these block segments will have its own set of responses to inputs, as well as its own form of output which feeds into the next block in sequence. Figure 3-1 below shows a suitable block diagram for an electro-optical imaging sensor.

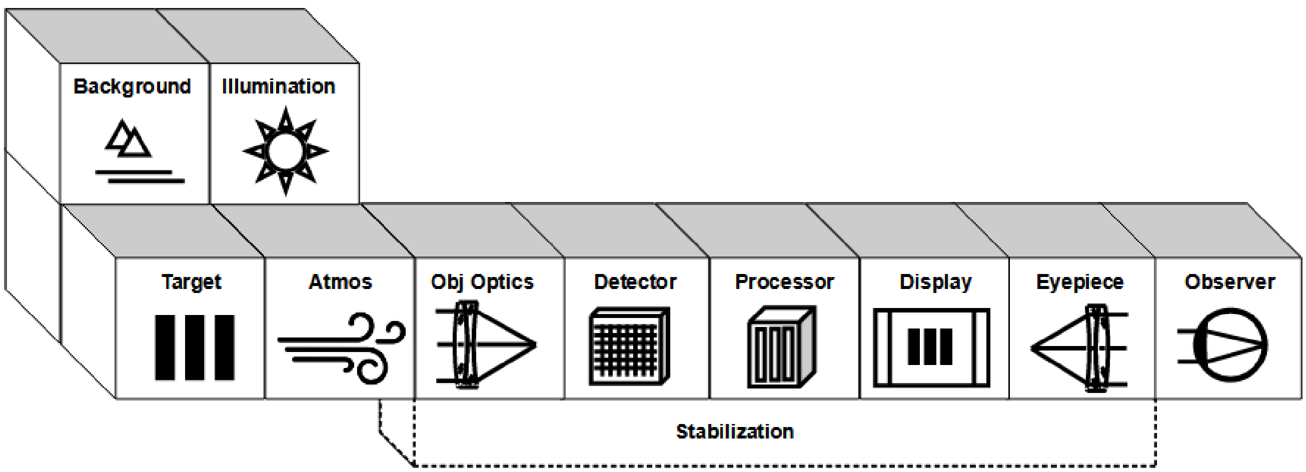

Figure 3-1: Block Diagram for Electro-Optical Sensor Performance Model

The target is a physical object, which from a mathematical point of view, is comprised of the superposition of a number of point sources, each emitting a measure of optical light within the spectrum of concern. The target optical emission signal must be contrasted against the emissions from surrounding background objects in order for a human to "see" it. Both target and background might also contain reflected energy from external sources of illumination, which could be for example the sun, moon & starlight, or perhaps man-made artificial lighting. The optical signal then propagates through the atmosphere and may encounter absorption and distortions as a function of the weather conditions and turbulence magnitude. The objective lens optics receive a portion of the target's optical emittance, and focus that light as an image onto the photo-detector. The detector is comprised of materials which convert the incoming light radiation into a corresponding electrical signal in such a way as to preserve as much as possible the intensity distribution of the original object. The electrical signal may then be amplified and eventually converted into a digital output signal. The digital signal is then operated upon by processor electronics which can provide various calibrations, noise abatement, and conditioning for the display block which follows. The display may be a conventional computer monitor which is directly viewed, or it may be a micro-screen which is viewed through a magnifying eyepiece. Stabilization, sometimes referred to as "jitter", may have contributions from either internal or external sources. And finally the human eye receives the image which is then to be processed by the human brain. From the system engineer point of view, it is not practical to expect to become an expert in all of the technical areas within the system model, but it is important to develop proficiency in the higher level critical parameters which are involved in the transfer from one block to the next. Indeed, even when dealing with only the high level parameters, there are more advanced system modeling theories which can be found in modern references [21]. The goal here is to have a working understanding of the fundamental physics involved within each system block, and how the outputs of one block become the inputs of the next. It is this holistic level of comprehension which enables the system-level "brainstorming" needed to solve the complicated problem of mitigating the impact of horizontal-path atmospheric turbulence. The sensor model provides the mathematical basis for determining the transfer of information from one block to the next, such that a range performance estimate can be generated. This shall now be explained in detail within the following subsections, beginning with a brief overview of linear systems theory.

3.1 Linear Systems Theory.

Linear systems theory is explained in great detail in several texts [22][23][24] and has become popular in optical system analysis [25]. A linear system can be defined mathematically as follows:

consider a system function operator (Ψ) which performs a math process upon two different inputs *x* and *y*, resulting in the outputs Ψ(*x*) = g(*x*) and Ψ(*y*) = g(*y*). The system function is linear if Ψ(*x*+*y*) = g(*x*) + g(*y*) [23]. This feature embodies the principle of *superposition*, whereupon the system's overall response to a linear combination of inputs is equal to a linear combination of the results when the function applied to the individual inputs. For example, consider f(x) = 2x, so then f(2 + 1) = 2(2 +1) = 6. This can also be solved by f(2) + f(1) = 4 + 2 = 6 for the same answer, and thus f(x) = 2x is a linear function. Oppenheim [26] suggests that it is often easier to to prove that a system is non-linear, and provides the following example: let $f(x_i) = \log_{10}(|x_i|)$. All that is needed is one case where non-linear behavior occurs. If we assign $x_1 = 1$ then $f(x_1) = 0$, whereas if we assign $x_2 = 10\, x_1 = 10(1) = 10$ then the result is $f(x_2) = 1$. Linearity would require that $f(x_2) = 10 \cdot f(x_1)$ which is not true, and therefore the equation is not linear.

Linear systems theory can be used to estimate performance of the sensor's ability to read the contrast of the target versus its background and then convey a useful video image to the operation, however any system in the real world will also suffer from non-linear effects. The linear system math models have proven to be an effective tool for the design of electro-optical sensor systems because they can be supported with quantifiable measurements of the system block sections [22]. *Linear filter* theory is a tool which can be used to describe the responses of an electro-optical system to various signals, to predict spatial resolution, and to facilitate post-process enhancements. Linear filters are a branch of Fourier transform analysis, and which may be applied to optical systems which map inputs to outputs via a convolution process [22]. The physical *sensor* is thus bounded for the purpose of this discussion as the combination of the objective lens optics, detector, electronic processor, and output display. Before looking in detail at each block, it is instructive to first explain generally how any of these blocks of a vision system interact with each other from a mathematical point of view. As the signal progresses from one system component to another, a mathematical *transfer function* can be defined which captures the nature of how the incoming signal is passed and transformed into an output signal going to the next system block. For example, a characterization of the optical aberrations induced by the turbulent atmosphere is one example of such a *transfer function* which will feed into the objective lens. The whole system end-to-end transfer function quantifies the quality of the image as viewed by the human operator. The sequence begins with the target object point source emissions, or *impulses*. The impulses set the system into operation and are transformed and passed along through each block. The concept of a transfer function in terms of a digitally pixellated system is illustrated in Figure 3-2 below, where for example a single ray of light is spread by diffraction at the aperture of the objective optics [27]. The modeling challenge is to define the appropriate mathematical transfer functions for each block.

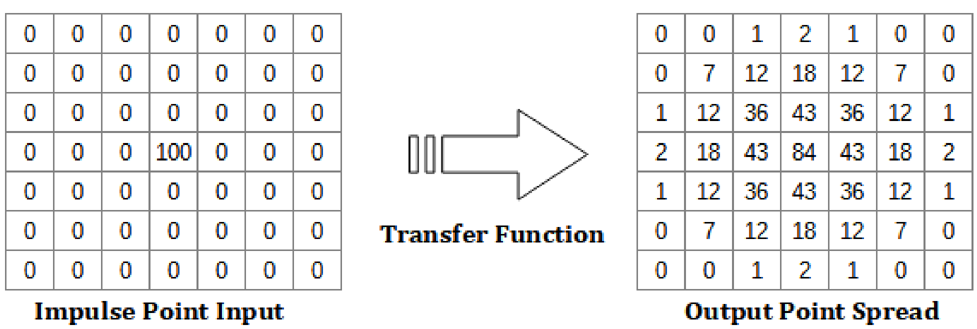

Figure 3-2: Illustration of a Transfer Function In Terms of a Rectangular Grid of Digital Pixel Values

There is also the property of *shift invariance*, which requires that if $\Psi(x) = g(x)$, then $\Psi(x - x_0) = g(x - x_0)$ where x_0 is a real constant value. The mathematics for Linear Shift Invariant (LSI) Systems are generally easier to manage when the functions involve differential equations, but in real situations the applicability of LSI properties is often restricted to a limited range of inputs [23]. O'Neil provides an explanation of how an optical imaging system can be modeled as an LSI, stating that in essence the concepts of the impulse response in electrical engineering texts is mathematically the same thing as the point spread function in optics or the Greene's Function in field theory [28]. The Figure 3-3 below is a graphical representation which shows the optical imager as a device causing a transform. This device "transform" may be a single lens or an assembly of lenses and other optical elements for the purposes of creating an optical image.

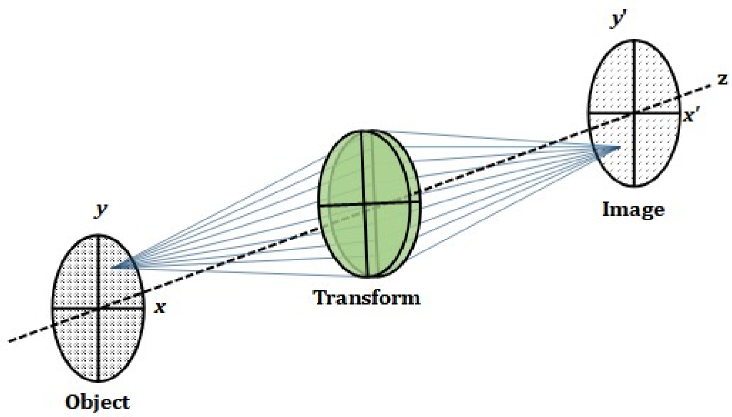

Figure 3-3: Image Formation Modeled as a Linear Shift Invariant (LSI) System

In the LSI model, the object is comprised of a number of incoherent point sources which radiate independently of each other, denoted mathematically as set of Dirac Delta impulse functions located in space coordinates (x, y). The object function describing the brightness intensity distribution is $\mathrm{o}(x, y)$. The transformal system, an imaging lens for example, performs a linear transform upon this object via some function $\mathrm{g}(x' - x,\ y' - y)$ which will result in an image plane intensity distribution given by $\mathrm{i}(x', y')$ which is then a weighted sum of the transformed impulse responses integrated over the object plane. The formulation is thus given by O'Neil as follows [28]:

$$\mathrm{i}(x', y') = \iint \mathrm{g}(x' - x,\ y' - y)\ \ \mathrm{o}(x, y)\ \mathrm{d}x\ \mathrm{d}y$$

A physical interpretation example can be created by imagining that the transform function $g(x' - x, y' - y)$ somehow involves a slight spread, or *blur*, in the resulting image plane. Mathematically, the blur due to a single impulse input is called the two-dimensional Point Spread Function (PSF). The integrated sum or superposition of all the point source PSF's comprises the two-dimensional image. The image is thus a convolution of the object with the PSF of the system. The two-dimensional Fourier Transform of the PSF is known as the Optical Transfer Function (OTF), of which the *modulus*, or absolute value in polar coordinates [27], is called the Modulation Transfer Function (MTF). The Fourier Transform process is useful because the component convolutions in the spatial domain become easier multiplications in the frequency domain. A real optical imaging system will tend to have a change in the PSF depending upon the position in the focal plane and thus is not truly shift invariant. This variance is due to aberrations and diffraction effects. The neighborhood in which the PSF remains fairly constant is called an *isoplanatic patch*, and only in this limited region can the optical system be considered shift invariant [29].

The development so far now leads to the need for a parameter metric which sufficiently characterizes the resolution quality of the image plane. Resolving power is defined by Jensen simply as the ability of the system to separate two closely spaced objects [25]. Obviously in order to discriminate two closely spaced object points, there must be a difference in their intensities, i.e., a *contrast*, otherwise the task is impossible. The contrast (C) between two points of different intensity values is defined by the following equation [22][30]:

$$C = (I_{max} - I_{min}) \div (I_{max} + I_{min})$$

The intensity of the brighter point is denoted as (I_{max}), and the intensity in the darker point is (I_{min}). If $I_{max} = I_{min}$ then the contrast $C = 0$ and no discrimination between the two adjacent points is possible. In all other cases, a non-zero value of C can be determined with an upper limit of 1.0 for the case when I_{min} is zero. The term "closely spaced" requires quantification. When an imaging system transfers the original image from one section to another, the impact to the image quality can be predicted via the contrast transfer functions for a set of different targets with varying *spatial frequencies*, which are the inverses of the spacing between the points or bars for any particular target and which are typically expressed in units of cycles/millimeter when visible wavelengths of light are considered. As the spacing between target bars gets smaller, the spatial frequency value rises. The Modulation Transfer Function (MTF) is the mathematical relation between contrast values (C) and their corresponding spatial frequencies. The MTF can be derived via Fourier analysis for a wide variety of transform functions, both optical and electronic, which will be discussed in later sections [30]. An MTF graphic plot typically shows spatial frequency scale along the horizontal axis and the contrast values along the vertical axis. The MTF vertical axis ranges from 0% to 100%, where 100% indicates that the image is a perfect re-creation of the object appearance for the given spatial frequency. MTF values are typically presented in both horizontal and vertical target orientations to account for potentially non-symmetric aspects of the system. Figure 3-4 below provides an illustration a typical MTF curve along with a visual representation of ideal and actual images in terms of bar target images.

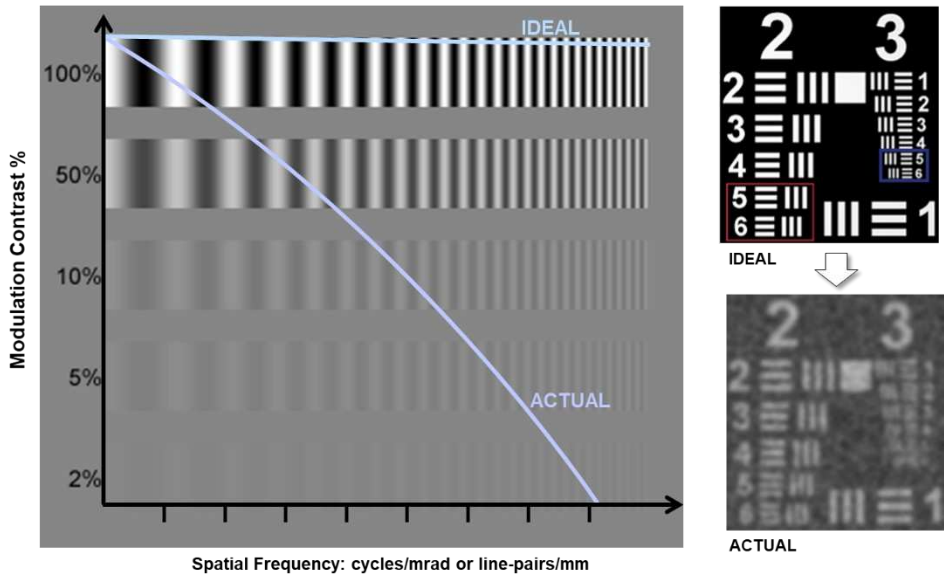

Figure 3-4: Modulation Transfer Function Ideal vs. Actual Graphical Representation & Interpretation

The *ideal* plot line represents the contrast of the original object target, and the *actual* plot line shows the results of the imaging system which accounts for all the transfer function losses at various stages within the sensor system. Traditional presentation uses a linear scale along the x-axis of the plot, with units of cycles/mm being most common. However, in some cases it is more informative to use a logarithmic scale when otherwise the linear units may not capture the entire shape of the curve [30]. Examples of loss contributors for a sensor may include atmospheric effects, blurring due to jitter, objective lens aberrations and diffraction limits, digital sampling, and even the response of the human eye itself. The individual MTF's of each of these components can be multiplied to produce a composite system MTF which then characterizes the system's linear response capability.

Linear system theory does have some significant limitations which must be addressed. Lloyd specifically states four major areas where non-linear behaviors are likely issues for sensor systems [22]:

1) The optical radiation is incoherent.

2) The electronic signal processing is linear.

3) The image is spatially invariant.

4) The system mapping is single-valued, meaning random or other noise effects are not significant.

The issue of radiation coherence is usually only a concern when laser sources are involved. In such cases, there are special transfer functions which can be applied, however random processes such a speckle can become problematic. These cases involve active illumination and so will not be considered any further here. The next three issues are certainly relevant. The conversion of an optical signal to an electronic signal may encounter practical boundaries where the detector is either *starved*, meaning its own internal noise dominates its output relative to the incoming low light signal, or *saturated*, whereupon the output signal reaches a constant maximum value and the system is no longer responsive to changes in the incoming optical signal. This threshold of the starvation effect is captured by the system's *signal to noise ratio* (SNR), where the strength of the incoming signal is ratioed to that of the system noise when no photon signal is present. Another issue common to optical imaging is that the quality of the PSF may not be consistent across the field of view of the objective lens. This is often the result of field-dependent aberrations which naturally occur in the lens design process, and it can also be a result of the optical turbulence effects which may create field variations. The non-linear coupling of the atmosphere's aberrational effects through the objective lens is a critical concept to understand when one is trying to mitigate the effects of turbulence. Within the lens assembly itself, the interactions from one lens to another are not linear because the aberrations of one lens may compensate for the aberrations of another [25]. Thus, a comprehensive system model must be comprised of a region of linear response (i.e., where the MTF is valid) bounded by the non-linear regions where the random noise becomes dominant or where the system becomes saturated to the point where there is no change in output as the signal strength increases. The next sections will describe each block within the system model in some detail. Each of these sections will identify the key characteristics and analysis parameters which impact the starvation SNR, linear MTF response, and saturation.

3.2 Target.

The target block describes the characteristics of the object within the scene which is to be viewed. The customer's primary target of interest is a commercial truck type of vehicle. An old 1942 Dodge Fargo truck model shown below in Figure 3-5 was thus chosen as being representative of a general class of similar man-made objects consistent with the customer objectives [31]. Assuming the dimensions are approximately 2.9 meters long, 2.0 meters wide, and 2.1 meters high, the geometric average is then given by $\sqrt[3]{(2.9 \times 2.1 \times 2.0)} = 2.3$ meters, which shall be labeled as the *target critical dimension* and assigned a symbolic variable (ʤ).

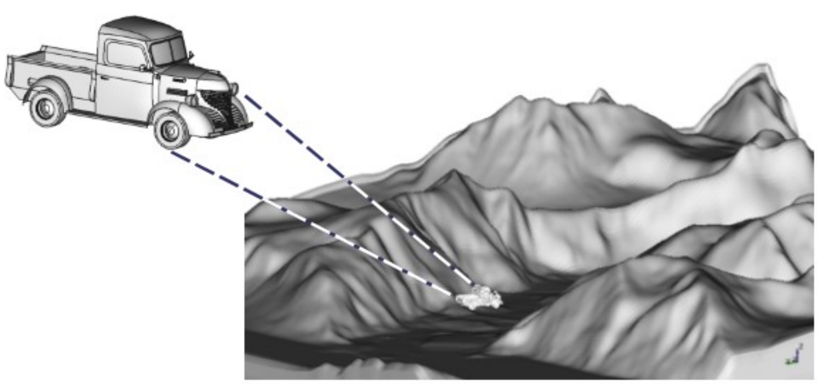

Figure 3-5: Truck Target Against Background Scene

The photon signal coming from the target comes from either external sources which are reflected by the target surface, or perhaps direct emissions as a function of the target's temperature. In the former case, sunlight during the day provides massive amounts of photon flux such that even shaded and dark targets will have a sizable signature. However, at night the visible illumination of stars and moonlight is several orders of magnitude less than daytime sunlight [32], and so a visible light solution is not promising for full 24-hour operation. In the thermal infrared spectrum, however, the target will continuously emit its own radiation regardless of time of day. This behavior is characterized by Planck's Law [33][34], which provides a means to calculate the flux emittance from a body as a function of its emissivity (ϵ) and temperature (T). The emissivity parameter measures how well a particular object behaves as a "blackbody", which is defined as an object which absorbs all incoming light radiation, has no reflection, and is not transparent to any light coming from behind. The spectral emittance of a blackbody is then purely a function of its temperature. An example of a near-ideal blackbody is the Sun. According to Kirchhoff's Law, a beam of light flux striking a material can be either absorbed (α), reflected (r) , or transmitted (Υ). Conservation of energy requires that in a closed system, the sum (α) + (r) + (Υ) = 100% of the total incident energy [35]. A perfect blackbody would thus have (α) = 1.0 and the other terms equal to zero. Therefore, the emissivity and absorbance are indeed the same parameter, (ϵ) = (α) and a perfect blackbody would have (ϵ) = (α) = 1.00 maximum value. If the emissivity is less than 1.00, then that means the object has properties of either reflection or transmission mixed in with the radiation due to absorption. If the emissivity is very low, perhaps on the order of 0.10 or less, then the object may be suitable for use as either a transmissive lens or a reflective mirror, depending upon which parameter is dominant. Fortunately, as shown by Driggers [24], the infrared 8-12 micron spectrum emissivities for natural materials tend to be quite high as follows:

Material	Emissivity (ϵ) in the 8-12 micron spectrum
Polished aluminum	0.05
Polished steel	0.07

Oil-based paint	0.94
Oxidized Steel	0.79
Brick	0.93
Soil	0.92
Sand	0.90
Snow	0.98
Water	0.96
Oak wood	0.90
Human epidermis	0.98

Planck demonstrated that the emission spectrum of a blackbody object will obey an exponential equation which is a function of a set of constants, the object temperature (T), and the specific wavelength in question (λ). A table of the constants is provided as follows:

Constant	Symbol	Value	Units
Planck Constant	h	6.63E-034	J-s
Boltzman Constant	k	1.38E-023	J/K
Speed of Light	c	299792458	m/s

The formulation for blackbody emittance B(T) in units of Watts / $(m^2 \cdot sr \cdot micron)$ is then given per the following [33][34]:

$$B(T) = [2hc^2/\lambda^5] \div [\exp(hc/\lambda kT) - 1]$$

The above Planck formula can then be integrated over a range of wavelengths, resulting in units of Watts/m^2/sr, where the m^2 term is the area of the surface and the sr unit denotes the steradians of solid angle subtended by the target to the observer. Before the era of computers, this calculation could be done using a special slide rule such as the General Electric GEN-15C [36]. In the modern computer era, the integration can be done numerically within a spreadsheet calculation software program. This calculation thus quantifies the target radiation. If the source is external such as the sun, an extra term for the reflectance of the target can be used to adjust the light emission. For both night and day operation, the infrared self-emittance of the target is a more consistent source of radiation. Examples of specific values will be provided in a later section. There is also a non-linear contribution inherent in blackbody radiation, which is photon noise. Lloyd states that source emitting N photons/second will exhibit a Poisson distribution with a mean value N and a standard distribution $\sqrt{N}$. Assuming no other losses, the signal-to-noise ratio (SNR) is thus at best $N \div \sqrt{N} = \sqrt{N}$. Boreman & Dereniak clarify that the Bose-Einstein distribution is more correct in general, but which does converge to the Poisson distribution when the wavelength temperature product $\lambda T \ll 14{,}500$ µm·K [35]. For example, at a temperature T = 300 K and wavelength = 10 µm, the product $\lambda T = 3{,}000$ which is much less than the threshold.

In order for a sensor to "see" a target, and as discussed previously regarding Linear Theory, there must be a contrast difference between the target and its background. Since the target is man-made of generally painted metal and plastic materials, the effective temperature difference relative to background terrain of plant-life and bare earth is expected to follow the same diurnal profile as measured by D'Agostino [37]. There are two times of the day at which the “thermal crossover” occurs, during which the average target temperature perfectly matches the background and thus the infrared signatures have no relative contrast. If a 30 minute time interval is allowed both before and after each crossover, then an estimated value of 1.25 K is a good minimum temperature contrast which will endure throughout roughly 90% of the rest of the day as indicated by the data plot in Figure 3-6 below.

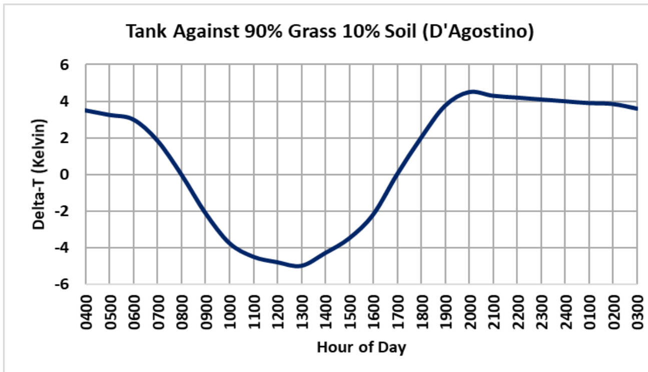

Figure 3-6: Target-to-Background Temperature Differential as a Function of Time During Day

3.3 Atmosphere.

Earth's atmosphere, comprised primarily of N_2 and O_2 gasses, has a very weak optical index of refraction (n_{air}). For a typical dry air laboratory environment, Jones reports the index is on the order of n_{air} = 1.000276517 for a wavelength λ = 632.8 nm, pressure 1.0 atmosphere, temperature 15° C, and about 300 ppm of CO_2 content [38]. Water vapors and other gasses may be present depending on weather conditions. Each of the gas materials has its own unique absorption spectra, and the result is that the atmosphere has spectral pass-bands of wavelength regions where transmission is very high, and others where there is a significant amount of absorption. The next Figure 3-7 below illustrates the measurements made available by the Gemini International Observatory, Hilo, HI [39] which matches well the data presented in the older RCA Electro-Optics Handbook [32].

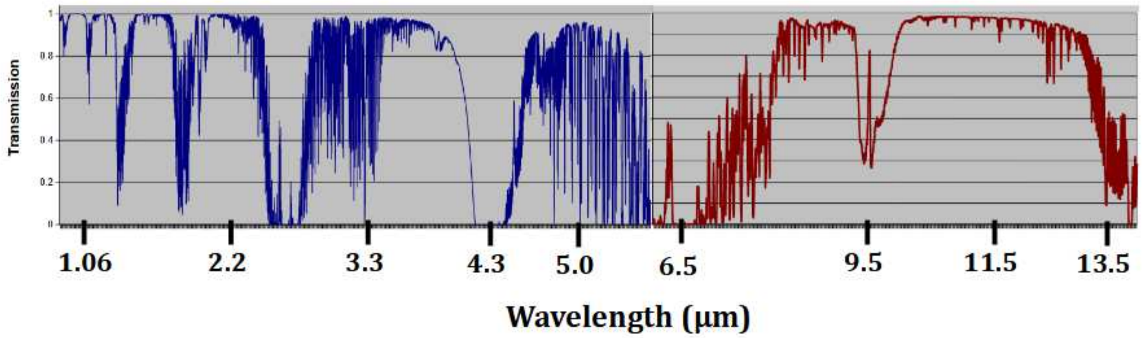

Figure 3-7 : Atmospheric Pass-bands Versus Wavelength

The human visual spectrum range of wavelengths is defined as λ = 0.38 to 0.76 μm [40]. Beyond 0.76 μm is the *infrared* spectrum. Within the infrared spectrum there are various definitions of specific regions which correspond to the atmospheric pass-bands. The nomenclatures are not universal and may change according to the source. For the purposes of this work, the spectral bands shall be defined as follows:

λ = 0.76 to 1.00 μm	near-infrared
λ = 1.00 to 2.50 μm	short-wave infrared
λ = 3.00 to 5.60 μm	mid-wave infrared
λ = 7.50 to 13.5 μm	long-wave infrared

Even within the atmospheric spectral pass-bands some absorption of light will occur, and as the distance traveled through the air increases, the absorption losses will likewise increase. Complex models such MODTRAN from the USAF have been developed to predict spectral transmission (ϒ) based on weather conditions, aerosols, land vs. maritime enthronements, latitude, etc. However, unless a great deal of rigor is required, a simplified method using the Lambert-Beer Law is suitable [41]. Beer noted that there is an exponential relationship between a solutions spectral transmittance as a function of the length of travel of the light through the solution. If the attenuation coefficient (a) does not change with path length (L), then the atmospheric transmission percentage (Υ_a) can be expressed by the following:

$$\Upsilon_a = e^{-aL}$$

The attenuation coefficient (a) is a numerical value less than 1.0 in units of inverse length, which in turn can be expressed in meters or kilometers in the case of the atmosphere, or often in cm for small materials. For example, if the attenuation coefficient for one kilometer of atmosphere is a = 0.70 km^{-1}, the resulting transmission at L = 1 km is Υ_a = 0.497, or about 50%. At an increased distance of 2 km, the total transmission drops to Υ_a = 0.247 which is roughly another 50% reduction in tandem, and so on.

Changes in the temperature, pressure, and gas content can shift the index of refraction as explained by Jones [38], whose work is based on the turbulence theory outlined by Kolmogorov originally in published in 1941 [42]. Kolmogorov surmised that velocity disturbances in the atmosphere occurs in the form of cells, called optical "turbules", which have a degree of statistical consistency that permits a meaningful theoretical treatment. While turbulence creates a relatively small change of index compared to that of common lens materials undergoing temperature and pressure changes, the fact is that there may be many large regions of index variation along a several kilometers long horizontal path through the atmosphere. Kolmogorov's paper discusses the "⅔ power law" that predicts how the atmosphere velocity structure function varies over separate measurement points. Tatarskii (1966) applied the Kolmogorov theory to thermal variations as well, stating that, "wind speed, air temperature, refractive index, and other similar physical quantities undergo irregular random fluctuations in a turbulent atmosphere" [43]. Probability characteristics may be used to characterize the magnitude of effect caused by the random variables, from which Tatarskii defines the parameter C_n^2, which is called the "structure function of the atmospheric index." . Likewise, the value of C_n^2 will also depend upon whether the sensor is looking horizontally or vertically through the atmosphere. Measurement of C_n^2 can be conducted with a scintillometer, which involves an optical or radio transmitter and a separate receiver unit which is placed at the other end of an atmospheric path length. According to Wang, et. al.[44], in the case where the scintillometer aperture is between the outer and inner scale of turbule size, the value of C_n^2 is determined by the following formula, where σ_{In}^2 is the variance of the logarithmic intensity (I_{In}), D is the scintillometer receiver aperture diameter, and L is the path length:

$$C_n^2 = (1.12)(\sigma_{In}^2)(D^{2.333})(L^{-3})$$

The value of C_n^2 along a horizontal path outdoors can vary by orders of magnitude during the course of a 24 hour time period. On a clear day, the passage of the sun has a dramatic impact on ground heating, and hence can cause great changes in atmospheric turbulence magnitudes. Figure 3-8 below by Walters & Kunkel [45] shows a broad range of C_n^2 measurements taken in a desert environment over the duration of a diurnal cycle. Data collected by Espinola, et. al. shows similar results for US Army testing performed at the White Sands Missile Range [10].

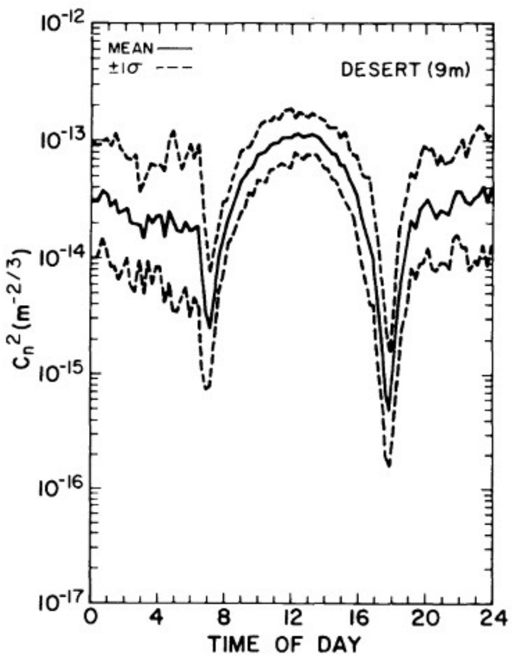

Figure 3-8 : Variance of C_n^2 *During the Diurnal Cycle at White Sands, NM (Walters & Kunkel, 1983)*

The data shows that variations can range from roughly $C_n^2 = 10^{-15}$ for very mild turbulence, to values of about $C_n^2 = 10^{-12}$ for times of very severe turbulence. Highest turbulence is often driven by solar heating effects which may reach a peak during the midday hours 12:00 – 15:00.

3.3.1 Isoplanatism.

The structure of atmospheric turbulence varies along the line of sight distance between the optical sensor and the target location. The turbulence impact is also a function of the solid angle of projection between the sensor optics and the point target in the scene. The solid angle of projection is dependent upon the range *L* as well as the aperture radius of the sensor optics. Fried defines an atmospheric coherence radius "r_0" which defines the maximum sensor optical aperture radius that can possibly achieve diffraction-limited resolution through the turbulent medium [46]. The solution for r_0, often called the "Fried Parameter" (mm), is given by the following equation where again *L* is the horizontal path length in km and wavelength λ in microns:

$$r_0 = [\ 6.88 \div [\ 2.91 \cdot (2\pi/\lambda)^2 \cdot (L) \ \cdot (3/8) \ \cdot (C_n^{\ 2})]\ ]^{0.6}$$

Lateral turbulence variations will also vary with the viewing angle relative to the sensor's optics. In optical terms, this means that the aberration coefficients for any point within the field of view may be uncorrelated to those of another point if the angular separation between the points is large enough. Close neighboring field points, however, may have the same basic turbulence structure and can be imagined as a "patch" within the larger field. The optical aberrations and hence PSF's of all points within a patch are correlated, and thus the term "isoplanatic" is used to describe the consistent optical behavior within the patch area. The maximum field angle θ_0, typically given in units of μrad, over which the optical wavefront can be assumed to be isoplanatic is given by the following equation [46]:

$$\theta_0 = [\ 2.91 \cdot (2\pi/\lambda)^2 \cdot (L)^{2.667} \ \cdot (3/8) \ \cdot (C_n^{\ 2})]\ ]^{-0.6}$$

The concept of a sensor image containing several random isoplanatic patches due to atmospheric turbulence is illustrated in Figure 3-9 below, where in the approximate boundaries of each example isoplanatic patch are indicated by the gray lines:

Figure 3-9: Concept Illustration of Random Distribution of Isoplanatic Patches Across the Field of View.

3.3.2 Temporal Characteristics.

The intensities and distributions of atmospheric turbulence effects will vary as a function of time. Fried discusses the fact that the temporal rate of random fluctuation can have an effect on an imaging system, depending on the integration time (τ) of the sensor's detector. If the sensor integration time is short compared to the turbulence change rate, then a captured frame of imagery will not suffer from blur effects due to image motion. However, if the integration exposure time is long, then the moving tilt and defocus effects will create an effective time-averaged blur in the image, in addition to any other types of aberrations. The temporal rate of change is related to the Fried Parameter (r_0) and the average wind velocity (v_{av}) as follows [46]:

$$t_0 = r_0 \div v_{av}$$

where v_{av} has units of m/sec and t_0 has units of msec. Avoidance of motion-induced blur thus requires that $\tau < t_0$ on average. The following Table 3-A shows the Fried Parameter results for a sensor viewing a target at 3 km distance in the long-wave infrared spectrum centered at 10 μm, and with a steady wind velocity of 10 m/sec (i.e., 22 mph):

Table 3-A: Example Calculations of Turbulence Optical Parameters

INPUT				**CALCULATION**		
λ (μm)	L (Km)	C_n^2 ($m^{-0.667}$)	v_{av} (m/sec)	r_0 (mm)	θ_0 (μrad)	t_0 (msec)
10	3	1.00E-15	10.00	2727.16	285.78	272.72
10	3	5.00E-15	10.00	1038.31	108.81	103.83
10	3	1.00E-14	10.00	685.03	71.79	68.50
10	3	5.00E-14	10.00	260.81	27.33	26.08
10	3	1.00E-13	10.00	172.07	18.03	17.21
10	3	5.00E-13	10.00	65.51	6.87	6.55
10	3	1.00E-12	10.00	43.22	4.53	4.32

Early research for modeling the MTF of turbulence is cited by Jensen, who in turn shows data originally published by Hufnagle which consisted of a Gaussian form which applied to a vertical path through the atmosphere [47]. The selected formula for the effects of turbulence on the system optical modulation transfer function (MTF_{tur}) is given by Kopeika, et. al. via the following equation where ξ is the spatial frequency in cycles per radian, C_n^2 is the index structure parameter in units of $m^{-0.667}$, λ is the wavelength in meters, L is the range length in meters, and D is the sensor aperture diameter in meters [48]:

$$MTF_{tur}(\xi) = \exp[(-57.4) \cdot (3/8) \cdot (\xi)^{1.667} \cdot (C_n^2) \cdot (\lambda)^{-0.333} \cdot L \cdot (1 - 0.5(\lambda\xi/D)^{0.333})]$$

3.4 Objective Optics.

The function of the objective lens is to collect light from a distant scene and then form an optical image of the target and its surroundings. The objective lens assembly may be a simple arrangement of just a few individual lens elements, or it may include complex telescoping optics and zoom lenses.

In any case, for the purpose of a long range imaging sensor it can be assumed that the object range distance is very great compared to the dimensions of the objective lens. In this case, the Newtonian formulation [49] for the first order properties of an imaging lens simplify because the object distance is effectively infinity, and hence many terms drop out. What is left is a set of four basic first order parameters, namely the pupil diameter (D), the input half-field angle (θ), the effective focal length (ƒ), and the image half-height (h). These parameters are shown in the Figure 3-10 below.

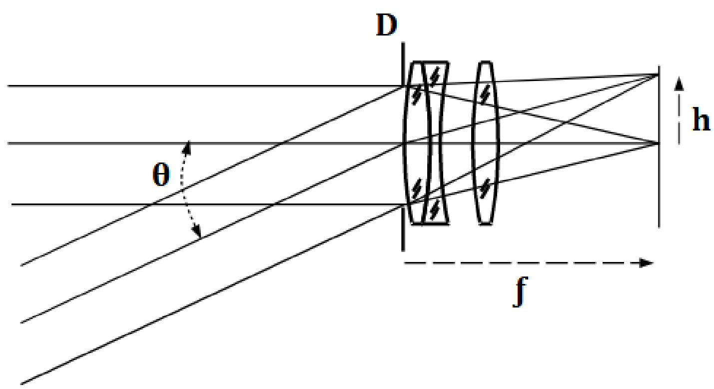

Figure 3-10: Objective Optics 1st Order Parameters (Infinite Object Distance)

In the above Figure 3-10, light is coming in from a distant object on the left side. Bundles of light rays enter the lens with angles of incidence spanning from 0.0° along the axis up to the maximum field of view angle, ± θ°. Each bundle is focused to a single point in the image place, where the height of each point is a function of the angle as given by the following [27]:

$$h = f \cdot \tan(\theta)$$

This relationship is thus a transform from angular space in the object field to linear dimensional space in the image plane. In terms of spatial frequency, the focal length parameter is indeed the conversion factor between cy/mrad in angular object space to cy/mm linear dimensions in the focal plane. For example, if ƒ = 125 mm, then an angle of 1mrad or ±0.5 mrad would correspond to an image height of h = ±0.0625 mm, or a full dimension of 0.125 mm.   Therefore for this value of ƒ, 1 cy/mrad = 1 cy/0.125 mm = 8.0 cy/mm.

The angular resolving power is the ability of the lens to image two objects in close proximity. There are a few slightly different criteria used to mathematically define resolution. One such measure as explained by Jensen uses the half-wave separation criteria [25], derived from Young's Double Slit Experiment which shows that destructive interference occurs when two traveling light waves are one-half of a wavelength (0.5λ) out of phase with one another [50]. This is the limit of linear behavior. To apply the criteria per Jensen's discussion, consider the outermost rays of the light bundles which converge to form two points in the image as shown below in Figure 3-11. The half-wave criterion requires that $L_1 - L_2 = 0.5\lambda$ such that destructive interference does not occur.

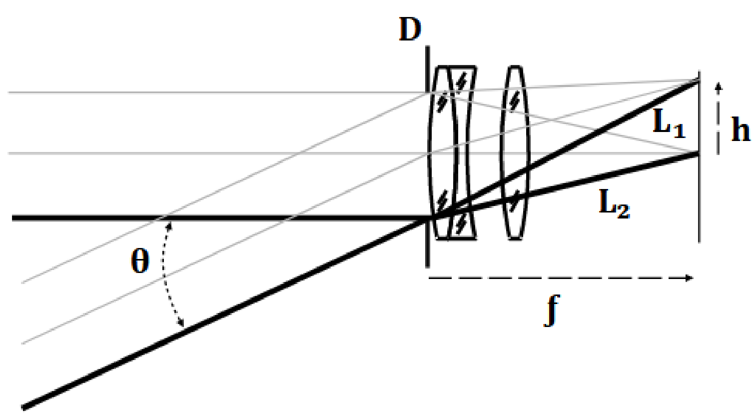

Figure 3-11: Derivation of Angular Resolution Limit

If L_2 corresponds to the on-axis image point, then h = 0 and the length is determined via triangle trigonometry as $L_2 = [\,f^{2} + (0.5D)^2]^{-0.5}$, and in likewise fashion for a small value of (h), the length $L_1 = [\,f^{2} + (0.5D + h)^2]^{-0.5}$. These equations can be re-written to divide out the focal length from each square root term as follows:

$$f \cdot \{\, [1 + (D/2f + 2h/2f)^2]^{-0.5} - [1 + (D/2f\,)^2]^{-0.5} = 0.5\lambda$$

In this form, the fractions can all be assumed to be < 1, and thus they can be expanded via polynomial series. Assuming h << D, then the remaining significant terms reduce to $hD/f = \lambda$, and since for small angles $h/f = \theta$, then the final result for the minimum resolvable angle (θ_{res}) is

$$\theta_{res} = \lambda/D \qquad \text{in units of radians (rad)}$$

This formula is extremely useful for a "back of the envelope" calculation to estimate whether a sensor design can meet a given resolution objective. Jensen notes that there are other criteria, such as Lord Rayleigh's limit based on the separation between the Airy Disk point spread functions, which turns out to be $\theta = 1.22\lambda/D$, but Jensen then points out via referencing work by F. H. Perrin that the half-wave definition appears to match real observations very well [51].

An additional parameter is often derived from the four first order parameters, the "F#" or "f-number", defined as F# = $f \div D$ [27]. The F# is thus a measure of the cone angle formed when the incoming ray bundles are brought to a focal point, and this angle in turn can be used to estimate the *solid angle* (Ω) of the incoming radiation which is important for radiometric photon flux calculations [52]. The solid angle subtended by a random shape relative to a distant point is defined by Boyd as the ratio of the area of the shape to the square of its distance from the point

[53]. Circular symmetry is often assumed for convenience, though it is not a requirement and it is possible to have rectangular or other shapes for the aperture. For a simple ideal imaging lens, the pupil plane defines the area and the focal length is the distance to the focal point. If the pupil diameter is D, then the area of the pupil is $\pi(D/2)^2$, and then the solid angle is $\Omega = \pi(D/2)^2 \div f^2$. Substituting $F\# = f \div D$, the solid angle equation for a lens can then be rewritten as follows:

$$\Omega = \pi\,(2F\#)^{-2}\ ; \text{ units of steradians (sr)}$$

Vincent [54] provides a discussion of several other possible sold angle geometries, including the more general circular spherical cone case where $\Omega = \pi \sin^2(\theta)$. Trigonometry shows that $F\# = 2\tan(\theta)^{-1}$, so as long as $\sin(\theta) \approx \tan(\theta)$ for small angles (θ), the relation for Ω shown above holds true.

The objective lens can be modeled with two primary components of the linear response MTF. The first component is the MTF caused by *diffraction*. Optical science has proven that diffraction, or spreading of a light beam, will occur at the boundaries of an aperture where the incoming wavefront is clipped [55]. This in turn will have an effect upon the resulting image of an objective lens system. There are a variety of mathematical representations for the MTF of a perfect optical system with a circular aperture, and the version used here is derived from Smith as follows [27]:

$$MTF_{opt}(\xi) = (2/\pi)\cdot[\eta - \cos(\eta)\sin(\eta)];\ \text{ where } \eta = \cos^{-1}(\lambda \cdot \xi \cdot F\#)$$

However, it cannot be expected that the optical system will always meet the diffraction limit, and that various structural changes such as thermal expansion resulting from changing environmental conditions or imperfections in fabrication and assembly may be present. The simplest and perhaps most dominant aberration in this case is *defocus*. See Appendix A for a more comprehensive review of optical aberrations in general. O'Neil provides a formulation to add a defocus term multiplier against the diffraction limit [28]. The one-dimensional version of the optical defocus term is shown below as follows:

$$MTF_{\beta} = \mathrm{sinc}[(4\ \xi\ \beta_{010} \div \lambda f_0)(1 - (\xi \div 2f_0))]$$

Where the sinc functions is defined by $\mathrm{sinc}(x) = \sin(\pi x) \div (\pi x)$, β_{010} is the defocus aberration amount typically as a fraction of the wavelength in mm, $2f_0 = (\lambda F\#)^{-1}$ is the spatial frequency diffraction limited cutoff in cy/mm, λ is the wavelength of light in millimeters, F# is the system F-number which is equivalent to the aperture diameter (D) divided by the focal length (f), and ξ is the spatial frequency in cycles/mm or equivalently, line pairs per millimeter (lp/mm). By substitution, this equation simplifies as follows:

$$MTF_{\beta} = \mathrm{sinc}[\ (8 \cdot \xi \cdot \beta_{010} \cdot F\#)(1 - (\xi \cdot \lambda \cdot F\#))\ ]$$

The general formulations for aberrations are detailed in Appendix A for reference, and O'Neill provides additional MTF formulations for each if such are needed [56].

The objective lens can also contribute to the non-linear system response as well, primarily through scattering and transmission losses which each increase the noise level. Optical scattering shall be loosely defined here as a property of the lens materials which alter the path of light away from its ideal geometric trajectory, and which may result in either light rays which do not reach the focal plane, or which reach the focal plane but not in the correct position according to the geometric ray trace. Transmission loss shall be defined as the absence of photons which from a geometric point of view should have reached the focal plane, but for some reason have not passed all the way through the optical system. Scattering is often the result of the lens or mirror element surface finish quality. Both ancient polishing and modern computer machining techniques have proven abilities to achieve surface finishes with Angstrom-level quality, and so it is reasonable to assume that a professional optics vendor can supply lenses and mirrors with negligible scatter effects. Nevertheless, if scattering is a concern for a particular application, there is a formulation for "total integrated scattering" (TIS) predictions offered by Gerchman [57]. The formula is as follows: $TIS = (4\pi\sigma/\lambda)^2$ where σ is the RMS roughness in Angstroms (Å) and when $\sigma << \lambda$ with wavelength λ in microns. The TIS value is a percentage of the amount of incoming light which will be scattered and thus appear as randomly positioned photons in the focal plane. Therefore, the transmission resulting from the TIS loss is $\Upsilon_s = 1 - TIS$.

Transmission losses are unavoidable and generally arises from two physical sources. The first source is reflection at the boundary layer between two materials with different *indices of refraction* (n), which is a fractional measure of the speed of light through a transmitting medium. These effects were studied intensely by Fresnel, for whom the transfer equations are named [58]. At normal incidence angles, the Fresnel equation for reflectance loss at a surface simplifies to $R = [(n_1 - n_0)/(n_1 + n_0)]^2$ where $n_0 = 1.0$ for air and n_1 might be in the range 2.4 – 4.0 for an infrared crystal or glass material. If the material has an index of $n_1 = 3.0$, then the solution for $R = [(3 - 1)/(3 + 1)]^2 = 25\%$ for that boundary interface. If the objective lens assembly has four individual lenses, for example, then the eight boundaries will result in a total transmission due to reflectance loss $\Upsilon_r = (1 - 0.25)^8 = 10\%$. To overcome these losses, lenses are dressed with thin film anti-reflection (AR) coatings which gradually buffer the otherwise abrupt boundary of index transition. AR coatings can yield $\Upsilon_r = 0.99$ or better per surface, and likewise for mirrors, highly reflective coatings can also achieve $\Upsilon_r = 0.98$ or 0.99 reflectance per surface.

Material absorption also causes transmission loss (Υ_m) as discussed previously for the atmosphere, where some photons are absorbed into the atomic structures of the transparent medium. Optical materials are measured to determine their absorption coefficient (α), which is an exponential coefficient for the equation $\Upsilon_m = \exp(-\alpha\, t)$ where (t) is the thickness of the material typically given in cm [41]. For example, Germanium at room temperature may have a coefficient of $\alpha = 0.03\ \text{cm}^{-1}$, and if the thickness (t) of a test sample is 1.0 cm, then $\Upsilon_m = 0.97$. For any given objective lens, all the transmission amounts stemming from reflectance, material absorption, and scattering must be multiplied together to calculate the net objective lens transmission value (Υ_β) summed for all index boundary surfaces, material bulk absorption, and scattering is as follows:

$$\Upsilon_\beta = \prod [\, \Upsilon_r \cdot \Upsilon_m \cdot \Upsilon_s \,]$$

3.5 Detector.

The primary function of the detector is to absorb photons of light and convert that photon energy into an electrical signal, typically either in terms of a change in output voltage or current which can then be fed into other processing electronics. There are many photo-responsive mechanisms, each with requisite material structures required to make an efficient detector. For the detection of infrared radiation in the 3 - 12 micron spectral range, common types of detectors may be broken into two main categories, photon detectors and thermal detectors. In the photon detector case, diodes made of semiconductor elements take advantage of the photo-electric effect within the electron lattice inside the material. When these materials are connected to an electrical circuit, changes in photon flux can result in changes to circuit voltage or current. Thermal detectors instead rely on the material's bulk heating to change as a function of photon intensity. The heat of the material may then change its electrical resistance, and so when placed in a circuit it possible to translate changes in photon flux to changes in either voltage or current within the circuit. Dereniak & Boreman point out that thermal heating will generally have a slower time response as compared to direct photon absorption making an electron-hole pair within a conductor [35].

The basic circuit for a photo-voltaic diode detector connected to a transimpedance amplifier is shown in Figure 3-12 below in accordance with Dereniak & Vincent [35][54]. Photons of light impinge upon the diode material, which in turn produces a voltage change within the circuit. A feedback resistor (R_F) is used to tune the response, and the operational amplifier (A) provides signal gain which allows interface to other electronic circuits and processors within the sensor system.

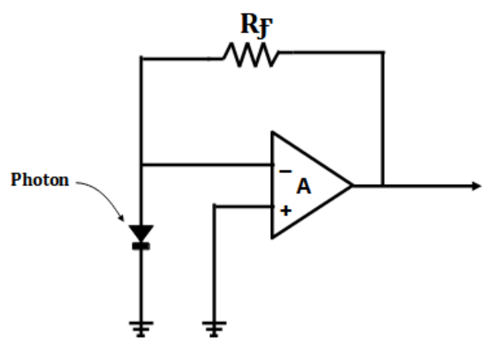

Figure 3-12: Simple Impedance Transfer Circuit of a Photo-detector

The detector pixel transfer function term (MTF_{pix}) is modeled in one dimension per Driggers [24] as a simple rectangular shape with a width (w_{pix}). If the detector is placed in the focal plane of an optical system with focal length ƒ, then the resulting angular subtense of the detector ω is given by $\omega = (w_{pix} \div f)$ in units of radians. The detector pitch (P) is defined as the center spacing between adjacent detector pixels, and for initial modeling purposes it is reasonable to assume that $P = w_{pix}$

until an actual detector device is selected. Per Driggers, the Fourier of Transform of a RECT function with angular extent ω yields the MTF_{pix} curved based on the normalized sinc function per the following equation:

$$MTF_{pix}(\xi) = [\sin(2\pi \cdot \omega \cdot \xi)] \div [2\pi \cdot \omega \cdot \xi] = \mathrm{sinc}(2\pi \cdot \omega \cdot \xi)$$

In terms of sampling by the detector pixel(s), the previous work by Nyquist in analyzing telegraph signals [59], and which was later more developed by C.E. Shannon, shows that one must provide twice the sampling resolution within the receiver as the smallest spatial frequency within the target input in order to reproduce the original target signal [60]. For example, in order to resolve a bar target which has a maximum frequency of 20 cy/mm, it is necessary for a sensor to resolve at least 40 lp/mm. While this is the limiting case, even when the Nyquist condition is met there is a chance that the sampling may be out of phase with the periodic waveform of the target, and lower contrast will result. Jensen notes that the minimum sampling ratio used in the television industry has traditionally been a slightly higher factor of $2\sqrt{2}$ in order to account for the phasing issue [25].

The detector functional block also plays a key and often dominant role in the non-linear response of the sensor system, particularly in regards to *starvation* and *saturation* conditions which were discussed earlier. The quantum efficiency (QE) is a measure of the conversion success rate in terms of converting a photon into an electron. It takes into account interactions within the photo-active detector material to include reflectance, absorption, scattering, and electron recombination. The QE is normalized to 1.0 maximum value, and it does not include any post-detection gain mechanisms within the detector circuit and processor [35]. The incoming energy of a photon is given by $E = hc\nu$, where h is Planck's constant, c is the speed of light, and $\nu = 1/\lambda$, then the energy of the detector material output in terms of effective electrons is $E_e = QE \cdot hc\nu$. The QE is often dependent on the values of λ, and can be plotted for various values of λ to obtain the detector's spectral response curve.

The detector linear and non-linear responses are shown below in Figure 3-13. When the incident photon signal is very low, the detector component's output will be dominated by its own internal noise, often referred to as the Dark Current noise. When the input photon signal becomes strong enough, the detector output will hopefully be linear on average, until that input flux reaches the saturation level, beyond which the detector output will be at a fixed maximum value regardless of the value how far the input signal is above the saturation threshold. Slight noise variations within the linear region are also likely to occur, and for an ideal case these would be due to the photon noise coming from the input signal itself. A complete discussion of detector noise sources can be found in references such as Boreman & Dereniak [35]. For the purpose of this model, only two categories of noise need be considered, namely the photon noise and then all the electrical noises root-sum-squared together into a composite total electronic noise.

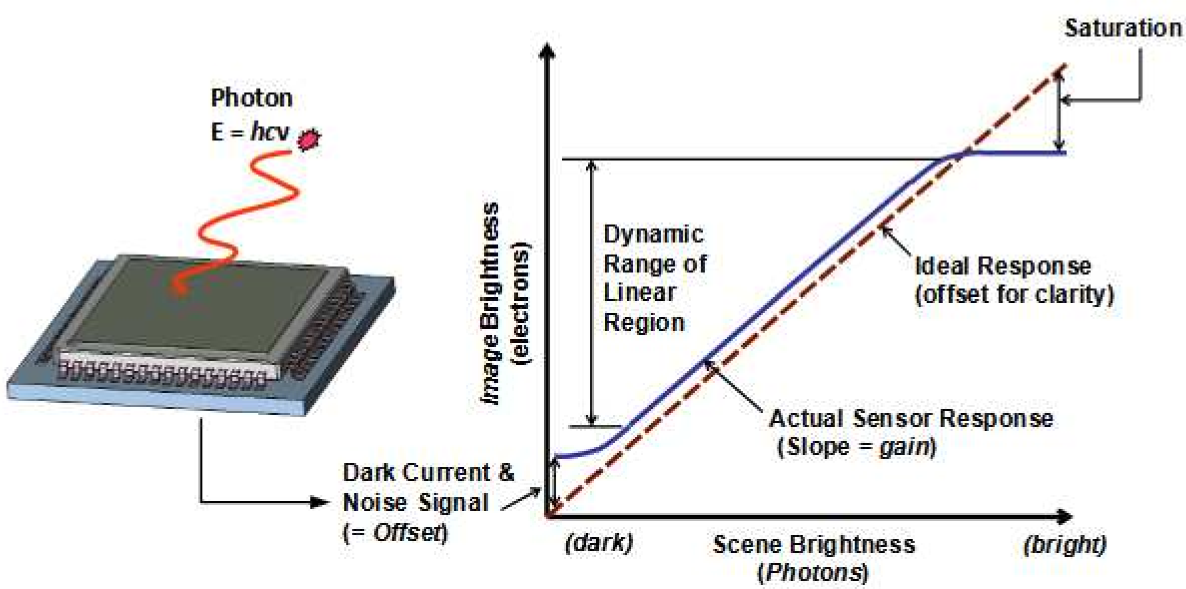

Figure 3-13: Detector Linear Non-Linear Response Characteristics

3.6 Electronic Processor.

There are a wide variety of electronic processing options, some of which are capable of drastically altering the frequency structure of the output signal, and all of which may possess their own unique transfer functions. Lloyd [22] stated that any single electrical filter or ensemble of filters can approximated by three types of filters based on ideal resistors (R) and capacitors (C). The "RC Filter" types are lowpass, highpass, and all-pass. In each case, the electrical frequency f in Hz can be related to the spatial frequency in cy/mrad by the ratio of the detector angular subtense (ω) to the detector integration time (τ) as follows:

$$f \; Hz = (f/\xi) \cdot (\omega \div \tau) \quad \text{cy/mrad}$$

Lloyd goes on to state that many detector circuits behave essentially as lowpass filters with a characteristic frequency of $f_0 = (2\pi RC)^{-1}$ and the resultant electronics $MTF_e(\xi)$ is given by

$$MTF_e(f/\xi) = [\,1 + ((f \div \xi)/ f_0)^2\,]^{-0.5} \quad \text{; where focal length is in meters}$$

Digital image processing can have a wide variety of effects beyond simple filtering, and is thus difficult to generalize in terms of a linear transfer function, so only a brief introduction is provided here. Castleman demonstrates that an array of number values can be used to represent the intensity distribution of an image, where each number is the *grey level* of the associated pixel [29]. Digitization of the detector pixel outputs involves reading the analog voltage or current levels and assigning a digital value typically according a digital bit range. A single digital video image frame is comprised of an array of pixels, and a succession of frames creates the moving video. A typical range of value for a displayed image is 8-bits, resulting in numerical values of 0 - 255. However, if complex math functions are required to process the image before final output to a display, it may be desirable to start with a higher bit sampling to avoid *quantization noise* [35]. This noise occurs when a smooth analog output is sampled in digital steps. To provide a simple example, consider a 2-bit sampled image which will have only $2^2 = 4$ levels of pixel brightness once digitized, namely binary values of either 00, 01, 10, or 11. If the original analog input was a voltage ranging between 0.0 - 40 mV, then an even sampling would have to bin together all the values 0-10 mV for the first brightness level (00), 11 - 20 mV for the second step (01), and so on. The noise interval is a function of the number of bits available versus the extent of the input signal. If the input signal ranges from zero to a maximum voltage (v_{max}) for example, then the quantization noise limit (Δv) for a number of bits (m) is given by $\Delta v = v_{max} \div 2^m$. Quantization noise is a non-linear operation because multiple inputs result in the same output within each increment. The bit level must be increased to reduce this noise, but at the expense of computer hardware and power. Once digitized, the pixels are assigned position indices based on their row (*m*) and column (*n*) coordinates within the image frame. Each image frame can thus be expressed mathematically as a matrix [**A**] with individual pixel element values A(*m*,*n*). The fundamental concept behind digital video processing is that one or more frame digital matrices [**A1**], [**A2**], etc., are inputs to a series of calculations upon the elements such that new resultant frame data matrix [**B**] is the output of the processor. A general concept for digital processing is shown below in Figure 3-14. For color effects, for example, it is common to have three output frames for the red [**B1**], green [**B2**], and blue [**B3**] components. A wide variety of processes can be applied, including additions, mapping functions, geometric transforms, and complex operations such as convolution.

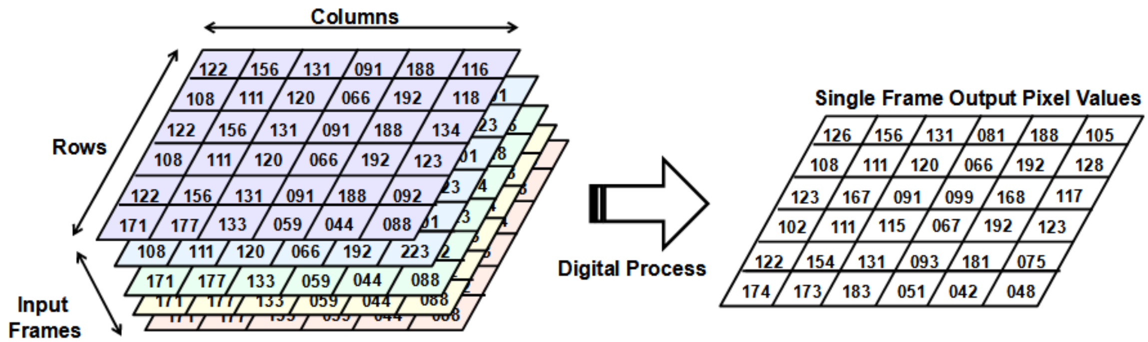

Figure 3-14: General Concept of Digital Processing

The options and types of processing options are nearly infinite, however two very important and related processes shall be discussed further here because they are frequently employed in sensor systems. The first type of calculation is the differential, which the subtraction of a set of pixels values from another. The sets can be contained in single or multiple frames as desired. Within a single frame, for example, a differential along the length of a row can be expressed mathematically for any particular pixel element as follows:

$$B(m,n) = A(m, n) - A(m+1,n)$$

Where [**A**] is the input matrix comprised of elements $A(m, n)$ and [**B**] is the output matrix of elements $B(m. n)$. This operation can be iteratively carried out for values in the matrix [**A**] except for the last element in the row, which is simply carried over as-is into the output matrix [**B**]. The elements of output matrix [**B**] will have high values when there is a large difference between the original element values in [**A**] in the direction of the rows. Likewise, similar calculations can be done along the columns, and the results can be averaged with that of the rows to create a two-dimensional differential output.

In addition to simple differentials, multiplications can also be implemented in a similar fashion. Modern computer math application software packages such as MATLAB and FreeMAT have special matrix operations available as built-in functions. One of these is the digital convolution, which is the second operation requiring discussion here. The convolution operation involves defining a function matrix called a "kernel" denoted here as [**K**] containing elements K(*u, v*) over *u* rows and *v* columns, which is then applied to the elements of input matrix [**A**] according to the following formula where the symbol * represents a convolution operation:

$$[\mathbf{B}] = [\mathbf{K}] * [\mathbf{A}] = \sum_u \sum_v K(u,v) \cdot A(m-u, n-v)$$

Convolution algorithms are widely used in digital discrete transforms and many other functions. For image processing in particular, a very simple set of convolution kernels can be used to detect edges within an image. An "edge" results when the difference between a given pixel and its nearest neighbors is very high. The difference may occur along either the rows or the columns, or both in the special case of a "corner". The two kernels operate along the rows and columns as follows:

$$D_u = (0.5)[1 \;\; 0 \;\; -1]$$

$$D_v = (0.5)[1 \;\; 0 \;\; -1]^T$$

where the symbol ^{T} indicates a transpose from a horizontal row to a vertical column matrix. The 0.5 factor is an amplitude scaling function to normalize the final results. This simple edge gradient detection process involves performing the two convolutions separately, $[D_u]*[\mathbf{A}]$ and $[D_v]*[\mathbf{A}]$, and then element-wise squaring the values of each resulting matrix. The squared matrices are then added to each other, and an element-wise square root is performed to create the final scaled output matrix image. A slightly more complex edge detection kernel is the famous Sobel Edge Detector, which is defined as follows using a notation where the semi-colon indicates the start of a new row in the 3× 3 sized matrix [61][62]:

$$S_u = (0.125)[1\ \ 0\ \ -1;\ 2\ \ 0\ \ -2;\ 1\ \ 0\ \ -1]$$

$$S_v = (0.125)[-1\ \ -2\ \ -1;\ 0\ \ 0\ \ 0;\ 1\ \ 2\ \ 1]$$

The Sobel kernel involves slightly more complicated calculations as compared to the simple edge detection shown earlier, but it has proven to be a standard benchmark against which other edge detection algorithms are often compared. An example of the output of a Sobel detection operation performed on the famous "Lena" image is provided as an example below in Figure 3-15. It is important to notice that the feature edges contain quite a bit of information in terms of defining the object characteristics. In fact, it is possible to add the edge detection result back to the original input image and then normalize that result, thereby enhancing or "boosting" the edges of the original. In terms of a system MTF analysis, this kind of operation can boost the contrast of certain high spatial frequencies.

Figure 3-15: Example of Sobel Edge Detection Processing

The Lena image with the edge detection has an appearance not unlike that of a high-pass filter and could be approximated as such. However, the use of digital processes such as this may also add non-linear noise into the system, which will generally have a dependence also upon the sampling bit levels available. The method of calculating the MTF of a symmetric FIR Response Linear Filter of either the odd or even cases is provided by Rabiner & Gold [63]. Castleman provides an example of how to derive the transform function corresponding to a given convolution kernel by using a Discrete Fourier Transform (DFT) [29]. An example for a non-symmetric simple edge enhancing convolution kernel can be run quickly in math software application programs such as FreeMAT or MathCAD via the following commands:

```
>  F = [0 0 0 1 0 -1 0 0 0];
>  V = fft(F)
> Mod = 0.5*abs(V)
> Plot(Mod)
```

The initial function "F" is the numerical kernel for a one-dimensional edge detector. The zeros on either end provide "padding" such that all non-zero points in the next convolution operations receive explicit values. This kernel (F) is then put through the Fast Fourier Transform operators, which results in a set of complex numbers now contained in an output vector (V), where each value has separate real and imaginary coefficients *A* & *B* according to the general equation which can be translated into polar coordinates using $A\cos(x) + iB\sin(x) = Mod[\cos(x + \theta)]$ where the modulus is the absolute value of the scaled value of V, is the MTF response of the kernel. The angle is the phase offset of the cosine wave. The scale factor of 0.5 is set to ensure the MTF is normalized to a peak value of 1.0. For a symmetric kernel with n odd number of terms, the one-dimensional MTF of a convolution filter kernel (MTF_{ker}) based on Rabiner & Gold [63] with some reformatting is given by the following:

$$MTF_{ker}(\gamma) = C_1 + 2 \sum_i C_i \cos[2\pi \cdot \gamma \cdot (i - 1)] \qquad \text{for } i = 2 \text{ to } N$$

where C_i is the i^{th} coefficient of array size N and the spatial frequency units (γ) are in cycles per *pixel*. The spatial frequency units can be converted by the pixel dimension. A detailed explanation of this process for digitally sampled measurement data is explained further in Appendix C [64].

3.7 Display.

The display block includes either option of a direct-view device such as a television screen or a computer monitor, or alternatively, a micro-screen which is then magnified through an eyepiece optic. In any case, the model shall assume the display is of a high enough quality in order to define the display transfer function as a simple Gaussian blur (φ) in units of mrad as seen by the human eye as follows:

$$MTF_{\varphi}(\psi) = \exp[-2(\pi\varphi\psi)^2]$$

With an ideal display, the human itself will be the limiting factor. The normal limit of the human eye with 20/20 Snellen acuity and 1X magnification is about 1 minute of arc, which is 0.29 mrad [65] [66]. In terms of a blur radius term, divide this by two to yield φ = 0.145 mrad. This is a reasonable estimate for the value of the display subsystem blur (φ) under the assumption that a chosen display will be designed to maximize the performance of the human eye. It is very important to realize that the display spatial frequency term (ψ) benefits from the total system magnification (M), which is the ratio of the input field of view to the apparent field angle of the displayed image to the human eye. The conversion of frequency axes is $\psi = (\xi \div M)$. For example, if the input field of view angle at the objective lens is 5° but the display's apparent field of view to the human eye subtends 40°, then the system has an M = 8 angular magnification factor which must be applied to the display MTF spatial frequency scale. Increasing the display magnification (M) through electronic means can further maximize the display MTF curve, and indeed this is a well known technique in digital systems sometimes referred to as electronic zoom or "e-zoom" [67]. Displays may feature digital pixels; this model assumes that the digital display matches or exceeds the pixel count and dynamic range provided by the detector block. As electronic magnification increases, the noises arising from sampling effects and quantization can create non-linear display artifacts, however these issues are not addressed in this simplified model.

3.8 Physical System Example.

At this point in the model discussion, all the blocks which comprise the sensor "system" as an engineered physical product have been discussed. The sensor "system" shall thus include the functions of the objective optics, the detector, the processor, and the display as shown below in Figure 3-16.

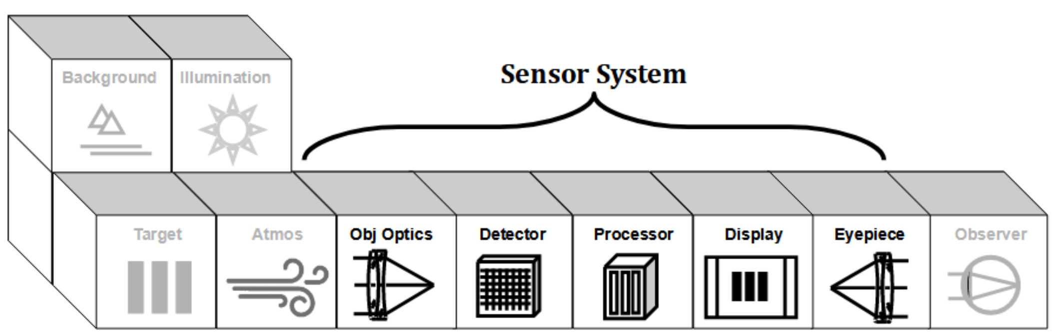

Figure 3-16: Sensor System Block Definition

It is now possible to describe an early form of an infrared imaging sensor within the context of the system model blocks. In the earliest incarnations of infrared imaging sensors, a red light emitting diode was attached to the detector output circuit of each detector pixel as shown below in Figure 3-17. Electrical biases in an intervening amplifier circuit would then be tuned such that changes in photon radiation from the scene striking the detector would result in a visible change in brightness output of the light emitting diode (LED). The arrangement of a linear array of such detector-to-LED components when combined with an image-forming objective lens optic onto the vertical detector array, a scanning mirror to sweep both the detector and LED arrays in the horizontal direction, and an eyepiece to view the scanned LED output is described by Lloyd as a "direct view parallel scan - parallel video system" [22]. Lloyd discusses how this arrangement became the basic architecture for the first generation of Forward Looking Infrared (FLIR) sensors used by the US military. The term FLIR was adopted to distinguish the two-dimensional image framing sensors from downward-looking single channel thermal mapping systems.

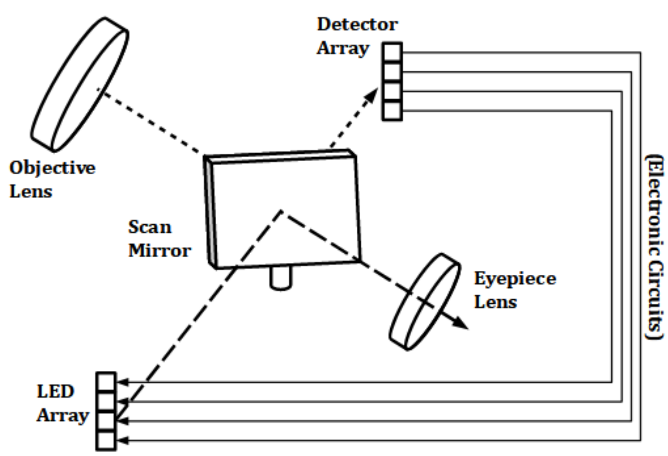

Figure 3-17: Early Architecture for Forward Looking Infrared (FLIR) Sensor Systems

Military developments later incorporated multi-functional optical subsystems, remote video displays, and computer video processing as described more fully in US Patent #5,510,618 [68]. In all cases, from the early to the more modern architectures, the sensor model block diagram remains valid in terms of mathematically predicting the performance of the system, which in turn embodies the functional blocks from the objective lens to the display. The system must now include one new term not yet discussed, which is the stabilization jitter $MTF_{jit}(\xi)$. This parameter applies to the physical stability of the sensor system as a whole integrated unit. As noted by Lloyd [22] and Howe [69], there are many sources of mechanical vibrations, or jitter, which may impact imaging system performance. These may include internal sensor vibration, relative target motion, induced vibrations from the earth, etc. Jitter can come from a variety of random sources which are potentially non-linear, but there is a statistical basis by which these sources can be approximated in a linear model. The Central Limit Theorem states [70] that the sum total of several random processes will eventually exhibit a Gaussian distribution. Therefore for modeling purposes, the summed stabilization jitter component uses a Gaussian random distribution based on an input ems jitter value σ in units of radians. The formulation for an MTF curve for the stabilization jitter contribution, where (σ_{jit}) is the angle of the RMS pointing error expressed in units of mrad, is recommended by both Howe [69] and O'Neil [28] is as follows:

$$MTF_{jit} = \exp[-2(\pi\, \sigma_{jit}\, \xi)^2]$$

It is important to notice that the random Gaussian blur resulting from stabilization jitter error has a different MTF response as compared to that of optical defocus. The stabilization jitter formula has a direct impact to the response cutoff, whereas optical defocus does not impact the system cutoff significantly until the defocus reaches a large value. This is illustrated in Figure 3-18 below which shows several component MTF curves which are multiplied to obtain the total system response curve. The Optics component curve shows the classic ¼ wave defocus Rayleigh limit for an F#/8.88

system at 0.55 micron wavelength, i.e., by setting $\beta_{010} = (¼)(\lambda) = 0.1375$ µm. The stabilization curve shows the performance of the random Gaussian with a stabilization value of 0.001 milli-radians (mrad). The optics Diffraction Limit and the 0.007 mm pitch Detector curves are shown for reference. Note how the Optics defocus curve converges to the diffraction limit at high spatial frequencies, whereas the Stabilization/Jitter curve starts out higher at low frequencies but cuts off more quickly in the high frequency region. It is thus demonstrated that optical defocus behaves much differently from mechanical stabilization jitter, and so during a system analysis each must be considered independently.

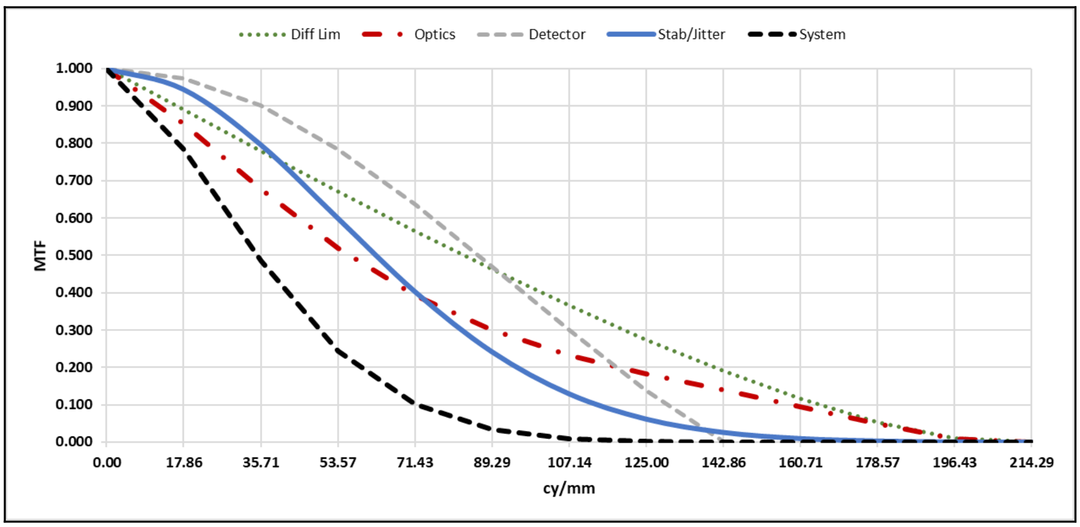

Figure 3-18: System MTF Example Shows Differences Between Optics Defocus & Stabilization/Jitter

Generally speaking, the noise sources for the entire sensor assembly can be combined via a root-sum-square (RSS) estimate as long as they are independent of each other. Each noise can be expressed in terms of a selected unit, perhaps a voltage or often times an electron count, and the individual component values will be squared, summed, and then the square root of the sum is the total system noise value. Optical transmission percentages modify the target signal, but may not necessarily affect the background radiation in a MWIR or LWIR sensor because of radiations internal to the sensor body. Note that the atmospheric transmission will be a function of range distance to the target. The system signal-to-noise ratio (SNR), and hence the *starvation* limit, is determined by comparing the strength of the incoming target signal versus that of the combined noise sources. The atmospheric components are functions of the range to the target, however, so knowledge of the sensor apparatus noises by themselves is not sufficient to estimate the performance when combined with real targets and atmospheres. The mathematical means to add range-dependent parameters are provided by the Johnson Criteria which will be discussed in the next system block.

3.9 Human Observer.

The final block in the system performance model is the Human Observer. The abilities of the human eye and associated brain processing are quite complex, and multiple studies are available which detail the human responses to various stimuli and different lighting levels and degrees of spatial complexity [71]. Given the prevalence of display products in the commercial industry, it is reasonable to assume during the concept development phase of the system engineering process that the loss factors caused by the display should be minimal. However, there is still a need for a link between the sensor output and the human operator which needs to be explained. The fundamental question is, what does the human need to see in order to perform a given task? This question was answered by John Johnson of the U.S. Army Night Vision Lab through a clever series of experiments and large amounts of statistical data. The Johnson experimental setup included small models of various military targets, each painted either as silhouettes or with real exterior paints similar to their real counterparts. A human observer would then view the painted, silhouette, and calibrated bar target pattern all at the same time through a sensor, typically an image intensifier scope as shown below in Figure 3-19. During the period of observation, the ambient light level was slowly raised until the observer felt they could achieve a certain task such as Identification, Recognition, or Detection against a uniform background. Over 20,000 readings were recorded [72].

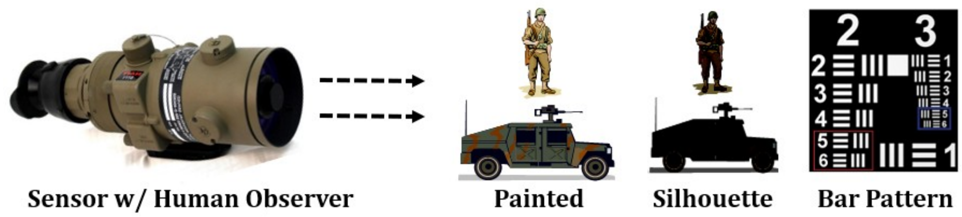

Figure 3-19: Johnson Experiment Illustration

The simultaneous viewing of the targets along with the bar target patterns normalized the test, such that only human performance was the variable being observed. Characteristics of the sensor such as noise, magnification, and so on were normalized by this process, despite claims by Rosell & Willson that it was a requirement of the Johnson experiment that the signal-to-noise and image contrast must also be "sufficient" [73]. This is clearly not the case, because the test method involved starting with light levels so low that the targets could not be seen at all. The test approach was limited, however, to a progressive increase in spatial frequencies, where the lower frequencies keep getting better as higher frequencies come into view. Also, the imagery was monochrome so color effects were not evaluated at all. Regardless of these limitations, the Johnson tests revealed a very simple relationship which specifies the resolution required in order to complete a given visual task or "decision" about the classification or identity of a target. In his 1958 report, Johnson states [74], "*It was found that these results indicated that complex military targets may be considered equivalent in a visual sense to repetitive resolution patterns of appropriate spatial frequencies for each decision level*." The published data table is reproduced in the Figure 3-20 below:

Table I - Optical Image Transformations

TARGET	RESOLUTION PER MINIMUM DIMENSION			
Broadside View	Detection	Orientation	Recognition	Identification
Truck	.90	1.25	4.5	8.0
M-48 Tank	.75	1.2	3.5	7.0
Stalin Tank	.75	1.2	3.3	6.0
Centurion Tank	.75	1.2	3.5	6.0
Half-track	1.0	1.50	4.0	5.0
Jeep	1.2	1.50	4.5	5.5
Command Car	1.2	1.5	4.3	5.5
Soldier (Standing)	1.5	1.8	3.8	8.0
105 Howitzer	1.0	1.5	4.8	6.0
Average	1.0 ± .25	1.4 ± .35	4.0 ± .8	6.4 ± 1.5

Figure 3-20: Johnson Criteria (copy from original paper, courtesy US Army)

It is important to note the error margins associated with each bar resolution nominal value. Johnson's report did not precisely explain the task meanings, but in the introductory section it does imply that detection is a sense that something of interest exists in the scene, recognition is a function of outer shape dimensions, and identification refers to specific details which uniquely describe the target as compared to others of a similar form. An example is provided here by referencing the following Figure 3-22 which uses pixel down-sampling to set the resolution limits.

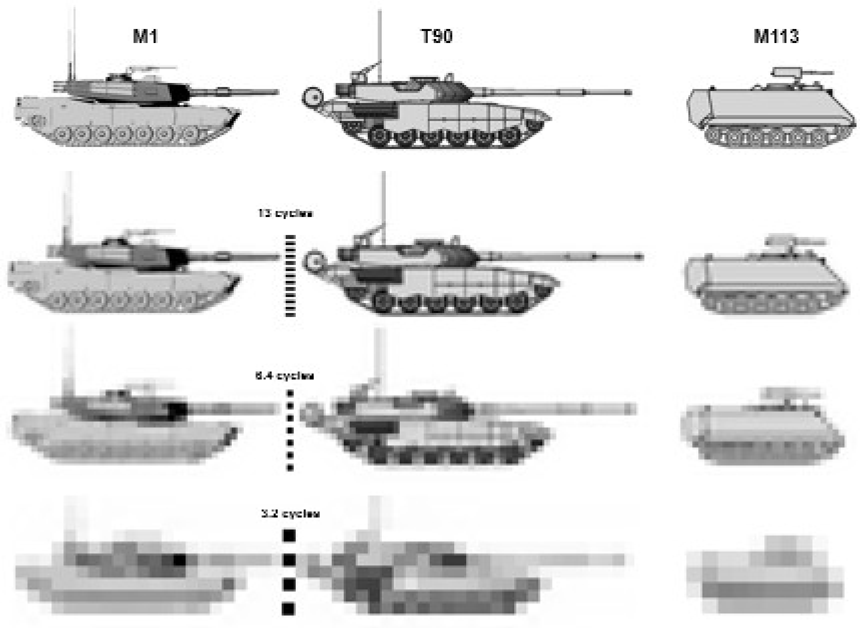

Figure 3-22: Illustrative Example Supports the Johnson Criteria

The task criteria based on military experiments relative to the truck target shall be explained here. The *detection* task is simply realizing there is a vehicle of some sort in the visual field. Since this task threshold requires only two pixels to resolve one cycle, it is not shown in the figure. *Recognition* is the ability to discern the general class of vehicle, such as a truck versus a sedan. Per Figure 3-22 above it is clear that 3.2 cycles is enough to confidently distinguish the two tanks from the M113 armored personnel carrier, but yet is not really enough to distinguish the M1 tank from the T90 tank with certainty. At 6.4 resolved bar pattern cycles, it is now possible to confidently *identify* which tank is the M1 and which is the T90. Therefore in terms of the truck target, identification involves discriminating between different types of trucks. Validation of the Johnson Criteria has been demonstrated for several different types of sensors [75]. The Johnson criteria is used to determine the required minimum resolvable angle of a sensor. As an example, consider a target dimension of 2.3 meters. In order to *identify* this target per Johnson, an average of 6.4 cycles will be required. Given that it takes two pixels to resolve one bar target cycle, then the minimum resolved dimension across the target is simply 2.3 ÷ 6.4 ÷ 2 = 0.18 meters. If this requirement is to be achieved at a range distance of 3 km, then the derived minimum resolvable angle requirement for the sensor is 0.18 ÷ 3000 = 0.06 mrad = 60 μrad.

The final discussion of the human observer block regards the limit of non-linear noise effects. The RCA/Burle Electro-Optics Handbooks states [32], "*Because the eye is normally considered to require an image contrast about three percent in order to appreciate the light-to-dark transitions in the bars, the limiting resolution in line-pairs/mm or in line-pairs per picture width can be considered as the spatial frequency at which the MTF (modulation transfer function) has fallen to a value of three percent*." However, this applies only a to bar target signal against a smooth, non-noisy background. At the point where the SNR = 1.0, the target signal is equal in magnitude to that of the noise. In such cases, there could be other contextual clues within the scenery that might reveal the presence of a target, but in general this cannot be assumed. Therefore, a subjective experiment was created where a short 6 second duration video having 640x480 pixels per frame at 30 frame/sec was created to estimate what gain factor above the noise threshold might need to be in order for a human observer to reliably spot a target pixel. Each frame within the video was comprised of 8-bit pixels having random values between 0 - 128 digital counts, which half to possible dynamic range of an 8-bit video signal. One target pixel was then assigned a different gain value , such that the random number for the single target pixel would be multiplied by the target gain factor (G_t) multiplier. A single video frame is shown in Figure 3-23 below. A series of target gain factors were evaluated, and based on the assessment of three human subjects observing the videos on a standard computer monitor having extra resolution such that the 640 × 480 pixel video was shown at full resolution and at whatever viewing distance was most comfortable for the observer. The observers did not know in advance where the target pixel would be located, and the task was to find it and report the location. The results showed that a target gain value of about G_t = 2.0 was sufficient for confident detection of the target pixel against the random noise background. Gain factors of $G_t = 3$ or more resulted in occasional saturation of the target pixel and were very easy to spot, whereas gain down to about $\sqrt{2} = 1.414$ was sometimes detectable but with a much lower success rate.

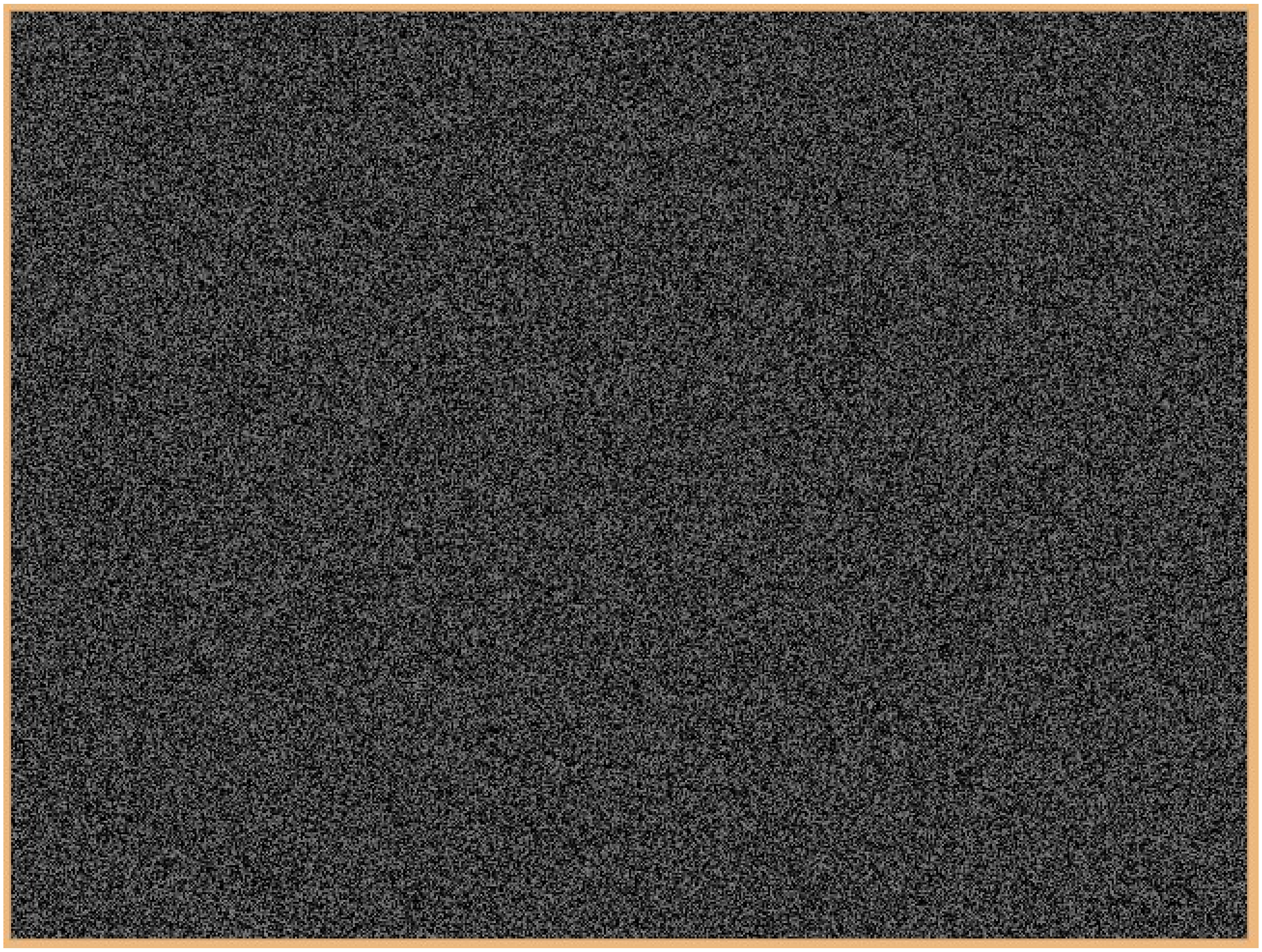

Figure 3-23: Screenshot 640 × 480 Pixel at 30Hz Video Test - Target Pixel Has Gain 2X Over Noise (can you find the bright pixel?)

3.10 Assumptions for Simplicity.

The integrated performance model bounds the linear response with the non-linear effects of saturation and starvation. Per the Linear Systems Theory, sensor device linear performance can be modeled as a cascade multiplication of the MTF's from each the various system components. The turbulence effects can also be approximated via MTF, which in turn allows the system analyst to determine which component factors are the primary contributors to the overall system response as follows:

$$MTF_{sys}(\xi) = MTF_{tur}(\xi) \cdot MTF_{opt}(\xi) \cdot MTF_{\beta}(\xi) \cdot MTF_{pix}(\xi) \cdot MTF_{jit}(\xi) \cdot MTF_{e}(\xi) \cdot MTF_{ker}(\xi) \cdot MTF_{mnt}(\xi)$$

For this model presentation, σ_p shall represent the RMS photon noise, which for N number of incident photons/sec shall be $\sigma_p = \sqrt{N}$, and then σ_e represents the RMS sum of all other fixed noises within the sensor itself, including dark current, quantization, and other system noises as discussed in the previous sections. The summarized general equation for total system RMS noise (σ_{rms} in units of electrons e^-) is as follows:

$$\sigma_{rms} = [\, \sigma_p^2 + \sigma_e^{\,2} \,]^{0.5}$$

The linear MTF response will be bounded by the saturation and starvation (noise) non-linear limits which set the *dynamic range* limits of the system [54]. The non-linear effects may be constant noise sources within the sensor apparatus which can be measured in a laboratory, and they may include range dependent parameters which generally must be measured either in the field or within an environmental simulator. It best to first develop the "lab measurement" predictions before adding the complexity of the atmosphere and range dependencies.

3.11 Saturation.

The lab test scenario removes the atmosphere and range-dependent parameters. Targets and backgrounds are provided via calibrated sources which may be placed at the focus of collimating optics in close proximity to the sensor. In most passive sensor systems it is reasonable to assume that the saturation limit will be determined by the ratio of the total incoming photon flux to the photo-detector's electron well fill capacity under normal viewing conditions. Abnormal conditions, such as when the sensor is struck with a high intensity laser, could cause damage to either or both of the objective lens and the detector, but those exceptional cases are considered out of scope for this performance model exercise. The procedure to check whether a sensor is saturated is as follows, where the brackets indicate the units of the output result at each step:

1. Start with the greater of either object or background temperature T [K]
2. Use Planck's Law to calculate radiance: $\int B(T)\, d\lambda$ over λ_1 to λ_2 [Watts/($m^2 \cdot sr$)]
3. Multiply by Objective Lens solid angle [Watts/m^2]
4. Multiply by Objective Lens transmission [Watts/m^2]
5. Multiply by detector pixel area [Watts = Joules/sec]
6. Multiply by detector integration time [Joules]
7. Convert Joules to Electron count using $e^- = \lambda_m/(hc)$ where $\lambda_m = 0.5(\lambda_1 + \lambda_2)$ [e^-]
8. Ratio the signal electrons e^- to detector well fill e^- maximum per component specification [%]
9. If the detector well is ≥ 100% full, sensor is saturated [logical: yes or no]

The calculation is reversible. By starting with the maximum allowed well fill electron count, the object temperature for saturation can be solved. However, doing the calculation in either direction will require evaluating Planck's Law iteratively to converge upon either the correct temperature or e^- ratio threshold value.

3.12 Signal-to-Noise Ratio (SNR).

Starvation for a thermal sensor is more a question of the target-to-background radiance difference, which is the real "signal", rather than the total signal photon flux. Plank's law shows that for earthly average temperatures around 300 K there is an abundance of self-emitted photons available in the infrared 3-12 micron spectrum. Therefore, the art of "seeing" in the infrared spectrum has more to do with the relative temperature differences, and hence photon flux differentials, between target and background objects. If the temperature difference (ΔT) converted into detector electrons (e^-) is within the range of the system RMS noise level, then the target cannot be reliably discriminated. Furthermore, the value of ΔT will vary as a function of the length of attenuating atmosphere between the target and the sensor aperture. The aggregate of system's independent noise parameters can be estimated as a single root-sum-square (RSS) value [35]. It is now possible to determine the sensor's signal-to-noise ratio (SNR) threshold where the "signal" is defined as the photon flux difference corresponding to the temperature differences (ΔT) between the target and its background. The flux differential must then be compared in a ratio to the total system noise. The steps for calculating a SNR are similar to the saturation process above, but in this case the differential $\Delta T \rightarrow \Delta e^-$ is then compared to the total noise σ_{rms} as follows:

1. Calculate both object & background temperature T & record the difference ΔT [K]
2. Use Planck's Law to calculate radiance $\int B(T)\, d\lambda$ over λ_1 to λ_2 [Watts/($m^2 \cdot sr$)]
3. Multiply each by Objective Lens solid angle [Watts/m^2]
4. Multiply each by Objective Lens transmission [Watts/m^2]
5. Multiply each by detector pixel area [Watts = Joules/sec]
6. Multiply each by detector integration time [Joules]
7. Convert each Joules to Electron count using $e^- = \lambda_m/(hc)$ where $\lambda_m = 0.5(\lambda_1 + \lambda_2)$ [e^-]
8. Calculate the photon noise $\sqrt{e^-}$ from higher of target or background [e^-]
9. Calculate difference (Δe^-) between target & background, which is now the "signal" [e^-]
10. RSS the photon noise with other fixed system noises to solve σ_{rms} [e^-]

11. Solve SNR = $(\Delta e^{-}) \div (\sigma_{rms})$ [unit-less ratio]

This calculation predicts the minimum detectable ΔT as if it were measured in a laboratory with no appreciable atmospheric loss. This is sometimes called the Noise Equivalent Temperature Difference (NETD)[35][22], or equivalently the Noise Equivalent ΔT written as NEΔT [75].

3.13 Non-Linear Load Line.

An excellent way to show the non-linear limits upon the MTF-based linear performance in a single graphic is to plot what is known as "load line" overlaid on top of system MTF response [24]. This technique was originally applied to sensor models based on Minimum Resolvable Temperature (MRT) curves, but the same principle can be extended to MTF curves as well. The Load Line shows the obverse or complement to the MTF, which is the "demand" in order to perform a resolution task. For the starvation case, the minimum contrast demand (C_{min}) with no range dependence is defined as follows:

$$C_{min} = 1 - [(\Delta T - (G_h \cdot NE\Delta T)) \div (\Delta T + (G_h \cdot NE\Delta T))]$$
$$= 1 - [(G_h \cdot NE\Delta T) \div \Delta T]$$

The system performance limit is where the system MTF crosses the load line for C_{min}. For example, if the actual target ΔT = 1.25 K, the human eye gain factor is $G_h = 2$, and the NEΔT = 0.0305 K, then $C_{min} =$ 0.15 (unit-less). This means that the range for which a system MTF curve above this contrast threshold will be above the non-linear noise threshold, and hence the task is possible. Ranges beyond this point are outside the capability of the system. Since the atmosphere and other range-dependent effects are not yet addressed, the C_{min} demand curve at this point is shown as a straight horizontal line across the MTF graph. Likewise, the saturation contrast limit (C_{sat}) can also be applied in a similar fashion, where the target ΔT is raised to the point where the detector well fill is 100% full (ΔT_{100}). Typically the C_{sat} demand value will be very low, and so the plot of this line will normally be close to the horizontal axis.

$$C_{sat} = 1 - [\, (\Delta T_{100} - (G_h \cdot NE\Delta T)) \div (\Delta T_{100} + (G_h \cdot NE\Delta T))\,]$$

An example of the combined plotting of a system MTF with the saturation and starvation limit load lines is shown in the following Figure 3-24. It is important to label the starvation (C_{min}) curve because it is unique to the actual target ΔT.

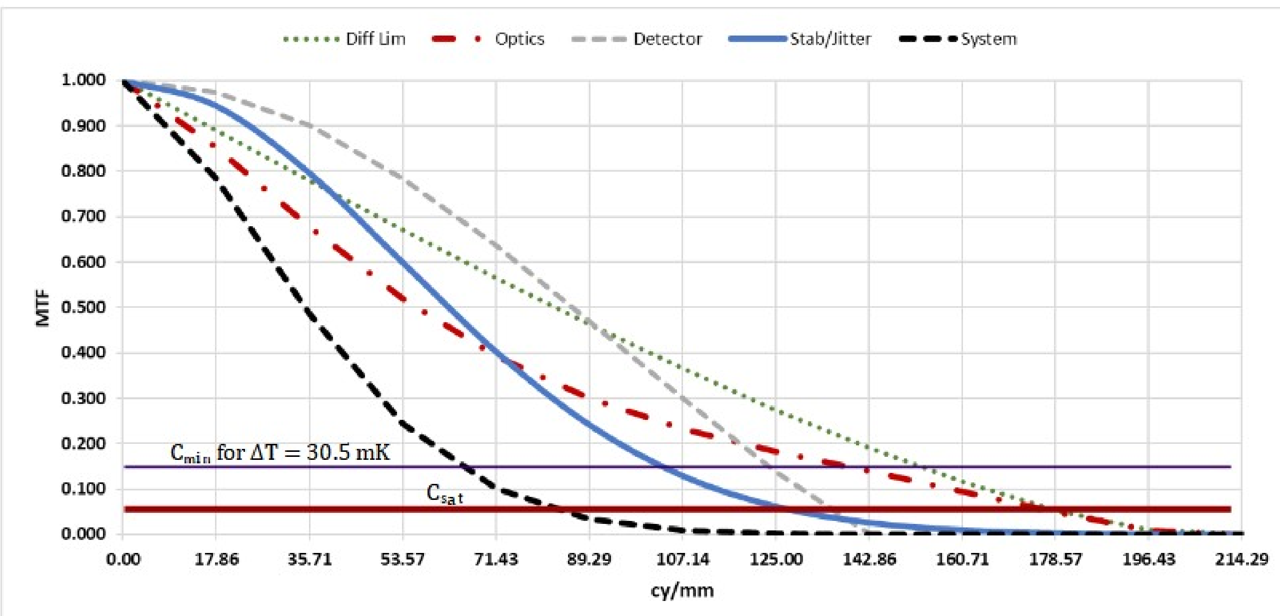

Figure 3-24: Example of Load Lines Showing Starvation and Saturation Boundaries to Linear MTF

The composite MTF & Load Line chart can be interpreted as follows: The spatial frequency where the starvation curve crosses the system MTF corresponds to the maximum contrast resolution for a specific target ΔT. The point where the saturation curve crosses the MTF is the highest spatial frequency the system could ever resolve, right at the threshold where the signal strength hits the maximum linear response of the system. The crossover point are thus the limits of the system's linear response, which is usually interpreted to be the maximum resolution and contrast capability of the sensor.

3.14 Range-Dependent Calculations.

Both the linear MTF and non-linear noise calculations involve range-dependent components which have not yet been addressed. What is needed first is a means to translate the units of the horizontal axis to a range value for a given task of either *detection*, *recognition*, or *identification*. This calculation is precisely what the Johnson Criteria provides. The first step is to translate MTF values in units of cy/mm in image space into cy/mrad in object space. This is done by scaling the axis with the objective lens focal length (ƒ), which if given in meters is solved by the following relation:

$$1.0 \text{ cy/mrad} = ƒ^{-1} \text{ cy/mm, with } ƒ \text{ in meters}$$

The next step is to apply the Johnson cycle criteria (Ɉ) to the critical target dimension (ʤ). The general formulation for the angular frequency ϕ in units of cy/mrad corresponding to the Johnson Criteria task resulting from trigonometry is as follows:

$$ϕ = [\ \tan^{-1}(\ ʤ \div \text{JC} \div L\ )\ ]^{-1}$$

This can be applied to any value of range distance (L) to create a continuous scale. For example, if the criteria for *identification* is $Ɉ_i$ = 6.4 cycles, the target critical dimension ʤ = 2.3 meters, and the range is L = 1000 meters, then the required angular frequency is $ϕ = [\tan^{-1}(2.3 \div 6.4 \div 1000)]^{-1}$ = 5.82 cy/mrad. Therefore, if the system MTF plot is above zero at a frequency value of 5.82 cy/mrad, then there is a chance that the identification task is possible at a range of 1000 meters. This calculation can be performed to scale any cy/mrad angular frequency to a specific range task range distance. The Johnson Criteria thus provides the conversion factor between the task-specific range and the frequency scale of the MTF curve. Additional axes can be generated for the other Johnson Criteria (detection, recognition) by similar means if desired. Indeed, it can be helpful to plot multiple horizontal axis below the basic MTF curve and thus a great deal of system performance information can be captured in a single graphic. The final steps in adjusting the model to handle range-dependent linear and non-linear contributors can now be accomplished, since a conversion factor between range in kilometers for a specific task versus the spatial frequency is available. For example, the turbulence MTF equation has both variables of spatial frequency (ξ) as well as range to target (L). Using the task-specific Johnson Criteria conversion, the expression can now be written in terms of single horizontal axis variable by substituting

$$\xi = (\text{ʃ}^{-1}) \cdot [\, \tan^{-1}(\, \text{ʤ} \div \text{ɟ} \div L \,)\,]^{-1}$$

The written form makes the calculation appear much more difficult than it really is when the formulae are set up in a spreadsheet software. It is important to realize that the calculations are a function of the selected Johnson Criteria for a specific task.

3.15 Complete System Model.

This section shall provide an example of a completed system model using parameters appropriate for the customer objectives. The model begins with the low turbulence conditions, and then higher turbulence can be entered and the resulting losses in range performance thereby become quantifiable. In terms of system engineering, there will be a set of input parameters, a series of mathematical processes, and then an output product which will be the integrated plot showing the system linear and non-linear response curves over a variety of range distances. Noise sources from quantization, sampling, and electronic filters shall be assumed to have negligible effects for now and will not be shown for convenience. An example set of inputs is provided below in Table 3-B.

Table 3-B: Model Input Example

Variable	**Description**	**Value**	**Units**
ʤ	Target critical dimension	2.3	meters
λ_1	Spectral band, lower limit	7.5	μm
λ_2	Spectral band, upper limit	12.0	μm
ΔT	Target-to-background temperature difference	1.25	K
T	Average Background Temperature	300	K
a	Atmos. Absorption coefficient (70% per km)	0.356	km^{-1}
$C_n{}^2$	Atmospheric Index Structure (mild turbulence)	1×10^{-15}	$m^{-0.667}$
ʃ	Objective Lens focal length	400	mm
F#	Objective Lens F#	3	(no unit)
Υ_β	Objective Lens total transmission	0.70	(%)
β_{010}	Objective Lens Defocus aberration	0.25	waves (λ_m)
P	Detector Element Pitch (square sides)	0.028	mm
W	Detector well capacity maximum	12M	e^-
QE	Detector Quantum Efficiency	0.80	(%)
τ	Detector integration time	7×10^{-5}	sec
σ_e	Detector & Electronics total RMS noise	1200	e^-
σ_{jit}	Stabilization/jitter RMS	.005	mrad
φ	Display Blur RMS	0.145	mrad
M	System Magnification	9.5	(scalar)
$ɟ_i$	Johnson Cycle Criteria for Identification	6.4	cycles

These parameters can be input into a spreadsheet which will then carry out the calculations and provide results. All angles are in radians, and care must be taken to ensure linear unit conversions are correct. Starting with the non-linear noise components, the first objective of the model is to manually find the target-to-background temperature difference which results in a SNR = 1. This will then later be used to establish the SNR for the actual target, expressed as a ratio of temperatures. The target and background temperatures are converted via Planck's equation into a spectral radiance in units of Watts/($m^2 \cdot sr$), which in turn are multiplied by the F# solid angle, the detector element area, the objective lens transmission, the detector integration time, and the detector QE.

Upon completion, the only remaining unit left is Joules, which are converted into units of electrons. The "signal" is the difference in electrons between the target and background radiation. The photon noise is the square root of the larger of either the target or background radiation electrons, and this is combined with other internal systems noise via root-sum-square (RSS) to obtain the total noise factor. The ratio of the "signal" to the total noise factor in units of electrons is the SNR. The temperature difference between target and background was adjusted manually until SNR =1 was achieved. Likewise, the detector well fill percentage was monitored to be sure saturation had not occurred. For the saturation limit load line, the target temperature input is increased until the well fill reaches 100%. In this example, that occurs when the T = The specific inputs and output results are shown in Figure 3-25 below:

Backgrnd T	Target T	λ_1	λ_m	λ_2	F#	P (w_{pix})	Υ_β	τ	QE	Max Well	σ_e
K	K	μm	μm	μm	(-)	mm	%	sec	%	e^-	e^-
300.000	300.027	7.5	9.75	12	3	0.028	0.7	7.00E-05	0.85	1.20E+07	1200
Backgrnd e^-	Target e^-	Well Fill	Δe^-	σ_p	σ_{rms}	SNR	ΔT				
5.9953E+06	5.9980E+06	50%	2,719	2,449	2,727	1.00	0.027				

Figure 3-25: Output of Model Results For Signal-to-Noise Ratio (SNR)

The next step is to model the linear MTF responses of the system, along with a linear representation of the turbulence component. The product of these MTF solves the system-level MTF as follows:

$$MTF_{sys}(\xi) = MTF_{tur}(\xi) \cdot MTF_{opt}(\xi) \cdot MTF_{\beta}(\xi) \cdot MTF_{pix}(\xi) \cdot MTF_{jit}(\xi) \cdot MTF_{\varphi}(\xi)$$

The next following Figure 3-26 shows the calculations for the given set of input parameters.

ʤ	λ_1	λ_2	ƒ	F#	β_{010}	P	σ_{jit}	φ	M	$ʄ_i$	C_n^2
2.3	7.5	12	0.4	3	0.15	0.028	0.005	0.145	9.5	6.4	1.00E-15
meter	micron	micron	meter	(no unit)	waves	mm	mrad	mrad	(scale)	cycles	$m^{-0.667}$
L	ƒ/ξ	ξ	$MTF_{tur}(\xi)$	$MTF_{opt}(\xi)$	$MTF_{\beta}(\xi)$	$MTF_{pix}(\xi)$	$MTF_{jit}(\xi)$	$MTF_{\varphi}(\xi/M)$			$MTF_{sys}(\xi)$
km	cy/mrad	cy/mm	%	%	%	%	%	%			%
0.00	0.00	0	1	1	1	1	1	1			1
0.25	0.70	1.74	1.000	0.935	0.994	0.996	1.000	0.998			0.924
0.50	1.39	3.48	1.000	0.871	0.980	0.984	0.999	0.991			0.832
0.75	2.09	5.22	1.000	0.806	0.961	0.965	0.998	0.980			0.731
1.00	2.78	6.96	1.000	0.743	0.939	0.939	0.996	0.965			0.629
1.25	3.48	8.70	0.999	0.680	0.917	0.905	0.994	0.946			0.530
1.50	4.17	10.43	0.999	0.618	0.897	0.865	0.991	0.923			0.438
1.75	4.87	12.17	0.998	0.556	0.880	0.820	0.988	0.897			0.355
2.00	5.57	13.91	0.998	0.497	0.868	0.768	0.985	0.867			0.282
2.25	6.26	15.65	0.997	0.438	0.860	0.713	0.981	0.835			0.219
2.50	6.96	17.39	0.996	0.381	0.858	0.653	0.976	0.800			0.167
2.75	7.65	19.13	0.995	0.327	0.862	0.591	0.972	0.764			0.123
3.00	8.35	20.87	0.994	0.274	0.871	0.526	0.966	0.726			0.088
3.25	9.04	22.61	0.993	0.224	0.885	0.460	0.960	0.687			0.060
3.50	9.74	24.35	0.991	0.177	0.903	0.393	0.954	0.647			0.038
3.75	10.43	26.09	0.990	0.133	0.924	0.326	0.948	0.606			0.023
4.00	11.13	27.83	0.988	0.094	0.947	0.261	0.941	0.566			0.012
4.25	11.83	29.57	0.986	0.058	0.968	0.198	0.933	0.526			0.005
4.50	12.52	31.30	0.984	0.029	0.986	0.137	0.926	0.486			0.002
4.75	13.22	33.04	0.982	0.007	0.998	0.080	0.917	0.448			0.000

Figure 3-26: MTF Calculations Based on Model Inputs

It is often helpful to plot the component MTF's versus the system MTF as shown below in Figure 3-27. This provides a quick means of identifying which parameters have the most influence upon the system response. In this example, the turbulence effects are negligible, whereas the optical diffraction and detector pixel pitch MTF's are the most dominant. Note also the shape of the optical defocus (MTF_{β}), which is strongest in the mid-frequency region but then becomes less important at the highest frequency end of the graph.

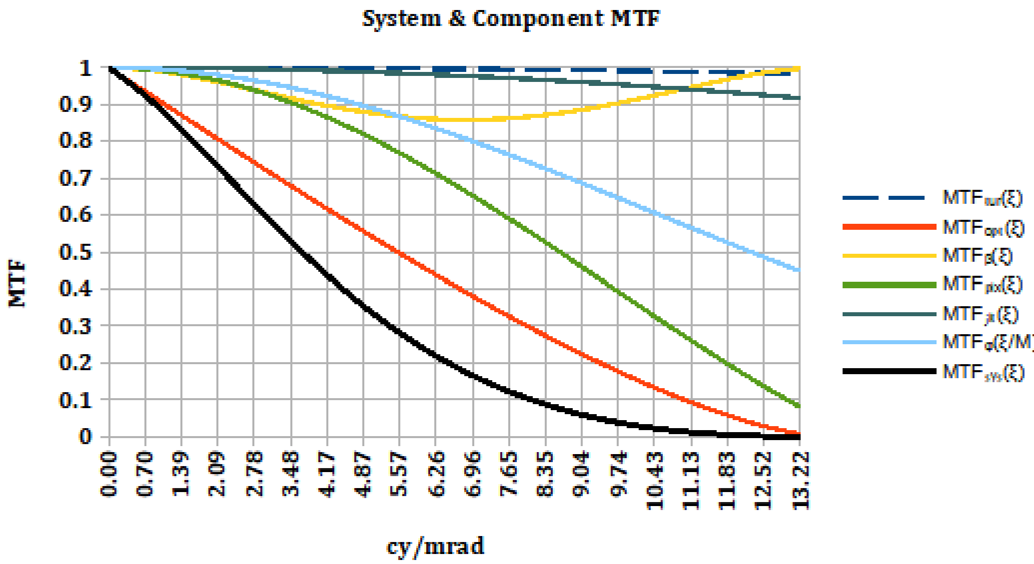

Figure 3-27: Plots of Component & System MTF

The final step is to then overlay the Load Line on top of the system MTF, where the Load Line compares the ratio of the target's apparent ΔT as it is attenuated through the atmosphere. The axis of this final graphic can now be changed from cy/mrad to range in kilometers (km) via the Johnson cycle criteria as a scale factor as shown below in Figure 3.28. The point where the Load Line crosses the System MTF is where the non-linear response takes over and the system's contrast resolving ability is no longer predictable, and so the corresponding range is considered the limit of the system for the specified visual task. In this example, the sensor is capable of identifying a 2.3 meter target dimension with ΔT = 1.25 K at a range of just over 2.75 km on a day with about 70% per km atmospheric transmission and low turbulence.

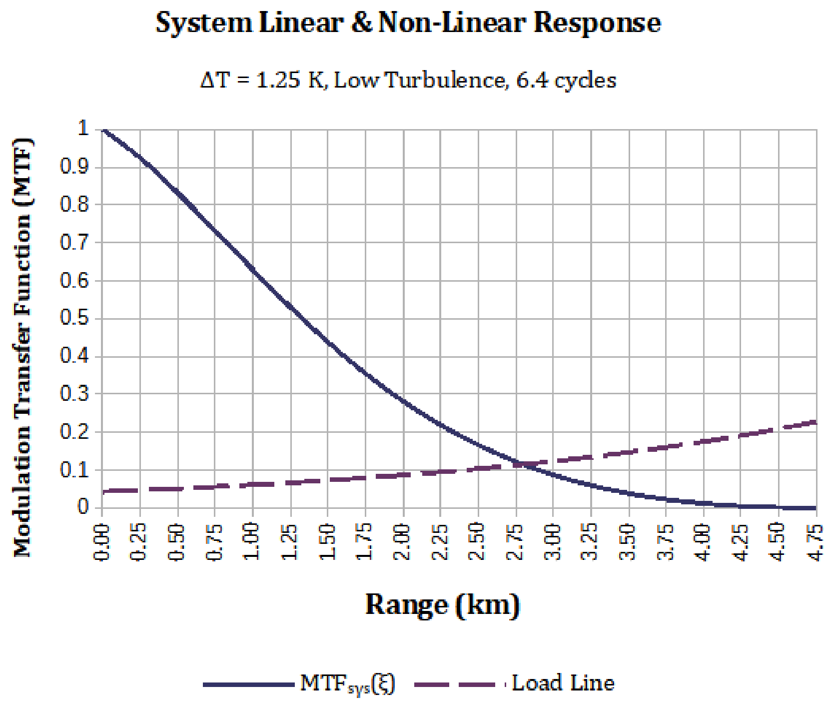

Figure 3-28: Sensor Maximum Range Occurs at Crossover Between Linear & Non-Linear Regions

The model can now also be used to show the predicted performance of the sensor when encountering turbulence. Leaving all other terms the same and changing only the C_n^2 term from 1.00E-15 to 5.00E-13 produces the following results, starting first with the component MTF plots per Figure 3-29 below:

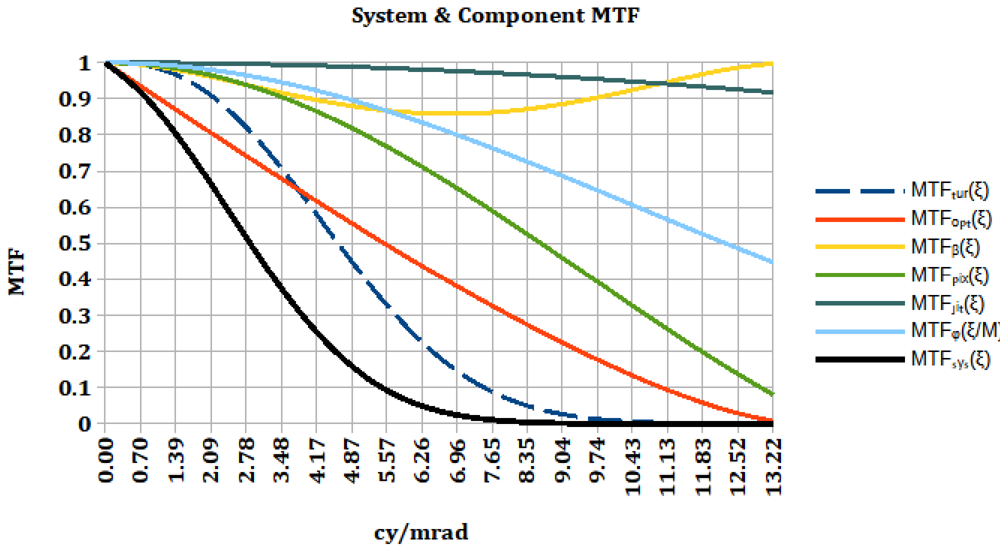

Figure 3-29: System & Component Linear MTF for High Turbulence

The increase in turbulence strength (C_n^2) results in a significant downward shift in the turbulence MTF curve (dotted line), which hits near-zero modulation at just over 9.74 cy/mrad and has now become the most dominant component for the System MTF. It is therefore expected that a significant range loss will occur, and this is confirmed in the next plot below which shows the System MTF versus the Load Line for the non-linear components. Indeed, the identification range is now reduced from just over 2.75 km to about 2.00 km as shown in Figure 3-30 below. The system no longer meets the customer requirement under these turbulence conditions.

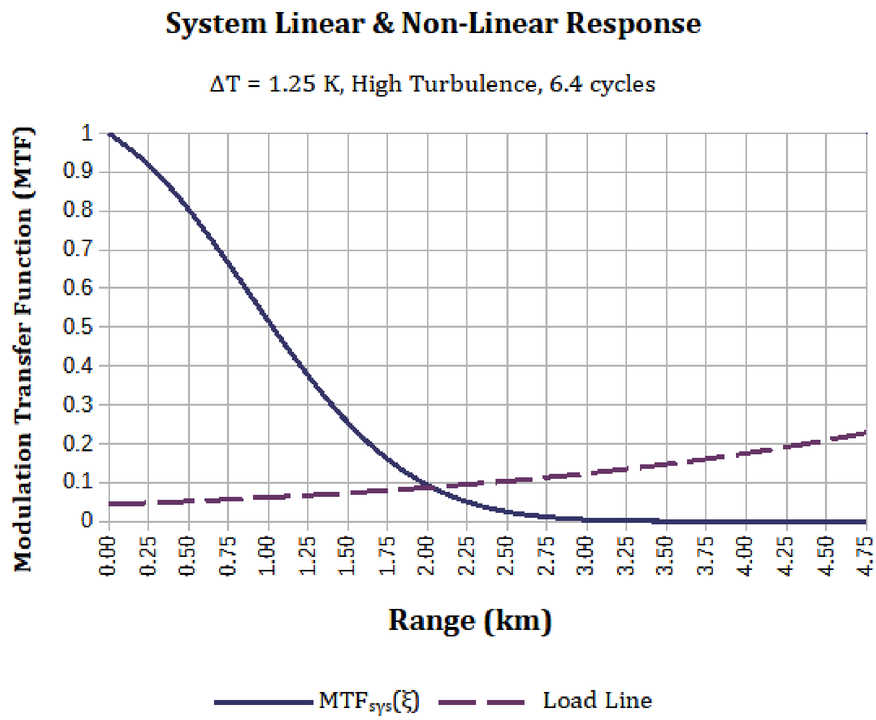

Figure 3-30: Sensor Range Crossover Point for High Turbulence

The system performance model is a very powerful tool to help govern the system design process. The model allows the system engineer to issue and monitor an *engineering budget* which can be flowed down to the design activity. For example, the actual objective lens transmission may at some point turn out to be higher or lower than what was originally estimated in the model. The impact of changes to the overall system can be quickly evaluated, and the sensitivity of each change can be assessed in order to perform trade studies and optimizations of parameters. As the design process continues, the initial model can be *re-baselined* with the updated values, and new budget allocations can be distributed to the design team.

3.16 Monte Carlo Sensitivity Analysis.

Monte Carlo statistical analyses can be accomplished by an iterative process of applying slight random variances to each input parameter and then keeping track of statistical spread of the output range values for each iteration [76]. An example is provided in Figure 3-31 below where a uniform ±5% tolerance is assigned to all the input parameters. A total of four iterations are then run, with each having a random number multiplier to generate sets of unique parameter values within the tolerance range.

Parameter	Value	Unit	± Tolerance	Trial 1	Trial 2	Trial 3	Trial 4
d_ζ	2.3	meter	5.00%	2.19	2.31	2.33	2.25
λ_1	7.5	μm	5.00%	7.46	7.63	7.67	7.40
λ_2	12	μm	5.00%	12.25	12.17	11.85	12.39
ΔT	1.25	K	5.00%	1.26	1.21	1.29	1.21
T	300	K	5.00%	300	285	300	298
a	0.35	km^{-1}	5.00%	0.346	0.349	0.338	0.336
C_n^2	5E-13	$m^{-0.667}$	5.00%	5.05E-13	4.89E-13	4.85E-13	5.10E-13
f	0.4	meter	5.00%	0.42	0.40	0.41	0.41
F#	3	no unit	5.00%	2.92	2.99	2.86	3.00
β_{010}	0.15	% of λ_m μm	5.00%	0.16	0.15	0.15	0.15
Υ_β	0.75	%	5.00%	0.72	0.75	0.74	0.73
P	0.028	mm	5.00%	0.0276	0.0279	0.0267	0.0283
W	8000000	e^-	5.00%	7.80E+06	8.14E+06	8.32E+06	8.05E+06
σ_e	1200	e^-	5.00%	1,259	1,147	1,223	1,216
QE	0.8	%	5.00%	0.80	0.77	0.82	0.76
τ	7E-05	sec	5.00%	7.10E-05	7.08E-05	7.15E-05	6.74E-05
σ_{jit}	0.005	mrad	5.00%	0.0048	0.0051	0.0051	0.0048
φ	0.145	mrad	5.00%	0.138	0.139	0.151	0.140
M	9.5	no unit	5.00%	9.74	9.49	9.83	9.12
G_h	2	scalar	5.00%	2.03	2.08	1.94	2.01
J_i	6.4	cycles	5.00%	6.56	6.63	6.19	6.28

Figure 3-31: Four Monte Carlo Trial Sets of Input Parameters

For each set of input parameters. the resulting system MTF and Load Line curves can be generated. Those curves may be plotted all together as shown in Figure 3-32 below. The statistical yield is visualized as the width of the collective overlay of curves for both the System MTF and the Load Lines. The minimum and maximum intersection points provide a measure of the region of expected system performance in terms of task range. This example shows only four iterations for clarity, but more iterations can be added to increase the statistical confidence of the exercise. In this example, the Trial 3 MTF curve stands out noticeably above the others. It is interesting to note that this particular trial had the smallest pixel pitch (P), fastest F#, lowest upper wavelength (λ_2), and highest magnification (M) of the four iterations. All of these would indeed contribute to a higher system MTF overall. This information gives valuable insight as to how the system performance might be optimized further. Indeed, the methods for numerical optimization are very closely related to Monte Carlo processes [77]. Even at the beginning stages of design when the system parameters are only estimates, the Monte Carlo analysis is a valuable tool for the System Engineer.

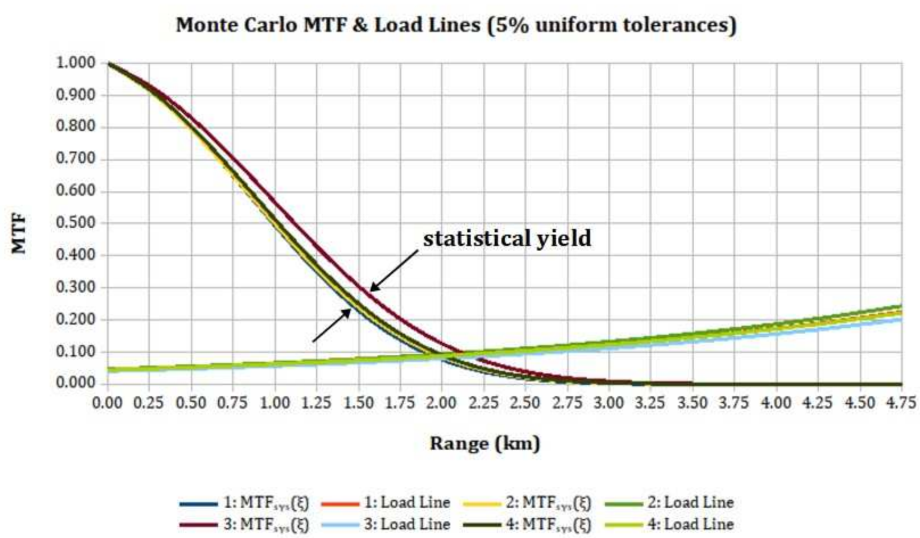

Figure 3-32: Monte Carlo Plot Overlays Show Statistical Yield

3.17 Model Verification.

A verification of the new sensor performance model was conducted by comparing results to a similar model effort described in Driggers [24]. Specifically, Figure 11.13 shows the composite system MTF for a series of sensor parameters shown in Table 11.5 which include an F# = 2.0, focal length of 250 mm, detector pitch of 0.030 mm, and an integration time of 0.010 msec. Driggers provides the other detector parameters using the normalized detectivity (D*) parameter [24][35]. This approach is not recommended in the current model, however, because while the D* does provide an estimate of the band-limited noise, it carries no information about the maximum well fill saturation limit. The example parameters were entered in the new model and the results were compared per the following Figure 3-33 which shows the Driggers MTF on the left and the new model on the right. The system MTF's are nearly identical.

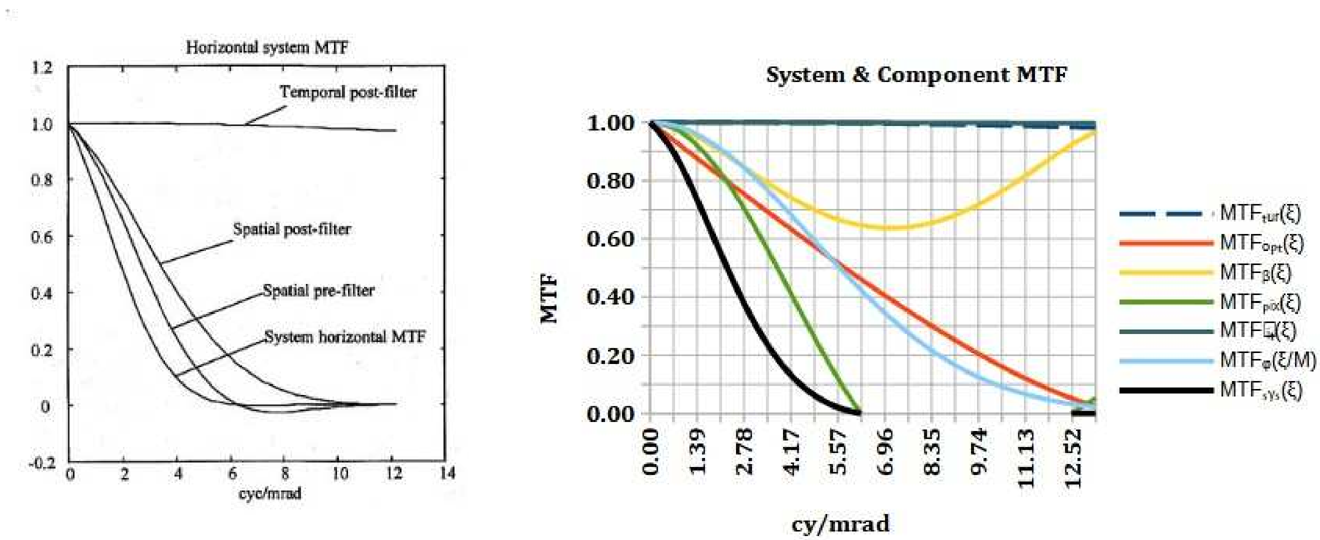

Figure 3-33: Verification of New Model (ref. Driggers, Fig 11.13 on left versus new model on right)

The Driggers discussion separates MTF components into two categories [24]. The "Pre-Filter" category includes the optics and detector characteristics, whereas the "Post-Filter" includes signal processing, display, and human eye components. This is roughly equivalent to the "front end" and "back end" terminology which will be used in this document. The system parameters in the Driggers text include extra display losses caused by the cathode ray tube (CRT) type of display system. The new model does not assume any particular method of display, and the suggested default is an ideal eye-limited case. The CRT parameters do degrade the mid-frequency response, and so this has been accounted for by adjusting the display-eye term (φ) parameter in the new model from a nominal 0.143 to 0.4. This change does not change the cutoff, but does lower the mid-frequency response somewhat. The dominant parameters for the optical diffraction and the detector width are the same, and the overall system MTF response is nearly identical. Overall, this analysis provides confidence that the new model is correctly predicting the system response based on its relatively simpler set of inputs.

Chapter 4 - Engineering Analysis

The system performance model shows how all the major system building blocks interact to achieve the desired performance. However, the model does not completely address many other factors and derived requirements which must be considered. One such parameter which has not yet been directly addressed is the sensor field of view, and thus a brief analysis on that topic is included in a later engineering analysis section. A second and more important issue is the fact that the previous system model addresses the effects of turbulence in terms of an average linear modulation transfer function (MTF), but without any insight as to how the optical wavefront effects propagate through the sensor and no information about how the system becomes highly shift-variant with significant changes occurring across the field of view. Indeed, this issue is addressed by assessing the desired *logical architecture* shown in Figure 4-1 below.

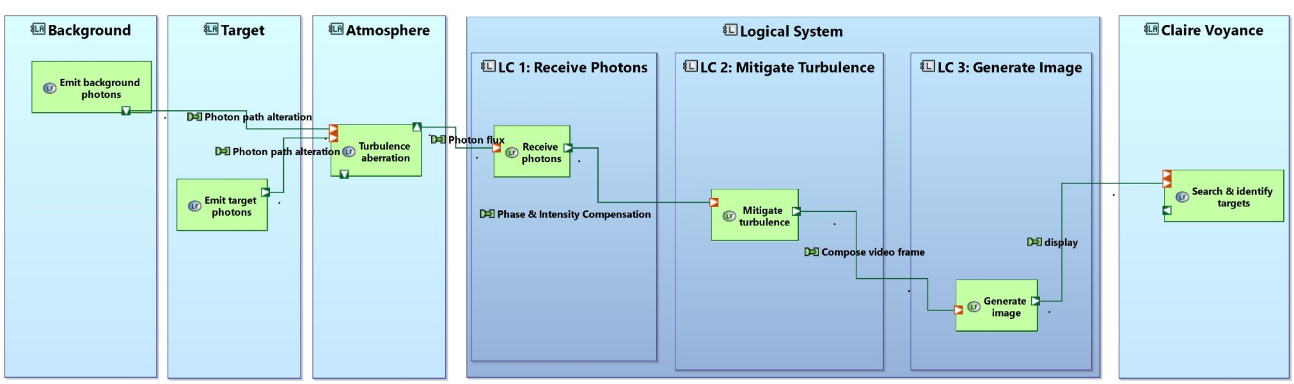

Figure 4-1: Logical Architecture

The new logical architecture shows that the sensor system must include a means of mitigating the atmospheric turbulence effects. This in turn brings up the questions, how can the performance of a mitigation technique be modeled in a away that is compatible with the existing system performance model? To solve this problem, a unique optical ray-tracing technique shall be described in the following sections which combines the actual system optical prescription with one or more turbulent phase-inducing surfaces, and which provides parameters to simulate the presence of multiple isoplanatic patches with the field of view.

4.1 Field of View.

The sensor magnification (M) for task accomplishment has already been discussed in the system MTF calculation. But to this point, the sensor total field of view has not yet been addressed. The focal length, pixel size, and magnification values are all provided by the model, but there is one more as yet unspecified parameter which is needed to determine the field of view, which is the total number of pixels in the focal plane. As long as the field is wide enough to image the full target, the model will be satisfied. The performance of the human visual system plays a major factor in determining the ideal total field of view, for once a value of M has been established then there is a link between the sensor input field of view and the apparent vision angle subtended to the eye by the display. The human must first *search* and locate the target before fixing region of the foveal vision to gain full resolution. Lloyd [22] states that ideally the sensor field of view, "*should be determined by a choice of an efficient display angle for search and by a recognition requirement*". Steedman & Backer studies showed that the target outer dimensions should occupy at least 12 arcmin (0.2°) and more conservatively up to 20 arcmin (0.333°) to facilitate search time [78]. This is consistent with Lloyd's recommended limit of a single pixel of resolution should not exceed more than 1 mrad (0.057°) at the eye, according to Bennett, et. al. , and so when multiplied by the Johnson

Criteria of 4 cycles for recognition, the result is 0.228° which is within the limits proposed by Steedman.

Lloyd discusses human factors studies by Enoch [79]. Enoch's study was based on a total experimental range of display-to-eye apparent field viewing angles between 3° and 51°, and a value of 9° was concluded to be the ideal case for target search. Field angles greater than this are justifiable only if needed for other purposes such as orientation and navigation, and apparent viewing angles less than 9° result in a significantly greater percentage of time where the human may not be looking at the display at all! This provides enough information to calculate a minimum field of view and pixel count for the system. Per the preceding model exercise, the desired system magnification (M) was found to be 9.5X, the Objective Lens focal length is f = 400 mm, and the pixel pitch is P = 0.028 mm. Therefore, assuming that a minimum display apparent viewing angle of 9° is required, then the minimum Objective Lens full field should be $(2\theta) = 9° \div 9.5 = 0.947°$. Using the optical relation between image half-height (h), focal length (f), and field half-angle (θ), solution is $h = f \cdot \tan(\theta) = \pm 3.31$ mm, or a total focal plane width of 6.62 mm. The minimum number of pixels required in this case is thus 6.62 ÷ 0.028 = 236 pixels.

4.2 Ray Trace Model.

The system performance model can estimate the average impact to the system MTF based on the turbulence strength, but this does not provide much detail about what is occurring at individual points within the field. There have been successful efforts toward creating mathematical models of anisoplanatic image segments [80] [81][82], and even real-time simulations have been proposed [83], but none of those methods are easily integrated into an optical model of the entire front-end system which includes the Objective Optics. This is a significant gap area between the researchers and the system designers. A method of ray-tracing through special surfaces to account for both intensity and phase is therefore offered here as a means of modeling a turbulent atmosphere as if it were a component within the Objective Lens optical system. Figure 4-2 below illustrates the impact to the system model, wherein now the MTF transfer functions of the atmospheric and objective optics are combined into a single value produced by the ray-tracing simulation.

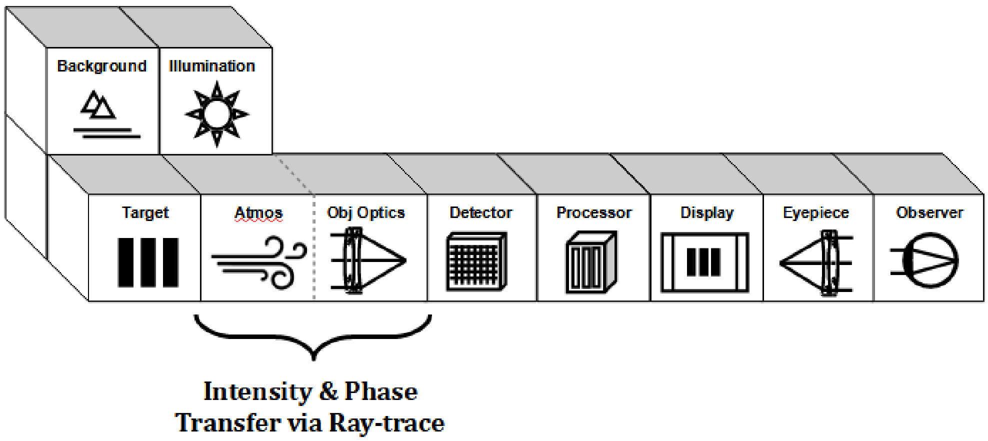

Figure 4-2: Modified System Model Combines Atmosphere and Objective Optics

The lens model technique can be implemented in commercial lens design software packages such as Zemax, CODE V, or the even venerable ACCOS V of which a modern version, KDP, is used herein for example. The nature of the ray-tracing model is best explained by walking through an actual case, and so begins with a simple imaging lens singlet made from Germanium material. The surface curvatures result in a net-positive optical power which focuses an incoming collimated beam of light to a focal plane. The focal length is 69.439 mm and the F# is 3.472, which is a reasonable value for detector which operates in the long-wave infrared spectrum centered at λ = 10 μm. A turbulence-simulation phaseplate is added to the lens and placed very near to the focal plane. In theory, the phaseplate could have been placed in the object space, perhaps several hundred meters in front of the lens, however doing so would have created a very large scale difference in the layouts. The phaseplate contains a surface sag function which causes different parts of the field of view to experience different amounts of optical aberration, thus providing a means to model the effects of multiple isoplanatic patches within the sensor's field of view as shown in Figure 4.3 below.

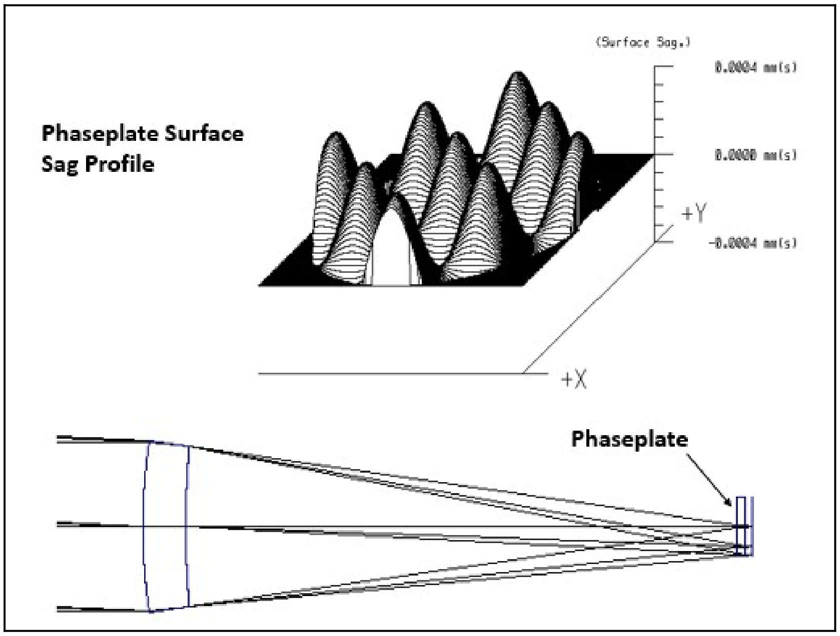

Figure 4-3: Image Forming Optical System with Phaseplate Turbulence Simulator Near Focal Plane of an Imaging Lens (Exaggerated Scale for Clarity)

The surface sag z for the phaseplate is given by the following equation, which adds two crossed sinusoidal waves to a basic lens curvature:

$$z = [(cr^2) \div [1 + (1 - (1 + k)c^2r^2)^{0.5}]] - A[(1/4)[1 + \cos(2\pi\alpha x)][1 + \cos(2\pi\beta y)] - 1]$$

The equation includes the conventional lens parameters for curvature c, the radial coordinate r within the aperture, and the conic constant k for parabolic or hyperbolic shapes. The scale parameter A is the peak-to-valley (PV) height in lens units (mm) of the cosine modulation terms. The values α and β are the spatial periods of the cosine oscillations in the x and y directions, respectively, in units of length (mm). The sag of the surface is zero at the vertex, however this may be displaced by decentering the position of the surface relative to other surfaces in the system. In the example above, the values of the sinusoidal periods α and β are equal at a value of 4.0 mm, thus giving a circular pattern to the peak sag profiles. Equality is not a necessary case, and various elliptical shapes can also be generated by having different values for values α and β. The optical model allows the user to input any value for the sag PV amplitude A, and through iterative experimentation of values it is possible to examine the effects of turbulence on the optical rays which progress through the system. Figure 4-4 below shows the difference resulting when $A = 0$ (i.e., no turbulence) versus when $A > 0.08$ mm to simulate the presence of turbulence.

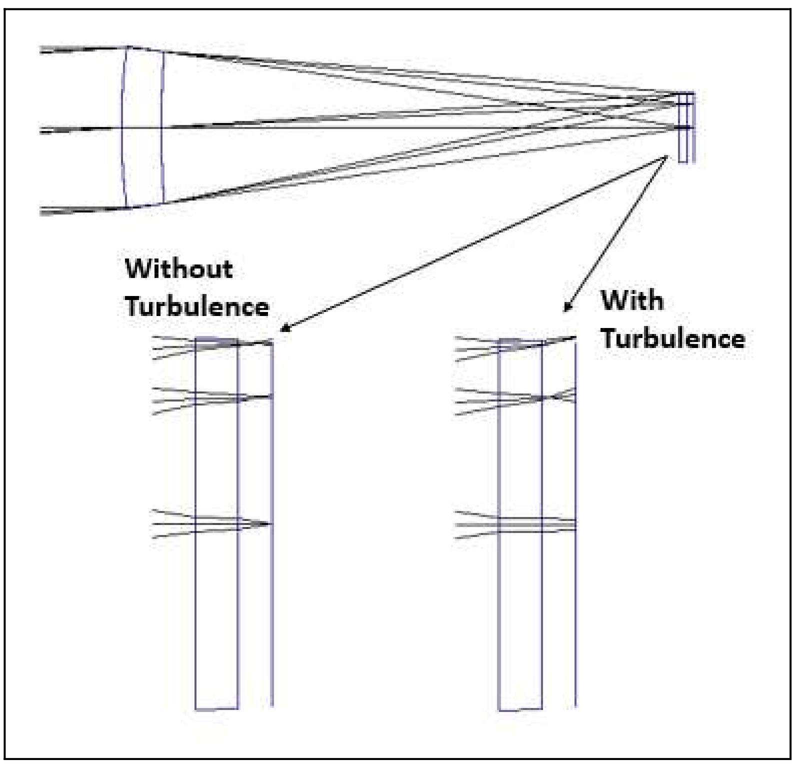

Figure 4-4: Ray-Trace Evaluation of Turbulence

The ability to examine the effects of a turbulent medium on the optical ray paths is very revealing. In the case of the uppermost ray bundle, corresponding to the edge of the field, it appears that the sharpness of focus is actually slightly enhanced, but yet the position of the focal point is significantly displaced compared to the non-turbulence case. This will appear as a distortion in the image. The middle ray bundle shows both a position distortion as well as a dramatic increase in the optical blur circle, which in turn will result in a lower MTF. The ray bundle along the optical axis is the lowermost shown, and here it is seen that the rays are drastically defocused, but yet still centered on the same position. The ray traces also allow more complex image analysis to be performed. The following figures show the effects of the turbulence phaseplate on the focused geometric spot size at different positions within the field of view (FOV). The spot diagrams are formed by tracing a grid of 500 random rays across the optical pupil, and plotting their intersections at the focal plane. Diffraction effects are ignored so that the geometric ray aberration amounts can be observed. The next Figure 4-5 below shows the spot size at FOV position x =-1.0° and y = +1.0° both without and with turbulence. In this case, the effects of the turbulence are drastic and a significant widening of the spot diameter along with roughly a 30 μm shift in the centroid position. If this optical system were using a focal plane detector with 0.012 mm pitch, then the displacement at this position within the FOV would be about 2.5 pixels.

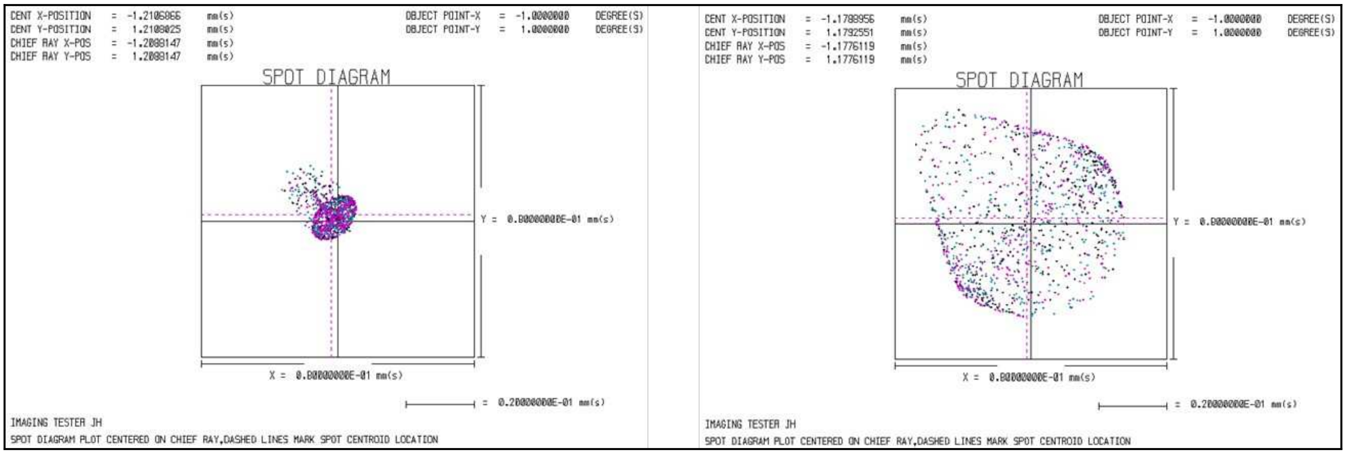

Figure 4-5: Spot Size at (-1.0°, +1.0°) FOV

Without Turbulence (Left) and With Turbulence (Right)

The next Figure 4-6 below shows another pair of spot diagrams located at FOV position x =-1.5° and y = -1.5° for which the turbulence has effects very different from the previous case. The spot diameter is only mildly affected by the turbulence, but the image displacement of the centroid is increased to roughly 34 μm, or nearly three pixels for a detector with 0.012 mm pitch.

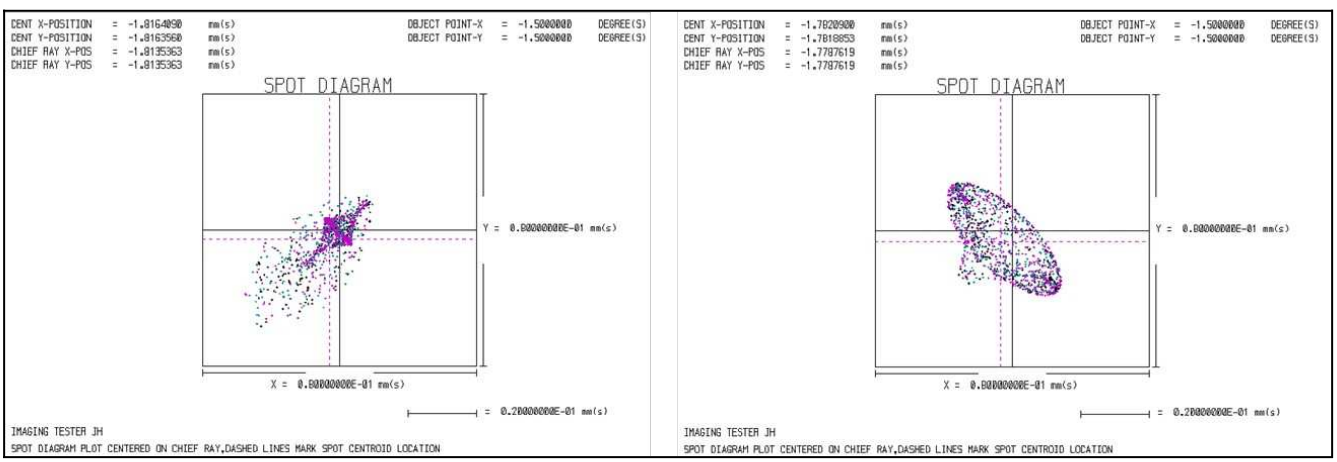

Figure 4-6: Geometric Spot Size at (-1.5°, -1.5°) FOV

Without Turbulence (Left) and With Turbulence (Right)

The result of this analysis indicates that the potential losses in MTF due to an enlarged spot size and the local distortions due to shifts in the image centroid locations will vary with position within the field of view and in accordance with the period and amplitude of the phaseplate surface sag. It also shows that the correlation between changes in spot size versus amounts of local distortion is not necessarily linear.

The optical ray-trace model can now be used to create simulated images of object scenes when viewed through turbulence. A nominal object scene can be loaded from a BMP image file and placed in the object plane of the optical system as an array of points. Geometric ray tracing then propagates light rays from each object point to its corresponding conjugate image position in the focal plane of the optics. Diffraction calculations can also be performed to account for the blurring effects caused by diffraction at the aperture stop of the optical system. This method involves a convolution of the diffraction-limited point spread function (PSF) with the geometric ray trace image. This entire process allows the creation of simulated imagery which is accompanied by a precise description of the optical aberration functions for all points within the field of view. The following Figure 4-7 is the source image used for this presentation. It is a long-wave infrared (LWIR) thermal image of a parking lot. The image contains a fairly large dynamic range of bright and dark areas, and it contains many objects which have relatively straight lines and sharp edges located in many places throughout the field of view. The original image format is 640 × 480 pixels and displays as a monochrome image.

Figure 4-7: Object Source Input, 640 × 480 Pixels

The image processing routines involve many parameters. In order to avoid sample aliasing artifacts, the output image is scaled down to 320 × 240 pixels. Figure 4-8 below shows the result of image sampling combined with only the geometric distortion caused by the turbulence phaseplate. The Fast-Fourier-Transform (FFT) plotting grid extent for plotting is set to 91 pixels to reduce wavefront-sampling artifacts based upon visual inspection of the quality of the output images. These sampling artifacts are not severe enough to prevent visual simulations of turbulated imagery, however they unfortunately do prevent accurate demonstrations of restoration algorithms because of the artificial increase in fixed pattern noise.

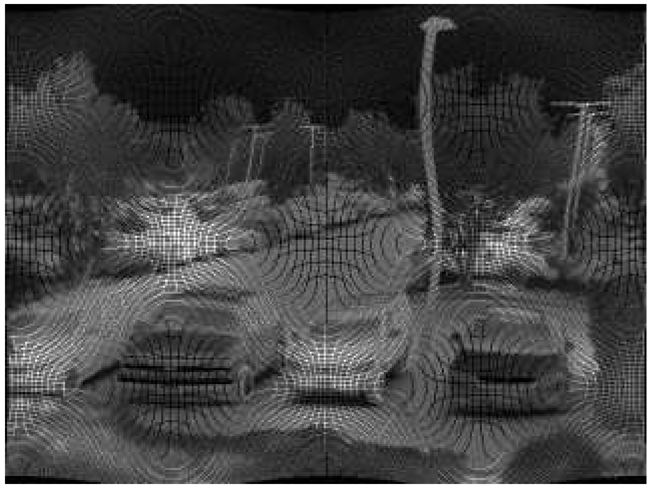

Figure 4-8: Intermediate Process Stage Showing Sampling Artifacts & Geometric Distortions

The FFT grid size for the convolution with the diffraction blur is 1024 × 1024 elements. The number of rays which span the exit pupil is set to 32. Processing time on an Intel i7-7600 CPU clock running at 2.8 MHz and with 8 GB of RAM is several minutes. Figure 4-9 below shows a side-by-side comparison of both non-turbulent (left) and turbulent (right) simulated imagery. Each image includes the full effects of the diffraction blur, and then the right-side image adds the effects of the turbulence phaseplate, resulting in the final "turbulated" version of the original image.

Figure 4-9: Comparison of Simulated LWIR Images

Without (Left) and With (Right) Turbulence

Just as predicted by the ray trace analysis, inspection of the turbulent scene imagery on the right side shows that certain areas experience greater losses in resolution and MTF, whereas other areas may retain most of the original resolution but might instead suffer from local distortion. For example, the image of the truck 2nd from the left side is mostly intact in terms of resolution, but the back-end of the vehicle is clearly distorted. The turbulent image of the telephone pole shows the extreme distortions across a large section of the vertical field of view. Figure 4-8 thus demonstrates a novel capability to create a realistic optical ray-trace model using a phaseplate which corresponds to the aberration magnitudes of a turbulent atmosphere, and that the ray model can then serve as a basis for developing simulated imagery.

4.3 Ray Trace Model Validation: Cassegrain Telescope Field Test

This section describes how a raytrace model was generated to approximate the results seen during a live data collection during several weeks of October 2022 [84]. An optical raytrace model was used to create simulations of turbulated images collected in the field experiment using a Celestron commercial telescope. An exact optical prescription of the telescope is not available in the public domain, therefore a reasonable lens prescription for the baseline telescope was independently created as described in Appendix B. The open-source software "KDP" [85] was chosen to develop the optical prescription. The telescope includes a Cassegrain two-mirror form objective image forming assembly which has a central obscuration as shown in the figure below. A camera focal plane detector can be either placed directly in the focus of the objective, or by affixing an imaging objective lens, it can view the image which is collimated through the telescope eyepiece. For the sake of simplicity, this analysis hereafter assumes that a camera is located directly in the focal plane of the objective mirror assembly. A complete listing of the developed optical prescription data is contained in Appendix A, and the raytrace plot is below in Figure 4-10. The optical system provides a 2000 mm focal length operating at an F#/8.88 which matches the parameters of the telescope used in the live data collection.

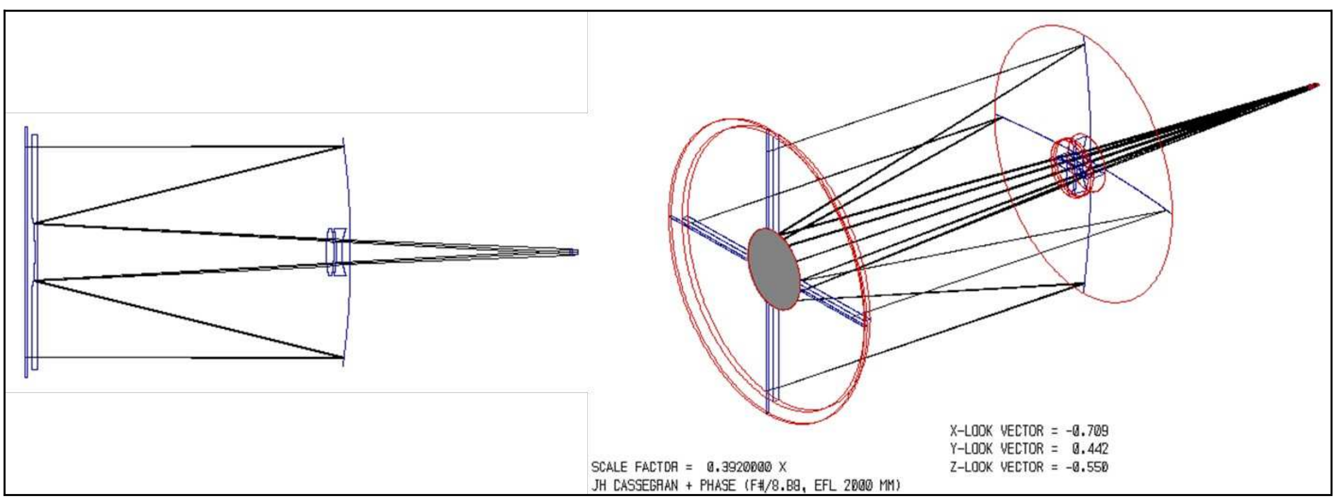

Figure 4-10: Celestron Telescope Objective Assembly Optical Raytrace Model

The raytrace prescription for the telescope was then modified by adding a 3 mm thick phaseplate near the focal plane. This position enables the phaseplate to affect different portions within the field of view with different amounts of aberration, thereby simulating the presence of multiple isoplanatic patches in the real scene. Surface #11 is where the phaseplate coefficients are active, using the "Type 4" special surface as described in the KDP manual. A high index glass is arbitrarily selected, Schott N-SF57 with a glass number of 847238. The final air gap thickness of the lens prescription is adjusted for focus to account for the extra path length of the phaseplate when there is zero turbulence phase added. The surface sag z for the phaseplate is given by the following equation, which adds crossed sinusoidal waves to a basic underlying lens curvature:

$$
\begin{aligned}
z = {} & [(cr^2) \div [1 + (1 - (1 + k)c^2r^2)^{0.5}]] \\
& - \mathrm{C1}[(\tfrac{1}{4})[1 + \cos(2\pi(\mathrm{C2})x)][1 + \cos(2\pi(\mathrm{C3})y)] - 1] \\
& - \mathrm{C4}[(\tfrac{1}{4})[1 + \cos(2\pi(\mathrm{C5})x)][1 + \cos(2\pi(\mathrm{C6})y)] - 1] \\
& - \mathrm{C7}[(\tfrac{1}{4})[1 + \cos(2\pi(\mathrm{C8})x)][1 + \cos(2\pi(\mathrm{C9})y)] - 1]
\end{aligned}
$$

The equation includes the conventional lens parameters for curvature c, the radial coordinate r within the aperture, and the conic constant k for parabolic or hyperbolic shapes. With curvature $c = 0$, the base curvature of the surface is flat planar. The scale parameters C1, C4, & C7 are the peak-to-valley (PV) height in lens units (mm) of the cosine modulation terms. The values C2, C3, C5, C6, C8, & C9 are the spatial periods of the cosine oscillations in the x and y directions, respectively, in units of length (mm). By setting the periods to large values, the aberration term begins to affect the entire image. By setting the periods to smaller values, the phaseplate introduces a modulation across the different field positions within the image. Mixing small and large periods therefore provides an opportunity to model both the near-aperture and down-range effects of turbulence all in one surface. Furthermore, mixing harmonic periods with the correct amplitudes can result in an additive or Fourier synthesis of periodic waveforms having more complex shapes than simple sinusoids. Figure 4-11 below shows the plot of the sinusoidal surface sag (i.e., phase) profile in an exaggerated vertical scale. It contains a long period (the large peaks) mixed with a much faster but smaller amplitude period (shown by the contour lines inside each peak).

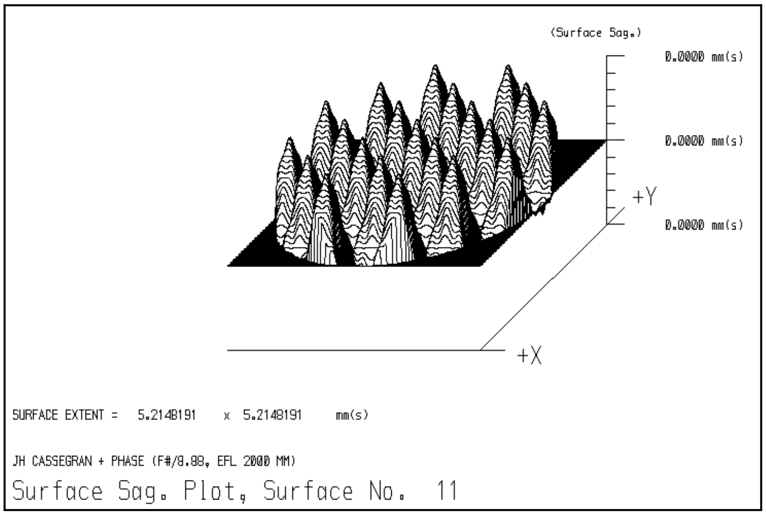

Figure 4-11: Surface Sag Plot of Two Mixed Sinusoid Phase Profiles

The following data listing contains the prescription information needed to create the optical model in KDP or other equivalent raytrace software. Details of the parameters and data formats can be found in the user manual, located on the KDP website [85]. It is informative to characterize the performance of the modified telescope prescription both with and without the added turbulence phase terms, such that the impact of the phase functions can be examined. Figure 4-12 below shows side-by-side plots of the MTF both without and then with the phase function. In the former case, the performance of the telescope objective with the phaseplate terms set to zero is nearly diffraction limited. Note also the expected dip in the mid-frequency range of the MTF curve which is caused by the central obscuration of the telescope. When the turbulence coefficients are activated with non-zero amplitudes, the optical performance deviates from the diffraction limit noticeably.

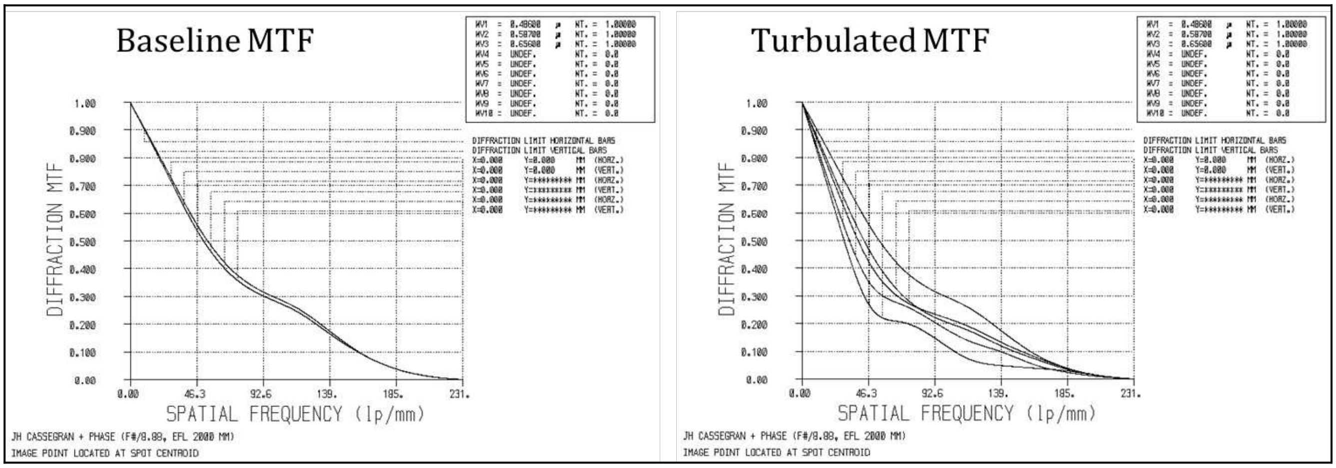

Figure 4-12: Comparison of Baseline & Turbulated Modulation Transfer Function (MTF)

The following Figure 4-13 shows the impacts of the turbulence phase upon the geometric spot size, which is perhaps a more intuitive measure of the optical performance, especially in comparison to the detector pixel size. In the baseline case where the turbulence amplitudes are all zero, the geometric spot size graphic vertical scale is 0.015 mm. With the turbulent phase added, the spot size scale becomes 0.039 mm, which is more than double the original value. It is also interesting to note that the turbulated spot loses its circular symmetry, and adopts more of the “checkerboard” pattern similar to the phaseplate element surface.

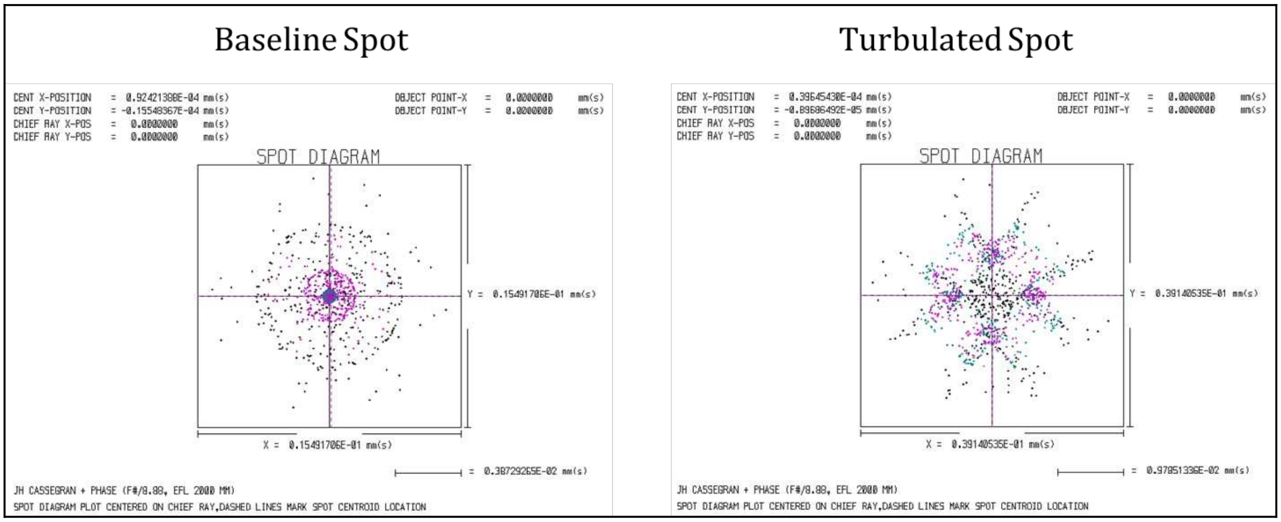

Figure 4-13: Comparison of Baseline & Turbulated Geometric Spot Sizes

(note the scale change between left & right sides)

The real target was composed of vertical and horizontal sinusoidal intensity "bars". Each set of bars is roughly two meters across horizontally. A side-by-side comparison of a "pristine" image and a turbulated image are shown in Figure 4-14 below. The "pristine" image of the target is from a photograph taken up close a few meters away from the target, with negligible intervening atmosphere. The turbulated image (14_oct_1538_Camera_4750.bmp) was captured under the following conditions: Time 15:38, 14 October 2023, Rytov = 1.162, Wind = 3.9 km/hr (i.e., about 1.08 meters/second), frame rate 500 Hz, integration time of 250 microsec, pixel pitch 0.007 mm, detector format size 660 × 306 pixels.

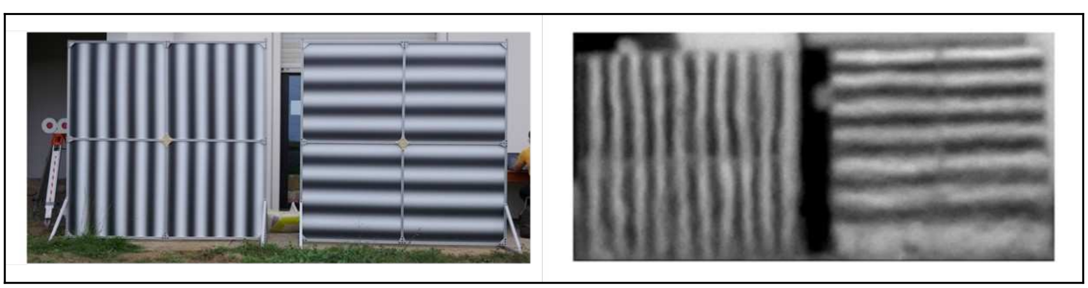

Figure 4-14: Pristine (left) and Turbulated (right) Real Images From Field Experiment

Visual inspection of the turbulated image yielded a brief set of observations as follows:

- Near-sinusoidal shape distortion, especially noticeable along some of the vertically-oriented bars but also present along the horizontal bars as well. There appear to be roughly two oscillation periods in the vertical directions.
- Variation of intensity along the lengths of both the vertical and horizontal bars
- "Roughness" of the edges along the lengths of the bars.
- The whole image appears to be uniformly blurred. This could be due to mechanical stabilization jitter effects. As demonstrated earlier in Section 3.0, even a minuscule 1.0 microrad jitter error will have a significant effect on the system-level MTF response curve because of the very long focal length.
- Random noise is present, giving the image a "granular" appearance. This is likely detector noise because the signal is low with the very fast integration time.

This section contains several details unique to the use of the KDP optical raytracing software. KDP is normally used for optical lens design, but it also has the ability to accept a bitmap photograph as an "object" input, and then convolve the object with the image created by tracing rays through the lens system. In this way, the actual imaging performance can be simulated. The details of how this was done is provided to assist re-creation or modification of the experiment. The pristine source (named POTVINX.BMP in this case) image format is 640 x 297 pixels. The OFROMBMP command in KDP loads this file as the object source for the raytrace. The <extent> parameter is set to 0.231E-17 mm, which with an object distance of 0.10E20 yields an image size which fits just inside the Celestron field of view for 660 pixels with 7 micron pitch. The NRD, PGR, and TGR sampling parameters are set to KDP default values. These setup parameters were entered into a KDP "macro" program for storage and timely execution as follows:

```
MACRO CASSPHAS,,,,,,
C,,,,,,TURBULENCE PROCESSING,F#/8.88,20 mm,660x306 pix
COLOR MONO,,,,,,
IIMAGEN,4.620,2.142,660.0,306.0,,
OFROMBMP,0.2310E+17,,,,,POTVINX
TGR,1024.,,,,,
NRD,32.0,,,,,
PGR,91.0,,,,,
OCDY,,,,,,
OCDX,,,,,,
IMTRACE1,,,,,,
PLTIMG,,,,,,
OCDY,,,,,,
OCDX,,,,,,
EOM,,,,,,
```

The IMTRACE1 command initiates a process which completes in about 2 seconds on a laptop computer with and Intel(R) Core(TM) i7-7600U CPU @ 2.80GHz, standard magnetic disk drive, and 16 MB RAM. IMTRACE1 calculates only the geometric position of the chief ray for each point in the field. This is a good way to quickly ensure that the system is set up properly. The output confirms that the OBFROMBMP parameters match expectations as shown in the following output:

```
>CASSPHAS
IMAGE PLANE ARRAY DIMENSION NX =          660
IMAGE PLANE ARRAY DIMENSION NY =          306
    IMAGE PLANE PIXEL X-LENGTH =   7.010622154779969E-003
    IMAGE PLANE PIXEL Y-LENGTH =   7.022950819672131E-003
    IMAGE PLANE ARRAY X-EXTENT =    4.62000000000000
    IMAGE PLANE ARRAY Y-EXTENT =    2.14200000000000
YZ-PLANE FIRST ORDER OPERATING CONDITIONS
 EFL          BFD          F-NUM        LENGTH      GIH
 2000.0       4.9565       8.8889       491.81      -1.0698
XZ-PLANE FIRST ORDER OPERATING CONDITIONS
 EFL          BFD          F-NUM        LENGTH      GIH
 2000.0       4.9565       8.8889       491.81      -2.3114
TRACING RAYS I COLOR #           1
IMTRACE1 IMAGE TRACING DONE
YZ-PLANE FIRST ORDER OPERATING CONDITIONS
 EFL          BFD          F-NUM        LENGTH      GIH
 2000.0       4.9565       8.8889       491.81      -1.0698
XZ-PLANE FIRST ORDER OPERATING CONDITIONS
 EFL          BFD          F-NUM        LENGTH      GIH
 2000.0       4.9565       8.8889       491.81      -2.3114
```

The PLTIMG command displays the result. In the output Figure 4-15 below, the phase grid sampling pattern is seen superimposed on top of the image. Each of the small turbulence regions within this "chickenwire" pattern can be considered as a small isoplanatic patch. At this point in the process, some of the geometric distortions are present, but the convolution with the point spread functions has not yet been done, and so the overall image quality is still similar to that of the pristine input image. The purpose here is to make sure the basic parameters are set up before committing several minutes or hours needed to run the full image transformation process.

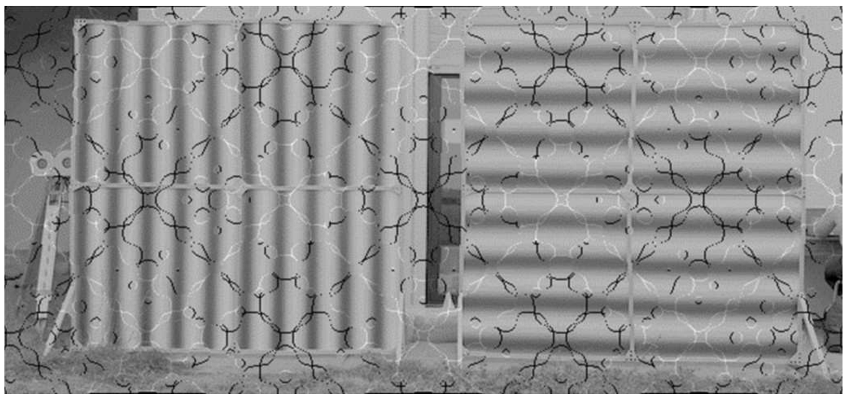

Figure 4-15: Interim Stage Process Confirms Setup Parameters

The next process step is to perform the full point-by-point convolution of each image pixel with its corresponding optical raytrace. This step requires a significant amount of time on the computer. The "IMTRACE3" command is issued to do this final processing. Figure 4-16 below shows the result for the lens prescription contained in Appendix B. The phaseplate includes two sinusoidal patterns, one with a slow period for the large area shape distortion, and then one with a faster period to induce the roughness along the lengths of the bars. This process generally takes nearly an hour, depending on what background programs may also be running inside the computer.

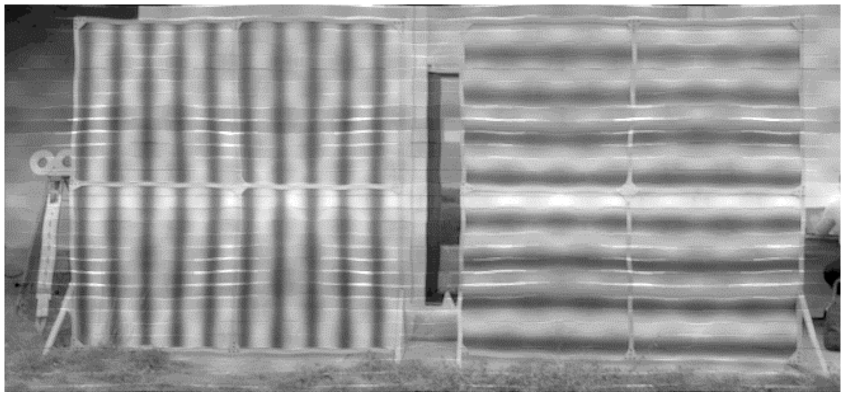

Figure 4-16: Image Simulation Via Raytrace Operations

The preceding raytrace simulated image in Figure 4-16 has some sampling artifacts. The image shape distortion and an amount of optical defocus are present, and some of the intensity modulations along the bars are visible, but the overall quality is not as degraded as the real image. It also looks too “clean” when compared to the real turbulated image. Increasing the amounts of phase amplitudes in the prescription would increase the defocus effects, but would also increase the shape distortion magnitudes. Several attempts were made to blur the entire image by placing a slight curvature on the normally flat front window, but once again increasing optical defocus at the aperture yielded unsatisfactory results. Based on this observation and recalling the analysis earlier in Section 3.0 which compares the effects of Gaussian blur versus optical defocus, it was then decided to see if the application of random Gaussian blur and perhaps also some random spot noise might make an improvement. The freeware software program “PhotoFiltre” [86] was used to test this hypothesis. PhotoFiltre has built-in routines to both add Gaussian and random white spot noises, and so the final combination of ray tracing, random Gaussian noise, and random “granular” detector noise resulted in a much better overall simulation of the real turbulated image. The following Figure 4-17 shows the pristine image, the real turbulated image captured during the field test, and then the final form of the simulated image. The results demonstrate that the optical raytrace model does indeed capture the characteristics and magnitudes of the turbulence effects, albeit perhaps with a more mathematically structured variance than the real imagery. Additional work applied to the phase plate parameters could result in more complex modulations of sinusoid patterns that better represent the actual scene, however this level of detail is not necessary since the general magnitudes and types of aberrations are currently already accounted for.

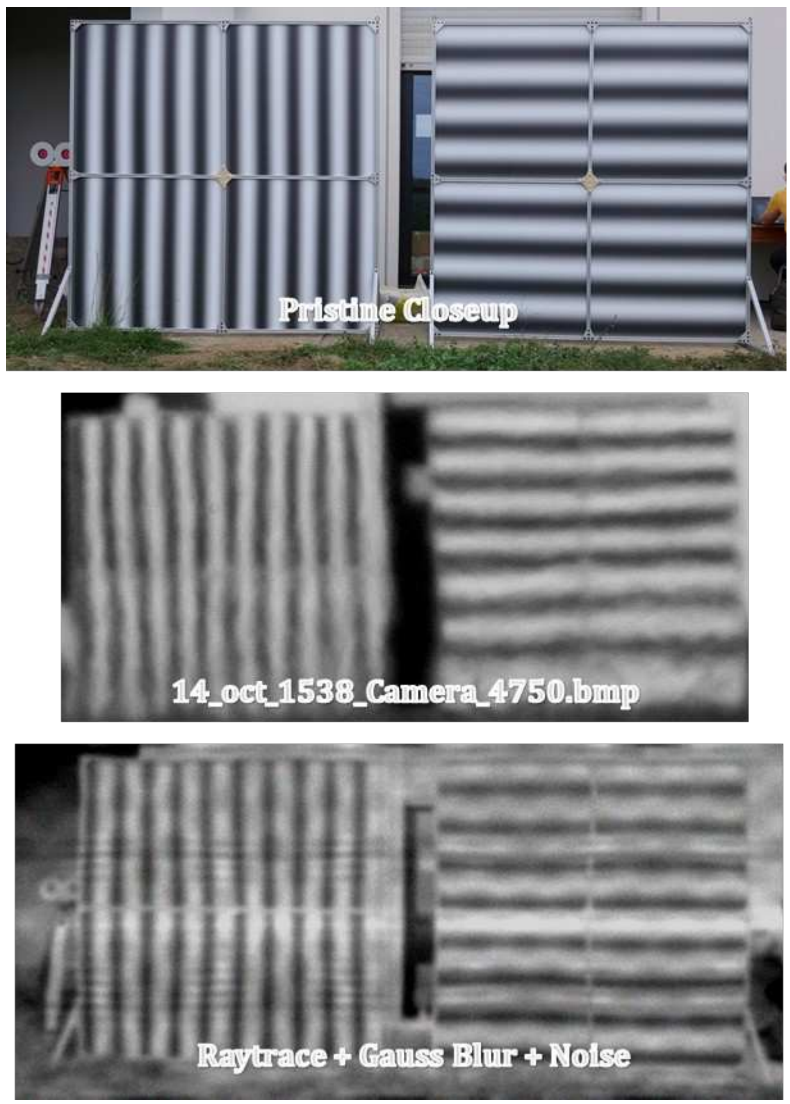

Figure 4-17: Comparison of the Pristine Image, Real Field Test Image, and Final Simulation Composed of Ray-tracing + Gaussian Motion Blur + Random Detector Noise

Chapter 5 - Brainstorming & Concept Development

Brainstorming can be described as a guided group creativity exercise wherein a number of possible approaches may be generated. The term appears to have originated as a result of Alex Osborn's corporate "group-thinking" sessions circa 1939 [87]. The intent of a brainstorm session is to elicit ideas from a group of people. It can be a formal process with rules for preparation and execution [18], but the emphasis should be on mutual encouragement and creative thinking applied to the problem. The sensor system model reveals a high level of complexity, and when applied to the task of designing a new system which is specifically made for turbulence mitigation, it is helpful to gather a team whose members have expertise in each of the model block topic areas. It shall be imagined that such a team has been assembled for the brainstorming and concept development activities described in this section.

5.1 Survey of Existing Turbulence Mitigation Techniques.

The existing approaches for turbulence mitigation as determined by literature search shall be discussed in the following sections. In each case, a general description of the functional aspects of the approach shall then be followed by a brief assessment of risks involved. This information provides the starting point for brainstorming sessions later conducted by the engineering team.

5.1.1 Astronomical Adaptive Optics.

The origins of what is now known as "adaptive optics" traces back at least as far as Babcock's 1953 paper from the Astronomical Society of the Pacific, in which he writes, "*If we had a means of continually measuring the deviation of rays from all parts of the mirror, and of amplifying and feeding back this information so as to correct locally the figure of the mirror in response to the schlieren pattern, we could expect to compensate both for seeing and for any inherent imperfections of optical* *figure*. " Babcock then proceeds to discuss the "Eidophor", a device invented by Professor F. Fischer, which is comprised of a mirror covered with an electrically active thin film of oil. An electron beam raster-scanning technique similar to that employed in Cathode Ray Tubes (CRTs) is used to stimulate the oil surface and distort the surface within a very small region. The following Figure 5-1 summarizes the main aspects of the Babcock approach [88]:

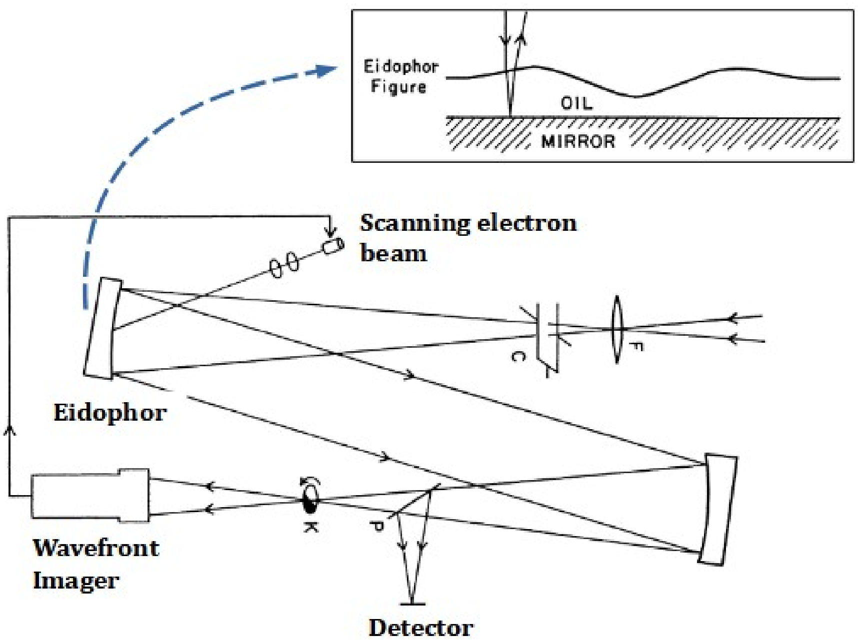

Figure 5-1: Babcock (1953) Astronomical Correction Apparatus Using the Eidophor

Since that time, efforts for a more efficient means of distorting the mirror surface have resulted in what is sometimes referred to as a "rubber mirror", wherein the mirror surface itself is flexible, and underneath is an array of tiny motorized pistons which can push upward or downward upon the mirror surface. Another modern innovation is the use of what is commonly known as the "Shack-Hartman" wavefront sensor. This device is comprised of a two-dimensional array of lenslets, each with its own imaging camera. Each lenslet images just a small fraction of the incoming pupil, and thereby captures the optical behavior for that specific portion. By comparing the results from each lenslet image, the electronic processor can determine the best means of compensating the wavefront via moving the mirror pistons. More advanced work has investigated the ability to sample the pupil in different planes along the optical (z) axis [19]. Figure 5-2 below illustrates the modern adaptive optics system architecture.

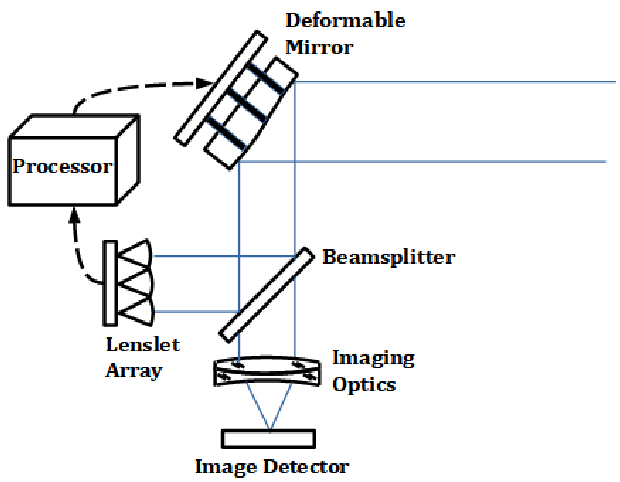

Figure 5-2: Basic Architecture of a Modern Adaptive Optical System

The adaptive optical system has proven very effective for astronomical applications. However, it must be noted that astronomical telescopes have two distinct advantages over typical horizontal-path images, namely that their fields of view angles are very small, and they are looking upward through the atmosphere such that only a small distance along the optical path experiences significant turbulence. They also have the advantage of being able to use active illumination to create a "guide star" or beacon which reflects off layers in the atmosphere [8]. Max [89] illustrates the first point by comparing images of Neptune captured with the Keck telescope, both with and without adaptive correction, in Figure 5-3. The image of the planet subtends a field of view angle of 2 arcsec, or 0.00056°. Max goes on to illustrate the second point by explaining that typical values of

r_0 on good astronomy nights looking upward is 10 - 15 cm. Thus for a 10 meter class telescope aperture, an array of approximately 67 piston-segments will cover the entire aperture. In the case of a horizontal path imager, however, the typical targeting sensor fields of view will be on the order of 2° - 10° and the typical Fried Parameter (r_0) values may easily be on the order of 6.5 cm or less depending on weather conditions and total range required.

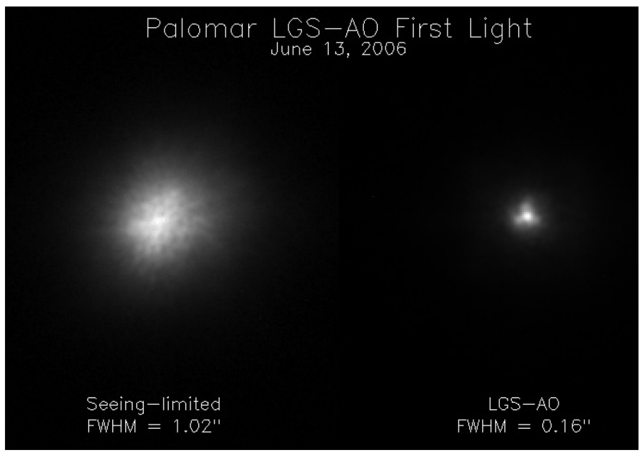

Figure 5-3: Palomar Conventional vs. Adaptive Optics Image Comparison

(public domain: https://ao.jpl.nasa.gov/assets/images/palomar_lgs_firstlight.jpg)

The differences between astronomical and terrestrial turbulence correction are analyzed extensively by Gronau [12] who states, "*It has been suggested, that adaptive optics may be implemented also for imaging at paths parallel to the ground, e.g. in military reconnaissance. It is shown here, that in such cases, it is possible to correct the wavefront only for a very small area of the field of view (FOV), typically too small for any useful application*." The crux of the issue is that the astronomical adaptive system provides wavefront sensing and correction in the pupil of the optical system, which is where all the field angles pass through. Thus, a correction can be solved for only one isoplanatic field angle at a time, and that result may actually be an overall degradation if applied to the image as a whole. Astronomical wavefront compensation via adaptive optics works in the vertical path because astronomical telescopes have very narrow fields of view, such that the aberrations induced by the layer of atmosphere, primarily within the first 1000 feet, near to the aperture are relatively common across all points within that field of view. For example, the Schulman telescope at Mt. Lemon, Arizona has a 0.367° degree field of view [90]. In terrestrial horizontal path applications, however, the fields of view are typically much wider, typically 1.5° – 10°, and multiple regions or "patches" of differing turbulence will exist along the several kilometers between the sensor and the target. Gronau goes to demonstrate an interesting calculation, where perhaps correction over the entire field of view is not necessary, but rather only enough coverage of both the target and its immediate background is required. Gronau suggests a region of 100 units of resolution, where a unit of resolution can be though of as a single pixel. This is a good approximation for the identification task, where per the Johnson Criteria about 13 pixels are needed across the target, and that leaves ± 43.5 pixels on either side for background context. This helps to avoid the "soda straw" effect, where the senor field of view is so small that it becomes difficult to find the target amid the background [91][92]. In such a case, Gronau performs the calculations for the maximum range (L_{max}) at which this criteria can be met as a function of the atmospheric index as follows:

$$L_{\mathrm{max}} < (1.96 \times 10^{-2}) \cdot (\lambda)^{0.125} \cdot (\mathrm{D})^{0.625} \cdot (\mathrm{C_n}^2)^{-0.375}$$

Gronau provides an example for D = 200 mm, λ = 0.7 microns, and $\mathrm{C_n}^2 = 1.96 \times 10^{-16}$ resulting in L_{max} < 400 meters which is likely to short for many reconnaissance requirements. VanEkeren, et. al., also confirm that astronomical adaptive techniques are not suited for terrestrial path turbulence mitigation as follows: "*In effect, the isoplanatic angle will often be much smaller than the field of view of the camera system. This means that a closed loop adaptive optics system such as used in an* *astronomy application does not work for ground-to-ground imaging*," [93].

5.1.2 Light Field/Plenoptic.

-The "light field", and its subset "plenoptic", approaches use a technique of adding a lens array at or near the focal plane of an imaging system [94]. The lens array divides the image into several sub-images wherein each sub-image is constructed from only a portion of the system aperture [95] as shown below in Figure 5-4. A detector is located some distance away from the array, and thus captures portions of the image corresponding to ray positions within the entrance aperture. The array can be placed directly in the focal plane of the optics, in which case it is called a "light field" configuration, or it can be placed some distance away in which case it is called a "plenoptic" configuration.

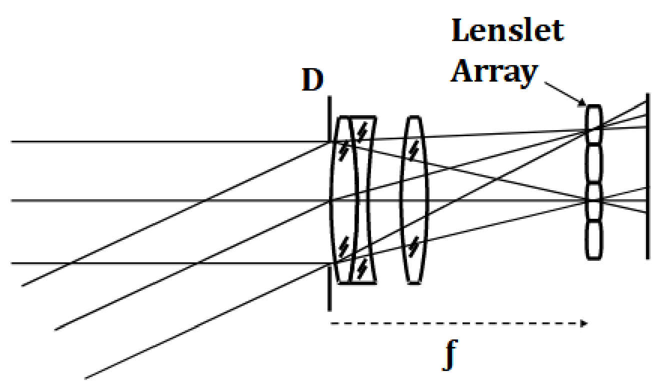

Figure 5-4: Light-Field Lenslet Array Configuration

Wu, et. al., provides an overview of the light-field & plenoptic approaches in terms of turbulence mitigation and in particular mentions the diffraction limit issue with the plenoptic version, and the micro-lens array sampling spacing for the in-focus version [96]. In either case, there will be a significant loss in resolution at the system level. Wu states, "This means the image correction algorithms for the light field cameras will inevitably downgrade the original image resolution as a trade-off for turbulence resilience." These issues will be even more concerning in the infrared spectrum, where the sensitivity to resolution and the diffraction limit are much more significant than with visible light cameras.

5.1.3 De-convolution.

VanEkeren summarizes the software processing approaches for turbulence mitigation as falling into two general categories, de-convolution and lucky imaging [93]. The basic idea behind de-convolution is to separate two convolved signals [97]. The signal representation of an image in the spatial domain may generally be given by $g(x, y) = h(x,y) \circledast f_0(x, y) + s(x,y)$ where $g(x, y)$ is the blurred image resulting from a convolution ($\circledast$) of the pristine un-blurred image $f_0(x, y)$ by a point spread function $h(x,y)$ along with added noise denoted by $s(x,y)$. It is often simpler to perform the convolution operations via multiplication in frequency space via Fourier Transform of each term, the result of which may then be written as $G(u, v) = H(u, v) \cdot F_0(u, v) + S(x,y)$. Rearranging terms gives the following:

$$F(u, v) = [\, G(u, v) - S(x,y)\,] \div H(u, v)$$

where F(u, v) is the best guess for the true image spectrum $F_0(u, v)$. In a "blind" operation, different forms and magnitudes of the point spread function H(u,v) are guessed, and the resulting output image F(u, v) must be evaluated by an image quality criteria such as edge sharpness or perhaps an MTF calculation. The process is iterated until the best possible form of F(u, v), and hence a reconstructed image in the spatial domain $f(x, y)$, can be output as the result. The noise term represents the non-linear behavior which is not possible to remove. Huebner compares three widely used methods of de-convolution which are broadly representative of the best de-convolution options as follows [97]:

a) Inverse Weiner Filtering. This is a very direct method adhering to the basic equation above. It requires significant iterations to blindly converge on a solution, and the noise factors can be troublesome especially at higher frequencies.

b) Lucy-Richard De-convolution.   This is a non-blind approach which requires some prior knowledge or at least a very good guess of the point spread function. It produces a Likelihood Function output which must still be iterated to find the best solution.

c) Iterative Blind De-convolution. This is an extension of the Lucy-Richardson technique which does not require prior knowledge. The penalty is an increase in processing operations required to obtain convergence.

d) Principle Component Analysis. This is a non-iterative method which uses statistical moments within the image and thus converges relatively quickly. In a blurred image, the high frequency content is smoothed out and the overall pixel-to-pixel variances will be low. As the estimated image approaches the true image, the edges will sharpen and the variances from the mean will increase. Simske & Li have disclosed an ability to use kurtosis, the fourth statistical moment, along with a de-convolution filter to unravel the blur functions of atmospheric turbulence affecting an image [98]. The kurtosis is a measure for the occurrence of data elements which are outside a single standard deviation from the mean value for a set of points. The process works by starting with an estimated blur factor and then applying a Wiener filter or similar de-convolution operation. The Wiener filter attempts to be the inverse of the estimated turbulence blur function. The resulting image is then analyzed for its kurtosis, and the process is iterated with different values of the blur function until the image with the minimum kurtosis score is found. This approach has an advantage because it is all performed within the processor, and requires no extra optical or mechanical hardware modifications to a standard sensor system. For an image with multiple isoplanatic patches, however, this method would likely require a "sliding window" approach wherein the "window" is subset of the whole image. As the window slides pixel by pixel, a new set of blur estimates would need to be created for each iteration. Work of this nature might be suited for AI network processing [99]. If the blur functions become too large, there is risk that the data will be undersampled and thus aliasing artifacts will be dominant. It is a fundamental limitation of all solutions relying on only digital processing that information lost in the atmosphere-optical system cannot be entirely regained within the digital domain.

Interestingly in all cases for software de-convolution, possession of a good estimate of the point spread function should be helpful for rapid convergence. As concluded by Huebner [97], "*Future work includes replacing the simple Gaussian filter by a more accurate estimate for the average atmospheric PSF and finding an analytical description for the correspondence between* C_n^2 *and edge width.*" Thus there may be an opportunity to improve algorithm performance using the optical ray-trace model as described previiously to provide a set of estimated spread functions which are unique to the specific design of the Objective Optics and a given C_n^2 turbulence value.

5.1.4 Lucky Patch.

One method of capturing more information in the digital domain uses sequences of images from the video stream, each gathered at a different time. Depending on the strength of the turbulence, there is a probability that over time a given patch of the image will experience low turbulence effects for a brief moment. The digital processor identifies the "lucky patch" occurrence, and for a given set of input image frames produces a single composite output image comprised of the luckiest patches from the sequence. This process is repeated with each video frame, and a continuous optimize video stream is displayed. The disadvantage of this approach is that because a set of input frames is required, there will be a time lag between the actual event and when it is displayed to the operator.

Vorontsov, et. al., describe their process via simulation where typically greater than 100 frames of imagery are needed in order to obtain meaningful improvement as shown in Figure 5-5 [13]. If this imagery were gathered at, for example, 60 Hz, then the collection time lag between the first and last input frames would be at least 1.667 seconds. Another challenge with this approach, similar to the de-convolution approach of Simske & Li, is that the sliding window kernel size must be determined via trial & error.

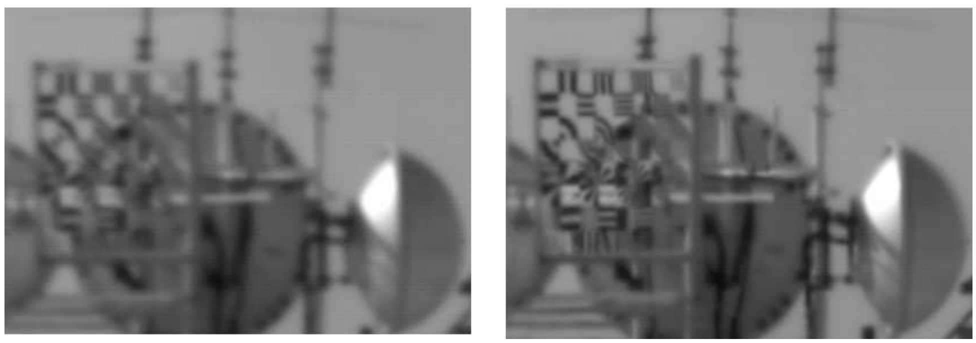

Figure 5-5: "Lucky Region" Example, Right Side Original, Left Side Lucky w/ Kernel Size 6.4 Pixels

5.1.5 Phase Diversity.

The concept of capturing a scene image with under conditions of different optical phase relations is sometimes referred to as "phase diversity" . The diversity is achieved by capturing the same image under conditions of altered phase, which in turn may involve change in focus, aperture piston, wavelength, or intensity [100]. An example of this technique is found in the Hubble Telescope "fix" [101]. An important subset of phase diversity options involves the use of simple defocus to provide estimates of the complete phase and intensity components of the optical transfer function (OTF). Recall O'Neill's formulation for the optical transfer function convolution integral discussed in the Linear Theory section:

$$i(x', y') = \iint g(x' - x,\ y' - y) \cdot o(x, y)\, dx\, dy$$

Convolution in the spatial domain becomes multiplication in the Fourier Transform frequency domain. The basic math process can be simply explained by assuming images in the frequency domain (I_1 and I_2) that can be defined by the following functions wherein D is a known phase perturbation such as defocus:

$$I_1 = O \cdot P$$

$$I_2 = O \cdot (P + D)$$

The values of I_1, I_2, and D are known. Rearranging terms and combining both equations yields the following:

$$O = P \div I_1 = (P + D) \div I_2$$

Here the object transform (O) term drops out, so then the fractions can be re-written as follows:

$$P \cdot I_2 = (P + D) \cdot I_1 = (P \cdot I_1) + (D \cdot I_1)$$

Rearranging again to solve for P which is the only remaining unknown:

$$P = (D \cdot I_1) \div (I_2 - I_1)$$

Once the transform function (P) is known, a de-convolution operator can be derived with which to obtain the ideal image, subject to the non-linear noise terms which propagate throughout the calculations. Desandre provides a more in-depth mathematical description as well as an experimental apparatus [102]. A study by Zhang, et. al. demonstrates an approach where three or more cameras are used to capture an image at three simultaneous defocus positions in an effort to improve the chances of finding a lucky patch in a turbulated image [103]. One camera is located at the normal focus of the optical system when no turbulence aberrations are present. The optical beam is split off to form two other image planes, wherein a second camera is placed slightly ahead of the ideal focus position, and the third camera is slightly behind the ideal focus by an equal amount. In this way, the fore and aft defocused images are captured along with the nominally focused image at the same time. When turbulence occurs, the image of the aft focus camera is subtracted from the image of the fore focus camera. The amount of difference between them indicates the strength of the turbulence, and Zang proposes a "region growing algorithm" which uses an 8 × 8 kernel convolution to establish a contrast threshold. When the turbulence strength goes below a certain threshold, the corresponding portion of the centered camera is saved to memory as a "lucky" region. This concept is very novel but suffers from significant limitations as follows:

1. The incoming optical beam is split three ways, therefore each channel can have at best one-third the total amount of input photon radiance. This can be a significant noise contributor in an infrared sensor.
2. The defocus subtraction technique indicates whether a lucky patch exists at the center focus, but otherwise it provides no correction to the non-lucky regions of the image, and so there is still a temporal component which may not support real-time operation.

5.1.6 Wavefront Coding.

Wavefront Coding is a technique which conditions the incoming optical wavefront at the aperture of the Objective Lens with a cubic or other odd-powered phase plate [104]. Gonzales-Amador, et. al., have proposed Jacobi-Fourier phase masks as an alternative to the cubic phase [105]. Wavefront Coding involves an optical phase element which has the effect of blurring the nominal focus, but it also has the unusual property of the resulting image being fairly invariant through various amounts of defocus as compared to a normal optical system. Figure 5.6 below shows the "L" shaped point spread function of a cubic phase versus a typical diffraction limited circular aperture

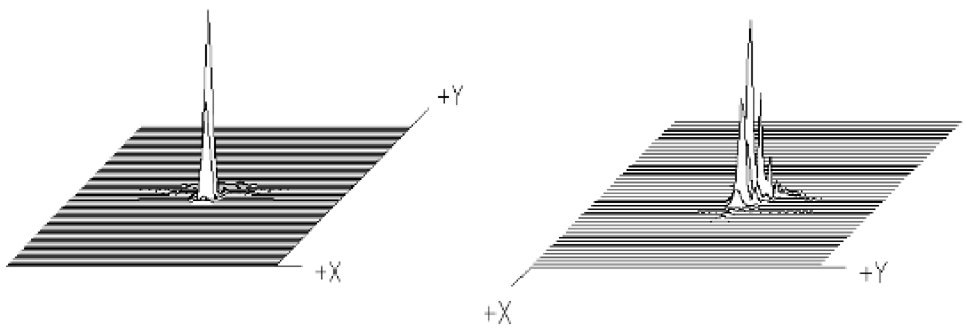

Figure 5-6: Comparison of PSF's for Airy Disk (left) and Induced Cubic Phase (right) Which Shows "L" Shaped Effect Upon the Point Spread Function

Since the cubic phase is known by design, it can be removed via de-convolution processes at the expense of increased noise and lower dynamic range. Lossless de-convolution is possible as long as the OTF of the entire system never crosses zero. In a broad sense, this technique trades dynamic range (i.e., noise floor) for an extended depth of focus. Some experimentation in Wavefront Coding for infrared sensors was conducted by Bryant and Kubala [106][107], who concluded that the degradation to the NEΔT (i.e., non-linear noise) can be a significant concern. Recent work by Olvera-Angeles , et. al., suggests the wavefront coding technique could be also used for turbulence mitigation in the visible wavelength spectrum [108], but the results show only limited success in cases of severe turbulence.

5.1.7 Neural Networks & Artificial Intelligence.

An new computing approach pertaining to neural networks and *artificial intelligence* (AI) has been making headway in many forms of digital data processing. The idea behind AI is to use computational processes mimicking the behavior of biological neuron cells, such that an interconnection of several neural cells can perform learning and optimization tasks. For illustrative purposes, the simplest binary model of a single neuron according to the McCulloch & Pitts model [109] is shown in the following Figure 5-7:

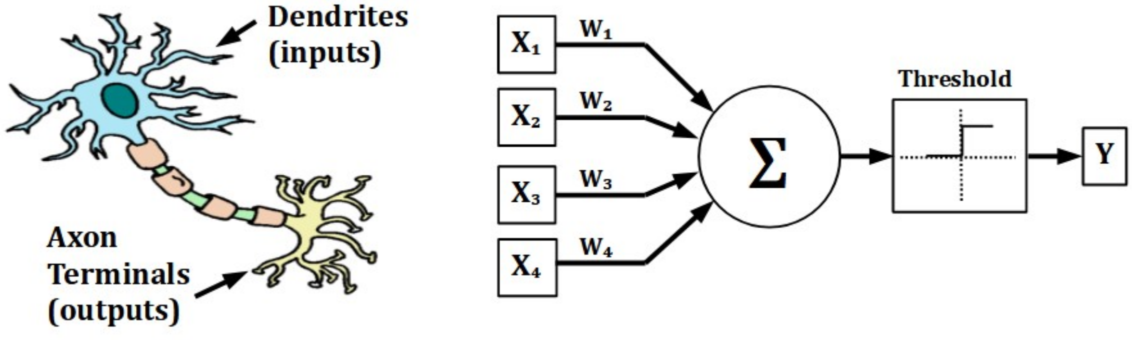

Figure 5-7: McCulloch & Pitts Binary Model of a Single Neuron

The biological neuron cell has an array of dendrites which serves as the input receivers for some external signal. When the weighted and summed output of the *dendrites* achieve a certain threshold value, they stimulate the cell to electrically activate the *axon terminals* as an output. The neuron can thus be somewhat thought of as a complex transistor. The system output is binary in the sense that the axon either fires or it doesn't, with no other state between a logical 1 or 0 output. For image processing applications, the sequence of inputs can be the pixel intensity values coming from the detector. A group of neurons can then be arranged to form a processing chain. The process chain may involve a fixed sequence of transfer from one to neuron to another, or more complex forms can be made where feedback loops exist between certain neurons. The phenomena of *learning* is associated with a permanent change in the structure of the network, which may be as simple as changing the threshold value or could perhaps include new connections and weighting functions [110]. For example, Rosenblatt's "Perceptron" [111] was developed to simulate the response of the human retina neurons to an optical stimulation. Rosenblatt proposed that the neural interconnect weighting functions are not determined by rigid boolean logic, but rather by probability distributions which in turn imply that an underlying random, non-linear function is also present to some degree. The application of neural processing for the task of turbulence mitigation is a relatively new field of study, and there are few citations in the literature for such. One study by Jain, et. al., from the San Diego State University appears to have successfully developed a process chain based on a neural processor which provides electronic image stabilization [112]. The authors demonstrate that the principles can be of use in the case of turbulence. A more recent study [113] revealed that the neural networks were unable to fully mitigate the effects of turbulence primarily because of two main reasons: 1) the turbulence between two successive images changes as a function of time, and 2) the networks were trained on single images. The neural processing option is a newcomer and there will likely be new breakthroughs as time progresses, but at this point in time, it does appear that the technique is dependent upon sequences of image frames over time, which in turn adds risk to the system goal of a real-time solution.

5.2 Brainstorm Ideas.

Based on the known state of the art, a brainstorm session by the imaginary team was held. At the end of the brainstorm session, the system engineer prepares a summary of the proposed approaches along with rating factors to show the strengths and weaknesses of each. This is not a ranked choice necessarily, as the optimal solution may yet involve some or none of the brainstorm ideas, but it is a method to stimulate more creative thought to focus on the particular challenge areas. Schutte, et. al., provide a good overall summary of options for mitigating turbulence effects along a horizontal imaging path [11]. Table 5-A below shows a comparison chart rating high level performance aspects as well as an assessment of the overall maturity of the approach. Symbols can be used alongside the verbal descriptions in order to facilitate rapid absorption of the information.

In this case, the symbol ⊙ represents a weak aspect of the approach, ⊚ represents a moderate capability is possible, and ⊛ corresponds to a strength of the particular aspect for the given approach.

Table 5-A: Comparison of Options

Approach	**Improve Image**	**Real Time**	**Maturity**
De-convolution	⊚ Moderate	⊙ Weak	⊛ Strong
Lucky Patch	⊛ Strong	⊙ Weak	⊛ Strong
Defocus/Phase-Diverse	⊙ Weak	⊚ Moderate	⊙ Weak
Wavefront Coding	⊙ Weak	⊛ Strong	⊙ Weak
Neural Process/AI	⊚ Moderate	⊙ Weak	⊙ Weak

This simple summary exercise provides a remarkable insight into the path toward an optimal system solution. The Figure shows that the mature Blind De-convolution and Lucky Patch techniques offer good image quality potential, but are limited by the real-time requirement. The Defocus Comparator approach, however, seems to offer some hope for a real-time solution but yet it is immature, and the image quality benefits of the approach to date are somewhat dubious. The Wavefront Coding technique is relatively new approach which has had some success in low turbulence conditions, but the fundamental trade with the SNR could be a significant limitation for an infrared detector system. Neural processors and AI algorithms do offer many new possibilities, but the current art indicates there is a significant risk in achieving real-time operation with a portable processor subsystem.

5.3 Focal Volume Concept.

The brainstorming session revealed several approaches, each with their challenges and benefits, and it appears that none of them provides a direct solution. The next step is to "follow-up" [18] by looking at the best ideas and then perhaps synthesize a new approach. The question, "What if ...." now shall be the guiding theme for the brainstorm follow-up work effort [114]. What if we can design a system which supports defocus phase retrieval technique (Zang) combined with other digital processing approaches (De-convolution, Lucky) to reconstruct an improved image in single-frame real time? In effect, this would be one example case for the more generalized "free running wavefront modulator" approach disclosed by Schutte. To answer this question, the "focal volume" system design concept is now synthesized herein. This concept borrows ideas from the approaches described previously, but instead of searching for lucky positions over *time* where the random turbulence is minimized, the search occurs through multiple planes of *space* (e.g., defocus) in the optical system within a single frame time, and in which case random luck may no longer be longer a requirement. Such an approach may also help solve the issue with de-convolution by recovering information that would otherwise have been permanently lost. The optical aspect of the concept is demonstrated in the Ray-trace Model, and is illustrated in more detail below in Figure 5-8. The left side shows the focal plane of a 400 mm focal length infrared lens at F#/3 with no aberration (Appendix B), and with turbulence applied via the phase plate placed near the focus. In the zero turbulence case, the focal plane is well-corrected and very flat across the field. In the turbulated case, however, there is a very visible amount of defocus of approximately 1 mm which will be dependent upon the location of the isoplanatic patches within the full image. *What if* all three focal positions can be captured, as well as perhaps two more positions mirrored on the other side of the nominal focal plane in case the phase change has negative power?

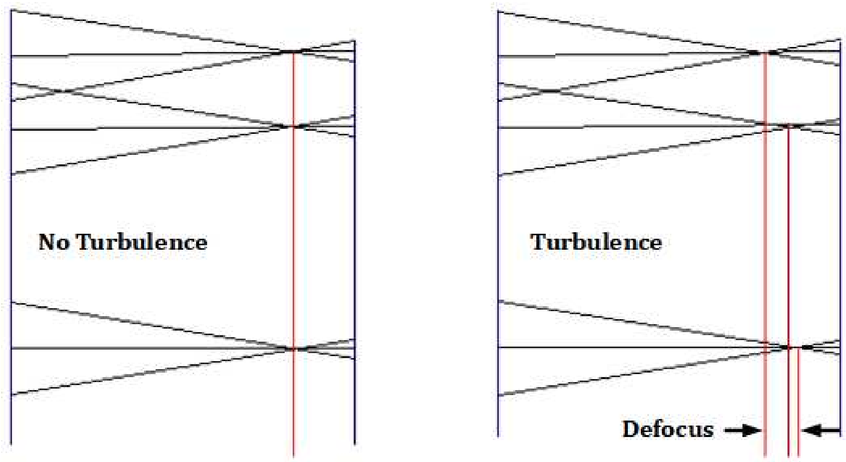

Figure 5-8: Ray Trace Model Shows Field-Dependent Defocus & Tilt Effects of Turbulence

The next Figure 5-9 below shows a sequence of intensity point spread functions (PSF's) through amounts of defocus for the 400 mm, F#/3 LWIR Objective Lens whose details can be found in Appendix B. The field position is selected to be on the optical axis (i.e., $\theta = 0°$) which encounters a maximum amount of turbulence effects. The top shows the baseline PSF plot with no turbulence for comparison, and then the $\Delta z = 0$ plot shows the PSF in the same focus position but with turbulence applied. The subsequent plots show how the PSF changes as the defocus increases. Position $\Delta z = 0.4$ seems to be the closest to the baseline, and then at $\Delta z = 0.6$ the blur width of the PSF is increasing again.

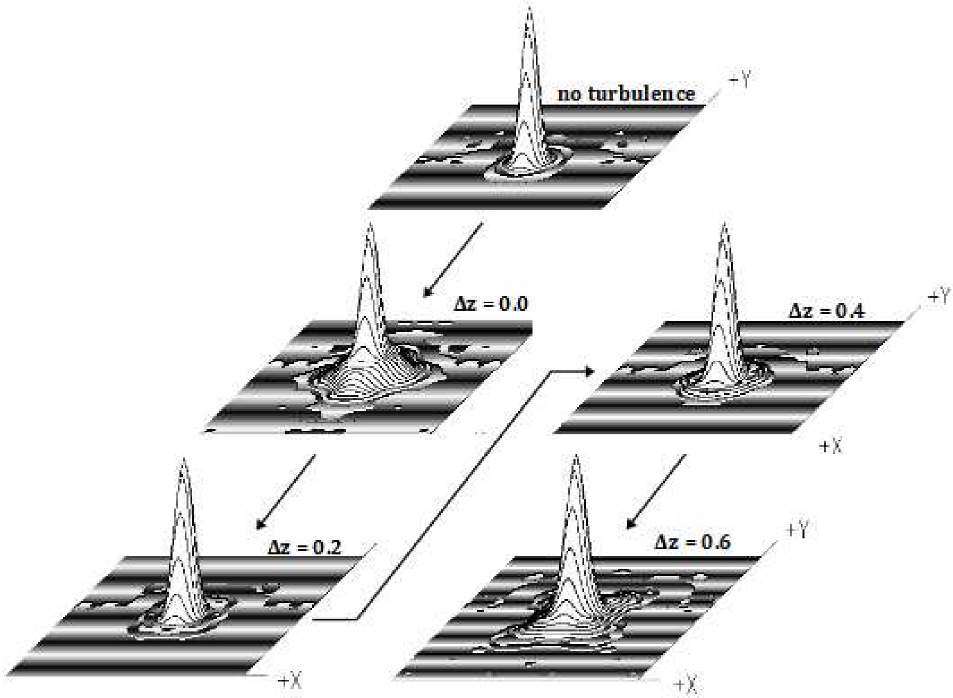

Figure 5-9: Through-Focus Behavior of the Turbulated PSF

Table 5-B below shows the numerical values for the defocus PSF positions, where "PV" refers to the peak-to-valley error at 10 μm wavelength and "RMS WFE" is the root-mean-square wavefront error value. The RMS WFE is an averaged value over all traced rays, so it is typically less than the PV which is the absolute value of the worst case error for a single traced ray. The two columns where Δz = 0 show the impact of the turbulence, which is about a 0.15 ÷ 0.036 = 417% increase (i.e., a degradation) in RMS WFE at the nominal focal plane position. At the defocus position of Δz = 0.4 mm, however, the degradation is reduced to about 0.07 ÷ 0.03 = 194% which is a substantial improvement simply by having alternate planes of defocus!

Table 5-B: Variation of WFE vs. Defocus Position

	no turbulence	**turbulence**	**defocus**	**defocus**	**defocus**
Δz	0.0	0.0	0.2	0.4	0.6

PV	0.21	0.56	0.33	0.37	0.60
RMS WFE	0.036	0.15	0.07	0.06	0.14

A digital algorithm can be used to choose the best focus position on a pixel-by-pixel basis. A very simple and speedy algorithm can calculate the edge gradients of the same pixel location in each of the five planes ("z") of focus. For any pixel position P(n,m) as a functions of n rows and m columns, the edge gradient score (EDG) can be defined as

$$EDG(P, z) = 4P(z, n,m) - P(z, n+1,m) - P(z, n-1,m) - P(z, n,m-1) - P(z, n,m+1)$$

This calculation is then performed in each plane of defocus captured by the sensor. The pixel value from the defocus plane with the highest edge gradient score will then be selected for the corresponding pixel coordinates in the algorithm output frame. Figure 5-10 below shows an example based upon five planes of defocus, designated as Defocus -2, Defocus -1, Defocus 0, Defocus +1, and Defocus +2. In each defocus plane, the pixel coordinate in question is compared to the values of its nearest horizontal and vertical neighbors. The gradient edge calculation is a simple subtraction of the neighbor values, and the plane position with the highest gradient score is selected for the output frame at the same (n,m) coordinates. The entire process can be called the "Focal Region Enhanced Edge Pixel" (FREEPIX) algorithm. In this example, the pixel at the Defocus 0 position has the highest simple gradient score, and so the output frame would receive a value of 121 at that same (n,m) coordinate. This process is repeated for all pixels until the output frame is fully populated.

Defocus -2

	100	
100	**110**	100
	100	

EDG 40

Defocus -1

	95	
92	**115**	97
	96	

EDG 80

Defocus 0

	89	
86	**121**	88
	90	

EDG 131

Defocus +1

	96	
91	**115**	95
	96	

EDG 82

Defocus +2

	97	
99	**108**	102
	99	

EDG 35

Figure 5-10: Example "FREEPIX" Algorithm Scoring Function

It is now possible to predict the result of using the focal volume technique by going back to the performance model and estimating the performance of a defocus-corrected sensor. Since the PSF improvement in the above analysis was improved by roughly a factor of 2X, it is a reasonable estimate that the MTF cutoff frequency of the turbulence component can likewise be improved by a factor of two. In the original model for high turbulence conditions where $C_n^2 = 5.05 \times 10^{-13}$, the $MTF_{tur}(\xi)$ component reached near zero contrast at about 10 cy/mrad. Therefore, decreasing the PSF by two would beneficially extend the cutoff to nearly 20 cy/mrad. The can be shown in the model by input of a "corrected" index structure parameter to about $C_n^2 = 1.00 \times 10^{-13}$. This changes increases the sensor targeting range from roughly 2.0 km under high turbulence conditions to 2.5 km with the new defocus correction applied as shown below in Figure 5-11. This is a significant increase and much closer to the range in non-turbulent conditions, which was about 2.85 km. It is also possible that further image processing techniques might be able to close the remaining gap. The system engineering model data therefore indicates that the proposed focal volume technique has a chance at making a significant improvement in range performance which meets customer expectations.

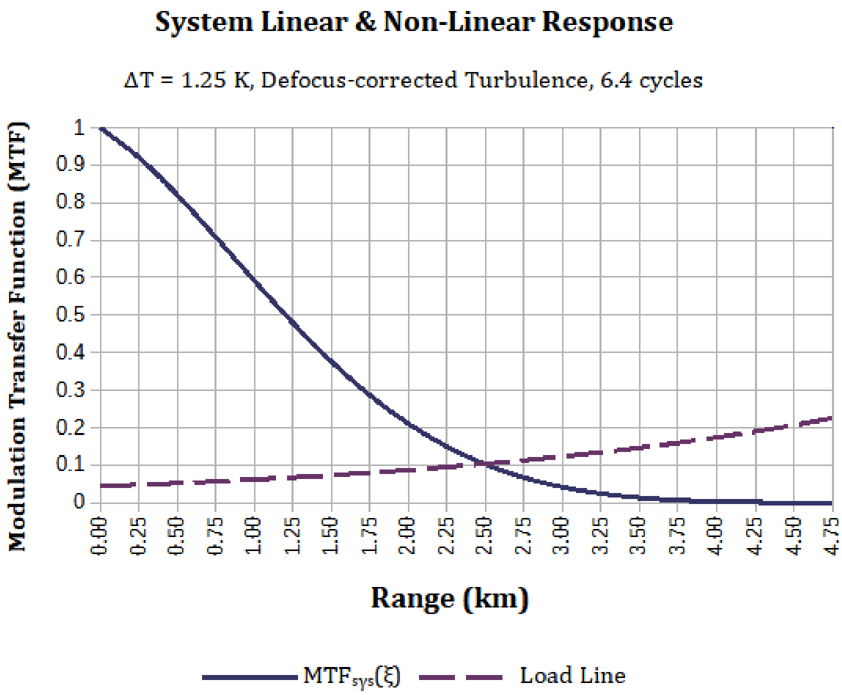

Figure 5-11: Range Model Analysis Shows Compliant Range Via FREEPIX

The local shape distortions caused by tilt aberrations can likewise be characterized and corrected [115]. Hardie describes a method based on Lucas & Kanade which begins with buffering and averaging the input frames, and then is followed by robust global translational registration is used to align the N frames the average [116]. Finally, a least-squares gradient-based registration algorithm is used. The technique assumes that the difference between two frames is small enough that an approximate guess can be made. However, if the PSF's are known for each frame, then the guess can be greatly improved. For example, if it is desired to overlay two functions such as F(x) = sin(x) and G(x) = sin(x + y) where y is a constant offset value, then Lucas & Kanade report that their the algorithm will operate only for the region where -π < y < π and therefore they recommend low-pass filtering the images first in order to reduce the spatial frequency content. However, by capturing multiple planes of defocus, an "optical flow" technique can be added. The "lucky" regions of low turbulence will be close to their ideal positions, whereas the highly turbulated pixels will be offset via the local tilt distortions. The centroid of the lucky region will not shift with defocus, whereas the turbulated areas will have greater shifts. By tracking the centroids across the planes of defocus, each pixel can be assigned a position vector. Figure 5-12 below illustrates the concept, where the image of two point source objects A and B are shown. In Defocus Plane 0, position A_1 contains a focused image of the first object point source, whereas position B_1 has a blurred image of the second object point source. In Defocus Plane +1, position A_2 shows a blurred image for which the centroid has not shifted in terms of its (x, y) coordinates. This means the images of object A are lucky ones with low turbulence effects. Position B_2, on the other hand, shows an improved focus but now is shifted in (x, y) compared to the centroid of the blurred image at position B_1 in Defocus Plane 0. This means that the image of object B is experiencing turbulence tilt and defocus shifts. Determination of these shifts can be facilitated if the Objective Optics are designed to be *telecentric* [117] whereupon the chief rays for each bundle of rays for each field point are normal to the focal plane. In that way, if there is no turbulence, then defocus of the telecentric Objective Optics will not change the centroid positions of each field point, and thus any shift which does occur would have to be caused by turbulence. Telecentricity is a common optical design technique used in rifle scope optics and in machine vision optics so that the focus adjustments change neither magnification nor boresight alignment [117].

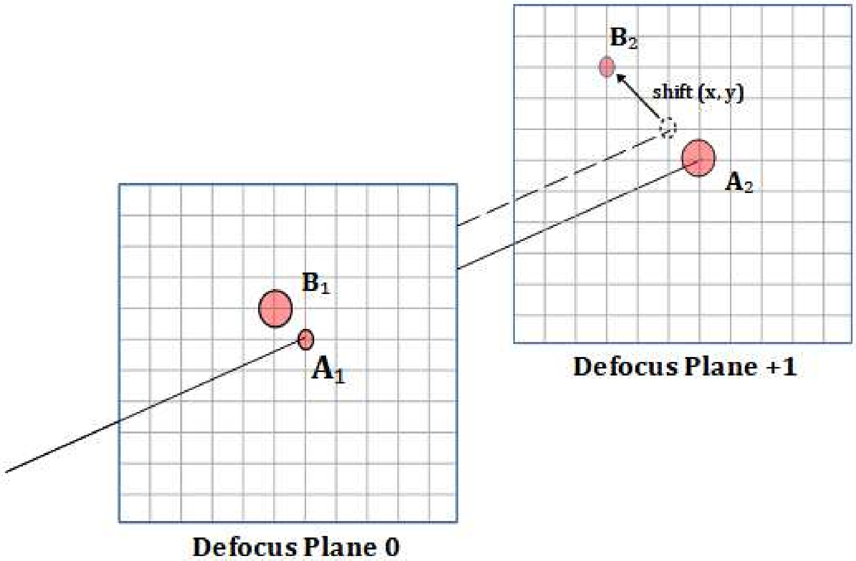

Figure 5-12: Concept for Image Registration Via Defocus Shift Correction

Furthermore, this new ability to capture multiple defocused images within the same frame time may also provide extra information about the behavior of the local area point spread function for a more deterministic means of seeding a de-convolution algorithm [118][119]. Figure 5-13 below shows a functional block flow diagram which embodies these concepts.

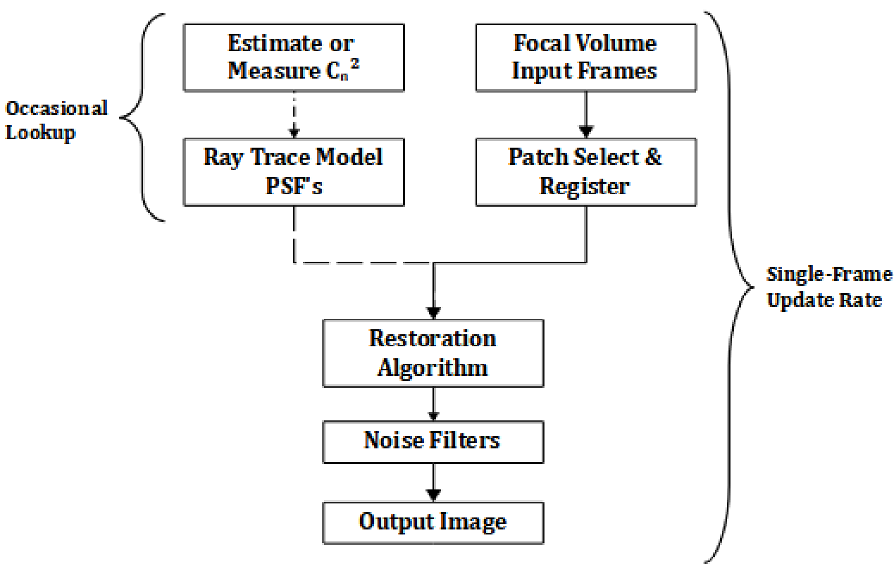

Figure 5-13: Functional Concept For a Turbulence Mitigation System

The signal flow diagram above shows that perhaps a combination of occasional updates combined with fast real-time processing can optimize the output results. The ray trace model can provide PSF estimates, and the focal volume collection can compile the best image portions from several planes of defocus. This information is then combined into the de-convolution processor which can provide the final solution. An extra noise filter block is included to mitigate sampling artifacts and other noise sources that might be inadvertently amplified by the previous processes. This general approach is submitted as the output of the brainstorming session as input to the next stage, which is a feasibility study to assess the risks of whether such an apparatus can be assembled with current technology.

Chapter 6 - Feasibililty Analysis

The output of the brainstorming exercise is an initial concept which requires capture of multiple planes of image defocus combined with a set of digital processing algorithms. In order to provide real-time operation, the real-time operations must be accomplished both within a single frame time and within the turbulence time constant. The next step in the system engineering process is to develop this initial concept into a feasible design approach. The Feasibility Study shall also address these technical derived requirements, and also new concerns such as availability of components, overall size, weight, and power, and unit cost. The focus for this exercise is more intense on the blocks which comprise the system itself, namely the objective optics, detector, processor, and display. It may be that certain blocks will have many interdependent aspects, especially between the objective optics and the detector which can be collectively labeled the "front end" of the system. The processing and display blocks shall be referred to as the "back-end" of the system.

6.1 Primary Risks.

The feasibility analysis begins with identifying the major "show stopper" risks, which if not resolved, could result in an unacceptable system concept. As the conceptual design matures, the big risks must be constantly assessed. The two biggest risks for this exercise are stated formally as follows:

1. There is a risk in obtaining the several planes of defocused images within the a single frame time. The risk is caused by the mechanism that induces defocus into the Objective Optics. The direct impact is loss of real-time operation. There is no recovery action possible. The impact to the program would be an inability to meet customer requirements with the given approach.
2. There is a risk that the processing requirements will require large computer volumes and large amounts of electrical power. The risk is caused by the amount of digital image processing needed to perform multiple operations including convolutions of large matrices of numbers. The direct impact is a significant burden in size, weight, and power at the system level. Heat management might also be a risk. A possible recovery would involve designing a custom processor chip with efficient machine code. The program impacts could include customer dissatisfaction and increased cost & schedule to develop custom processor electronics.

6.2 Front-End Design.

The front-end concept involves the objective optics and the detector. Figure 6-1 below summarizes the principle that needs to be investigated. Light rays from a point source object enter the objective optics and are focused to a point somewhere with a focal volume in spatial coordinates (x, y, z). In conditions of zero turbulence, it can be assumed that the objective optics provide a flat focal plane for all points across the field. This is the normal design condition for most commercially available cameras and focal plane detector devices. However, when turbulence is present, various amounts of tilt and defocus will displace the focal convergence somewhere with the focal volume. The front-end system will capture the image multiple planes of defocus, all within a single frame time period. Positions along the z-axis are notated using $\mathbf{Z}_{-2}$ and $\mathbf{Z}_{-1}$ naming the planes of defocus in front of the non-turbulated center focus setting $\mathbf{Z}_0$, and then $\mathbf{Z}_{+1}$ and $\mathbf{Z}_{+2}$ naming the two planes which are past the center plane at $\mathbf{Z}_0$. The sensor performance model has already provided several geometric optical and detector parameters. The objective optics will need to have roughly a 400 mm focal length and an F#/3.0. The detector will need to have roughly 0.028 mm pixel pitch. The optical raytrace model has provided a sense of the amounts of defocus that are likely to occur as a result of different strengths of turbulence. From this data, it appears that a total of five focal positions covering a region ± 1 mm along the z-axis is desired. The detector integration time was found via the system performance model to be on the order of 7×10^{-5} seconds for a LWIR detector, so a total of five frames could be captured in 35×10^{-5} seconds, which will fit well within a single 60 Hz image frame time of 1.67×10^{-2} seconds and leave plenty of time for other electronic read-out operations within the detector. Additionally, the worst case turbulence temporal stability is on the order of $t_0 = 4.32 \times 10^{-3}$ seconds at 3 km for high turbulence conditions where $C_n^2 = 1 \times 10^{-12}$.

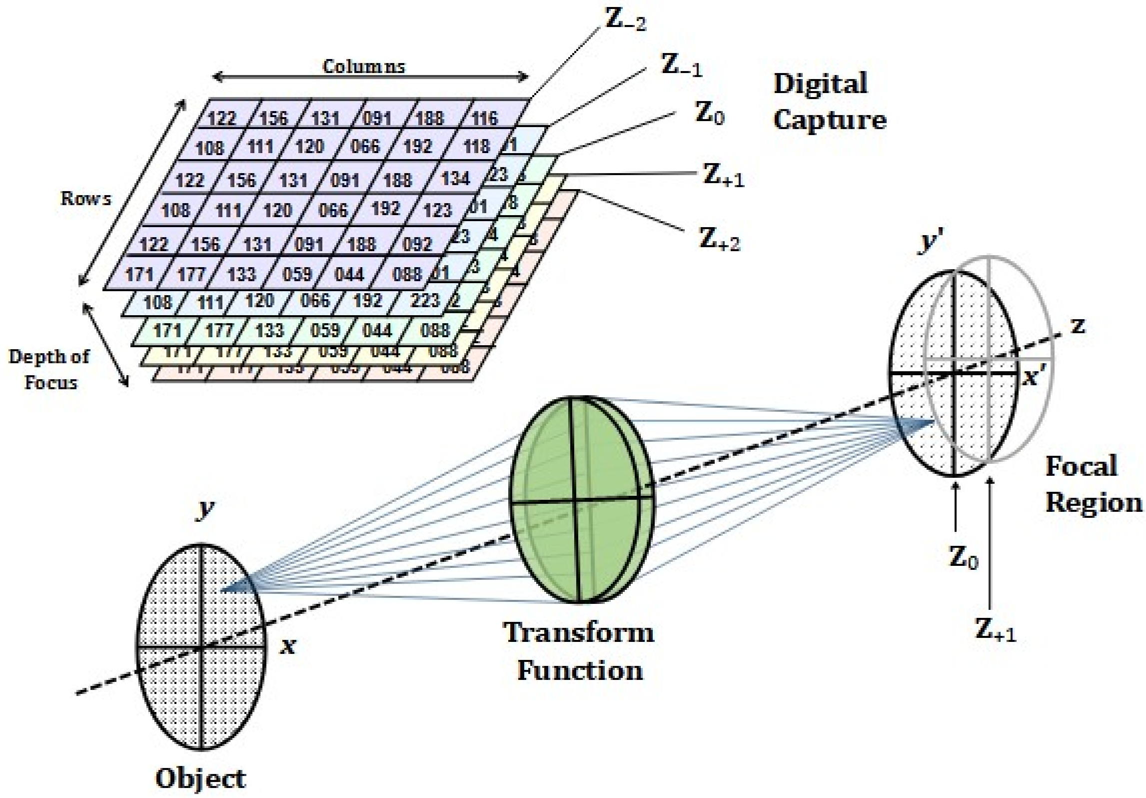

Figure 6-1: Illustration of Front-End System Operational Principle

6.2.1 LWIR vs. MWIR Spectrum.

The analysis up to this point has focused on LWIR infrared spectral band for the sensor system, but there could also be solutions in the MWIR spectral pass-band of the atmosphere. The sensor performance model can be modified to see what happens in the MWIR spectrum. For a first trial, all of the original LWIR model sensor parameters are left unchanged except for the wavelengths, now with λ_1 = 3.5 microns and λ_2 = 5.0 microns. Then the target ΔT is changed to find the point where the SNR = 1.0, which occurs as 0.312 K. This value becomes the NEΔT, and then the true target ΔT is entered as 1.25 K. The results are that the load line rises very quickly, and the detector well fill percentage is a very low 1% value as shown below in Figure 6-2. This is no surprise, as Planck's Law clearly shows there are far fewer photons in the MWIR spectral region than there are in the LWIR region at a nominal 300 K background. The system MTF curve does move upward because of the better optical diffraction limit, however this system is so dominated by the non-linear noise characteristics that the optics MTF offers little relief.

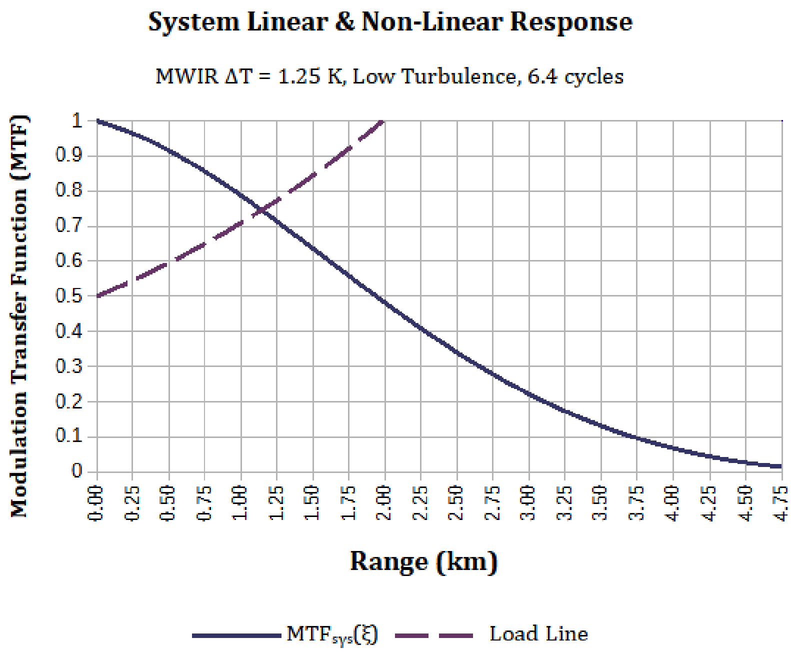

Figure 6-2: MWIR Performance With Otherwise Original Model Parameters

Assuming that the detector geometry and objective lens parameters are already in the realm of available components, the remaining parameter left to change is the detector integration time. Currently the value is $\tau = 7 \times 10^{-5}$ seconds. By increasing this value, more photons will be captured and the load line move downwards in the desirable direction. After a few iterations, it is found that raising the integration time to $\tau = 0.5 \times 10^{-3}$ seconds results in a SNR =1 with an NEΔT = 0.053 K, and a target identification range on par with the LWIR solution. Figure 6-3 below shows that the range performance is comparable to the LWIR solution. However, the longer integration time creates a risk in terms of being able to capture multiple defocus positions within the high turbulence temporal stability value of $t_0 = 4.32 \times 10^{-3}$ seconds. Indeed, if five defocus frames were required, that would occupy a minimum of 2.5×10^{-3} seconds which is already more than half of the t_0 value. The analysis thus shows that equivalent MWIR range performance might be obtained, but at the risk of increasing the integration time by orders of magnitude greater than the LWIR approach. And while there are other means to improve the NEΔT such as using a faster (i.e., lower value) F#, the approach from this point forward shall focus on the LWIR solution which is less constrained.

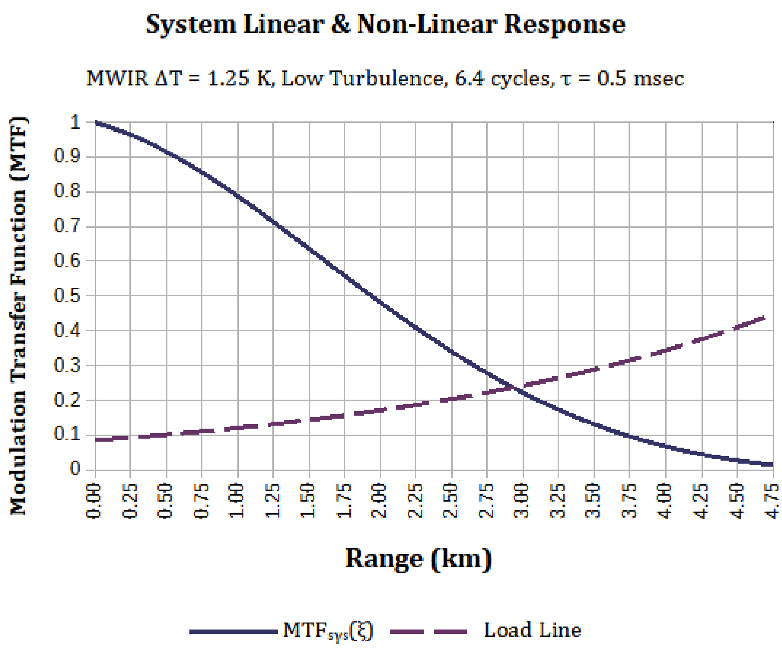

Figure 6-3: MWIR Solution with Longer Integration Time (τ) Matches LWIR Solution Range, But Integration Time Exceeds Allowance

6.2.2 Methods for Focal Volume Capture.

The question now is, how can the "front-end" be designed so as to capture the focal volume within a single frame time, and within the turbulence temporal stability t_0 value?   Here again is a need to hold a brainstorming session, though perhaps with a more limited membership by those who have experience in optical subsystems. The result of this brainstorm session produced the following suggestions:

1. Mechanically move or vibrate a two-dimensional detector array through focus along the z-axis.
2. Mechanically move or vibrate a focus lens assembly in front of a fixed mounted two-dimensional detector array.
3. Use a linear scanned detector array, where five or more columns of the detector are optically adjusted to be at different defocus positions.

The suggested approaches were then rated against high level criteria of engineering simplicity, minimization of size, weight, and power (SW&P), and overall maturity in terms of whether systems of a similar nature have already been built and used successfully. Table 6-A shows the results. In all cases, a score of "⊛ High" is the best outcome, with "⊚ Moderate" and then "⊙ Weak" scores following in diminishing desirability.

Table 6A: Evaluation of Approaches for Focal Region Capture

Approach	**Simplicity**	**Minimum SW&P**	**Maturity**
Oscillating 2D Array	⊙ Weak	⊙ Weak	⊙ Weak
Oscillating Lens, 2D Array	⊚ Moderate	⊚ Moderate	⊙ Weak
Linear Scan, Linear 1D Array	⊚ Moderate	⊚ Moderate	⊛ High

The idea of putting the focal plane detector in a state of constant back-and-forth motion is not desirable from an engineering standpoint. An infrared detector assembly which meets the model parameters will require cryogenic cooling and an insulating vacuum Dewar assembly to house the detector array [120]. These devices will require electronic cabling and shielded connections. Therefore, setting the focal plane in motion will require moving the much larger mass of this entire sub-assembly, and all cabling connections would require extra strain relief to accommodate the motion. Vibration isolation will also be a challenge, as any linear displacement error will transfer directly to the pixel location within the optical focus. The concept of moving a de-focusing lens element is more palatable as compared to moving the entire detector-cooler assembly, as a single lens will have a much reduced mass and no direct electrical cabling. Depending on the refractive power and position of the lens, however, the range of physical motion in order to create a corresponding defocus amount at the focal position might not necessarily be a 1:1 basis. For example, a weakly powered lens may need to move over 1.0 mm in order to achieve a 0.5 mm defocus excursion. This may rule out some of the mechanisms such as piezoelectric motors which have very limited ranges of travel. The lens may also introduce higher order aberrations in addition to the desired defocus. For this application, the scanning rate will be fairly high (at least 30 Hz), which will induce an amount of stress into the lens material as it is driven back and forth many times per second. There are risks, but overall this approach does appear to have a moderate chance of success. A survey of commercial units reveals, however, that this approach is not often seen in commercial products and hence the maturity is a risk. On the other hand, the linear scanned array system concept is several decades old and continues to find applications into the current era [121] [122]. Linear arrays on the order of 240 or 480 detector elements in a column can be fabricated economically when compared to comparable two-dimensional mosaic arrays which occupy a much larger area.

6.2.3 Galvanometer Scan Mirror.

Lloyd [22] discusses a variety of means for adding a scanning function into an optical sensor system. It is possible to obtain the desired optical beam deflection by setting into motion prisms, mirrors, lenses, or diffraction gratings. Lloyd discusses common approaches including oscillating mirrors, rotating polygon mirrors, and rotating prisms. Similar effects can also be generated by decentering lens elements. The integral mechanical motion devices are explored in more detailed by Reich [123] , and one of these known as a "galvanometer" type device has the capability to meet very precise requirements. A galvanometer is a device used to measure the flow of electric current. The general principle is that the flow of electric current will cause a physical change in some material which is designed to be observable. For example, the magnetic needle of a compass can be used to detect an electric field. Another type of apparatus may use a mirror mounted to a magnet, such that the deflection of a beam of light bouncing off the mirror indicates the strength of a local electric field. The following major events highlight the history of the development and terminology for a device known today as a"galvanometer" [124]:

1786: Galvani observed twitching of dissected frog legs when subject to electrical current.

1802: Bischof names his electrostatic instrument a "Galvanometer"

1820: H. C. Oersted publishes magnetic influence of a flowing electrical current.

1820: Ampere refers to Oersted's device as a "Galvanometer".

1826: Poggendorf discloses idea to use reflected light instead of a compass needle [125].

1858: William Thompson (Lord Kelvin) patents design for mirror galvanometer [126].

The mirror galvanometer mechanical operation can be mathematically modeled via the same principles as an electric motor, where an incoming electric current is used to create very precise angular positioning of a mirror attached to the motor shaft as illustrated in Figure 6-4. The motor is comprised of two major sections, the *stator* which is the stationary component, and the *rotor* which is the part which moves, typically in a circular rotation. The mechanism which switches the direction of the electrical current in order to support continuous rotation is known as the *commutator*. In a permanent magnet type of motor, either the stator or the rotor contains a permanent magnet material such as neodymium. The other remaining part will contain a set of wire windings wrapped around a core material such as iron which becomes magnetic once an electric charge is provided. The number north/south magnetic pairs is referred to as the number of *poles* of the system. By pulsing the electric current step-wise through a series of windings, a circular rotation of the magnetic field will pull the permanent magnet in like fashion [127]. The rotor will include ball or cylindrical bearings to facilitate the rotary motion and reduce friction. The rotating parts such as the rotor shaft and the mirror may be made from special beryllium alloys in order to provide stiffness and low mass [128]. The moving magnet type of motor, where the permanent magnet is part of the rotor, is a popular means to produce precise scanning of optical beams at fast frequencies and its performance can be modeled by iteratively solving a set of simultaneous differential equations [129] [130].

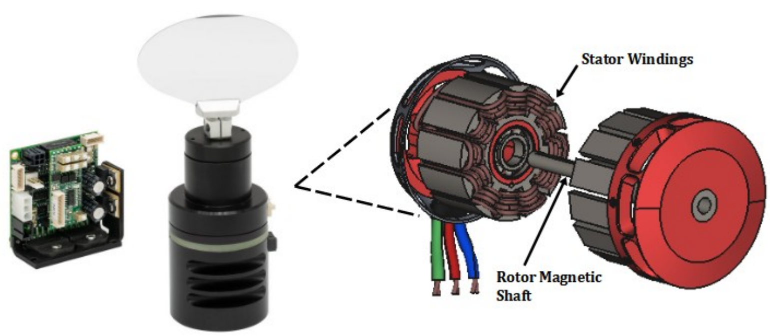

Figure 6-4: Exploded View of Rotating Magnet Motor Inside a Scanning Galvanometer

The scanner sweeps through its total range of travel in one frame time. For example, at 60 Hz frame rate the duration of a single scan cycle is 16.667. If a linear detector array is oriented so that the detector elements are in the vertical direction, then the horizontal "pixel" is collected by shuttering the linear detector in time as the scanner sweeps the field of view. Scan travel can be bidirectional or unidirectional. In a bidirectional scheme, the first frame is scanned from left to right, and the next frame is then read out in reverse order from right to left. One potential issue with the bidirectional approach is that there is a uneven time interval for any given pixel coordinate between each successive frame. This in turn may lead to motion artifacts [131]. A unidirectional scanning scheme will not have the variable time phase problem, but will require consideration because it will need time to return to the zero position before each scan cycle. A unidirectional scan cycle will generally be driven with a sawtooth voltage waveform [128] as shown below in Figure 6-5. The scan cycle can be divided into two major parts, the first being a linear region where the detector will synchronize the integration times to capture the photons, and secondly a "fast-flyback" interval where the mirror returns to start the next scan cycle.

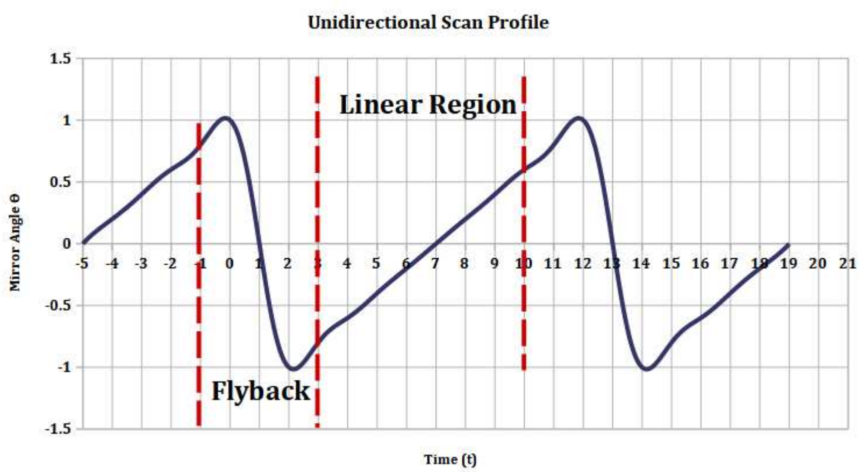

Figure 6-5: Example Unidirectional Fast-Flyback Scan Mirror Profile

A critical system-impacting parameter is the *scan efficiency*, which is the percentage of the cycle occupied by the linear region of angular travel. For example, if the scan cycle for 60 Hz frame rate is 16.667 msec and the scan efficiency is 70%, then 11.7 msec of time per frame is available for detector integration. Harkening back to the range performance model, the desired detector integration time was assumed to be 7×10^{-5} sec, or 0.07 msec. If the detector is comprised of five linear columns of detectors in close proximity but at different planes of defocus, then they can all be captured simultaneously during each scan cycle. This is analogous to the "time delayed integration" technique used in scanning infrared sensors [68], except that in this system each column is in a different plane of focus. Therefore, the total number of horizontal pixels that can be captured in this example is 11.7 ÷ 0.07 = 167 pixels. Assuming each pixel shall have an equivalent spatial dimension of 0.028 mm per the model, and with a focal length f = 400 mm and magnification M = 9.5, the resulting total horizontal field of view is 6.36° as displayed to the human eye. If the vertical pixel count is assumed to also be 167 pixels for an equivalent view angle, then the resulting diagonal extent of the field of view turns out to be 9.00° which is consistent with the recommendation by Lloyd [22] & Enoch [79] .

It is critical that the detector integration times be synchronized with the scanner cycle in order to create the horizontal "pixels". For closed-loop control, the scanner assembly may include either a position encoder or an optical position sensor, either of which reports the angle of the mirror. An example control loop is shown below in Figure 6-6 based on Chen [132], which shows the general outline of a feedback system. The reference signal can be a clock within the processor which provides precise timing information.

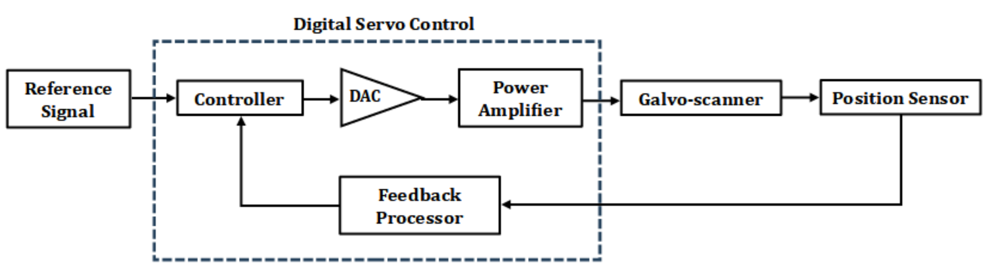

Figure 6-6: Example Scanner Control Loop

There are fortunately a number of galvanometer scanner devices already available in the market. The QS45X-AG available from ThorLabs [133] is such a device which is optimized for optical scanning. This unit has a moving magnet rotor, capacitive position sensor, and an included proportional-integral-derivative (PID) servo driver circuits with advanced current damping. The step response is 1200 microsec over a maximum possible rotation angle of ± 22.5°. The rotor inertial load is 5.1 g/cm^2, and the angular position repeatability 15 microrad. Once critical aspect of this component, however, is that the maximum mirror size is roughly a 25 × 50 mm ellipse. This is too small to use in front of the entrance aperture diameter of the Objective Lens which is on the order of 133 mm. The scan mirror size limit will thus have to be considered as a derived requirement for the Objective Optics design effort.

6.2.4 Objective Optics.

The Objective Optics need to satisfy the basic requirements for focal length (f = 400 mm) and F#(3.0) per the range performance model as well as the derivative requirements imposed by the scanner mirror size limitation and the need for somehow achieving focal depths for linear arrays on the order of -0.5 mm to +0.5 mm. Beginning with the scanning mirror, Lloyd discusses options where the mirror might be located in either collimated space or non-collimated, focusing beams [22]. In order to reduce aberrations induced by the mirror motion, operation within collimated optical space is a good option. This in turn shall require a split optical system, with an afocal telescope in the front, then the scan mirror, and then an imaging optic in the rear to create the final image. The afocal telescope needs to reduce the required aperture size from 133.3 mm down to the scan mirror size which is less than 30 mm in the vertical direction. An afocal with 4.55X power would output a pupil height of 29.3 mm. The image forming lens assembly will therefore need a focal length of about 400 ÷ 4.55 = 87.9 mm at the same F#/3.0. Lens designs of this general form can be found in optical design references [117], and by means of scaling and slight re-optimization, a new lens prescription which meets the current requirements can be quickly achieved. The results are shown in the ray-trace per Figure 6-7 below. A full prescription detail is provided for reference in Appendix B.

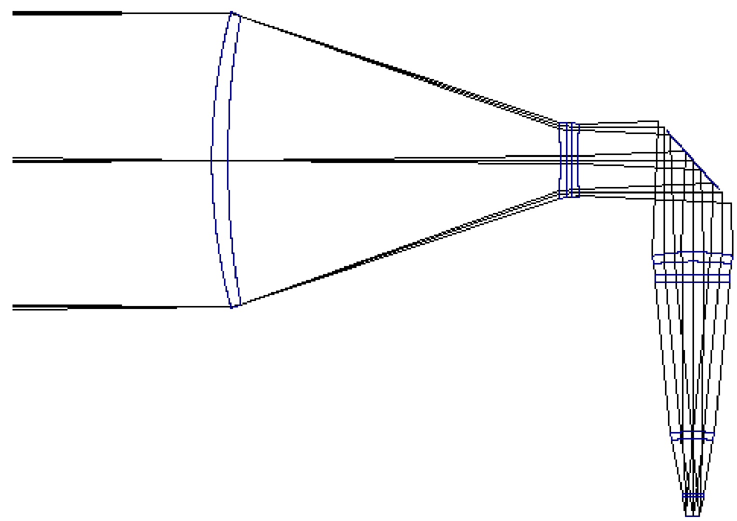

Figure 6-7: Feasible Lens Design Having 4.55X Afocal, Scan Mirror, & 87.9 mm Imager

The lens system has a total of three elements in the afocal, and then three lens elements in the Imager. The front lens can serve as the sensor window if desired. An additional fold can be added in the imager in order make the overall volume more compact. The chief rays approaching the final image are nearly perpendicular to the focal plane, which is the desired telecentric condition. The next Figure 6-8 below shows the MTF of the optical system, accounting for both diffraction and any geometric aberrations. The diffraction limit dominates the performance, which is the ideal situation.

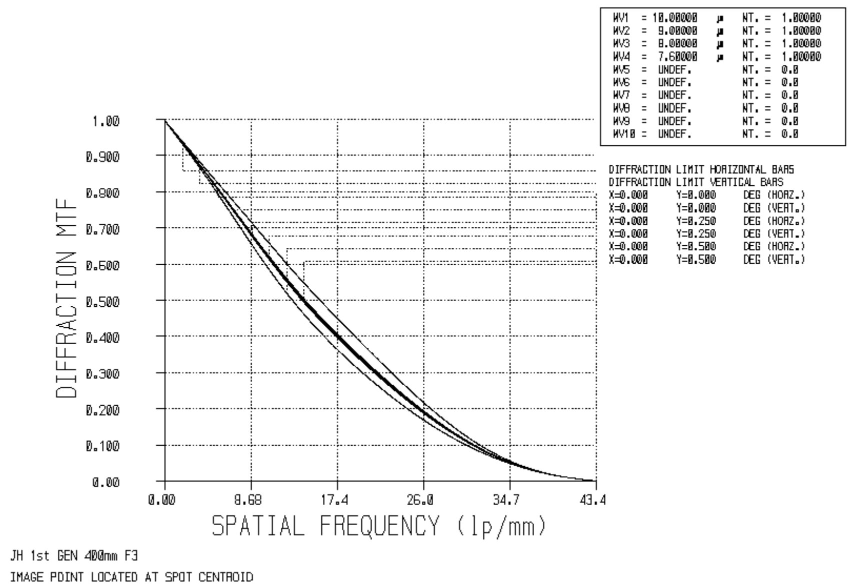

Figure 6-8: Feasible Optical Design Analysis Shows Diffraction Is Dominate MTF Component

The ray-trace model can then be exported into a mechanical Computer Automated Design (CAD) software package, wherein the scanner mechanism model can also be added and superimposed with the optical surface representing the mirror. The next Figure 6-9 below shows a view of the CAD assembly. The ray positions verify that the beam size is indeed a good match for the actual mirror size. The CAD model is a good way to start visualizing the physical structure of the system.

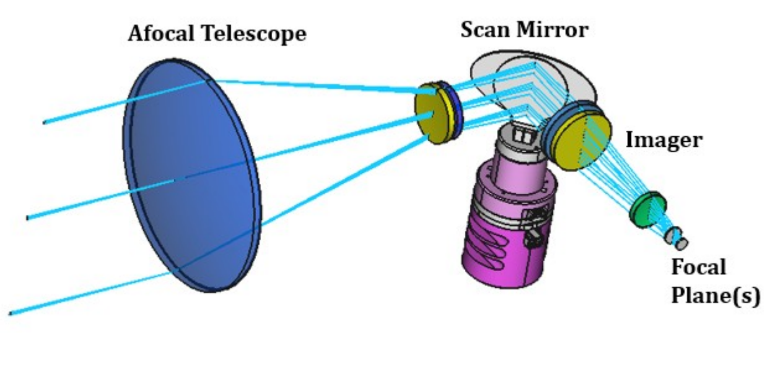

Figure 6-9: Opto-Mechanical Assembly Concept CAD Model

The next step for the Objective Optics subsystem is to determine a way to achieve the focal plane defocus. The turbulence ray trace model indicated that a total depth of -0.5 to +0.5 mm would be enough to cover the amount of aberrations caused by high turbulence. One obvious method would be to physically tilt the detector array relative to the optical axis. In such a case, the tilt angle of the mount and the spacing of the five linear columns would be the design variables. If the tilt angle is too steep, then the rays will eventually exceed Brewster's angle and will bounce away [27]. If the column spread is too wide, then the scanner will have to travel too far to allow adequate integration for a given number of horizontal pixels. For example, in order to create a drop depth of a total of 1 mm with a 30° tilt angle, the detector spacing for five column arrays would have to be = $[5 \cdot \sin(30°)]^{-1}$ = 0.40 mm, for a total focal plane width of 2.0 mm and a projected width to the optical axis of 1.73 mm. This is a relatively large value compared to the detector element size (0.028 mm), and it would consume a great deal of the linear scan region thereby reducing the number of pixels available for the horizontal field of view. A flat plate window can add defocus to an optical path without requiring any tilt angles relative to the optical axis. The optical path length change induced by a thin plate of thickness (thick) and index (n) is given by defocus = (thick)(n-1) ÷ (n) [134]. Assuming Germanium optical material with a high index n = 4, the following results in Table 6-B are obtained:

Table 6-B: Defocus Amounts vs. Germanium Plate Thickness

index (n)	thick (mm)	defocus
4	0	0.00
4	0.35	0.26
4	0.7	0.53
4	1.05	0.79
4	1.45	1.09

Optical prisms can be used to emulate a physical tilt, and will combine the effects of the tilted plate but with an added variance caused by the prism apex angle. In a sense, the prism approach might provide the best of both prior options, physical tilt combined with a change in path length from a flat plate. Figure 6-10 below shows an example 1 mm center-line thickness prism made from Germanium material (n = 4) and with a 5° physical tilt on the first surface relative to the optical axis. The prism does introduce non-symmetric aberrations, however, which can be mitigated by closing the gap between the prism exit face and the location of the detector array. This approach appears to be quite feasible in principle, however the detailed design is identified by the system engineer as a Gap Area which still needs to be explored in greater detail because it is likely that the prism design would need to be mounted integrally with the focal plane array package.

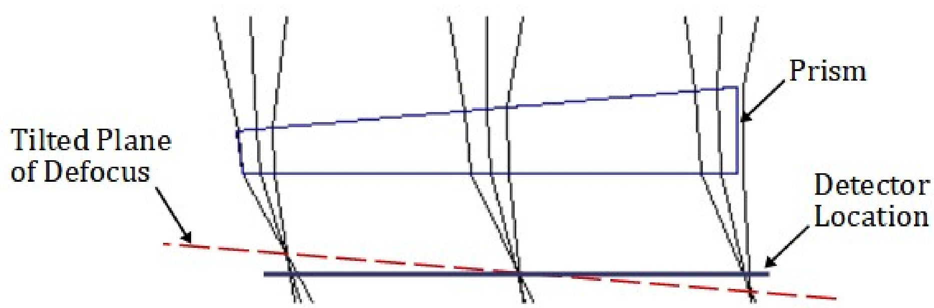

Figure 6-10: Prism Induced Defocus Example

6.2.5 Detector Subassembly.

The previous system modeling and Objective Optics analysis now permits a preliminary set of derived requirements for the infrared detector sub-assembly. A summary of such requirements is provided below:

Five parallel linear arrays, minimum pixels 167 × 5.

F#/3.0 incoming optical focus cone angle.

Noise less than 800 e^-

QE > 0.80 in the LWIR spectrum

Minimum well depth 12 million e^-

Integration time 7×10^{-5} sec

Filachev,et. al., [135] performed a market survey for infrared detectors in 2003, and listed several sources for linear scanned arrays with pixel row × column counts typically ranging from 240×4 up to 480×6, with pixel sizes ranging from 25 - 38 microns, integration times in the tens of microseconds regime, and quantum efficiencies up to QE =90% for detectors made from HgCdTe materials. These are produced by companies such as DRS, Raytheon, SOFRADIR, and AIM. Filachev also notes that these devices require cryogenic cooling, and so they are often sold as packages within a dewar assembly along with a split-cycle Stirling cooling system capable of 1 -2 Watts of thermal load [136][121][137] as shown in Figure 6-11. The bit level resolution of the typical raw video output signal from these detectors is usually in the range of 14 - 16 bits. Filachev does not provide the electron noise factors, but does cite NEΔT values which are in the range of 18 - 70 mK for factory-level test specifications. Well capacities, when stated, are in the range of 15 million e^-.

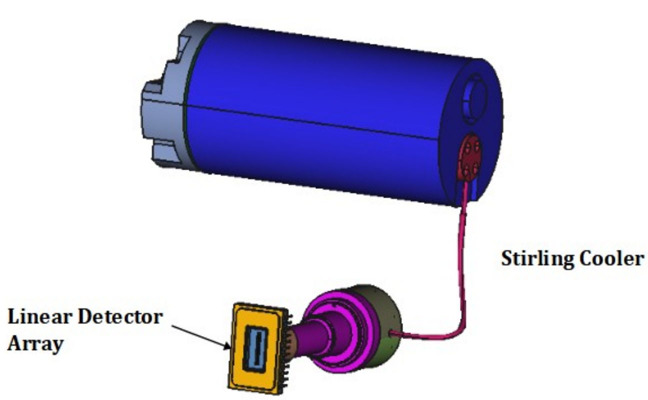

Figure 6-11: Visualization of Detector Array with Stirling Cooler Assembly (Dewar Removed)

6.3 Back-End Feasibility.

The back-end of the system consists of the electronics processor, display, and human eye/observer blocks. One of the major technical challenges for the back-end is to choose or develop processing algorithms which can operate within the "real time" requirements. It is thus important to first establish a working knowledge of computer processor throughput data rates as will be explained in the next section below.

6.3.1 Digital Processor.

Before examining the details of a modern digital video processor, it is beneficial to first establish a vocabulary based on the architecture of a digital computer in the general sense. A typical digital computer is comprised of three major blocks [138]. The first major block is the Central Processing Unit (CPU) which contains the timing clock(s), the arithmetic logic unit (ALU) which performs the numerical operations, and the temporary data register referred to as the accumulator. The second major block is the memory unit which stores the sequences of commands which instruct the CPU to perform its tasks. Each memory cell has a unique address. The final block is the input/output peripheral section (I/O), which in a conventional microcomputer system would include the keyboard, display, and printer. The conduits by which these blocks communicate data with each other are called *busses*. The common three bus architecture includes the *address bus* which points to the desired memory cell, the *control bus* which triggers the read & write activities, and the *data bus* which carries the data from memory into the CPU and its instruction register. Figure 6-12 below illustrates this basic architecture.

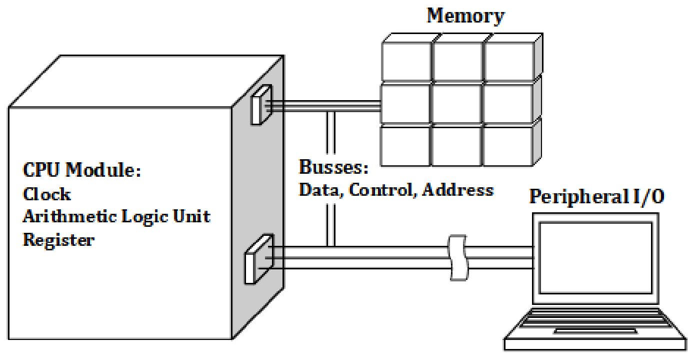

Figure 6-12: Basic Digital Computer Architecture

The operation of the computer involves a step-by step sequence of *fetch and execute* functions. The *machine cycle* of any computer consists of four basic steps as follows [29]:

1. Fetch data from the memory per the memory cell number stored in the count register.
2. Add 1 to the counter address value.
3. Execute the command.
4. Go back to step 1 and repeat.

In the case of digital video signal processing for this application, it is important that the computational device possesses adequate clock speeds, memory allocation, and bus transfer speeds in order to execute the software algorithms in real-time for the appropriate amount of incoming video data supplied by the detector. The video data size is fairly straightforward to calculate, with the number of pixels per frame multiplied by their bit-depth and the number frames per second. For example, a video signal from a 640 x 480 pixel array with 8-bit resolution at a 60 Hz frame rate would equate to $(640 \cdot 480 \cdot 8 \cdot 60) = 1.47 \times 10^8$ bits per second, or 147 Mbits/sec. But when performing video processing, it may be better to intercept the raw signal coming from the detector which may be 12 or 14 bits in depth at the source. Processing on the raw signal allows the processor more dynamic range in order to keep noise suppressed until the final step where an 8-bit depth image is sent to the display for human observation. In order to reduce the burden on the electronics hardware, it is common to use compression algorithms to reduce the data, typically by factors in the range of 10 - 15 depending on how much data loss is acceptable. These data management functions can be built into the processor hardware. To that end, the commercial market now provides a wide array of products which are specifically designed for video processing functions. Many of these are based on reduced instruction set computer (RISC) processor architectures which generally means each instruction performs one single operation [139]. A specific example of the Texas Instrument's "DaVinci" processor shall be expanded upon here by reviewing information contained within its published datasheet. The venerable TMS320DM6467T device is what is known as a "system on chip" (SOC) which integrates an Advanced RISC Machine (ARM) CPU running on a 500 MHz clock, along with a higher speed "C64X+" core running at 1 GHz clock rates with a set of six ALU's and sixty-four general purpose registers. The C64X+ core can perform 8000 million instructions per second (MIPS). The TMS320C64x+ digital signal processor chip is included in the package. This can perform up to four 16-bit multiply-accumulate (MAC) operations per clock cycle. Assuming the typical two-rounding operations per MAC, this is equivalent to eight floating operations per clock cycle. The on-chip cache includes both 256 Kbit and 640 Kbit assignable memory blocks. Additional external memory can be added as needed. The SOC also includes on-board interfaces and pinouts for peripheral device support such as USB and ethernet connections. To support software development activities, the SOC can be purchased with a developer kit such as the DM6467T Digital Video Evaluation Module. This kit includes a variety of interface peripherals and provides the ability to write and run programs on the SOC. Figure 6-13 below shows a TI DaVinci SOC integrated onto a printed circuit board (PCB) containing other components for power management and peripheral communications.

Figure 6-13: TI DaVinci SOC Integrated Into a Printed Circuit Board (PCB)

More powerful electronic processors than the aforementioned TI DaVinci have been used for higher resolution sensor systems. For example, the Xlinix Virtek-II Pro FPGA has been used for sensor video processing by way of its 15.625 MHz FPA readout and a full frame 14-bits for up to 1280 × 720 pixel formats at 60 Hz frame rates. The system used a 3.125 Gbit/sec serial link transmit to video processor FPGA [140]. The DaVinci and Virtex II are just samples of the many commercial products which are currently available. The propensity of these devices supports a conclusion that the hardware to run a processing block for algorithms based on the FREEPIX concept described earlier has acceptable risk in terms of availability and bandwidth capacity. Algorithms which rely on more intense computations, especially in which matrix division or Fourier Transforms are required, are at much greater risk of exceeding the real-time objective. In any case, until a breadboard system has actually been demonstrated with the desired software processing functions, there is always a risk that the end-to-end pipeline of data flow will have lag time greater than what is needed for a "real-time" requirement.

Benchmark test data is often performed by manufacturers to demonstrate the capability of their digital signal processor products. For example, Texas Instruments published a benchmark test for their DaVinci series TMS320C6678 SoC which features eight cores at a maximum 1.25 GHz clock, and is thus capable of 160 GFLOPS (giga or billion floating operations per second) [141]. The simple formula for number of FLOPS, if given the information, is the number of cores multiplied by the clock cycle frequency multiplied by the number of floating operations per clock cycle. Thus for the TMS320C6678, the calculation is as follows:

$$160 \text{ GFLOPS} = (1.25 \text{ GHz clock}) \times (8 \text{ cores}) \times (16 \text{ floating operations per core})$$

In a similar fashion, the previously discussed TMS320C64x+ DSP chip capability calculates to roughly 64 GFLOPS. The TMS320C6678 benchmark test ran a Fast Fourier Transform (FFT) algorithm based on the Takahashi algorithm which is known to be fairly efficient [142]. The clock speed was limited to 1GHz during the test, and various array sizes for the FFT were evaluated. The maximum size array was 1024,000 elements, corresponding to a two-dimensional detector array equivalent of about 1012×1012 pixels. With all eight cores running in parallel, the total process time was about 6.4 msec. This is a significant amount of time when compared to the real-time requirement for the whole system being limited to 33⅓ msec. The benchmark also tested the case for a smaller image input size of 32,000 elements, corresponding to a two-dimensional array of about 179×179 pixels. Again with all eight cores running, the process time was down to just under 0.2 msec, which is substantially less of a risk in terms of real-time operation. Figure 6-14 below shows the full results of the Texas Instruments benchmarking test.

FFT size	Performance of Computing Very Large FFT (time, ms) TMS320C6678-1 GHz, DDR-1330 MHz			
	1 core	2 cores	4 cores	8 cores
16K	0.473	0.261	0.159	0.131
32K	0.915	0.478	0.278	0.198
64K	1.857	0.922	0.508	0.315
128K	4.100	2.004	1.060	0.641
256K	8.795	4.323	2.228	1.186
512K	18.669	9.291	4.704	3.103
1024K	38.557	19.328	9.605	6.403

Figure 6-14: Results of Texas Instruments Benchmark Testing for FFT Operations

The processor feasibility analysis reveals that there are critical interactions between the software algorithms and their host processor. At this early stage it may not be practical to set a timing budget just yet, but certainly this issue should be tracked as a significant risk which will require system architecture coordination. Algorithms which rely on large-scale multiple FFT operations and inverse transforms (i.e., de-convolution) relying on matrix division are at much greater risk of violating the real-time requirement. And although parameter calculations involving clock rates, number of parallel cores, and number of mathematical operation per core are helpful, it is ultimately the benchmark testing which will be needed to prove the viability of any particular approach.

6.3.2 Display.

There are a wide variety of commercially available display devices, ranging from large area television viewers and computer monitors, down to cell phone-sized screens, and then micro-displays which usually include magnifying eyepieces. The minimum pixel format of 167 × 167 for this application fits well within a commercial Quarter Video Graphics Array (QVGA) standard of 240 × 320 pixel format units. A number of industrial monitor and display products with QVGA resolution can be evaluated for selection via distributor company websites such as Mouser or DigiKey. For one example of many, the DisplayTech DT028BTFT provides QVGA pixel resolution in a 2.8" screen size which is adequate for direct viewing with the human eye. Figure 6-15 shows the brochure graphics for this product.

Figure 6-15: Example of Commercially Available Medium-Format, Direct-View Display Module

Microdisplays such as the Kopin VGA 0.47" monochrome display may also be used, with the infrared image displayed either 1:1 in the central region, or expanded over a larger format area by simply doubling the pixels in each direction. Either way, the image would be too small for the human eye to obtain full resolution, and so it should be combined with an eyepiece lens such as the Edmund Optics catalog #87-311 MicroDisplay Eyepiece which has a 33 mm focal length. The eyepiece allows the user to set a comfortable focus, typically at or near infinity for more relaxed viewing. However, review of the cost data indicates that the micro-display approach would incur an order of magnitude more cost than a commercial supply direct view display, therefore the latter is recommended for this application. The system can be equipped with a video display output port if an external eyepiece module or head-mounted display accessory is desired later.

6.3.2.1 Biocular Eyepiece Option.

Another option is to use a *biocular lens* to magnify the direct-view display, either mounted directly to the sensor chassis or used as a remote display unit inside the host vehicle. A *biocular* display is generally defined as a display device which allows both eyes to view a single display source. An example is a microscope with two eyepieces, left and right, which both see through the same objective lens. A *biocular lens* is defined as a single lens assembly which provides a pupil large enough such that both left and right human eyes can peer through the lens assembly and view a single display source [27][117][143]. US Patent #10,520,720 [144] describes such a biocular lens optimized for use with a standard cell-phone sized display panel. Such a device could be included in the system as an attachment with particular use in the Alternative Scenario Use Case where the sensor is being viewed while "on the move". In this situation, vibrations can create a relative lateral displacement motion between the observer's eye and the display panel which will in turn cause the image of the panel formed on the eye's retina to shift position as well. This can be fatiguing over time. With the biocular lens attachment, the output of the display becomes collimated, and so as long as the lens optical aberrations are controlled over the pupil area, the human eye can now be laterally displaced within the pupil area without experiencing an image shift on the retina. This creates a much more comfortable viewing condition and dramatically minimizes the effects of vibration in a moving vehicle. Figure 6-16 below illustrates the biocular approach, which may be beneficial for the customer's alternate use case involving sensor operation while in a moving vehicle.

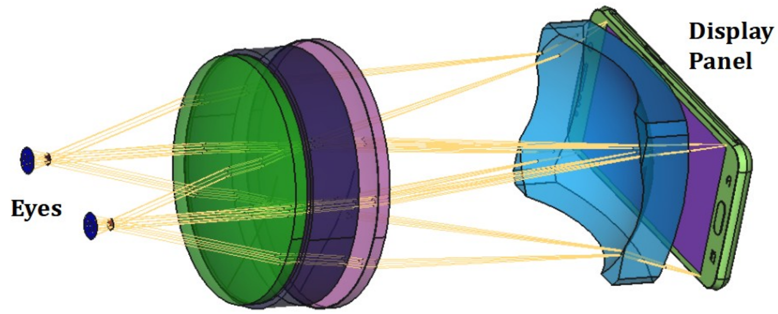

Figure 6-16: Biocular Display Eyepiece Attachment Option for Alternate Use Case

6.4 Feasibility Summary.

The preceding feasibility sections indicate that the critical components required for the system approach are within the current state-of-the-art capabilities. Where custom components such as imaging optics are required, the means of design and fabrication are well established. Commercially available components such as detector arrays, cryogenic cooler & dewar packages, video processor electronics and galvanometer scanners are already in existence. A physical visualization of the system can now be started by assembling the components within a computer automated design (CAD) software package. Figure 6-17 below shows the ensemble of components arranged such that critical placements are accurately represented. The objective optics, scanner, and detector array must be located with precision and in proper sequence, starting with the afocal magnifier front lens facing outward toward the scene. The electronics might be located on the "floor" of the package to facilitate heat transfer. The display unit shall be located on the back-side where the operator will be located.

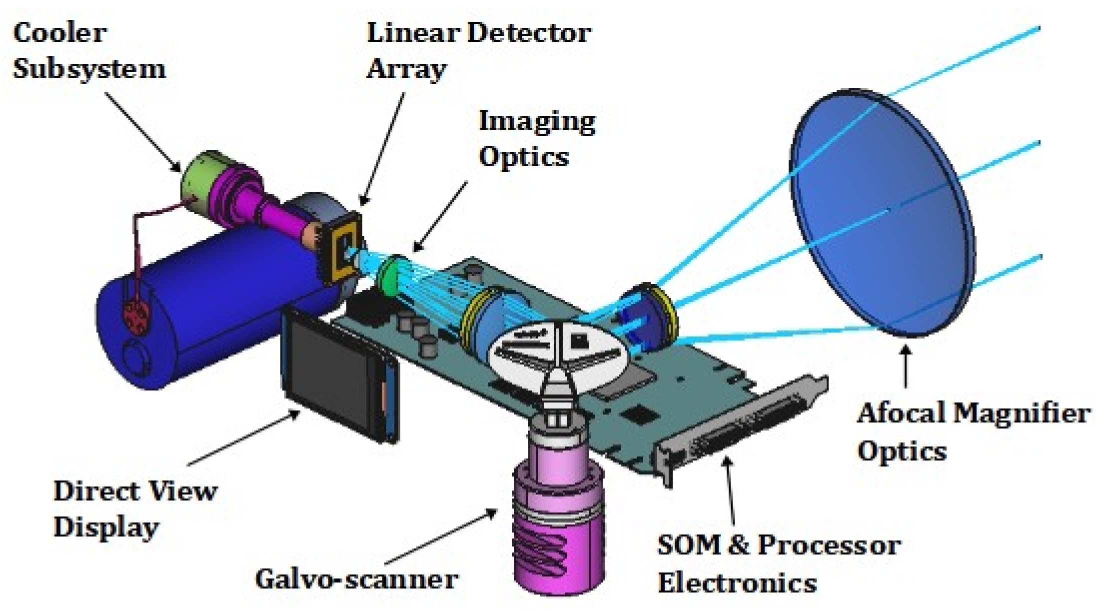

Figure 6-17: Visualization of Sensor Critical Components

The following Table 6-C summarizes the technical risks assessed during the feasibility study. The Maturity column indicates whether the design approach is within the known art. The Supply column indicates whether the subsystem components or software products are commercially available, with an associated implication of whether the costs will be reasonable. The symbol ⊙ represents a weak aspect of the approach, ⊚ represents a moderate capability is possible, and ⊛ corresponds to a strength and hence low risk of the particular aspect for the given approach. The final column indicates whether a Gap Area exists for the system, meaning that more focused development work on one or more system blocks will be required in order for the system to succeed.

Table 6-C: Component Feasibility Assessment

System Block	Maturity	Supply	Gap Area
Objective Optics	⊛ strong	⊚ moderate	Yes

Detector	⊛ strong	⊙ moderate	Yes
Processor (Hardware)	⊛ strong	⊛ strong	No
Processor (Software)	⊙ moderate	⊙ weak	Yes
Display	⊛ strong	⊛ strong	No

The Objective Optics and Detector Gap Areas are intertwined, as both are likely to be involved in the method by which optical defocus is introduced to the scanned columns of linear detector arrays. The previous section discussed means of adding optical elements such as micro-prisms directly on top of the detector pixel elements, but doing so would impact the mechanical package of the detector and its cryogenic dewar package. The software Gap Area refers to the development required to fully exploit the expanded information made available by the focal volume technique.

6.4.1 Discovery - New Use Case.

During the course of the feasibility review, it was discovered that the system architecture could also be applied to new Use Cases wherein the system performs the function of measurement of atmospheric turbulence, i.e., as a meteorological instrument. This is an excellent example of how the system engineering process is constantly re-evaluating and iterating the development cycle. The new Use Case is described as follows:

Context: Mr. Max Welhaus is a meteorologist assigned to monitor the magnitude of wind turbulence along the runway of an airport. The turbulence measurement apparatus is a permanent installation residing in a blockhouse at one end and to the side of the runway. At the other end of the runway is another structure which contains a patterned target such as a grid of circle shapes which passively have a high optical signal contrast against their background wall. An advantage of the system is that it is passive, meaning there is no need to address laser eye safety concerns. When the blockhouse window is opened, the sensor system has an unobstructed view of the distant target as shown in Figure 6.4.1-A below.

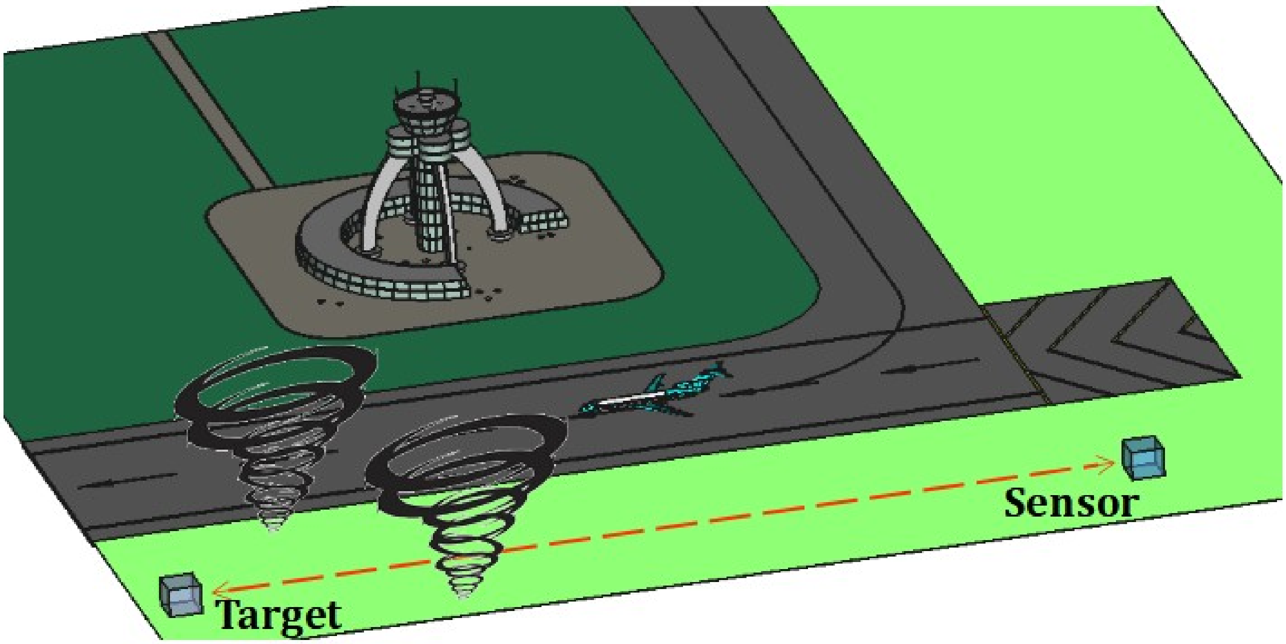

Figure 6.4.1-A: Meteorology Scenario in an Airport Setting

Use Scenario: Mr. Max Welhaus drives out to the blockhouse containing the turbulence sensor system. He enters the building and turns on the power supplies. Max then powers up the sensor system and starts the boot operations. The sensor system has already been installed and is pre-aligned to center on distant target structures at the other end of the runway. While the sensor is starting up, Max opens the blockhouse window so that the sensor can see the target structure. Max runs a calibration routine on the sensor to ensure it is functioning properly. Max then engages the sensor system to run in a continuous mode of operation. Data from the sensor is exported to a computer system which records the multi-focal image captures and performs calculations to generate time-stamped metrics such as C_n^2 for the magnitude of the wind turbulence as evidenced by the optical transformation of the known distant target.

Chapter 7 - Path Ahead

This section contains information for progressing into the next phase of the system engineering lifecycle, which is Engineering Development. The output of the feasibility analysis from the previous section enables an initial estimate of the physical architecture, which in turn has been captured in Capella as shown in Figure 7.1 below.

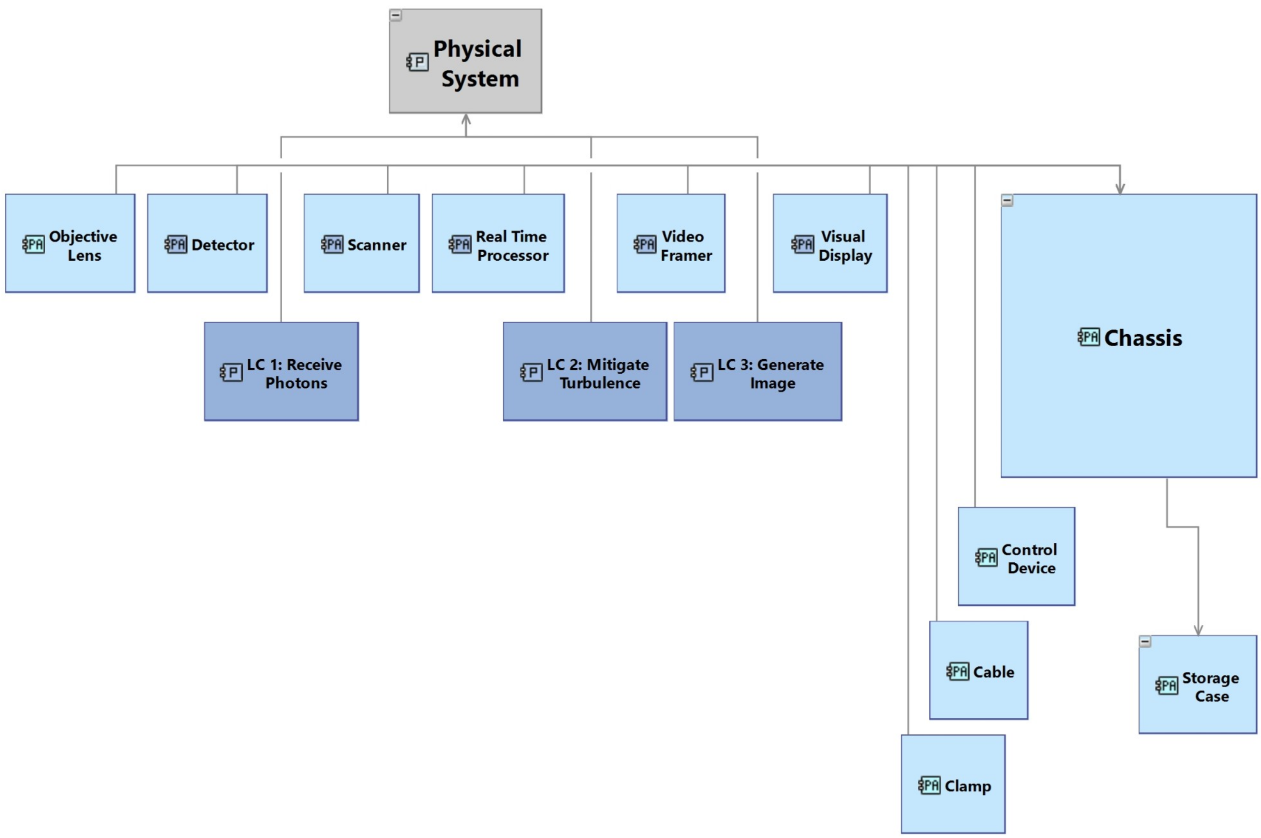

Figure 7-1: Initial Physical Architecture Diagram

Several work products need to be generated as inputs for the next phase to include critical system budgets, a development specification, and an initial risk analysis. In the context of the full set of system documentation, the shaded items in Figure 7.2 below indicate which artifacts are of primary interest in this early development phase:

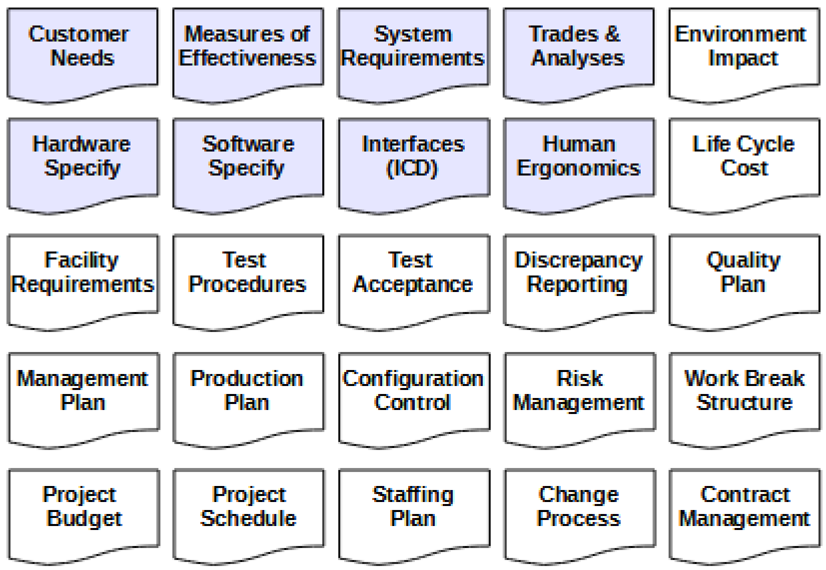

Figure 7.2: System Document & Data Artifacts

Documentation will evolve to cover many other aspects of the system as its design matures. User interfaces and manuals may include software guidelines for graphical user interface (GUI) and modes of operation to include status and maintenance. Environmental and safety concerns will be addressed. Management documents will establish plans and procedures for team conduct, financial allocations, and reporting, and so on.

7.1 Critical Engineering Budgets.

The conceptual design and subsequent feasibility studies provide enough information to establish the initial critical engineering estimates for size, weight, electrical power, and reliability. Along with those estimates, it is also time to derive additional requirements from other customer objectives such as single-person carry, host power supply, and the maintenance warranty period. The combination of the predicted parameters along with the derived requirement limitations established the initial critical engineering budgets.

7.1.1 Size.

The Use Case and customer objectives indicate that a one-person lift is going to be a frequent exercise. Since otherwise no specific limits on the sensor volume were given, the single-person lift requirements stated in MIL-STD-1472F, para. 5.9.11.3.3 appear to be reasonable [145]. The cited standard specifies a maximum lift volume of 18" x 18" x 12", where the 12" (305 mm) dimension is in the direction away from the lifter. The CAD model of the major system components is encased within the prescribed volume limit, and as can be seen in Figure 7-3 below, it appears that there is a good chance the final system design, imagining an outer chassis and other exterior features, will still be less than the maximum volume.

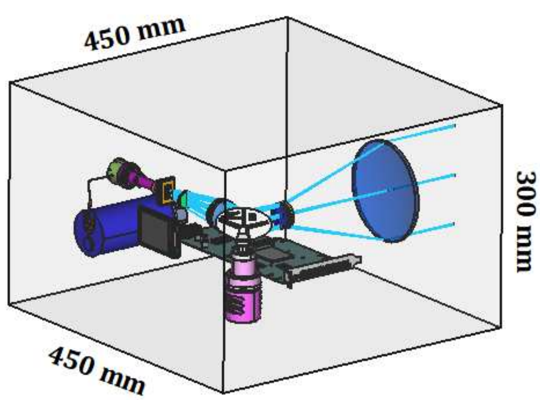

Figure 7-3: Core Components Fit Easily Within MIL-STD-1472 Volume Limit

7.1.2 Weight.

Similar to the volume analysis, the one-person lift user objective is the source of the system weight specification. Once again the military standards provide sound guidance, and this case the applicable specification is found in MIL-STD-1472F, para. 5.9.11.3.5, Table XVII, for handling function A, male and female population. The requirement for a one-person carry is thus 37 lbs. maximum item weight. The detailed system design does not yet exist, and so an initial budget estimate is obtained from internally generated CAD models and available commercial data for similar parts and components. Table 7-A below shows the results.

Table 7-A: Initial Weight Budget Shows Risk

Component	**Data Source**	**Weight (lbs)**
IR Optics	Optical ray-trace CAD model	1.25
Scanner Module	ThorLabs QS45X-AG	3.0
Cooler Package	Cobham LC1065 data sheet	2.5
Focal Plane Detector	ref. King, based on 4 lb IDECA	1.5
Display Panel	DisplayTech DT028BTFT	.25
Processor electronics	GeForce GTX 560	1.75
Inner bench structure	CAD estimate, aluminum	8.75
Outer chassis	Hoffman A16H1608AALP aluminum enclosure	14.0
Misc. parts & cables	Engineering Estimate	3.5
TOTAL		**36.5**

Unlike the volume analysis, the weight budget indicates a risk in meeting the 37 lbs total system specification. There is almost no margin in this initial estimate. The system weight is thus a candidate for specially focused weight reduction activities, and might require a special oversight team to monitor the design process closely. The "big hitters" for weight are the interior bench and outer chassis mechanical parts, and the challenge will be to reduce total mass while at the same time providing structural rigidity and vibration isolation. This effort may thus involve complex ribbing structures and possibly alternative materials such as magnesium metal.

7.1.3 Power.

The initial power budget can be estimated by using specifications from components that similar to what the new sensor will require. The ThorLabs QS45X-AG scanner runs on a 15V input power supply, but the current depends on how it is driven as well as the mass load on the motor shaft. The quiescent mode draws 220 mA, and the maximum RMS draw is rated at 4,000 mA. Using the relation between units of Watts = Volts × Amps, an initial estimate of 25 Watts appears to be a reasonable guess, slightly less than half of the maximum rated RMS power. The detector device focal plane assembly per the cooling analysis shall be assumed to have at least a 0.450 W electrical power draw. In the case of the cooler, it shall be assumed that the detector array heat load will be on the order of 450 mW total [121]. According to the data sheet provided for the Cobham LC1065, that will require a steady state draw of roughly 22 W at room temperature of 23 C as shown in Figure 7-4.

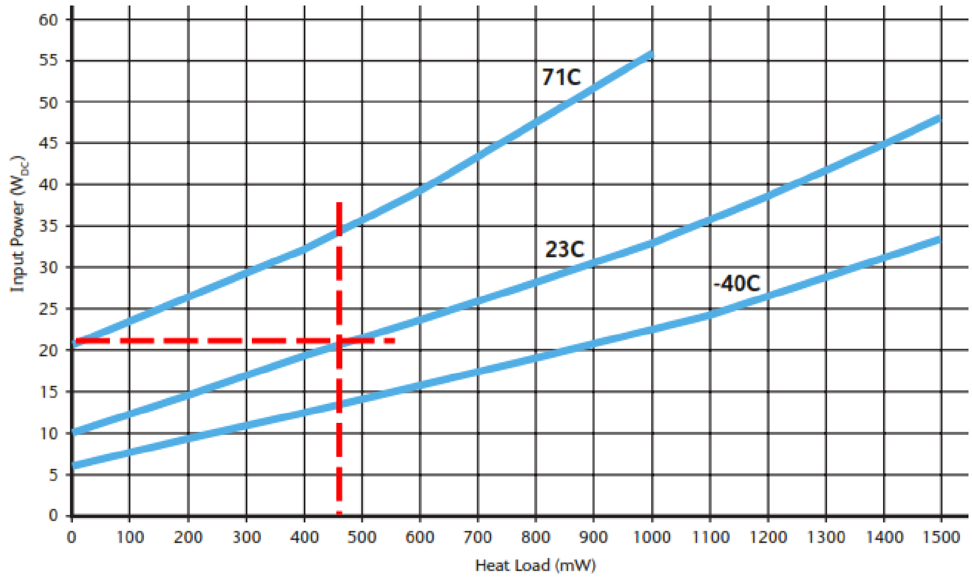

Figure 7-4: Cobham LC1065 Cooler Heat Load vs. Power Draw

The system electronics estimate is based on the commercial GeForce GTX 560 video processor, whose power consumption is rated at about 150 W. For the display, the Displaytech DT028BTFT liquid crystal display panel is referenced as an "as-like" component. Its operating current is reported to be 80 mA at an input voltage of 3V, resulting in a total power draw of 0.240 W. The sum of these component estimates provides a sound basis for the initial budget estimate. In some cases, it is also necessary to assign an upper range limit to account for issues such as exterior environmental temperatures or power-on surges. Both nominal and surge/limit cases are provided in the initial system power budget per Table 7-B below.

Table 7-B: Initial System Power Budget

Component	**Nominal (W)**	**Surge/Limit (W)**
Scanner	25.0	60.0
Detector	1.0	1.0
Cooler	35.0	70.0
Electronics	100.0	150.0

Display	0.50	0.50
TOTAL (W)	161.5	281.50

The customer objective for electrical power maximum was 24 volts at 60 amps, which equates to 1440 Watts of available power via the host platform. The system power budget is thus well under this value and is not considered a significant risk, even in the case of a temporary power surge. Nevertheless, a value-added exceptional use case might involve operation on battery power only. In order to keep this option available, a system goal to be under the current nominal wattage value shall be imposed.

7.1.4 Reliability.

The Reliability analysis is essential to support the product warranty which defines the responsibility of the original equipment manufacturer (OEM) in the event that the system for some reason fails to operate properly. The procedures for establishing reliability estimates are explained thoroughly in MIL-STD-781, published by the US Department of Defense [146]. Revision C of this document is particularly useful because it contains details of the mathematics involved. The engineering reliability budget begins by first collecting the Mean Time Between Failure (MTBF) of the subsystems and components. MTBF data given in units of hours, or its reciprocal failure rate per million hours (Λ), is often available from the component manufacturers. The conversion between the two, when MTBF is given in hours, is as follows:

$$\Lambda = (\mathrm{MTBF})^{-1}$$

MIL-HDBK-217 [147] also contains sets of data for common electronics components . For example, if a component has a published MTBF value of 250,000 hours then the failure rate is $\Lambda = 4.0 \times 10^{-6}$

failures per hour of operation. The reliability (REL), or "probability of survival" for a given time interval (t), is then an exponential function given by the following equation:

$$REL(t) = \exp(-\Lambda t)$$

For example, the probability of the system functioning for the time period (t) of one system-level MBTF, i.e., where $t = MTBF = \Lambda^{-1}$, solves as REL = exp(-1) = 0.3678, or 36.78%.

MIL-HDBK-338B [148] provides a basic approach for reliability of simple system structures, beginning with serial component inputs. It should be noted that statistical benefits can be realized if components have redundancy, meaning that the system will continue to operate if only one of the two or more parallel items survive, but that situation is not relevant at the highest system level. For coolers after about 1983, it was recognized that cooler lifetime was dominated not by random failures, but rather by component wear-out and contamination which are both functions of operating time. In such cases, the lifetime is a direct function of usage time and therefore the failures are not random. Because of this, a switch in the industry was made in to use Mean Time To Failure (MTTF) instead of MTBF [149]. In this case, the Cobham LC1605 cooler MTTF is advertised to exceed 20,000 hours. However, it is still possible to derive MTBF values for modern cooler systems as demonstrated by Estrada & Fan who show MTBF values for 1.0 Watt class coolers being over 143,000 hours [150]. Thus the estimate used in this example is conservative. For the sensor system, the following Table 7-C shows an initial high-level reliability budget:

Table 7-C: Initial Reliability Budget

Item	**MTBF**	**$\Lambda = (MTBF)^{-1}$**
Afocal Optic	200,000	5.00E-06

Image Optic	250,000	4.00E-06
Galvo-scan	100,000	1.00E-05
Detector	60,000	1.67E-05
Cryo-Cooler	40,000	2.50E-05
SOM/elect	400,000	2.50E-06
Display	600,000	1.67E-06

As the system design evolves with more detailed component information, each major item in the above breakdown can be in turn be broken into a summation of failure rates for the lower levels of components. With all the items used in series with no redundancy, the system-level failure rate is the sum of the individual item rates, i.e.,

$$\Lambda_{sys} = \sum_n \Lambda_n$$

For the above example, $\Lambda_{sys} = 6.48 \times 10^{-5}$ becomes the input value to feed the reliability (REL) calculation for a range of time values (t). Since the function is exponential, it is helpful to show most of curve on a log scale ranging from zero to one million hours per the following Figure 7-5:

REL(t) = exp(-Λt)	
Λ_{sys}	6.48E-005
t	R(t)
0	1.0000
10	0.9994
100	0.9935
300	0.9807
1,000	0.9372
5,000	0.7231
10,000	0.5229
30,000	0.1430
100,000	0.0015
300,000	0.0000
1,000,000	0.0000
2190	0.8676

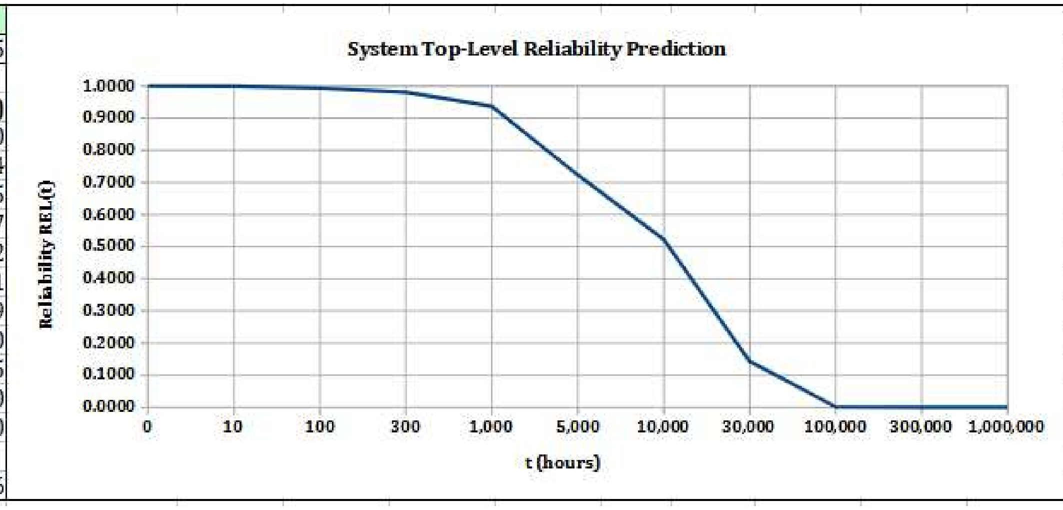

Figure 7-5: Example Reliability Prediction

The interpretation of the reliability data and graph is that 93.7% of the units are expected to operate without fail for at least 1,000 hours. After 5,000 hours of usage, it is expected that roughly 72.3% of the system units will still be fully operational, and so on. In terms of warranty coverage, it can helpful to estimate a value of (t) corresponding to an expected usage for the period of coverage. If the warranty is, for example, two years with an estimated duty cycle of 3 hours use per day, 365 days per year, the total average hours per warranty period is thus 2190. Based on the above initial system estimate, it is expected that 86.8% of the system units will be functioning properly at the end of the warranty period. In the beginning of the engineering design process, it is likely that a great deal of component details will not yet be available, but it is still worthwhile to start with estimates at the highest level in order to set budgetary targets. Then as the data comes in, the reliability budget analysis can be updated, re-balanced, and expanded for greater accuracy.

7.2 Development Specification Cross Matrix.

The system development specification describes the various properties and operational functions of the system to be engineered [19], and is a primary output of the concept development and feasibility study efforts. Technical specifications are distinct from other types of requirements such as delivery schedules, price negotiations, shipping requirements, legal arrangements, test and acceptance events, and other items which are normally captured within a Statement of Work (SOW) [151]. The specifications thus describe the deliverable item which may be referenced within a SOW. In the early stages of development, the specification tends to contain mostly high-level system aspects. As the design matures through more advanced stages, the specification will tend to branch downward to provide more details for the subsystems and components. It is important at any stage of development that each specification statement possesses several characteristics [18], of which the most critical aspects are condensed as follows:

- *Singularity*. Each specification statement must concisely describe a singular or "atomic" property, and must never combine separable requirements. The principle of singularity is essential for configuration change management.
- *Traceable*. The specification source must be derived from an original performance objective or some other type of constraint, and then the connection may flow throughout the system detailed design elements.
- *Verifiable*. The specification must be able to be verified by some means producing objective evidence, often characterized as either an analysis, demonstration, inspection, or test.

A cross-matrix is an efficient way to show how system specifications at all levels can be traced back to the original customer performance objectives. The Table 7-D below shows a matrix which shows traceability of development specifications back to one or more of the original customer objectives. Specifications for environmental effects and human ergonomics and safety have been added to round out the listing. During advanced development, details of each subsystem and component will result in additional specifications and detailed tolerance ranges which may be added to this initial listing [19]. Once the design matures, additional cross-matrix columns can be added to group together common quality verification such as the First Article Test, Operational Test, and production Acceptance Test.

Table 7-D: Development Specification Traceability Matrix

#	**Requirement**	**Value**	**Customer Objective**						
			1	*2*	*3*	*4*	*5*	*6*	*7*
	RANGE MODEL & TURBULENCE PARAMETERS								
1.1	Target Identification Range Minimum	2.5 km	x	x	x				
1.2	Target critical dimension	2.3 meter		x	x		x		
1.3	Spectral band, lower limit	7.5 micron			x		x		
1.4	Spectral band, upper limit	12.0 micron			x		x		
1.5	Target-to-background temperature difference	1.25 K		x	x		x		
1.6	Average Background Temperature	300 K		x	x		x		
1.7	Atmos. Absorption coefficient (70% per km)	0.356		x	x		x		
1.8	Atmospheric Index Structure (low turbulence)	1×10^{-15}					x		
1.9	Atmospheric Index Structure (strong turb)	5×10^{-12}					x		
1.10	Objective Lens focal length	400 mm		x					
1.11	Objective Lens F#	3		x					
1.12	Objective Lens total transmission	0.70		x					
1.13	Objective Lens Maximum Aberration	0.25λ		x					
1.14	Detector Element Pitch (square sides)	0.028 mm		x					
1.15	Detector well capacity maximum	12M		x	x				
1.16	Detector Quantum Efficiency	0.80		x	x				
1.17	Detector integration time	7×10^{-5} sec		x	x	x			
1.18	Detector & Electronics total RMS noise	1200 e^-		x	x				
1.19	Stabilization/jitter RMS	0.005 mrad		x	x		x	x	
1.20	Maximum Display Blur RMS	0.145 mrad	x	x	x				
1.21	System Magnification	9.5X	x	x	x				
1.22	Johnson Criteria for Identification	6.4 cycles	x	x	x		x		
1.23	Focal Capture Defocus Steps (total)	5 steps		x	x				
1.24	Focal Capture Defocus Step Increment	±0.30 mm		x	x				

1.25	Focal Capture Total Time Period Maximum	Single Frame		x	x	x			
1.26	Frame Rate	60 Hz	x	x	x	x			
1.27	Total Video Lag Time Maximum	16 msec	x	x	x	x			
	PHYSICAL SPECIFICATIONS								
2.1	Weight/Mass	35.25 lbs						x	
2.2	Size/Volume	18" × 18" × 12"						x	
2.3	Electrical Power Maximum	24v, 60 amp							x
2.4	Reliability	90% at 1000 hrs			x			x	
2.5	Maintenance Kit	(shall be developed)	x						
2.6	Electrical Interfaces	ref. Interface Control Document (ICD)		x					
2.7	Mechanical Interfaces	ref. Interface Control Document (ICD)							
	ENVIRONMENTAL SPECIFICATIONS								
3.1	Operating Temperature Range	-40 to +71 C		x	x				
3.2	Humidity	MIL-STD-810F, 507.4		x	x				
3.3	Cargo Bounce	MIL-STD-810F, 514.5		x	x				
3.4	Vibration (Composite Wheeled Vehicle)	MIL-STD-810F, 514.5							
3.5	Sand & Dust	MIL-STD-810F, 510.4		x	x				
3.6	Solar Radiation	MIL-STD-810F, 505.4		x	x				
	SAFETY								
4.1	Maximum Surface Touch Temperature	MIL-STD-1472F, para 5.13.4.6	x						
4.2	Incorrect Electrical Connections	Unique Keyed	x						
4.3	Electrical Hazards	MIL-STD-1472F, section 5.13.7.1	x						
4.4	Fault Indication	Built-in Test (BIT) w/ flags	x						

7.3 Risk Management.

The term "risk" incorporates the notion of an uncertainty whether a negative outcome will result [76]. The degree of uncertainty is often characterized by a probability of occurrence, and the magnitude of the negative outcome can be parameterized via a severity rating. Risks can occur in all phases of a product lifecycle, and may include topic areas such as technical, personnel, cost, supply chain, hazards, legal, ecological, etc. In many instances, certain actions may be taken to mitigate the risks. In other instances, there may not be any possible actions and the decision is made to carry on regardless.

The process of risk management begins with identifying the risk areas. A formal risk statement is a method to capture the essence of the risk and its potential impacts.   For example, the previousl feasibility analysis indicated some risk in the overall system weight budget. The formal risk statement may thus be as follows:

> *There is a risk that* .... the system will be several pounds over the one-person carry limit.
>
> *The risk is caused by* .... accumulation of item masses interior to the sensor which were not originally included in the budget allowances, which itself had little margin.
>
> *The direct impact of the risk is* .... the system will not be transportable by the entire 95-percentile human population, and personal injury could result if a lift were so attempted. There may also be minor impacts on shipping and transportation costs.
>
> *The recovery action would be* .... to re-design the system with lower mass chassis, cables, and components. This would involve significant non-recurring cost and schedule, and possibly additional recurring costs in the unit price.
>
> *The impact on the program is* ... if unsolved, the customer may reject the system and the company will need to decide whether to pursue a recovery action. Engineering management shall therefore include weight as a key risk parameter during advanced development stages, flow requirements down to the component level as the design matures, and provide regular budget updates.

One method of organizing risks is illustrated by Figure 7-6 below which is extracted from MIL-STD-

882 [152] which specifically address safety risks, but can also be used broadly as a template for all types of risks. This rating scheme includes the popular "severity" and "probability" axes, along with adjectival descriptions. It is somewhat unique in that it also includes an "eliminated" category which is useful for tracking progress and maintaining history over time.

Risk Assessment Matrix		Severity			
		(1) Catastropic	(2) Critical	(3) Marginal	(4) Negligible
Probability	(A) Frequent	High	High	Serious	Medium
	(B) Probable	High	High	Serious	Medium
	(C) Occasional	High	Serious	Medium	Low
	(D) Remote	Serious	Medium	Medium	Low
	(E) Improbable	Medium	Medium	Medium	Low
	(F) Eliminated	Eliminated			

Figure 7-6: Risk Assessment Format Per MIL-STD-882

Each risk element can thus be rated against the assessment graphic, and a suggested set of mitigation actions may also be proposed for consideration in later program planning. It may also be helpful to track the risk status over time. An example risk tracker format is demonstrated below in Table 7-E, which includes a brief topic summary of the risk element, a mitigation action, and then status over time for both probability and severity, to include the original assessment, the estimates based on the last report, and the new estimates for the current date of report. In this way, the progress of the design team can be captured and easily shared with the group. Color coding can be used per the scheme in MIL-STD-882 to help quickly draw attention to critical risk areas.

Table 7-E: Risk Tracking Table

Risk Tracker			**Orig**		**Last**		**Now**	
#	**Risk Area:**	**Mitigation**	**P**	**S**	**P**	**S**	**P**	**S**
1	Missed Requirements	Conduct system reqts review (SRR), involve stakeholders in config management process.	C	2	-	-	-	-
2	Exceed size, weight, power, cost, schedule budgets	Routine budget reviews with design team.	B	2	-	-	-	-
3	Role & Responsibility confusion	Kickoff meeting with task leads & action	C	3	-	-	-	-

		assignments.						
4	Long Lead Item Procurement	Early release purchase orders.	C	2	-	-	-	-
5	Insufficiently skilled staff	Define team roster w/ personnel qualifications.	E	3	-	-	-	-

7.4 Quality Planning.

It is helpful to outline the Quality Plan in the early stages of system development in order to design the system for efficiency during verification and validation operations. As shown in Figure 7.7 below, the product life begins with its requirements and then proceeds through the design phase with procedural steps such as a Preliminary Design Review followed by a Critical Design Review to verify that the design work is done properly. Upon design confirmation, a lot of 1st Article units may then be built and submitted for an Operational Test which validates that the system performs the functions required by the customer. Feedback from the Operational Test may be documented in Failed Item Analysis Reports (FIAR), and may thus modify the requirements. Once the system has been validated, the quality program then emphasizes the ability to produce the system repeatably. This process will involve an Initial Lot Build (ILB) of units which will go through a series of tests to ensure that the work instructions, tooling, and equipment are able to engage in a reliable production operation. Failures at this stage will be captured during the Failure Reporting, Analysis, and Corrective Action System (FRACAS) process. Once the ILB units have resolved all issues as documented by the FRACAS, a Physical Configuration Audit (PCA) of the Technical Data Package (TDP) is performed to identify the final system configuration and lock it down. After the PCA, no product changes to the TDP are allowed unless authorized by all major stakeholders. The PCA is the last gate before authorization for full production. The production team will define acceptance tests (AT) to be conducted upon 100% of the units produced, as well as occasional Conformance Tests (CT) which take samples from the production line and exposes them to longer duration types of testing. The FRACAS process will track failures detected during AT & CT, and if necessary, will provide feedback for corrective and preventive actions. Any required changes to the system design will be formally controlled via Engineering Change Requests (ECR) followed by an approved Engineering Change Order (ECO) and an adjusted TDP if necessary. Production units which pass AT & CT are then shipped to the customers in the field. If a failure occurs in the field, then a Return Material Authorization (RMA) process is invoked which will identify the nature and cause of the failure, and will thereafter follow the Warranty terms if they apply.

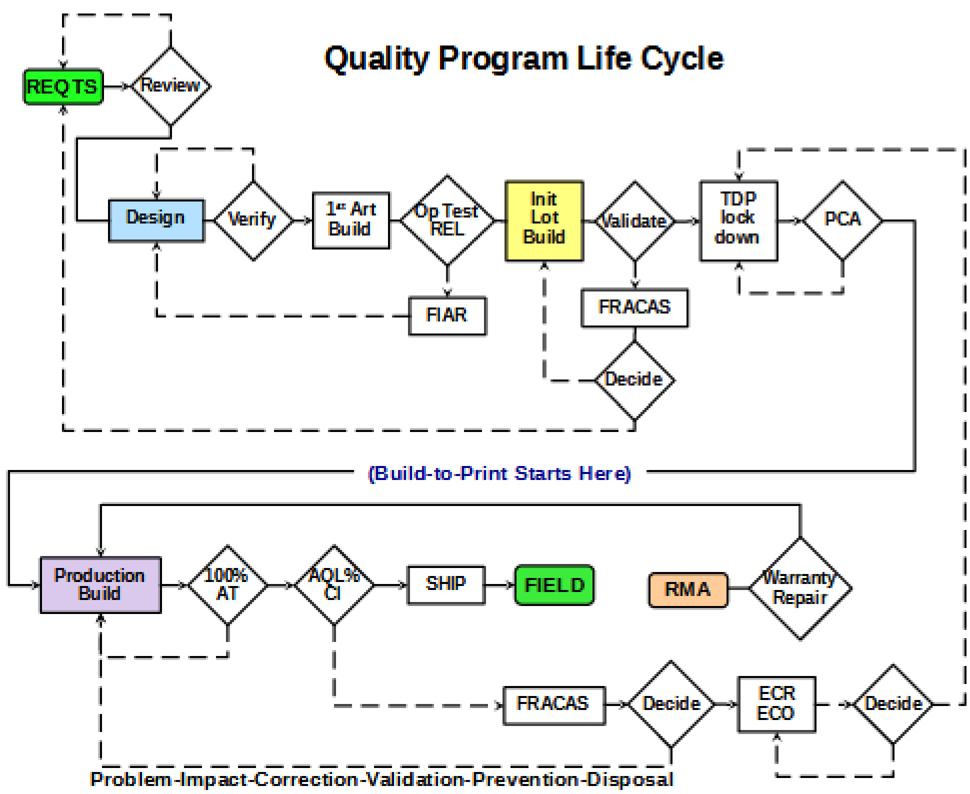

Figure 7.7: Program Quality Life-cycle

7.4.1 Special Test Equipment.

Each type of system may have its own unique needs for test equipment. In the case of an electro-optical sensor it is often desired to have an integrated optical test station such as shown in Figure 7.8 below. The test station is comprised of a luminous target sub-assembly which emits light into a collimator mirror to simulate the target projection from an infinite optical distance. A flat fold mirror attached to a rotary stage is used to change the incident angle of view as the light then enters the Unit Under Test (UUT). The test station can be automated via computer control, which will direct actions to the light source and the fold mirror stage and at the same time collect video output data from the UUT. The computer may then perform data processing and produce test reports.

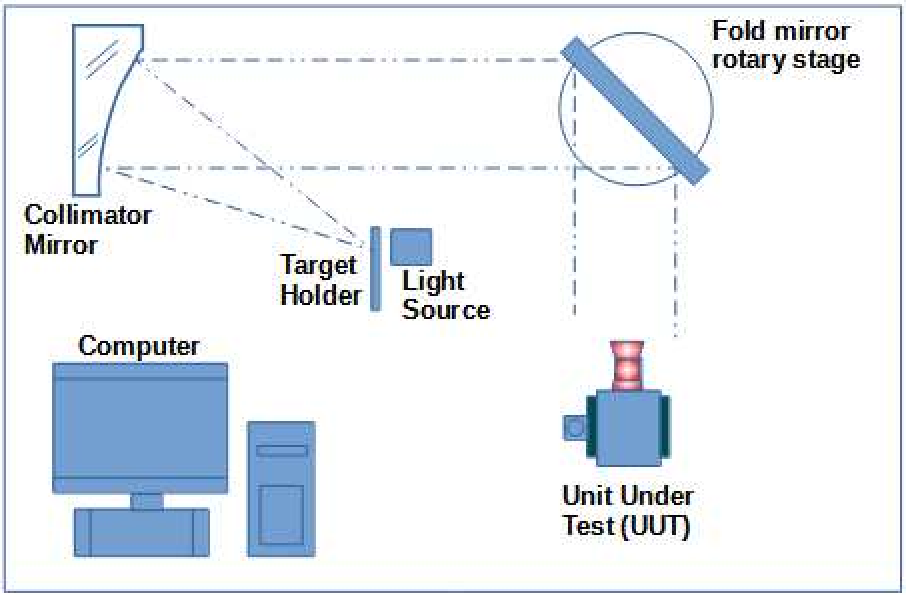

Figure 7.8: Basic Electro-Optical Test Apparatus

It is important to consider system design features which facilitate the use of test equipment. For example, in order to minimize alignment time, it may be helpful if the system includes a reference flat mirror near the front aperture. This mirror will retro-reflect the collimated light beam back toward the target source, and so can be used as a quick way to set the zero-degree position for the field of view angle.

Chapter 8 - Conclusion

This work has achieved the objective of demonstrating the early phase of system development for a novel imaging sensor which mitigates the effects of horizontal path atmospheric turbulence. A system concept has been thoroughly analyzed, new analysis tools have been developed, and a feasible system concept has been presented. Several key factors contribute the to comprehension of the problem per the following:

- The system engineering process was summarized and used as a planning guide, parallel with the US Government's Technology Readiness Level (TRL) scale, to direct the workflow and define critical artifacts which become inputs to successive lifecycle phases.
- System operational analyses were conducted in order to elicit customer and stakeholder objectives and then derive engineering requirements. These analyses included the development of a Use Case, an IDEF0 functional diagram, and a System Based Model using Capella software.
- A survey of existing turbulence mitigation techniques shows that many methods are possible, some of which require specific hardware apparatus and all of which require digital image processing. However, no approach to date has achieved theoretical limits in the case of terrestrial path, horizontal turbulence mitigation in real time.
- A significant effort was applied to develop a mathematical performance model. Real imaging systems are characterized by linear & non-linear behaviors, both of which must be considered. Monte Carlo statistical techniques provide initial tolerance ranges for parameters, and can also be used to help optimize the overall design.
- Current sensor model state-of-the-art usually involves a linear (MTF) prediction of turbulence effects. While this is accurate enough for performance prediction, it provides little insight into the nature of the problem. Disclosed herein is a novel means of performing optical ray-trace modeling of turbulence effects, accounting for both the atmosphere and the

objective optics of the system in the same model.

- The ray-trace model yielded breakthrough insight into the nature of turbulence, and intuitively lead towards a particular solution which addresses the presence of multiple isoplanatic patches within the field of view. It also provided a means to simulate imagery examples.
- As a result of the model analysis and intuition gained from the ray-trace technique, a novel system architecture for an infrared sensor which enhances the probability of successful imaging through turbulence is described. A key aspect of this system approach is an opto-mechanical architecture which captures multiple planes of defocus, followed by the proposed FREEPIX method of extracting the highest contrast pixel values among those several planes of image defocus in real time.
- The feasibility of the proposed solution is supported by analysis of commercially available components, optical and mechanical design approaches, electronic processor capability analysis, and a cross-walk between the customer goals and the system requirements.

The path ahead for the Engineering Development phase is facilitated by generating additional artifacts for input to this next phase, including critical engineering budgets, a development specification, and an initial risk assessment. The work to date culminates with ample justification and a set of solid artifacts to continue the effort into the Engineering Development phase.

References

1: Chan, S., *Tilt-Then-Blur or Blur-Then-Tilt? Clarifying the Atmospheric Turbulence Model*, IEEE Signal Processing Letters, Vol. 29, 2022.

2: VanHelden, A., *The Invention of the Telescope*, Transactions of The American Philosophical Society, Vol. 64, Part 4, 1977.

3: Bate, J., The Mysteries of Nature and Art, (unknown publisher), London, 1654.

4: Robinson, D., From Peep Show to Palace: The Birth of American Film, Columbia University Press, New York, 1996.

5: Rash, E., et. al., Helmet-Mounted Displays: Sensation, Perception and Cognition Issues, US Army Aeromedical Research Laboratory, Alabama, USA, 2009.

6: Hecht, S., Shlaer, S., *Intermittent Stimulation by Light : v. the Relation Between Intensity and Critical Frequency for Different Parts of the Spectrum*, Journal of General Physiology, Vol. 19, 1936.

7: Whitaker, J., Benson, K., Standard Handbook of Video and Television Engineering, McGraw-Hill, New York, 2000.

8: Roggeman, M., Welsh, B., Imaging Through Turbulence, CRC Press, FL, 1996.

9: Velluet, M. T., et. al., *Data collection and preliminary results on turbulence characterisation and mitigation techniques*, Proceedings of SPIE, Vol. 11159, Technology & Applications XVI, 2019.

10: Espinola, R., Leonard, K., Thompson, R., Tofsted, D., D'Arcy, S., *DARPA Super Resolution Vision System (SRVS) robust turbulence data collection and analysis*, Proc. SPIE, Vol. 9071, Infrared Imaging Systems: Design, Analysis, Modeling, and Testing XXV, 2014.

11: Schutte, K., van Eekeren, A., Dijk, J., Schwering, P., van Iersel,M., Doelman N., *An overview of turbulence compensation*, Procedings of SPIE, Vol. 8542, Electro-Optical Remote Sensing, Photonic Technologies, and Applications VI, 2012.

12: Gronau, Y., *Limitations of Adaptive Optics for Imaging at Horizontal Paths*, Proceedings of SPIE, Vol. 1968, Atmospherics Propagation and Remote Sensing II, 1993.

13: Aubailly, M., Vorontsov, M., Carhart, G., Valley, M., *Automated video enhancement from a stream of atmospherically-distorted images: the lucky-region fusion approach*, Proc. SPIE, Vol. 7463, Atmospheric Optics: Models, Measurements, and Target-in-the-Loop Propagation III, 2009.

14: Droege, D., Hardie, R., Allen, B., Dapore, A., Blevins, J., *A real-time atmospheric turbulence mitigation and superresolution solution for infrared imaging systems*, Proc. SPIE, Vol. 8355, Infrared Imaging Systems: Design, Analysis, Modeling, and Testing XXIII, 2012.

15: Kossiakoff, A., Sweet, W., Seymour, S., Biemer, S., Systems Engineering Principles and Practice, John Wiley & Sons, Inc., Hoboken, NJ, 2011.

16: International Council on Systems Engineering (INCOSE), Systems Engineering Handbook, Wiley & Sons, New Jersey, 2015.

17: , DoD 5000.2-R: MANDATORY PROCEDURES FOR MAJOR DEFENSE ACQUISITION PROGRAMS (MDAPS) AND MAJOR AUTOMATED INFORMATION SYSTEM (MAIS) ACQUISITION PROGRAMS, 2001, https://apps.dtic.mil/sti/citations/ADA396213.

18: Pohl, K., Requirements Engineering Fundamentals, Principles, and Techniques, Springer-Berlag, Berlin-Heidelderg, 2010.

19: Blanchard, P., Burnett, J., Erry, G., Greenaway, A., Harrison, P., Harvey, A., Woods, S., *Optical propagation through low-level turbulence*, Proc. SPIE, Vol. 3494, Atmospheric Propagation, Adaptive Systems, and Lidar Techniques for Remote Sensing II, 1998.

20: Baron, C., Grenier, L., Ostapenko, V., Xue R., *Using the ARCADIA/Capella Systems Engineering Method andTool to Design Manufacturing Systems—Case Study andIndustrial Feedback*, MDPI, Systems, Vol 2023, 11, 429, 2023.

21: Vollmerhausen, R., Reago, D., Driggers, R., Analysis and Evaluation of Sampled Imaging Systems, SPIE Press, Bellingham, WA, 2010.

22: Lloyd, J. M., Thermal Imaging Systems, Plenum Press, New York, 1975.

23: Gaskill, J., Linear Systems, Fourier Transforms, and Optics, Wiley & Sons, New York, 1978.

24: Driggers, R., Cox, P., Edwards, T., Introduction to Infrared and Electro-Optical Sytems, Artech House, Norwood, MA, 1999.

25: Jensen, N., Optical and Photographic Reconaissance Systems, John Wiley & Sons, Inc., New York, 1968.

26: Oppenheim, A., Shafer, R., Discrete Time Signal Processing, Prentice Hall, , 1999.

27: Smith, W., Modern Optical Engineering, McGraw Hill, New York, 1966.

28: O'Neill, E. L., Introduction to Statistical Optics, Addison-Wesley, Reading, MA, 1963.

29: Castleman, K., Digital Image Processing, Prentice-Hall, New Jersey, 1996.

30: Scott, R., *The Practical Applications of Modulation Transfer Functions*, Optical Engineering, Vol. 2, No. 4, 1964.

31: Singh, V., 1942 Dodge Fargo CAD Model, , https://grabcad.com/library/dodge-fargo-1942.

32: Barnes, Electro-Optics Handbook, Radio Corp. of America (RCA), Harrison, NJ, 1968.

33: Planck, M., *Ueber das Gesetz der Energieverteilung im Normalspectrum*, Annalen der Physik, pp. 553-563, March, 1901.

34: Planck, M., *On the Theory of the Energy Distribution Law of the Normal Spectrum*, Verhandlungenden Deutsche Physikalische Gesellshaft, Vol. 2, 237, December, 1900.

35: Dereniak, E., Boreman, G., Infrared Detectors and Systems, Wiley & Sons, New York, 1996.

36: Wolfe, et. al., Handbook of Military Infrared Technology, Office of Naval Research, Washington, D. C., 1965.

37: D'Agostino, J., *The Space Thermal Signature Model: Principles And Applications*, Proc. SPIE, Vol. 0781, Infrared Image Processing andEnhancement, 1987.

38: Jones, F. E., *The Refractivity of Air*, National Bureau of Standards, , Journal of Research, Vol. 86, No 1, 1981.

39: Gemini Observatory, Atmospheric Transmission, 1999, http://www.gemini.edu/sciops/ObsProcess/obsConstraints/ocTransSpectra.html

40: Hopkins, et. al., Military Standardization Handbook 141: Optical Design, Defense Supply Agency, Washington DC, 1962.

41: Beer, A., *Bestimmung der Absorption des rothen Lichts in farbigen Flüssigkeiten*, Annalen der Physik und Chemie, Leipzig, 1852.

42: Kolmorgorov, A. N., *The Local Structure of Turbulence in Incompressible Viscous Fluid for Very Large Reynolds' Numbers*, Doklady Akademiia Nauk SSSR, Vol. 30, ppg 299-303, 1941.

43: Tatarskii, V. I., The Effects of Turbulent Atmosphere on Wave Propagation, U.S. Dept. of Commerce/NOAA, Washington DC, TT 68-50464, 1971.

44: Wang, T. I., Ochs, G.R., Clifford, S. F., *Saturation-resistant optical scintillometer to measure* Cn^2, J.

Opt. Soc. America, 68 (3), 1978.

45: Walters, D. L., Kunkel, K. E., Hoidale, G. B., *Diurnal And Seasonal Variations In The Atmospheric Structure Parameter (Cn^2) That Affect The Atmospheric Modulation Transfer Function (MTF)*, Procedings of SPIE, Vol. 0277, Atmospheric Transmission, 1981.

46: Fried, D., *Optical Resolution Through a Randomly Inhomogeneous Medium for Very Long and Very Short Exposures*, J. Opt. Soc. America, Vol. 56, No. 10, 1966.

47: Hufnagel, R., Stanley, N., *Modulation Transfer Function Associated with Image Transmission through Turbulent Media*, J. Opt. Soc. America, Vol. 54, 1964.

48: Sadot, D., Shamirz, S., Sasson, I., Dror, I., Kopeika N.S., *Prediction of Overall Atmospheric Modulation Transfer Function with Standard Weather Parameters: Comparison with Measurements with Two Imaging Systems*, Optical Engineering (OE), Vol. 34 (11), 1995.

49: Newton, I., Opticks: or a Treatise of the Reflections, Refractions, Inflecetions, and Colours of Light, William & John Innys, London, 1721.

50: Young, Thomas, Miscellaneous Works of the Late Thomas Young, John Murray, London, 1855.

51: Perrin, F. H., *Methods of Appraising Photographic Systems, Part I*, J. Soc. Motion Picture Television Engineers (SMPTE), Vol. 69, 1960

52: Hall, J., Encyclopedia of Optical and Photonic Engineering, "F-Number, Numerical Aperture, and Depth of Focus", Taylor & Francis - CRC Press, FL, 2016

53: Boyd, R., Radiometry and the Detection of Optical Radiation, Wiley & Sons, New York, 1983.

54: Vincent, J. D., Fundamentals of Infrared Detector Operation & Testing, Santa Barbara Research Center, John Wiley & Sons, New York, 1990.

55: Born, M., Wolf, E., Principles of Optics, Pergammon Press, Oxford, UK, 1970.

56: Mahajan,V., Mouroulis, P., Encyclopedia of Optical Engineering, "Aberrations", Marcel Dekker, New York, 2003.

57: Gerchman, M., *Specifications And Manufacturing Considerations Of Diamond Machined Optical Components*, Proc. SPIE, Vol. 0607, Optical Component Specifications for Laser-based Systems and Other Modern Optical Systems, 1986.

58: Fresnel, A., *Note sur le calcul des teintes que la polarisation développe dans les lames cristallisées*, Annales de Chimie et de Physique, Vol. 17, 1821.

59: Nyquist, H., *Certain Factors Affecting Telegraph Speed*, Bell Systems Technical Journal, pp. 324-346, April, 1924.

60: Shannon, C., Weaver, W., The Mathematical Theory of Communication, University of Illinois Press, Urbana, IL, 1949.

61: Sobel, I., *A 3x3 Isotropic Gradient Operator for Image Processing*, Stanford Artificial Intelligence Project, 1968.

62: Danielsson, P., Seger, O., Machine Vision for Three-Dimensional Scenes, "Generalized and Separable Sobel Operators", Academic Press, San Diego, CA, 1990.

63: Rabiner, R., Gold, B., *Theory and Applications of Digital Signal Processing*, Prentice Hall, NJ, 1975

64: Efkeman A., Spande R., *Testing and Specification for Infrared (IR) Optics for Infrared Imaging*, Proc. SPIE, Vol. 0181, Contemporary Optical Systems & Components Specifications, 1979.

65: Snellen, H., Probebuchstaben zur Bestimmung der Sehschärfe, Van de Weijer, Ultrecht, Netherlands,1862.

66: Farrell, R. J., Booth, J. M., Design Handbook for Imagery Interpretation Equipment, Boeing Aerospace Corp., Seattle, WA, 1984.

67: Driard, B., Lucien, F., *Eletronic Zoom Image Intensifier Tube*, US Patent Office, Patent #3439222, April, 1969.

68: Blecha, Coty, Curry, Graves, Guckian, Hall, McDowell, Nguyen, Samuels, Smith, Wiedman, & Wright, *Second Generation FLIR Common Modules*, Unites States Patent Office, #5510618, 1996.

69: Howe, J., et. al., The Infrared and Electro-Optical Systems Handbook, Vol. 4, SPIE Press, Bellingham, Washington, 1993.

70: LaPlace, P., Théorie analytique des probabilités, Gauthier-Villars, Paris, 1812.

71: Blackwell, *Contrast Threshold of the Human Eye*, J. Opt. Soc. America, Vol. 36, No. 11, 1946.

72: Wiseman, R., *Birth and evolution of visionics*, Proc. SPIE, Vol. 1689, Infrared Imaging Systems: Design, Analysis, Modeling, and Testing III, 1992.

73: Rosell, F., Willson, R., *Basics Of Detection, Recognition And Identification In Electro Optical Formed Imagery*, Proc. of SPIE, Vol. 0033, Solving Problems in Security, Surveillance and Law Enforcement with Optical Instrumentation, 1973.

74: Johnson, J., *Analysis of Image Forming Systems*, US Army Engineering Research & Development Laboratories, Proceedings of the Image Intensifier Symposium, 1958.

75: Ratches, J., *Night Vision Laboratory Static Performance Model*, US Army Electronics Command, 1975.

76: Ostrom, L., Wilhelmsen, C., Risk Assessment: Tools, Techniques, and Their Applications, Wiley & Sons, Hoboken, NJ, 2019.

77: Spencer, G., *A Computer Oriented Automatic Lens Correction Procedure*, University of Rochester, Institute of Optics, 2nd Printing, 1966.

78: Steedman, W., Backer, C., *Target Size and Visual Recognition*, Human Factors, Vol. 2, 1960.

79: Enoch, M., *Effect of the Size of a Complex Display Upon Visual Search*, J. Opt. Soc. America, Vol. 49, No. 3, 1959.

80: Chimitt, N., Chan, S., *Simulating anisoplanatic turbulence by sampling intermodal and spatially correlated Zernike coefficients*, Optical Engineering, Vol. 59, 2020.

81: Potvin, G., *Linear perturbation model for simulating imaging through weak turbulence*, Optical Engineering, Vol. 59, No. 3, 2020.

82: Bos, J., Roggeman, M., *Technique for simulating anisoplanatic image formation over long horizontal paths*, Optical Engineering, Vol. 51, No. 10, 2012.

83: Vorontsov, M., Ricklin, J., Miller, W., Irochnikov, N., *Optical simulation of imaging systems using multiple turbulent phase screens*, Proc. SPIE, Vol. 2312, Optics in Atmospheric Propagation and Random Phenomena, 1994.

84: Grundmark, J., Henriksson, M., *Turbulence characterization and investigation of correlations to meteorological parameters: results from NATO SET-304 field trial in Le Fauga-Mauzac, France*, Proc. SPIE, Vol. 12731, Environmental Effects on Light Propagation and Adaptive Systems VI, 2023.

85: Klein, J., Klein's Design Program (KDP), 2017, http://engineeringcalculations.com.

86: PhotoFiltre, http://photofiltre.free.fr/download_en.htm.

87: Osborn, A., Your Creative Power (How To Use Imagination), Charles Scribner's Sons, New York, 1948.

88: Babock, H. W., *The Possibility of Compensating Astronomical Seeing*, Publications of the Astronomical Society of the Pacific (PASP), Vol. 65, No. 386, 1953.

89: Oppenheim, A., Shafer, R., Discrete Time Signal Processing, Prentice Hall, New Jersey, 1999

90: Mt. Lemon Skycenter, Remote Astrophotogrpahy, 2023, https://skycenter.arizona.edu/remote-astrophotography.

91: Biberman, L., Alluisi, E., *Pilot Errors Involving Head-Up Displays (HUDs),Helmet-Mounted Displays (HMDs),and Night Vision Goggles (NVGs)* , Institute for Defence Analysis, IDA Paper P-2638, 1992.

92: Krebs, W., Scribner, D., Miller, G., Ogawa, J., Schuler, J., *Beyond third generation: a sensor-fusion targeting FLIR pod for the F/A-18*, Proc. SPIE, Vol. 3376, Sensor Fusion: Architectures, Algorithms, and Applications II, 1998.

93: van Eekeren, A., Schutte, K., Dijk, J., Schwering, P., Kruithof, M., van Iersel, M., *Patch-based local turbulence compensation in anisoplanatic conditions*, Proc. SPIE, Vol. 8355, Infrared Imaging Systems: Design, Analysis, Modeling, and Testing XXIII, 2012.

94: Lippmann, G., *Epreuves reversibles, photographies integrales*, Academie des Sciences, No. 446451, 1908.

95: Michels, T., Koch, R., *Ray Tracing-Guided Design of Plenoptic Cameras*, IEEE, 2021 International Conference on 3D Vision (3DV), 2021.

96: Wu, C., Paulson, D., Rzasa, J., Davis, C., *Comparison between the plenoptic sensor and the light field camera in restoring images through turbulence*, OSA Continuum, Vol. 2, No. 9, 2019.

97: Huebner, C., Greco, M., *Blind deconvolution algorithms for the restoration of atmospherically degraded imagery: a comparative analysis*, Proc. SPIE, Vol. 7108, Optics in Atmospheric Propagation and Adaptive Systems XI, 2008.

98: Simske, S., Dalong, L., *Atmospheric Turbulence Degraded-Image Restoration by Kurtosis Minimization*, IEEE, Geoscience and Remote Sensing Letters, Vol. 6, 2009.

99: Yasarla, R., Patel, V., *Learning to restore images degraded by atmospheric turbulence using uncertainty*, IEEE, International Conference on Image Processing (ICIP), 2021.

100: Dong, L., et. al., *Defocused Spatial Diversity Technology With Aperture Scanning for Aberration Detection and Image Restoration in Aberrated Imaging Systems*, Optical Engineering, Vol. 57(8), 2018.

101: Gonsalves, R., *Phase diversity: math, methods and prospects, including sequential diversity imaging*, Proc. SPIE, Vol. 10677, Unconventional Optical Imaging, 2018.

102: DeSandre, L., Langston, P., Pentony, J., Marrs, C., Ogloza, A., *Characterization of turbulent atmospheric-induced optical distortion by passive phase diversity techniques*, Proc. SPIE, Vol. 4376, Laser Weapons Technology II, 2001.

103: Zhang, W., Ning, Y., Cao, Y., Zhang, X., *Lucky region imaging based on front and back defocus images comparison*, Proc. SPIE, Vol. 9796, Selected Papers of the Photoelectronic Technology Committee Conferences held November 2015, 2016.

104: Cathey, T., Dowski, E., *Extended Depth of Field Through Wavefront Coding*, Applied Optics, Vol. 34, No. 11, 1995.

105: González-Amador, E., Padilla-Vivanco, A., Toxqui-Quitl, C., Olvera-Angeles, M., Arines, J., Acosta, E., *Wavefront coding with Jacobi-Fourier phase masks*, Proc. SPIE, Vol. 11104, Current Developments in Lens Design and Optical Engineering XX, 2019.

106: Bryant, K., Edwards, D., Rogers, R., *Low-cost computational imaging infrared sensor*, Proc. SPIE, Vol. 9071, Infrared Imaging Systems: Design, Analysis, Modeling, and Testing XXV, 2014.

107: Kubala, K., Wach, H., Chumachenko, V., Dowski, E., *Increasing the depth of field in an LWIR system for improved object identification*, Proc. SPIE, Vol. 5784, Infrared Imaging Systems: Design, Analysis, Modeling, and Testing XVI, 2005.

108: Olvera-Angeles, M, González-Amador, E., Arines, J., Sasian, J., Schwiegerling, J., Acosta, E. , *Jacobi-Fourier phase masks to increase performance of wavefront-coded optical systems for random or varying aberration alleviation*, Japanese Journal of Applied Physics, Vol. 59, No. SO, 2020.

109: Greenwood, P., Ward, L., Stochastic Neuron Models, Springer International Publishing, Switzerland, 2016.

110: McCulloch, W. S., & Pitts, W., *A logical calculus of the ideas immanent in nervous activity*, Bulletin of Mathematical Biophysics, Vol. 5, 1943.

111: Rosenblatt, F., *The Perceptron: A Probabilistic Model For Information Storage And Organization In The Brain*, Psychological Review, Vol. 65, No. 6, 1958.

112: Jain, T., Lubien, M., Gilles, J., *Evaluation of Neural Network Algorithms for Atmospheric Turbulence Mitigation*, Proc. SPIE, Vol. 12122, Signal Processing, Sensor/Information Fusion, and Target Recognition XXXI, 2022.

113: Vint, D., Caterina, G., Soraghan, J., Lamb, R., Humphreys, D., *Analysis of Deep Learning Architectures for Turbulence Mitigation in Long-Range Imagery*, Proc. SPIE, Vol. 11543, Artificial Intelligence and Machine Learning in Defense Applications II, 2020.

114: Hall, B., Private exchange, 2023.

115: Anantrasirichai, N., Achim, A., Kingsbury, N., Bull, D., *Atmospheric turbulence mitigation using complex wavelet-based fusion*, IEEE Transactions on Image Processing, Vol. 22, Issue 6, 2013.

116: Hardie, R., Rucci, M., Dapore, A., Karch, B., *Block matching and Wiener filtering approach to optical turbulence mitigation and its application to simulated and real imagery with quantitative error analysis*, Optical Engineering, Vol. 56, No. 7, 2017.

117: Laikin, M., Lens Design, Taylor-Francis CRC Press, FL, 2006.

118: Hunt, B., Iler, A., Bailey, C., Rucci, M., *Synthesis of atmospheric turbulence point spread functions by sparse and redundant representations*, Optical Engineering, Vol. 57, No. 2, 2018.

119: Voitsekhovich, V., Cuevas S., *Adaptive optics and the outer scale of turbulence*, J. Opt. Soc. America, Vol. 12, No. 11, 1995.

120: Fischer, R., *Optical Design for the Infrared*, Proc. SPIE, Vol. 0531, Geometrical Optics, 1985.

121: Briere, T., Hohenberger, R., Chatard, J., *System design of a long-wavelength IR CCD camera based on a 240X4 MCT focal plane array,*, Proc. SPIE, Vol. 1341, Infrared Technology XVI, 1990.

122: Mackin, J., Wiltsie, D., *U.S. Army development of the second-generation horizontal technology integration forward-looking infrared (FLIR)*, Proc. SPIE, Vol. 2764, Digitization of the Battlefield, 1996.

123: Reich, S., *The Use Of Electro-Mechanical Mirror Scanning Devices*, Proc. SPIE, Vol. 0084, Laser Scanning Components and Techniques: Design Considerations/Trends, 1977.

124: Chipman, R., The Earliest Electromagnetic Instruments, Smithsonian Press, Bulletin 240, Paper 38, Washington, DC, 1966.

125: Poggendorf, J., *Ein Vorschlag zum Messen der Magnetischen Abweichung*, Analen der Physik und Chemie, Vol. 7, 1826.

126: Science Museum Group, Thomson's Mirror Marine Galvonometer, 1858, https://collection.sciencemuseumgroup.org.uk/objects/co6212/thomsons-mirror-marine-galvanometer-1858-galvanometer.

127: Krause, P., Wasynczuk, O., Perkarek, S., Electromechanical Motion Devices, Wiley & Sons, Hoboken, NJ, 2012.

128: Gadhok, J., *Achieving high-duty cycle sawtooth scanning with galvanometric scanners*, Proc. SPIE, Vol. 3787, Optical Scanning: Design and Application, 1999.

129: Brosens, P., *Scanning speed and accuracy of moving magnet optical scanners*, Optical Engineering, Vol. 34, No. 1, 1995.

130: Mirtchev, T., Weeks, R., Minko, S., *Optimizing the Feedback Control of Galvo Scanners for Laser Manufacturing Systems*, Proc. of SPIE, Vol. 7750, Photonics North 2010, 2010.

131: Ju, *Effective bidirectional scanning pattern for optical coherence tomography angiography*, Biomedical Optics Express, Vol.. 9(5):2336, 2018.

132: Chen, G.; Wang, Y., *Control of a Digital Galvanometer Scanner Using a Discrete-Time Sliding-Mode Variable-Structure Controller Based on a Decoupled Disturbance Compensator*, Appl. Sci., Vol. 11, 9788, 2021.

133: ThorLabs (catalog), QS45X-AG Scanner, 2023, https://www.thorlabs.com/thorproduct.cfm?partnumber=QS45X-AG.

134: Riedl, M., Optical Design Fundamentals for Infrared Systems, SPIE Press, Washington, 2001.

135: Filachev, A., Ponomarenko, V., Taubkin, I., Ushakova, M., *Infrared focal plane arrays: state of the art and development trends*, Proc. SPIE, Vol. 5126, 17th International Conference on Photoelectronics and Night Vision Devices, 2003.

136: Horn, S., *Cryogenic Cooling Options For Forward Looking Infrared (FLIR)*, Proc. SPIE, Vol. 0245, Cryogenically Cooled Sensor Technology, 1980.

137: Chellis, F., *An Introduction To Closed Cycle Cryogenic Coolers*, Proc. SPIE, Vol. 0245, Cryogenically Cooled Sensor Technology, 1980.

138: Uffenbeck, J., Microcomputers and Microprocessors, Prentice-Hall, NJ, 19991.

139: Aletan, S., Barnes, F., *An overview of RISC Architecture*, Proceedings of SPIE, 1992 ACM/SIGAPP Symposium on Applied computing: technological challenges of the 1990's, 1992.

140: King, D., et. al., *3rd generation MW/LWIR sensor engine for advanced tactical systems* , Proc. SPIE, Vol. 6940, Infrared Technology and Applications XXXIV, 2008.

141: Smith, S., The Scientist and Engineer's Guide to Digital Signal Processing, California Technnical Publishing, San Diego, CA, 1999.

142: Li, X., Blinka, E., *Very Large FFT for TMS320C6678 Processors,* Texas Instruments Inc., 2015.

143: Yoder, P., Mounting Optics in Optical Instruments, SPIE Press, Bellingham, WA, 2008.

144: Hall, J., *Large Format Biocular Lens*, US Patent Office, #10520720, 2019.

145: MIL-STD-1472F, Human Engineering, 1999.

146: MIL-STD-781C, Reliability Design Qualification and Production Acceptance Tests: Exponential Distribution, 1977.

147: MIL-HDBK-217, Reliability Prediction of Electrical Equipment, 1991.

148: MIL-HDBK-338, Electronic Reliability Design Handbook, 1988.

149: Pruitt, G., *Reliability growth of coolers for advanced optical systems and instruments*, Proc. SPIE, Vol. 1340, Cryogenic Optical Systems and Instruments IV, 1990.

150: Estrada, R., Kuo, D., Phan, Q., *Reliability Growth of Stirling-Cycle Coolers at L-3 CE*, Proceedings of the 15th International Cryocooler Conference (ICC), Cryocoolers 15, 2009.

151: MIL-HDBK-245D, Handbook for Preparation of Statement of Work (SOW), 1991

152: MIL-STD-882E, System Safety, 2012.

Note: US Military Standards and Handbooks in PDF format are available for free download via the Defense Logistics Agency website <https://quicksearch.dla.mil/>.

Appendix A: Optical Aberrations

The basis for geometric optical aberration theory is the premise that a point source will emit light in diverging spherical wavefronts. The reverse is also assumed true, that a converging spherical wavefront shall constitute a perfect "point" image as shown in the figure below. In one form or another, the purpose of an imaging optical system is to produce an image of a given object to the best degree possible.

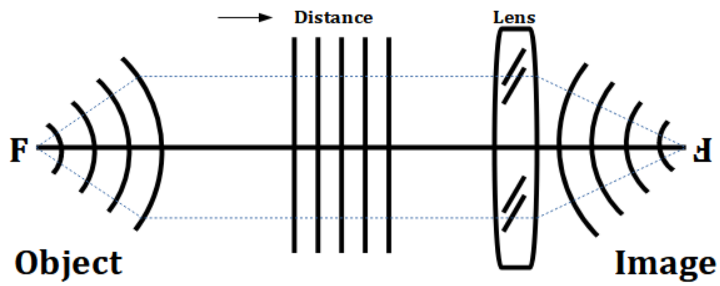

However, as an optical wavefront propagates through a real optical lens system, the resultant wavefront convergence toward the focal point may deviate from a perfect spherical section; this amount of deviation is then quantified as the "aberration". A mathematical model may be constructed to characterize the degree and form of the aberration. For a spherical light wave converging towards a point, the wavefront surface $S(x,y,z,r)$ would satisfy the equation of a sphere,

$$x^2 + y^2 + r^2 = z^2$$

where x, y, and z are linear positions along orthogonal axes, and r is the radial distance from the origin to any point on the spherical surface. As the light wave converges to a focus toward the origin, the value of r approaches zero for each successive wavefront. For the purpose of argument, an "afocal" optical system, in which a plane wave is the desired output, can be considered to produce a spherical wavefront with an infinite radius of curvature r, and hence the discussion herein applies to such systems as well.

A good optical focusing system will attempt to create such a spherical converging wavefront $S(x,y,z)$, but depending upon the geometry of the optical elements, it may deviate from the desired wave shape. The difference between the actual wavefront $A(x,y,z)$ and the ideal spherical shape is then characterized as the aberration. Thus, an aberration function $W(x,y,z)$ is described as a difference between the actual wavefront and the spherical "reference surface." Each (x,y,z) coordinate along the ideal wavefront would then have an ideal value, and actual value, and a corresponding aberrational difference.

$$W(x,y,z) = S(x,y,z) - A(x,y,z)$$

In the most general analysis, the function W could have any value for any given (x,y,z) position. Consider an example of a parabolic mirror attempting to focus a plane wave, where the mirror surface has perhaps been covered with dust or sand particles. Each particle could contribute some random value to the aberration coefficient at various positions along the wavefront, and there would likely be little more than a statistical correlation from one place to another. Characterizations of this type, where the aberration contributions are perhaps discontinuous or random, are not generally covered in the classical aberration theory (see O'Neil, Statistical Optics) and are usually accounted for in practice by other means such as interferometric analysis.

For classical geometric aberration theory, the function $W(x,y,z)$ is assumed to be mathematically continuous, such that it can be represented as a polynomial expansion in the optical system coordinates. In other words, classical aberration theory assumes that the function $W(x,y,z)$ is continuous and finite such that a polynomial curve fit representation can be applied. Indeed, in practice it is the geometric parameters that are the first concern in an optical design process, and then random or discontinuous errors are usually in the domain of the material fabrication process. For example, a simple polynomial expansion or curve-fit for $W(x,y,z)$ for a wavefront propagating normal to the z-axis would have the general form as follows:

$$W(x,y,z) = \alpha_0 W^0 + \alpha_1 W^1 + \alpha_2 W^2 + \alpha_3 W^3 + \ldots$$

where each successive power of W^i is assigned a coefficient α_i and where the power of a multidimensional W is the sum total exponential power of its (x,y,z) components, i.e.,

$$\alpha_0 W^0 = \text{constant}$$

$$\alpha_1 W^1 = \sum (\beta_1 x^l + \beta_2 y^m + \beta_3 z^n) \text{ for all cases where } (l + n + m) = 1$$

The pattern continues for higher orders. For example, the second power W^2 consists of the following six terms, each of which having their own unique coefficients with $(l + n + m) = 2$ shown as follows:

$$\alpha_2 W^2 = \sum (\gamma_1 x^l + \gamma_2 y^m + \gamma_3 z^n) = \gamma_1(x^2) + \gamma_2(y^2) + \gamma_3(z^2) + \gamma_4(xy) + \gamma_5(xz) + \gamma_6(yz)$$

where each γ_i is a new coefficient for each term. Note that the sum of (x,y,z) powers in each term adds up to two. As higher orders are included, it is seen that the total number n of terms in each order $(l+m+n)$ increases geometrically, with ten terms at the third power, and so on. This technique may be applied to describing the spherical departure of an optical wavefront propagating along the optical axis. However, this conceptual example must now be broadened to account for spherical wave propagation from an originating point at some chosen angle relative to the chosen optical axis.

An optical system may be characterized by analysis of rays propagating from a point source object through the exit pupil of the optical system, and finally converging to a point focus in the image plane. The image of a perfect point is assumed to result only if the incoming wavefront is spherical, although in the general case for an optical system the focal point need not necessarily lie upon the optical axis. The first step in developing this general wavefront analysis is to determine the minimum number of variables which uniquely define the passage of a light ray from an object to the exit pupil and then to a given location on the focal plane. The optical system analysis must expand the previously discussed fundamental mathematical case to include accounting of off-axis image points, wherein the reference sphere is tilted and the chief ray of propagation for a given convergent bundle is at some angle relative to the optical z-axis.

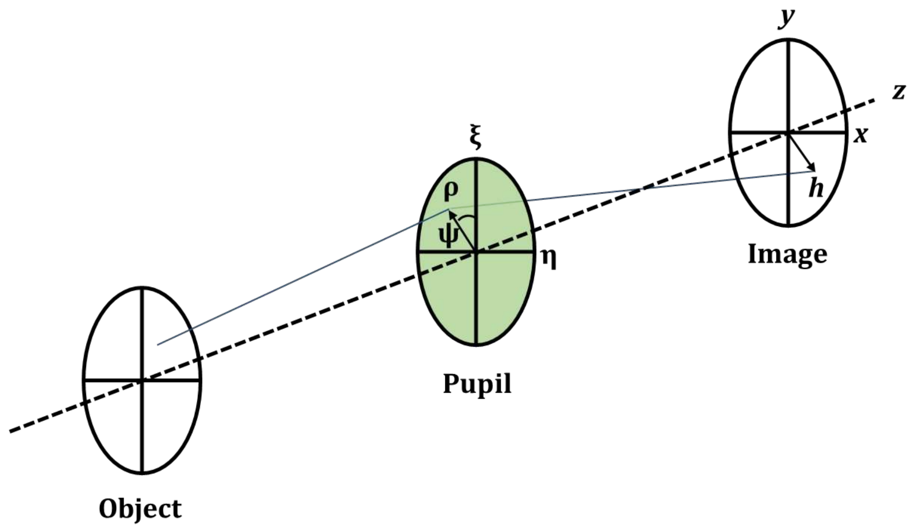

The optical system pupil will intercept a section of a light wave from a diverging point source, and if perfect imaging occurs, each light ray from the pupil will progress to the image plane and converge to a perfect point in the (x, y) image plane. Referencing the optical system figure below, the plane of the exit pupil $P(\xi, \eta)$ is considered tangent to the vertex of the reference sphere. This is not a requirement, but merely a convenience in defining the coordinate system. The image plane $I(x, y)$ is then located some distance along the z-axis away from the exit pupil. A ray originating in the pupil plane will have some coordinates (ξ, η) and will impact the focal plane with some value of (x, y) in the plane normal to the z-axis. The aberration function W then must uniquely describe the characteristics of a single ray as defined by its endpoints, and hence has the dependence shown by

$$W(\xi, \eta, x, y)$$

where there is no longer an explicit z dependence as the distance along the z-axis between $P(\xi, \eta)$ and $I(x, y)$ is assumed constant. This step is necessary to account for both the on-axis imaging wavefront, and the tilted wavefront for an off-axis position in a focal plane. Note that at this point we have not defined the wavefront error function (W) itself, but only the minimum number of component variables that it must account for. We now proceed with a conversion to cylindrical coordinates where

$$\rho^2 = \xi^2 + \eta^2 \quad \text{and} \quad h^2 = x^2 + y^2$$

These coordinates define the vector radial distances or heights from the z-axis for the Exit Pupil and Focal Plane, respectively. By the nature of perfect optical imaging, we know that rays exiting from the pupil will strike the focal plane in exactly one position at some height, h. The next step is to show that the general polynomial form can be simplified to account for rotational and bi-lateral symmetry in the optical coordinate system. The aberration function which uniquely defines a single ray can have the dependence shown by

$$W(\xi, \eta, x, y) = W(\rho^2, h^2, \xi x + \eta y)$$

This takes advantage of the bilateral symmetry of a decentered conic surface. The ρ^2 and h^2 terms represent radial zone heights in the pupil and focal planes, respectively. Once those radial zones are known, the scalar value ($\xi x + \eta y$) is then all that is required to uniquely define a ray position between the either symmetric half of the pupil plane and any one quadrant in the (x, y) image plane. This is all that is required due to the observation that the decentered conic surface of the ray bundle is *bilaterally symmetric* about the radial height vector of length $h^2 = x^2 + y^2$. Note that this new set of base variables for W is not necessarily simpler than what we started with, but it does give a more intuitive look into the system and it allows the simplifications which follow. As an illustrative example of the completeness of the variable choice, consider a point in the image plane located at coordinates ($x = 0$, $y = 1$). The cone of light from the exit pupil is symmetric about h, which happens to fall upon the y-axis, and only half of the exit pupil plane coordinates (either half-plane of $+\xi$ or $-\xi$ in this case) are required to characterize any particular ray endpoint. This observation continues to hold true for any endpoint position in the *x-y* image plane, with the axis of symmetry in the pupil plane following the vector of magnitude h. By combining the assumption that curve fitting will give a general formulation for an aberrated wavefront with the symmetry of the optical coordinate system, we now assume that a polynomial expansion for the aberration function can be expressed as follows:

$$W(\rho^2, h^2, \xi x + \eta y) = \sum \alpha_i (\rho^2)^l \, (h^2)^m \, (\xi x + \eta y)^n$$

The first order terms are those for which the powers $l+m+n = 1$, second order when $l+m+n = 2$, and so on. The coefficient term α_i represents the multiplication of individual coefficients for each component. As discussed above, this general notation can now be further simplified to the case where the axis of symmetry is aligned with either coordinate axis. This symmetry coordinates are chosen such that $x = 0$ and $y = h$. This simplifies the aberration polynomial further without loss of accuracy as shown below.

$$W(\rho^2, h^2, h\eta) = \sum \alpha_i (h^2)^l \, (\rho^2)^m \, (h\eta)^n$$

The exit pupil coordinates can also be represented in circular coordinates, with a maximum normalized radial distance of length ρ_0 at any angle ψ where

$$\eta = \rho \cos(\psi)$$

The wave aberration polynomial then takes the common form which has dependency on only three geometric variables as follows:

$$W(h, \rho, \psi) = \sum \alpha_i (h)^{2l} \, (\rho)^{2m} \, (h\rho \cos \psi)^n$$

This final form of the aberration polynomial is used as the basis for description of the classical optical aberration coefficients. Polynomial order is still a function of the original coefficients l, m, and n. The three first order terms can be solved as follows:

l	***m***	***n***	$W(h, \rho, \psi)$	**Description**
1	0	0	$W_{100}\, h^2$	“piston”
0	1	0	$W_{010}\, \rho^2$	“defocus”
0	0	1	$W_{001}\, h\rho(\cos \psi)$	“tilt”

There are then six terms for the next order defined by $l+m+n = 2$. These are tabulated below, and with the exception of high order piston which is usually ignored, correspond to the five classical Seidel Aberrations well known in the field of optics.

l	***m***	***n***	$W(h, \rho, \psi)$	**Description**
2	0	0	$W_{200}\, h^4$	Piston
0	2	0	$W_{020}\, \rho^4$	Spherical
0	0	2	$W_{002}\, h^2\rho^2(\cos^2\psi)$	Astigmatism
1	1	0	$W_{110}\, h^2\rho^2$	Field Curvature (Petzval)
0	1	1	$W_{011}\, h\rho^3(\cos\psi)$	Coma
1	0	1	$W_{101}\, h^3\rho\, (\cos\psi)$	Distortion

These five primary aberrations (Spherical, Astigmatism, Field Curvature, Coma, & Distortion) are known as the "Seidel" aberration coefficients. Seidel was a scientist who converted the pupil wavefront errors shown here into transverse ray aberration errors in the focal plane. This conversion is done by taking the derivative of the wavefront aberration polynomial $W(h, \rho, \psi)$, so instead of a 4^{th} power exponentials, the results are 3^{rd} power. Hence, the Seidel aberrations are often referred to as "3^{rd} Order".

Appendix B: Optical Prescriptions

This appendix contains the prescriptions for the original optical design work contained within this document. All prescriptions were generated in KDP software, available freeware and manual at <engineeringcalculations.com>.

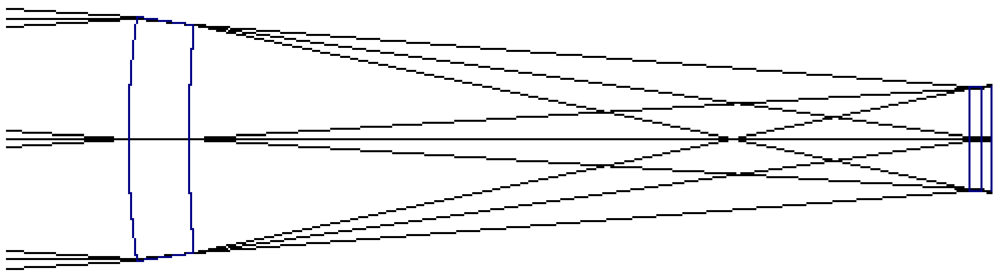

```
JH SPSRF LWIR F#/3.5 70MM TURBULENCE
UNITS = MILLIMETERS

YZ-PLANE FIRST ORDER OPERATING CONDITIONS
 EFL          BFD          F-NUM        LENGTH      GIH
 69.439      0.78744       3.4720       81.287       4.2355

REF OBJ Y-HT                   REF AP Y-HT         OBJ SF#  REF SF#  IMG SF#
-0.611626E+54(  3.500     DG)      9.488                0        3        7

REF OBJ X-HT                   REF AP X-HT         OBJ SF#  REF SF#  IMG SF#
-0.611626E+54(  3.500     DG)      9.488                0        3        7
EVALUATION MODE IS FOCAL
THE CURRENT APERTURE STOP SURFACE IS SURFACE #   3

SEMI-APERTURE REFERENCE RAY HEIGHT AT SURFACE #1
SAY(YZ-PLANE IN LENS UNITS) =    0.100000000000000D+02

THERE ARE CURRENTLY            3 ANALYSIS FIELD POSITIONS DEFINED
UNITS ARE DEGREES
POS # =  1 X-VALUE =   0.00000     Y-VALUE =   0.00000
POS # =  2 X-VALUE =   0.00000     Y-VALUE =  0.500000
POS # =  3 X-VALUE =   0.00000     Y-VALUE =   1.00000

REFERENCE OBJECT ANGLE
SCY FANG(YZ-PLANE IN DEGREES)=   0.350000000000000D+01 ,   0.000000000000000D+0
REF. OBJ. HT. SET BY OBJECT ANGLE

BASIC LENS DATA (RADIUS MODE)

SURF  RADIUS        THICKNESS          MATERIAL          INDEX        V-NUM
 0    0.00000      0.100000E+56         AIR
 1    0.00000       10.0000             AIR
 2    73.2243       5.00000     MATL    GERMPC          4.00310      0.230E+05
 3*   107.070       63.5000             AIR
 3*REFS,STOP
 4    0.00000       1.00000             AIR
 5*   0.00000       1.00000     MATL    ZNSE            2.40651      0.116E+04
 5*Special
 6    0.00000      0.787443             AIR
 7    0.00000       0.00000             LAST SURFACE

NO CONIC OR 4th through 10th ORDER ASPHERIC DATA
```

NO 12th through 20th ORDER ASPHERIC DATA

REFRACTIVE INDEX DATA (WAVELENGTHS #1 TO #5)

SURF	N1	N2	N3	N4	N5
2 MATL		GERMPC			
2	4.00324	4.00310	4.00297	1.00000	1.00000
5 MATL		ZNSE			
5	2.40770	2.40651	2.40530	1.00000	1.00000

NO CLEAR APERTURE OR OBSCURATION DATA

WAVL NBR	1	2	3	4	5
WAVELENGTH	9.8000	10.000	10.200	0.0000	0.0000
SPECTRAL WT	1.000	1.000	1.000	0.000	0.000
WAVL NBR	6	7	8	9	10
WAVELENGTH	0.0000	0.0000	0.0000	0.0000	0.0000
SPECTRAL WT	0.000	0.000	0.000	0.000	0.000

NO TILT AND DECENTER DATA

SPECIAL SURFACE DATA
SURFACE = 5 SPECIAL SURFACE TYPE = 4- ON
SINUSOIDAL ERROR SURFACE

1ST PEAK TO VALLY ERROR (WAVES)	=	0.10000000	
1ST X-PERIOD (SPATIAL FREQUENCY)	=	2.0000000	MM
1ST Y-PERIOD (SPATIAL FREQUENCY)	=	2.0000000	MM
2ND PEAK TO VALLY ERROR (WAVES)	=	0.0000000	
2ND X-PERIOD (SPATIAL FREQUENCY)	=	0.0000000	MM
2ND Y-PERIOD (SPATIAL FREQUENCY)	=	0.0000000	MM
3RD PEAK TO VALLY ERROR (WAVES)	=	0.0000000	
3RD X-PERIOD (SPATIAL FREQUENCY)	=	0.0000000	MM
3RD Y-PERIOD (SPATIAL FREQUENCY)	=	0.0000000	MM
4TH PEAK TO VALLY ERROR (WAVES)	=	0.0000000	
4TH X-PERIOD (SPATIAL FREQUENCY)	=	0.0000000	MM
4TH Y-PERIOD (SPATIAL FREQUENCY)	=	0.0000000	MM
5TH PEAK TO VALLY ERROR (WAVES)	=	0.0000000	
5TH X-PERIOD (SPATIAL FREQUENCY)	=	0.0000000	MM
5TH Y-PERIOD (SPATIAL FREQUENCY)	=	0.0000000	MM

NO CONFIG DATA

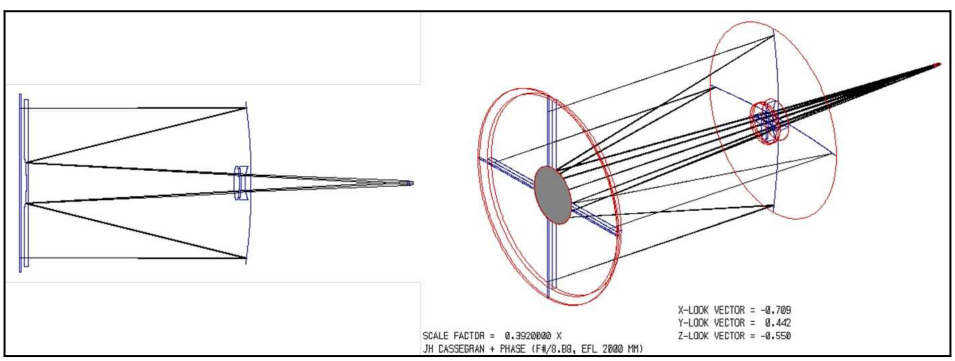

JH CASSEGRAN + PHASE (F#/8.88, EFL 2000 MM)
UNITS = MILLIMETERS
YZ-PLANE FIRST ORDER OPERATING CONDITIONS

EFL	BFD	F-NUM	LENGTH	GIH
2000.0	4.9565	8.8889	491.81	-1.0698

```
XZ-PLANE FIRST ORDER OPERATING CONDITIONS
 EFL          BFD          F-NUM        LENGTH      GIH
 2000.0       4.9565       8.8889       491.81      -2.3114
REF OBJ Y-HT                    REF AP Y-HT         OBJ SF#  REF SF#  IMG SF#
0.534560E+16(-0.3063E-01 DG)      105.0                 0        3       13

REF OBJ X-HT                    REF AP X-HT         OBJ SF#  REF SF#  IMG SF#
0.115500E+17(-0.6618E-01 DG)      105.0                 0        3       13
EVALUATION MODE IS FOCAL
THE CURRENT APERTURE STOP SURFACE IS SURFACE #   3
SEMI-APERTURE REFERENCE RAY HEIGHT AT SURFACE #1
SAY(YZ-PLANE IN LENS UNITS) =    0.112500000000000D+03
THERE ARE CURRENTLY            3 ANALYSIS FIELD POSITIONS DEFINED
UNITS ARE DEGREES
POS # =  1 X-VALUE =   0.00000     Y-VALUE =   0.00000
POS # =  2 X-VALUE =   0.00000     Y-VALUE =  0.700000
POS # =  3 X-VALUE =   0.00000     Y-VALUE =   1.00000

REFERENCE OBJECT ANGLE
SCY FANG(YZ-PLANE IN DEGREES)=  -0.306280255014091D-01 ,   0.000000000000000D+0
REF. OBJ. HT. SET BY OBJECT HEIGHT

BASIC LENS DATA (RADIUS MODE)

SURF  RADIUS        THICKNESS          MATERIAL          INDEX        V-NUM
 0    0.00000      0.100000E+20         AIR
 1*   0.00000       2.14407     SCH2000 N-SF57          1.87215       85.2
 1*Special
 2    0.00000       4.00000             AIR
 3*   0.00000       4.75270     SCHOTT  BK7             1.52239       210.
 3*Asphere,REFS,STOP
 4   -202851.       278.608             AIR
 5*  -773.296      -281.052             REFL
 5*Conic
 6*  -273.012       259.433             REFL
 6*Conic
 7    106.275       6.87890     SCHOTT  SK15            1.63048       192.
 8   -122.927       2.06367             AIR
 9   -122.927       4.91350     SCHOTT  K7              1.51701       199.
10    58.9620       202.972             AIR
11*   0.00000       2.14407     SCH2000 N-SF57          1.87215       85.2
11*Special
12    0.00000       4.95646             AIR
13    0.00000       0.00000             LAST SURFACE
CONIC AND 4th THROUGH 10th ORDER ASPHERIC DATA
(+) - DESIGNATES A PLANO SURFACE WITH A 2ND ORDER ASPHERIC
TERM IN THE SECOND COLUMN INSTEAD OF A CONIC CONSTANT

SURF   CC/AC           AD            AE             AF             AG
 3   0.00000     -0.532033E-09 -0.730172E-16   0.00000       0.00000     (+)
 5 -0.270300
 6 -0.479600
NO 12th through 20th ORDER ASPHERIC DATA
NO TILT AND DECENTER DATA
REFRACTIVE INDEX DATA (WAVELENGTHS #1 TO #5)

SURF    N1              N2             N3             N4             N5
 1 SCH2000       N-SF57
 1    1.87215        1.84676        1.83653        1.00000        1.00000
 3 SCHOTT        BK7
 3    1.52239        1.51682        1.51433        1.00000        1.00000
 7 SCHOTT        SK15
 7    1.63048        1.62302        1.61974        1.00000        1.00000
 9 SCHOTT        K7
 9    1.51701        1.51115        1.50855        1.00000        1.00000
11 SCH2000       N-SF57
11    1.87215        1.84676        1.83653        1.00000        1.00000
CLEAR APERTURES AND OBSCURATIONS

SURF    TYPE   Y-SEMI.    X-SEMI.    Y-DEC      X-DEC  CORNER-RADIUS TILT(DEG)
             (RADIUS)   (N-POLY)
```

```
                        (RAD-FLT)                              (DELTA-Z)
 3     CIRC   105.       105.
 3 OB  CIRC   30.0
 4     CIRC   105.       105.
 5     CIRC   102.       102.
 6     CIRC   30.0       30.0
 7     CIRC   21.4       21.4
 8     CIRC   21.4       21.4
 9     CIRC   21.4       21.4
10     CIRC   21.4       21.4
WAVL NBR          1            2            3            4            5
WAVELENGTH    0.48600      0.58700      0.65600      0.0000       0.0000
SPECTRAL WT    1.000        1.000        1.000        0.000        0.000
WAVL NBR          6            7            8            9           10
WAVELENGTH     0.0000       0.0000       0.0000       0.0000       0.0000
SPECTRAL WT    0.000        0.000        0.000        0.000        0.000
SPECIAL SURFACE DATA
SPECIAL SURFACE DATA
SURFACE =  1  SPECIAL SURFACE TYPE = 4- ON
SINUSOIDAL ERROR SURFACE
1ST PEAK TO VALLY ERROR (WAVES)  =   0.0000000
1ST X-PERIOD (SPATIAL FREQUENCY) =   35.734564     MM
1ST Y-PERIOD (SPATIAL FREQUENCY) =   35.734564     MM
2ND PEAK TO VALLY ERROR (WAVES)  =   0.0000000
2ND X-PERIOD (SPATIAL FREQUENCY) =   32.161108     MM
2ND Y-PERIOD (SPATIAL FREQUENCY) =   32.161108     MM
3RD PEAK TO VALLY ERROR (WAVES)  =   0.0000000
3RD X-PERIOD (SPATIAL FREQUENCY) =   0.0000000     MM
3RD Y-PERIOD (SPATIAL FREQUENCY) =   0.0000000     MM
4TH PEAK TO VALLY ERROR (WAVES)  =   0.0000000
4TH X-PERIOD (SPATIAL FREQUENCY) =   0.0000000     MM
4TH Y-PERIOD (SPATIAL FREQUENCY) =   0.0000000     MM
5TH PEAK TO VALLY ERROR (WAVES)  =   0.0000000
5TH X-PERIOD (SPATIAL FREQUENCY) =   0.0000000     MM
5TH Y-PERIOD (SPATIAL FREQUENCY) =   0.0000000     MM
SURFACE = 11  SPECIAL SURFACE TYPE = 4- ON
SINUSOIDAL ERROR SURFACE
1ST PEAK TO VALLY ERROR (WAVES)  =   0.0000000
1ST X-PERIOD (SPATIAL FREQUENCY) =   2.8587651     MM
1ST Y-PERIOD (SPATIAL FREQUENCY) =   2.8587651     MM
2ND PEAK TO VALLY ERROR (WAVES)  =   0.0000000
2ND X-PERIOD (SPATIAL FREQUENCY) =  0.53601846     MM
2ND Y-PERIOD (SPATIAL FREQUENCY) =  0.53601846     MM
3RD PEAK TO VALLY ERROR (WAVES)  =   0.0000000
3RD X-PERIOD (SPATIAL FREQUENCY) =  0.46454934     MM
3RD Y-PERIOD (SPATIAL FREQUENCY) =  0.46454934     MM
4TH PEAK TO VALLY ERROR (WAVES)  =   0.0000000
4TH X-PERIOD (SPATIAL FREQUENCY) =   0.0000000     MM
4TH Y-PERIOD (SPATIAL FREQUENCY) =   0.0000000     MM
5TH PEAK TO VALLY ERROR (WAVES)  =   0.0000000
5TH X-PERIOD (SPATIAL FREQUENCY) =   0.0000000     MM
5TH Y-PERIOD (SPATIAL FREQUENCY) =   0.0000000     MM
NO CONFIG DATA
```

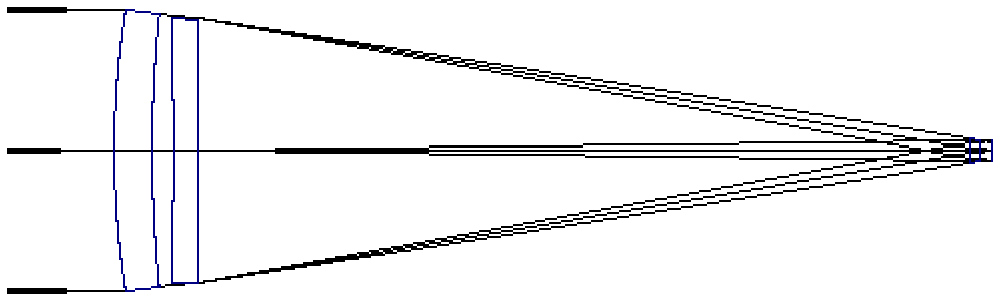

```
TURBULENCE LENS LWIR 400MM F#/3
UNITS = MILLIMETERS

YZ-PLANE FIRST ORDER OPERATING CONDITIONS
 EFL          BFD          F-NUM        LENGTH      GIH
 400.00       1.0000       3.0000       465.44      -3.3655

REF OBJ Y-HT                    REF AP Y-HT         OBJ SF#  REF SF#  IMG SF#
0.839562E+18(-0.4810     DG)      64.43                 0        3        9

REF OBJ X-HT                    REF AP X-HT         OBJ SF#  REF SF#  IMG SF#
0.112000E+19(-0.6417     DG)      64.43                 0        3        9
EVALUATION MODE IS FOCAL
THE CURRENT APERTURE STOP SURFACE IS SURFACE #   3

SEMI-APERTURE REFERENCE RAY HEIGHT AT SURFACE #1
SAY(YZ-PLANE IN LENS UNITS) =    0.666667000000000D+02

THERE ARE CURRENTLY            3 ANALYSIS FIELD POSITIONS DEFINED
UNITS ARE DEGREES
POS # =  1 X-VALUE =   0.00000     Y-VALUE =   0.00000
POS # =  2 X-VALUE =   0.00000     Y-VALUE =  0.700000
POS # =  3 X-VALUE =   0.00000     Y-VALUE =   1.00000

REFERENCE OBJECT ANGLE
SCY FANG(YZ-PLANE IN DEGREES)=  -0.481022184962255D+00 ,   0.458839666697080D+0
REF. OBJ. HT. SET BY OBJECT HEIGHT

BASIC LENS DATA (RADIUS MODE)

SURF  RADIUS        THICKNESS          MATERIAL          INDEX        V-NUM
 0    0.00000      0.100000E+21         AIR
 1    0.00000       50.0000             AIR
 2    403.316       18.0000     MATL    GERMPC          4.00310      0.291E+04
 3*   607.823       10.0000             AIR
 3*REFS,STOP
 4   -2418.98       12.0000     MATL    ZNSE            2.40651       104.
 5   -3478.30       365.443             AIR
 6*   0.00000       5.00000     MATL    ZNSE            2.40651       104.
 6*Special
 7    0.00000       4.00000             AIR
 8    0.00000       1.00000             AIR
 9    0.00000       0.00000             LAST SURFACE

NO CONIC OR 4th through 10th ORDER ASPHERIC DATA
NO 12th through 20th ORDER ASPHERIC DATA

REFRACTIVE INDEX DATA (WAVELENGTHS #1 TO #5)

SURF    N1              N2              N3              N4              N5
 2 MATL          GERMPC
 2    4.00587        4.00310        4.00207        1.00000        1.00000
 4 MATL          ZNSE
 4    2.41922        2.40651        2.39302        1.00000        1.00000
 6 MATL          ZNSE
```

6	2.41922	2.40651	2.39302	1.00000	1.00000

NO CLEAR APERTURE OR OBSCURATION DATA

WAVL NBR	1	2	3	4	5
WAVELENGTH	7.6000	10.000	12.000	0.0000	0.0000
SPECTRAL WT	1.000	1.000	1.000	0.000	0.000
WAVL NBR	6	7	8	9	10
WAVELENGTH	0.0000	0.0000	0.0000	0.0000	0.0000
SPECTRAL WT	0.000	0.000	0.000	0.000	0.000

NO TILT AND DECENTER DATA

SPECIAL SURFACE DATA
SURFACE = 6 SPECIAL SURFACE TYPE = 4- ON
SINUSOIDAL ERROR SURFACE

1ST PEAK TO VALLY ERROR (WAVES)	=	0.0000000	
1ST X-PERIOD (SPATIAL FREQUENCY)	=	3.0000000	MM
1ST Y-PERIOD (SPATIAL FREQUENCY)	=	3.0000000	MM
2ND PEAK TO VALLY ERROR (WAVES)	=	0.0000000	
2ND X-PERIOD (SPATIAL FREQUENCY)	=	0.0000000	MM
2ND Y-PERIOD (SPATIAL FREQUENCY)	=	0.0000000	MM
3RD PEAK TO VALLY ERROR (WAVES)	=	0.0000000	
3RD X-PERIOD (SPATIAL FREQUENCY)	=	0.0000000	MM
3RD Y-PERIOD (SPATIAL FREQUENCY)	=	0.0000000	MM
4TH PEAK TO VALLY ERROR (WAVES)	=	0.0000000	
4TH X-PERIOD (SPATIAL FREQUENCY)	=	0.0000000	MM
4TH Y-PERIOD (SPATIAL FREQUENCY)	=	0.0000000	MM
5TH PEAK TO VALLY ERROR (WAVES)	=	0.0000000	
5TH X-PERIOD (SPATIAL FREQUENCY)	=	0.0000000	MM
5TH Y-PERIOD (SPATIAL FREQUENCY)	=	0.0000000	MM

NO CONFIG DATA

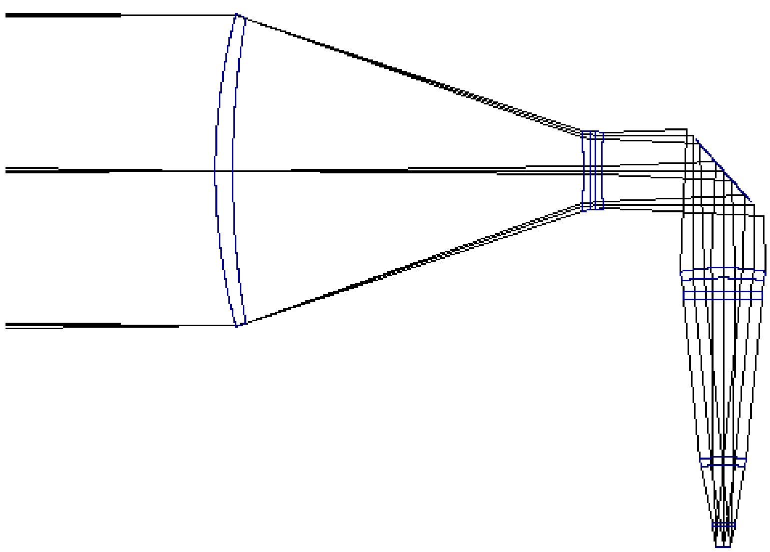

JH 400mm F3
UNITS = MILLIMETERS

YZ-PLANE FIRST ORDER OPERATING CONDITIONS

EFL	BFD	F-NUM	LENGTH	GIH
-400.25	0.0000	-3.0322	181.43	3.4892

REF OBJ Y-HT	REF AP Y-HT	OBJ SF#	REF SF#	IMG SF#
-0.872687E+18(0.5000 DG)	64.23	0	3	21

```
REF OBJ X-HT                    REF AP X-HT         OBJ SF#  REF SF#  IMG SF#
-0.872687E+18( 0.5000     DG)      64.23                 0        3       21
EVALUATION MODE IS FOCAL
THE CURRENT APERTURE STOP SURFACE IS SURFACE #   3

SEMI-APERTURE REFERENCE RAY HEIGHT AT SURFACE #1
SAY(YZ-PLANE IN LENS UNITS) =    0.660000000000000D+02

THERE ARE CURRENTLY            3 ANALYSIS FIELD POSITIONS DEFINED
UNITS ARE DEGREES
POS # =  1 X-VALUE =   0.00000     Y-VALUE =   0.00000
POS # =  2 X-VALUE =   0.00000     Y-VALUE =  0.500000
POS # =  3 X-VALUE =   0.00000     Y-VALUE =   1.00000

REFERENCE OBJECT ANGLE
SCY FANG(YZ-PLANE IN DEGREES)=   0.500000000000000D+00 ,   0.000000000000000D+0
REF. OBJ. HT. SET BY OBJECT ANGLE

BASIC LENS DATA (RADIUS MODE)

SURF  RADIUS        THICKNESS          MATERIAL          INDEX        V-NUM
 0    0.00000      0.100000E+21         AIR
 1    0.00000       99.0190             AIR
 2    227.381       8.12000     MATL    GERMSC          4.00506      0.278E+04
 3*   333.530       166.266             AIR
 3*REFS,STOP
 4   -358.945       3.30100     MATL    AMTIR3          2.60880       488.
 5    358.945       1.98000             AIR
 6    345.049       3.30100     MATL    GERMSC          4.00506      0.278E+04
 7    153.711       57.6030             AIR
 8    0.00000       0.00000             AIR
 9*   0.00000       0.00000             REFL
 9*Tilt
10    0.00000       0.00000             AIR
11    0.00000      -40.9280             AIR
12   -116.051      -4.29100     MATL    GERMSC         -4.00506      0.278E+04
13   -173.835      -5.77600             AIR
14    1066.11      -3.36100     MATL    AMTIR3         -2.60880       488.
15    0.00000      -66.3430             AIR
16   -71.0630      -3.36100     MATL    GERMSC         -4.00506      0.278E+04
17   -85.7510      -24.4250             AIR
18    0.00000     -0.990000     MATL    GERMSC         -4.00506      0.278E+04
19    0.00000      -8.68852             AIR
20    0.00000       0.00000             AIR
21    0.00000       0.00000             LAST SURFACE

NO CONIC OR 4th through 10th ORDER ASPHERIC DATA
NO 12th through 20th ORDER ASPHERIC DATA

REFRACTIVE INDEX DATA (WAVELENGTHS #1 TO #5)

SURF    N1             N2             N3             N4             N5
 2 MATL          GERMSC
 2    4.00320        4.00398        4.00506        4.00568        1.00000
 4 MATL          AMTIR3
 4    2.60230        2.60550        2.60880        2.61004        1.00000
 6 MATL          GERMSC
 6    4.00320        4.00398        4.00506        4.00568        1.00000
12 MATL          GERMSC
12   -4.00320       -4.00398       -4.00506       -4.00568       -1.00000
14 MATL          AMTIR3
14   -2.60230       -2.60550       -2.60880       -2.61004       -1.00000
16 MATL          GERMSC
16   -4.00320       -4.00398       -4.00506       -4.00568       -1.00000
18 MATL          GERMSC
18   -4.00320       -4.00398       -4.00506       -4.00568       -1.00000

NO CLEAR APERTURE OR OBSCURATION DATA

WAVL NBR          1             2             3             4             5
```

WAVELENGTH	10.000	9.0000	8.0000	7.6000	0.0000
SPECTRAL WT	1.000	1.000	1.000	1.000	0.000
WAVL NBR	6	7	8	9	10
WAVELENGTH	0.0000	0.0000	0.0000	0.0000	0.0000
SPECTRAL WT	0.000	0.000	0.000	0.000	0.000

SURF TYPE	ALPHA	BETA	GAMMA	RETURN SURF
9 TILT BEN	45.000000	0.0000000	0.0000000	

NO SPECIAL SURFACE DATA

NO CONFIG DATA

	Volume cc	Density g/cc	Mass g
Element surf 2 to 3	90.714718	5.327000	483.237305
Element surf 4 to 5	3.456161	4.700000	16.243957
Element surf 6 to 7	3.073704	5.327000	16.373620
Element surf 12 to 13	5.111588	5.327000	27.229431
Element surf 14 to 15	4.248251	4.700000	19.966779
Element surf 16 to 17	1.354820	5.327000	7.217128
Element surf 18 to 19	0.087779	5.327000	0.467597

Total Mass: 570.735817

Appendix C: Discrete Fourier Transform

The Fourier Transform can be applied to a digital sequence of numbers of finite dimension, in which case it is called the Discrete Fourier Transform (DFT). This is the typical case in situations where the point spread function (PSF) of a point source input, or perhaps the Line Spread Function (LSF) of a sharp edge target, is sampled and read out as a set of digital pixel values. In a digital imaging system, a row or columns of a fixed number of pixels (γ) will create a sequence of digital number values x per the set given by $x_n = \{ x_0, x_1, x_2, ... x_{\gamma-1} \}$. The DFT of this series is going to be another series of equivalent number of elements, $X_k = \{ X_0, X_1, X_2, ... X_{\gamma-1} \}$ where the transformation function in one dimension is as follows:

$$\mathscr{F}(x_n) = X_k = \sum_n f(x_n)\, e^{-j(2pi)(kn\not{}\gamma)}$$

where n and k are position indices in each respective series and the [⸝] symbol denotes division in the exponential terms. It is important to realize that every single value for X_k is going to be a function involving *all* values from the original input sequence x_n. Generation of all the sequence values for X_k will thus require iteration of the formula with an increase in step k = 0, 1, 2 ..., γ-1. Furthermore, the numerical results are typically expressed in the complex form (x + jy) which requires applying Euler's formula relating sinusoids to the exponential. Euler's formula is given generally by $e^{j\Phi} = \cos(\phi) + j\sin(\phi)$.

It is a somewhat tedious work to do these calculations by hand, and less prone to error when done via a computer, but a manual demonstration with a small sequence of number values is manageable and instructive to provide the engineer a "hands-on" feel for how the calculation is performed. Consider a sequence of digital pixel values expressed as a one-dimensional matrix as follows: $a_n = \{ a_0, a_1, a_2, a_3, a_4 \}$ with actual numerical values [0, 1, 3, 1, 0]. This matrix has five terms, therefore γ = 5 and $\gamma^{-1} = 0.2$. The DFT of this matrix (A_k) will also have five terms. In order to provide a worked example for at least one value, the solution for the second term at k = 1 (recall the sequence started with k =0) is provided as follows:

$$\sum_n f(x_n)\, e^{-j(2pi)(kn\not{}\gamma)} \quad \text{at } k = 1 \text{ and and } \gamma^{-1} = 0.2 \text{ for each } n = 0, 1, 2, 3, 4$$

$$A_1 = (0)\, e^{-j(2pi)(0)} + (1)\, e^{-j(2pi)(1)(1)(0.2)} + (3)\, e^{-j(2pi)(1)(2)(0.2)} + (1)\, e^{-j(2pi)(1)(3)(0.2)} + (0)\, e^{-j(2pi)(1)(4)(0.2)}$$

where (2pi) is equivalent to (2π). The arithmetic can be simplified within the exponents as follows:

$$A_1 = (0)\, e^{(0)} + (1)\, e^{-j(2pi)(0.2)} + (3)\, e^{-j(2pi)(0.4)} + (1)\, e^{-j(2pi)(0.6\ )} + (0)\, e^{-j(2pi)(.0.8)}$$

There are now only three remaining non-zero terms. At this point a conversion via Euler's formula can be made as follows:

A_2 = [cos(-0.4π)+ jsin(-0.4π)]+ (3)[cos(-0.8π)+jsin(-0.8π)] + [cos(-1.2π)+jsin(-1.2π)]
A_2 = [0.3090 - j0.9511] + (3)[-0.8090 - j0.5878] + [-0.8090 + j0.5878]
A_2 = [0.3090 - 2.427 - 0.8090] + j[-0.9511 - 1.7634 + 0.5878]
A_2 = -2.927 - j2.1267

Repeating the same steps for all the other values of A_k yields the following complex valued matrix (with some extra precision in the decimal values):

A_k = [5.0000 + j0.0000, -2.9271 - j2.1266, 0.4271 + j1.3143, 0.4271 - j1.3143, -2.9271 + j2.1266]

The matrix A_k is now in rectangular coordinates (x, y) located along the real axis (Re) and the imaginary axis (Im). Those same points can be located by converting to cylindrical coordinates based on a radial distance (r) from the origin and an angle (ϕ). Reference the following Figure C-1:

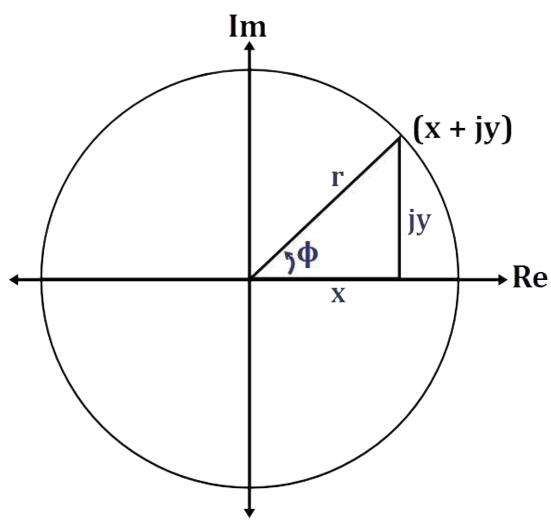

Figure C-1: Real & Imaginary Relationships

The absolute value of a complex number r = x + jy is the value $|r|=\sqrt{(x^2 + y^2)}$ where x and y are real numbers. The absolute value of a complex number is also called a complex modulus. For example, the second term in matrix A_k is (-2.9271 - 2.1266i), therefore $SQRT[(-2.9271)^2 + (-2.1266)^2]$ = SQRT(13.09) = 3.618. Repeating this for all terms in the matrix yields the following:

Modulus(A_k) = [5.0000, 3.6180, 1.3820, 1.3820, 3.6180]

The modulus can be normalized to the maximum value within the sequence to give the MTF. The spatial frequency is in units of cycles/pixel:

MTF(A_k) = [1.0000 0.7236 0.2764 0.2764 0.7236]

The spatial frequency scale for the MTF is determined by the pixel pitch sample spacing used in the original data set, $a_n = \{ a_0, a_1, a_2, a_3, a_4 \}$. Assume these data points were gathered by a detector array with uniformly spaced pixel pitch (P) of 0.028 mm. Thus, point a_0 begins the sequence at 0.0 mm, then a_1 occurs at 0.028 mm, a_2 at 0.056 mm, and so on. The transform of the original sequence, A_k, is now in inverse units $(P^{-1}) = (0.028)^{-1}$ = 35.7143 mm^{-1} for which there are $\gamma = 5$ samples total. Therefore, the frequency interval $(\Delta\xi)$ for each point in the MTF curve is

$$(\Delta\xi) = (P^{-1}) \cdot (\gamma^{-1}) = 35.7 \div 5 = 7.143 \text{ cy/mm}$$

The spatial frequency interval $(\Delta\xi)$ is then multiplied by position index (k) to obtain the specific spatial frequency value for each individual point in the matrix $MTF(A_k)$ as shown below in the following Figure C-2

$MTF(A_k)$	1.0000	0.7236	0.2764	0.2764	0.7236
k	0	1	2	3	4
ξ (cy/mm)	0.000	7.143	14.286	21.428	28.571

Figure C-2: MTF Frequency Scale Example for DFT

While the values of a_n were arbitrary in this example, consider the similarity to an optical MTF where the wavelength λ = 0.010 mm and F# = 3.0. The Airy Disk diameter = 2.4 4 $\cdot \lambda \cdot$ F# = 0.0732 mm, and the corresponding optics MTF cutoff is $(\lambda \cdot F\#)^{-1}$ = 33.3 cy/mm.

The cylindrical coordinate phase is the angle (ϕ) of the radial vector, defined as ϕ = arctan(y/x). The angular units are radians. Again as an example for the second term in matrix A_k the phase angle solution is ϕ = arctan[(-2.1266) ÷ (-2.9271)]. NB: to do this calculation by hand with a calculator it is important to realize the quadrant in which the point is located. Negative values along both axes place this point in the 3rd quadrant, so the angle must be between π and 3π/2 radians. Calculating on a hand calculator gives arctan[(-2.1266) ÷ (-2.9271)] = arctan[0.7265] = 0.628 radians. Now shift into the 3rd quadrant by adding 0.628 + π = 0.628 + 3.14159 = 3.77 radians. Equivalently this can be expressed as 3.77 - 2π = -2.513 radians. The results for all the Phase terms with proper quadrant locations such as used in FreeMAT or MATLAB software packages are as follows:

$$\text{Phase}(A_k) = 0 \quad -2.5133 \quad 1.2566 \quad -1.2566 \quad 2.5133$$

REFERENCE:

Efkeman A. & Spande R., "Testing and Specification for Infrared (IR) Optics for Infrared Imaging", Proc. of SPIE Vol. 0181, Contemporary Optical Systems & Components Specifications, ed. Robert E. Fischer (Apr 1979) Copyright SPIE.